

Processing, structure and thermo-mechanical properties of reclaimed nanoclay, and its application in polyamide 6 and low-density polyethylene nanocomposites.

SIDDIQUE, S.A.

2020

The author of this thesis retains the right to be identified as such on any occasion in which content from this thesis is referenced or re-used. The licence under which this thesis is distributed applies to the text and any original images only – re-use of any third-party content must still be cleared with the original copyright holder.



**PROCESSING, STRUCTURE AND THERMO-MECHANICAL
PROPERTIES OF RECLAIMED NANOCCLAY AND ITS
APPLICATION IN POLYAMIDE 6 AND LOW-DENSITY
POLYETHYLENE NANOCOMPOSITES**

A thesis submitted to The Robert Gordon University for the degree of
Doctor of Philosophy (PhD) in the Faculty of Engineering

Shohel Ahmed Siddique

School of Engineering

Robert Gordon University

April 2020



ROBERT GORDON
UNIVERSITY ABERDEEN

School of Engineering

PhD THESIS

SHOHEL AHMED SIDDIQUE

PROCESSING, STRUCTURE AND THERMO-MECHANICAL
PROPERTIES OF RECLAIMED NANOCCLAY REINFORCED
POLYAMIDE 6 AND LOW-DENSITY POLYETHYLENE
NANOCOMPOSITES

Supervisors: Professor James Njuguna
Dr Kyari Yates

April 2020

© Robert Gordon University, Aberdeen, 2020. All right reserved. No part of this publication
may be produced without the written permission of the copyright owner

This thesis is submitted in partial fulfilment of the requirements for the degree of Doctor of
Philosophy

Declaration

I hereby declare that the research report in this thesis is original and have been completed independently by myself (Shohel Ahmed Siddique), under the supervision of Professor James Njuguna and Dr Kyari Yates. This PhD thesis has not been submitted for the award of any other degree or professional qualification.

Where other sources are quoted full references are given.

Shohel Ahmed Siddique

April 2020

Dedication

This thesis is dedicated to:

Late Nurul Haque Prodhan;

Late M.A. Baten Miah;

Late Setara Begum

And

Late A.K.M. Aminul Haque

Acknowledgement

First and foremost, I would like to express my endless gratefulness to Allah S.W.T. for granting me inspiration and strength to complete this thesis.

I would like thank my supervisor Professor James Njuguna for giving me the opportunity to carry out this study and for supporting me throughout my 4 years research work. Your knowledge, advices and patience has given me learning inspiration of new techniques and understanding different aspects of this research project. Surely, completion of this thesis journey would not be possible without your help, support and guidance.

I am thankful to my loving wife for her endless love and support throughout this journey. I am thankful to my parents (Abu Baker Siddique and Umme Kulsum Khanam), my wife Rozlen, my sons (Zawaad Siddique and Abu Baker Siddique), my brother Farukh Ahmed Siddique and my sister Rehena Siddiqua Happy for their unconditional support, financially and morally.

My appreciation extends to the lecturers, technicians, friends and colleagues in the School of Engineering, School of Pharmacy and Life Sciences especially Dr Kyari Yates, Dr Kerr Matthews, Dr Laurie Smith, Lorraine Bakah-Kwoffie, Kofi Addae-Afoakwa, Urenna Adegbotulu, Grant Smith, Adam Novak, Emin Guliyev, Mr Allan MacPherson, Mr David Smith, Dr Laszlo Csetenyi, Dr Ken Leung and Dr Kristof Starost for their support throughout my research study.

Abstract

Oil-based mud (OBM) wastes generated every year all over the world and remain a serious challenge for the oil and gas industry. The potential solution of this global problem is either to destroy these hazardous chemicals completely which is a big challenge or to use/utilise them for beneficial applications. The aim of this thesis therefore is to develop a detailed understanding of the synergistic effects of different clay minerals that exist in OBM waste in influencing structural, morphological, rheological and thermo-mechanical behaviour of LDPE and PA6 nanocomposite materials.

A critical literature review was conducted covering oil-based mud (OBM) waste treatments, polymer nanocomposites and their manufacturing, thermal degradation behaviour and mechanical performance. This is followed by a detailed characterisation of OBM waste to determine elemental composition, structural and thermal properties. To evaluate their performance as a filler in polymer composites, both mechanical and thermal properties of polyamide 6 (PA6) and low-density polyethylene (LDPE) based nanocomposites were manufactured through the process of melt compounding followed by injection and compression moulding with different amounts (wt%) of oil-based mud fillers (OBMFs).

The study on thermal degradation of LDPE/OBM slurry shows that the nanocomposites with higher percentage filler contents in case of 7.5 and 10 wt% decreased the heat capacity value by 33% and 17% in LDPE respectively.

OBM slurry shows superior improvements in storage modulus, loss modulus and damping property ($\tan \delta$) in LDPE matrix compared to those of LDPE/MMT nanocomposites. However, the study shows decrease of tensile and flexural properties for the LDPE/OBM slurry nanocomposites.

The follow up study focused on thermally treated OBM waste (OBMFs) in powder form and their effect on thermo-mechanical properties of LDPE matrix. It was observed that OBMFs was compatible with LDPE matrix which led to a strong interfacial interaction between the clay layers and polymer. Further, the clay minerals present in OBMFs formed chemical bonds in microstructure within the nanocomposites. The OBMFs (10wt %) /LDPE nanocomposite produced highest onset degradation temperature at 5 weight% loss (TD5%) and 50 weight% loss (TD50%) among the nanocomposites. An enhancement of mechanical properties of composites was identified which showed a gain of 14% Young's modulus and 18% increase on tensile strength at 10 wt% OBMFs loading compared to those properties of neat LDPE.

The crystallinity and thermal degradation behaviours of polyamide 6/oil-based mud fillers (PA6/OBMFs) nanocomposites were also investigated. TGA indicates the onset decomposition temperature of D1/2 (half-decomposition) is 16° C higher for PA6 with 10 wt% of OBMFs than that of PA6 and also registered a 47% specific heat capacity reduction. The Youngs' moduli were increased by 42% and 35% in PA6 with 7.5 and 10 wt% OBMFs nanocomposites respectively whereas the tensile strengths were increased by 24% and 16% in PA6 with 7.5 and 10 wt% OBMFs nanocomposites respectively. The flexural strength increased by 26% with the addition of OBMFs from 0 to 10 wt% in PA6 nanocomposites.

In conclusion, a loading amount of 10 wt% OBMFs on both polymer matrices was found to be the most desirable enhanced mechanical and thermal stability properties. However, 10 wt% OBMFs showed increased storage modulus and drop in loss modulus in both LDPE and PA6 matrices leading to conclusion that OBMFs improves thermo-mechanical properties in LDPE and PA6 matrices in dynamic condition. Considering findings from this study, this material shows high potential for low cost structural insulation materials as an alternative of conventional expensive materials. All the proposed treatment techniques presented in literature and in industrial practices dealing with OBM waste, passes pollution from one stage to another. This study explores the opportunity to utilise the useful reclaimed clay minerals from OBM waste as filler in nanocomposite manufacturing.

Keywords: Sustainable waste management, resource recovery from waste, reclaimed nanoclay, oil based mud waste characterisation, LDPE-OBMFs nanocomposites, PA6-OBMFs nanocomposites, thermal degradation, mechanical properties, dispersion characteristics and interfacial adhesion.

Achievements

Journal articles:

- Siddique S, Kwoffie L, Addae-Afoakwa K, Yates K, Njuguna J. The crystallinity and thermal degradation behaviour of polyamide 6/Oil Based Mud Fillers (PA6/OBMFs) nanocomposites. *Polymer Degradation and Stability*. 2019 Jan 1; 159:139-52.
- Siddique S, Smith GD, Yates K, Mishra AK, Matthews K, Csetenyi LJ, Njuguna J. Structural and thermal degradation behaviour of reclaimed clay nano-reinforced low-density polyethylene nanocomposites. *Journal of Polymer Research*. 2019 Jun 1; 26(6):154.
- Siddique S, Kwoffie L, Addae-Afoakwa K, Yates K, Njuguna J. Valorisation of spent oil based mud: an opportunity to turn a hazardous waste to wealth, *Journal of waste management and research*, 2019 (Submitted).
- Siddique S, Yates K, Njuguna J. Influence of a novel nanoclay on the mechanical and rheological behaviour of low density polyethylene nanocomposites, *Journal of Waste and Biomass Valorization*, 2020 (Submitted).
- Siddique S, Yates K, Njuguna J. The influence of reclaimed nanoclay from OBM waste on the mechanical and rheological behaviour of PA6/OBMFs nanocomposites, *Journal of Petroleum Science and Engineering*, 2020 (Submitted).

Conference proceedings:

- Siddique S, Kwoffie L, Addae-Afoakwa K, Yates K, Njuguna J. Oil based drilling fluid waste: an overview on highly reported but less explored sink for environmentally persistent pollutants, *IOP conference series: Materials Science and Engineering* 195, 2017, 012008.
- Characterisation of oil based mud waste to explore the possibility in transforming waste into a value added product, *NAXOS 2018 conference proceedings* available online at: <http://uest.ntua.gr/naxos2018/proceedings/proceedings.html#friday>
- Shohel Siddique and James Njuguna. Oil-based Mud Waste Reclamation and Utilisation in Low Density Polyethylene (LDPE) Composites, *Wasteengg*, 8th International Conference on Engineering for Waste and Biomass Valorisation, Guelph, Canada.

Posters:

- Poster presentation at The 3rd International Conference on Structural Nano composites 'Nanostruc 2016' conference- Siddique S, Kwoffie L, Addae-Afoakwa K, Yates K, Njuguna J. Thermal Stability, Flame Retardancy and Mechanical Properties of Polyamide/Montmorillonite Nanocomposites Prepared By Melt Processing.

- Poster presentation at The 6th International Conference on Sustainable Solid Waste Management 'NAXOS 2018' conference- Thermo-chemical characterisation of Oil Based Mud wastes.
- Poster presentation at The 4th International Conference on Structural Nano Composites 'Nanostruc 2018' conference- Mechanical, Thermal, and Flammability Behaviour of Low Density Polyethylene - Oil Based Mud Fillers Nanocomposites.

List of Abbreviations

API	American petroleum institute
ATR-FTIR	Attenuated total reflection-fourier transform infra-red
CNT	Carbon nanotube
COCs	Chemicals of concerns
DSC	Differential scanning calorimetry
EDXA	Energy dispersive X-ray analysis
EMOBMs	Enhanced mineral oil-based muds
EVA	Ethylene-vinyl acetate
HDPE	High-density polyethylene
ICP-OES	Inductively coupled plasma optical emission spectrometry
LDPE	Low density polyethylene
LLDPE	Linear low density polyethylene
LTMOs	Low toxicity mineral oils
MAF	Mobile amorphous fraction
MMT	Montmorillonite
NADM	Non-aqueous drilling mud
NCS	Norwegian continental shelf
NORM	Naturally occurring radioactive materials
OBM	Oil based mud
OBFMs	Oil based mud fillers
OMMT	Organically modified montmorillonite
OSPAR	Oslo and Paris commission
OWR	Oil/water ratio
PA6	Polyamide 6
PAA	Polyacrylic acid
PAHs	Polycyclic aromatic hydrocarbons
PAN	Polyacrylonitrile
PE	Polyethylene
PEMA	Poly(ethyl methacrylate)
PEO	Polyethylene oxide
PLA	Poly(lactic acid)
PLS	Polymer/layered silicate

PP	Polypropylene
PVA	Polyethylene vinyl alcohol
PVOH	Polyvinyl alcohol
PVP	Polyvinyl pyrrolidone
PW	Produced water
RAF	Rigid amorphous fraction
SAED	Selected area electron diffraction
SAXD	Small angle X-ray diffraction
SBM	Synthetic based drilling muds
SEM	Scanning electron microscopy
TCC	Thermomechanical cuttings cleaner
TCE	Tetrachloroethylene
TEM	Transmission electron microscopy
TGA	Thermogravimetric analysis
UKCS	United Kingdom Continental Shelf
U.S. EPA	United States environmental protection agency
WAXD	Wide angle X-ray diffraction
WBM	Water-based mud
WD	Working distance
WFD	Waste framework directive
XRD	X-ray powder diffraction

List of Tables

Table 2. 1 NADM Classification Groups and Descriptions (KOH and TEH, 2011)	10
Table 2. 2 Types of Waste Discharges from Exploration and Production (Bashat, 2002)	11
Table 2. 3 Concentration of metals in Water Based Mud and Drill Cuttings from two offshore platforms in Southern California (Phillip et al., 1998).	15
Table 2. 4 List I and II pollutants in environment (DIRECTIVE HAT, 1976)	21
Table 2.5 Elemental composition of typical water-based drilling fluid constituents (mg/Kg) (Onwukwe and Nwakaudu, 2012)	23
Table 3.1 Elemental analysis of raw OBM waste using ICP-OES	53
Table 3. 2 EDXA analysis of OBM waste powder	54
Table 3.3 Endothermic reactions of different clay minerals at different temperature stages at TGA (Grim and Rowland, 1942)	59
Table 4.1 EDXA of OBM waste powder, neat LDPE, LDPE/MMT and LDPE/OBM slurry nanocomposites	77
Table 4.2 XRF analysis of OBM waste powder, neat LDPE, LDPE/MMT and LDPE/OBM slurry nanocomposites	78
Table 4.3 Structural composition and thermal properties details of neat LDPE, LDPE/MMT and LDPE/OBM slurry nanocomposites	84
Table 4.4 TGA analysis at different decomposition stages of LDPE, LDPE/MMT and LDPE/OBM slurry nanocomposites	87
Table 6.1 ATR-FTIR peak assignments of LDPE and its nanocomposites	110
Table 6.2 Structural composition and thermal properties details of LDPE and its nanocomposites	121
Table 6.3 TGA analysis at different decomposition stages of LDPE and its nanocomposites with different clay contents	125
Table 6.4 Mechanical properties of LDPE and its nanocomposites	129
Table 7.1 ATR FT-IR peak assignments (Chen et al., 2004; Pramoda et al, 2003; Socrates, 2004 and Vasanthan and Salem, 2001)	136
Table 7.2 TGA analysis at different decomposition stages of PA6 and its nanocomposites with different clay loadings	146
Table 7.3 % of crystallinity of PA6 and its nanocomposite using DSC	150
Table 7.4 Heat capacity of PA6 and its nanocomposite	151
Table 7. 5 TIF determination using DSC	152

List of Figures

Figure 1.1 Methodology overview, workflow and critical analysis of the research showing the sample preparation and experimental procedures	1.4
knowledge and motivation for research	4
Figure 2.1 Water Based Mud Composition (Melton et al., 2003)	9
Figure 2.2 non-aqueous Drilling Mud compositions (Melton et al., 2003)	10
Figure 2.3 Percentage of individual chemical constituents present in OBM and WBM discharge adapted from Hudgins (Hudgins and Charles, 1994)	13
Figure 2.4 Waste Generated Offshore (Oil & Gas UK 2015)	17
Figure 2.5 Cuttings Discharged to Sea (Oil & Gas UK 2015)	17
Figure 2.6 Drill cuttings in 1 cm scale (Colliver and Carter, 2000)	19
Figure 2.7 Cuttings Movement in Drilling Mud (Oil & Gas UK, 2015)	19
Figure 2.8 Presentation of 3d structure of tetrahedral and octahedral sheets forming 1:1 and 2:1 layer clay (Christidis, 2011)	26
Figure 2.9 SEM images of: (a) kaolinite; (b) tubular crystals of halloysite; (c) spheroidal crystals of halloysite; (d) wavy subhedral montmorillonite crystals; (e) flaky illite crystals and (f) fibrous illite (Christidis, 2011)	27
Figure 2.10 TEM micrographs of: (a) kaolinite; (b) tubular crystals of halloysite; (c) wavy subhedral montmorillonite crystals; (d) illite crystals	28
Figure 2.11 XRD pattern of: (a) kaolinite (Kłosek-Wawrzyn et al. 2013); (b) halloysite (Falcón et al. 2015); (c) montmorillonite (Djowe et al. 2013); (d) illite (Poppe et al. 2001) and (e) different clay minerals under different phase condition (Zhao et al., 2018)	30
Figure 2.12 Alkyl chain sandwiched in layered silicates forming: a) lateral monolayer; b) lateral bilayer; c) paraffinic mono layer and d) paraffinic bilayer (Alexandre and Dubois, 2000)	33
Figure 2.13 Alkyl chain aggregation model: a) lateral monolayer of short alkyl chain; b) lateral bilayer with in-plane disorder; and c) internal order increment by the formed internal chain aggregation. (Alexandre and Dubois, 2000)	33
Figure 2.14 Schematic presentation of different polymer/layered silicates nanocomposites (Ray and Okamoto, 2003)	34
Figure 2.15 Schematic illustrations of conventional micro and nanoscale manufacturing approach (Gao, 2004)	35
Figure 2.16 Schematic illustration of clay platelets expansion to improve interaction between polymer chains and clay platelets (Fischer, 2003)	36
Figure 2.17 A schematic illustration of solution processing (Gou et al., 2012)	36

Figure 2.18 A schematic illustration of <i>In-situ</i> polymerisation process (Guo et al., 2014)	37
Figure 2.19 A schematic illustration of template synthesis process of PAN-inorganic nanocomposites (Fernández-Saavedra et al., 2009)	38
Figure 2.20 A schematic illustration of melt compounding process (Guo et al., 2018)	39
Figure 3.1 SEM images of (a) Montmorillonite as a reference material and (b) OBM waste dry powder	48
Figure 3.2 ATR-FTIR full scale spectra of (a) OBM waste slurry; (b) OBM waste residue after TGA analysis and (c) OBM waste dry powder	50
Figure 3.3 WAXD patterns of (a) MMT and (b) OBM waste	52
Figure 3.4 DSC thermograms of OBM waste at (a) glass transition temperature (T _g); (b) melting temperature (T _m) and (c) crystallisation temperature (T _c)	56
Figure 3.5 TGA thermograms of OBM waste at (a) onset degradation at 5% weight loss; (b) onset degradation at 10% weight loss; (c) onset degradation at 65% weight loss and (d) residue at 1000°C	58
Figure 4.1 Manufacturing of LDPE/MMT and LDPE/OBM slurry nanocomposites using (a) LDPE pellets; (b) MMT filler; (c) OBM slurry; (d) uniform mixing of LDPE and OBM slurry; and (e) LDPE/OBM slurry compounds in pellet forms after extrusion	61
Figure 4.2 SEM images of (a) neat LDPE; (b) LDPE with 2.5 wt% MMT; (c) LDPE with 5.0 wt% MMT; (d) LDPE with 7.5 wt% MMT and (e) LDPE with 10.0 wt% MMT	66
Figure 4.3 SEM images of (a) neat LDPE; (b) LDPE with 2.5 wt% OBM slurry; (c) LDPE with 5.0 wt% OBM slurry; (d) LDPE with 7.5 wt% OBM slurry and (e) LDPE with 10.0 wt% OBM slurry	69
Figure 4.4 Comparison of ATR-FTIR common scale spectra of LDPE and LDPE/MMT nanocomposites	71
Figure 4.5 Comparison of ATR-FTIR common scale spectra of LDPE and LDPE/OBM slurry nanocomposites	72
Figure 4.6 WAXD patterns of (a) MMT and (b) OBM waste	73
Figure 4.7 Different XRD patterns of LDPE and LDPE/MMT nanocomposites at (a) WAXD; (b) SAXD	74
Figure 4.8 Different XRD patterns of LDPE and LDPE/OBM slurry nanocomposites at (a) WAXD; (b) SAXD	76

Figure 4.9 DSC thermograms of LDPE and LDPE/MMT nanocomposites at (a) glass transition temperature (T _g); (b) melting temperature (T _m) and (c) crystallisation temperature (T _c)	80
Figure 4.10 DSC thermograms of LDPE and LDPE/OBM slurry nanocomposites at (a) glass transition temperature (T _g); (b) melting temperature (T _m) and (c) crystallisation temperature (T _c)	83
Figure 4.11 TGA thermograms of neat LDPE and LDPE/MMT nanocomposites	86
Figure 4. 12 TGA thermograms of neat LDPE and LDPE/OBM slurry	87
Figure 5.1 Array of tensile test specimen of (a) neat LDPE and LDPE/MMT nanocomposites; (b) neat LDPE and LDPE/OBM slurry nanocomposites and presentation of (c) tensile test set up and (d) observation of plastic deformation through the reduced area of sample	91
Figure 5.2 Array of 3-point bending test specimen of (a) neat LDPE and LDPE/MMT nanocomposites; (b) neat LDPE and LDPE/OBM slurry nanocomposites and (c) observation of 3-point bending test of sample	92
Figure 5.3 Stress-strain curves of (a) neat LDPE and LDPE/MMT and (b) neat LDPE and LDPE/OBM slurry nanocomposites	94
Figure 5.4 Comparison of tensile strength between LDPE/MMT and LDPE/OBM slurry nanocomposites considering tensile strength of neat LDPE as a baseline	94
Figure 5.5 Comparison of modulus of elasticity in tension of neat LDPE, LDPE/MMT and LDPE/OBM slurry nanocomposites	95
Figure 5.6 Comparison of percentage elongation at yield of neat LDPE, LDPE/MMT and LDPE/OBM slurry nanocomposites	96
Figure 5.7 Flexural stress-strain curves from 3-point bend test of neat LDPE, LDPE/MMT and LDPE/OBM slurry nanocomposites	97
Figure 5.8 Comparison of flexural strength of neat LDPE, LDPE/MMT and LDPE/OBM slurry nanocomposites	98
Figure 5. 9 (a) Comparison of modulus of elasticity in bending of neat LDPE, LDPE/MMT and LDPE/OBM slurry nanocomposites; (b) a schematic illustration of applied force in tension and bending test and the distribution of MMT and OBM slurry nanoplatelets through the sample	99
Figure 5.10 Influence of applied shear stress on the storage modulus of (a) neat LDPE and LDPE/MMT and (b) neat LDPE and LDPE/OBM slurry nanocomposites	101

Figure 5.11 Influence of applied shear stress on the loss modulus of (a) neat LDPE and LDPE/MMT and (b) neat LDPE and LDPE/OBM slurry nanocomposites	103
Figure 5. 12 Influence of applied shear stress on damping property of (a) neat LDPE and LDPE/MMT and (b) neat LDPE and LDPE/OBM slurry nanocomposites	104
Figure 6.1 Comparison of ATR-FTIR common scale spectra of LDPE and its nanocomposite	109
Figure 6.2 EDXA spectra of (a) LDPE; (b) LDPE+2.5 wt% OBMFs; (c) LDPE+5 wt% OBMFs; (d) LDPE+7.5 wt% OBMFs and (e) LDPE+10 wt% OBMFs	111
Figure 6.3 SEM images of (a) OBMFs; (b) neat LDPE; (c) LDPE with 2.5 wt% OBMFs; (d) LDPE with 5.0 wt% OBMFs; (e) LDPE with 7.5 wt% OBMFs and (f) LDPE with 10.0 wt% OBMFs	115
Figure 6.4 Different XRD patterns of LDPE and its nanocomposites at (a) WAXD; (b) SAXD; (c) WAXD patterns of MMT and OBMFs and (d) potential peak initiation in LDPE polymer matrix due to addition with OBMFs	116
Figure 6.5 TEM micrographs of (a) LDPE with 2.5 wt% OBMFs; (b) LDPE with 5.0 wt% OBMFs; (c) LDPE with 7.5 wt% OBMFs ;(d) LDPE with 10.0 wt% OBMFs nanocomposite and (e) schematic diagram of nanoparticles orientation and tensile stress direction	118
Figure 6.6 DSC thermograms of LDPE and its nanocomposites at (a) T _g ; (b) T _m and (c) T _c	120
Figure 6.7 TGA thermograms of LDPE and its nanocomposites at: (a) onset degradation at 5% weight loss; (b) onset degradation at 50% weight loss; (C) D-half (50% weight loss) time and (d) residue at 1000°C	124
Figure 6.8 Variation of (a) storage modulus, (b) loss modulus and (c) damping intensity (tanδ) with temperature of LDPE and its nanocomposites	127
Figure 6.9 Tensile stress-strain curves of neat LDPE and its nanocomposites	129
Figure 7.1 Flow diagram of PA6/OBMFs nanocomposites sample manufacturing process	134
Figure 7.2 Comparison of FTIR full scale spectra of PA6 and its nanocomposite	135
Figure 7.3 Comparison of FTIR spectra between 1200-525 of PA6 and its nanocomposite	137
Figure 7.4 SEM images of (a) montmorillonite; (b) OBMFs; (c) PA6; (d) PA6 with 2.5 wt% OBMFs; (e) PA6 with 5.0 wt% OBMFs; (f) PA6 with 7.5 wt% OBMFs; and (g) PA6 with 10.0 wt% OBMFs	139

Figure 7.5 EDX spectra of (a) OBMFs; (b) PA6; (c) PA6+2.5 wt% OBMFs; (d) PA6+5.0 wt% OBMFs; (e) PA6+7.5 wt% OBMFs and (f) PA6+10.0 wt% OBMFs	142
Figure 7.6 TGA of PA6 and PA6/OBMFs nanocomposites at: (a) complete thermograms of all samples; (b) 250°C; (c) D ½; (d) 600 °C	145
Figure 7.7 DSC thermograms of PA6 and its nanocomposites at (a) T _g ; (b) T _m and (c) T _c	149
Figure 7.8 Relation between TIF and dispersion behaviour of OBMFs in PA6 matrix	153
Figure 7.9 Schematic diagram of OBMFs platelets associated with MAF and RIF of PA6 matrix	153
Figure 7.10 WAXD patterns of (a) OBMFs and PA6/OBMFs nanocomposite in stack form; (b) nanocomposite in common scale; and (c) OBMFs and MMT	155
Figure 7.11 WAXD patterns of (a) mineral composition of different nanocomposite; (b) new peaks identification in nanocomposites	156
Figure 7.12 SAXD patterns of (a) OBMFs and PA6/OBMFs nanocomposite in stack form; (b) nanocomposite in common scale; and (c) smoothed nanocomposite profile	158
Figure 7.13 TEM images of PA6 with 2.5 wt% OBMFs nanocomposites (a) and (b) and PA6 with 10.0 wt% OBMFs nanocomposites (c) and (d)	159
Figure 8.1 Tensile test of PA6/OBMFs nanocomposites: (a) test rig set up and (b) plastic deformation of sample is on progress	162
Figure 8.2 Flexural test of PA6/OBMFs nanocomposites: (a) test rig set up and (b) deformation of sample is on progress	163
Figure 8.3 Impact test of PA6/OBMFs nanocomposites: (a) V-notch sample cutter; (b) a set of 5 samples are on progress for v-notch sample; (c) impact test rig and (d) V-notch sample sitting on sample holder for test	165
Figure 8.4 Tensile test samples before and after the test	167
Figure 8.5 Stress-strain curves of neat PA6 and PA6/OBMFs nanocomposites	167
Figure 8.6 Young's modulus and tensile strength of neat PA6 and PA6/OBMFs nanocomposites with filler loading of 2.5, 5, 7.5 and 10 wt%	168
Figure 8.7 Comparison of percentage elongation at yield of neat PA6 and OBMFs reinforced PA6 nanocomposites	169

Figure 8.8	Presentation of flexural test sample after the test	170
Figure 8.9	Flexural stress-strain curve from 3-point bend test of neat PA6 and PA6/OBMFs nanocomposites with varying OBMFs concentrations	171
Figure 8.10	Comparison of modulus of elasticity in bending and flexural strength of neat PA6 and OBMFs reinforced PA6/OBMFs nanocomposites with varying OBMFs concentrations	172
Figure 8.11	Impact strength of both notched and un-notched neat PA6 and OBMFs reinforced PA6/OBMFs nanocomposites with varying OBMFs concentrations	173
Figure 8.12	Comparison and fracture analysis of Impact test samples	174
Figure 8.13	Dependence of storage modulus on temperature for neat PA6 and OBMFs reinforced PA6/OBMFs nanocomposites with varying OBMFs concentrations	175
Figure 8.14	Dependence of loss modulus on temperature for neat PA6 and OBMFs reinforced PA6/OBMFs nanocomposites with varying OBMFs concentrations	176
Figure 8.15	Dependence of loss factor (tan delta) on temperature for neat PA6 and OBMFs reinforced PA6/OBMFs nanocomposites with varying OBMFs concentrations	177
Figure A. 1	OBM waste	206
Figure A. 2	OBM waste residue after TGA	207
Figure A.3	OBM waste dry powder	208
Figure B.1	Comparison of ATR-FTIR spectra of LDPE and LDPE/MMT nanocomposites	209
Figure B.2	Comparison of ATR-FTIR spectra of LDPE and LDPE/OBM slurry nanocomposites	210
Figure B. 3	FTIR spectra of (a) LDPE; (b) LDPE with 2.5 wt% OBMFs; (c) LDPE with 5.0 wt% OBMFs; (d) LDPE with 7.5 wt% OBMFs; and (e) LDPE with 10.0 wt% OBMFs nanocomposites	211
Figure C.1	ATR-FTIR spectra of PA6	212
Figure C.2	ATR-FTIR spectra of PA6 with 2.5 wt% OBMFs	212
Figure C.3	ATR-FTIR spectra of PA6 with 5 wt% OBMFs	213
Figure C. 4	ATR-FTIR spectra of PA6 with 7.5 wt% OBMFs	213
Figure C.5	ATR-FTIR spectra of PA6 with 10 wt% OBMFs	214
Figure D.1	Inspection of recovered drilling fluid waste (a) visual inspection and (b) SEM analysis	215

Figure D.2 SEM images of untreated OBFs in different magnifications settings (a) 10.00 KX and (b) 25.00 KX

215

Table of Contents

Dedication	iv
Acknowledgement	v
Abstract	vi
Achievements	viii
List of Abbreviations	x
List of Tables	xii
Chapter 1: Introduction	1
1.1 Background.....	1
1.2 Aim and objectives.....	2
1.3 Methodology.....	3
Figure 1.1 Methodology overview, workflow and critical analysis of the research showing the sample preparation and experimental procedures.....	4
1.4 Gap in knowledge and motivation for research.....	4
1.5 Thesis structure.....	5
Chapter 2: Literature Review	8
2.1 Introduction.....	8
2.2 Drilling mud waste.....	8
2.3 Characteristics of drilling wastes.....	12
2.4 Environmentally concerned constituents in drilling waste.....	16
2.5 Clay nanoplatelet and its influence in polymer/clay nanocomposites.....	25
2.5.1 Clay nanoplatelets.....	25
2.5.2 Polymer clay nanocomposites.....	31
2.6 Preparation of polymer clay nanocomposites.....	35
2.6.1 Solution processing.....	36
2.6.2 <i>In-situ</i> polymerisation.....	37
2.6.3 Template synthesis.....	38
2.6.4 Melt processing.....	39
2.7 LDPE clay nanocomposites.....	40
2.8 PA6- clay nanocomposites.....	41
2.9 Conclusion.....	42
Chapter 3: Thermal Treatment Process and Characterisation of Oil Based Mud Waste	45
3.1. Introduction.....	45
3.2. Experiment.....	46
3.2.1. Materials and samples preparation.....	46
3.2.2. Structural and morphology analysis.....	46
3.2.3. Element analysis.....	47
3.2.4. Thermal analysis.....	48

3.3. Result and discussion	48
3.3.1. Morphology study	48
3.3.2. Chemical structure analysis	49
3.3.3. Mineral composition analysis	51
3.3.4. Elemental analysis	52
3.3.5. Thermal properties	54
3.5. Conclusions	59
Chapter 4: The Crystallinity and Thermal Degradation Behaviour of LDPE/Oil Based Mud Waste Slurry Nanocomposites.....	60
4.1. Introduction	60
4.2. Materials and experimental details	60
4.2.1. Materials and samples preparation	60
4.2.2. LDPE/OBM slurry and LDPE/MMT nanocomposite manufacturing process	61
4.2.3. Structural and morphology analysis	62
4.2.4. Element analysis	62
4.2.5. Thermal analysis	62
4.3. Result and discussion	63
4.3.1. Morphology study	63
4.3.2. Chemical structure analysis	70
4.3.3. Mineral composition analysis	72
4.3.4. Elemental analysis	77
4.3.5. Thermal properties	79
4.5. Conclusions	88
Chapter 5: Mechanical and Rheological Properties of LDPE/MMT and LDPE/Oil Based Mud Waste Slurry Nanocomposites.....	89
5.1. Introduction	89
5.2. Experimental	90
5.2.1. Materials and samples preparation	90
5.2.2. LDPE/OBM slurry nanocomposite manufacturing process	90
5.2.3. Morphology	90
5.2.4. Mechanical testing	90
5.2.5. Rheological characterisation	92
5.3. Results and discussion	93
5.3.1. Morphology study of LDPE/MMT and LDPE/OBM slurry nanocomposites	93
5.3.2. Tensile properties of neat LDPE, LDPE/MMT and LDPE/OBM slurry nanocomposites	93
5.3.3. Flexural properties of neat LDPE, LDPE/MMT and LDPE/OBM slurry nanocomposites	97
5.3.4. Rheological characterisation of neat LDPE, LDPE/MMT and LDPE/OBM slurry nanocomposites	100
5.4. Conclusions	105

Chapter 6: Structural and thermal degradation behaviour of reclaimed clay nano-reinforced low-density polyethylene nanocomposites	106
6.1. Introduction	106
6.2. Experimental.....	107
6.2.1. Materials.....	107
6.2.2. OBMFs manufacturing process	108
6.2.3. LDPE/OBMFs nanocomposite manufacturing process	108
6.2. 4. Sample characterisation	108
6.2.5. Testing	109
6.3. Results and discussion	109
6.3.1. Elemental analysis of nanocomposite materials using ATR-FTIR study and EDXA	109
6.3.3. Micro-structure by XRD and TEM	116
6.3.4. Thermal properties by DSC and TGA	118
6.3.5. Dynamic mechanical properties	126
6.3.6. Tensile properties of LDPE/OBMFs nanocomposites	128
6.4. Conclusions	130
Chapter 7: The Crystallinity and Thermal Degradation Behaviour of Polyamide 6/Oil Based Mud Fillers (PA6/OBMFs) nanocomposites	132
7.1. Introduction	132
7.2. Experimental.....	133
7.2.1. Materials.....	133
7.2.2. OBMFs manufacturing process	133
7.2.3. PA6/OBMFs nanocomposite manufacturing process	133
7.2.4. Characterisation	134
7.3. Results and discussion	135
7.3.1. ATR-FTIR analysis of materials	135
7.3.2. Morphology of OBMFs and polyamide/OBMFs nanocomposite materials.....	138
7.3.3. Elemental Composition.....	140
7.3.4. Thermogravimetric analysis (TGA)	143
7.3.5. Differential Scanning Calorimetry (DSC).....	147
7.3.6. X-ray Diffraction (XRD) analysis	154
7.3.7. TEM analysis	159
7.4. Conclusion	160
Chapter 8: Mechanical properties of PA6/ Oil Based Mud Fillers nanocomposites	161
8.1. Introduction	161
8.2. Experiments.....	161
8.2.1. Materials.....	161
8.2.2. OBMFs manufacturing process	162
8.2.3. PA6/OBMFs nanocomposite manufacturing process	162

8.2.4. Testing and characterisation.....	162
8.3. Results and discussion	166
8.3.1. Morphology of PA6/OBMFs nanocomposites	166
8.3.2. Tensile properties of PA6/OBMFs nanocomposites.....	166
8.3.3. Flexural properties of PA6/OBMFs nanocomposites.....	170
8.3.4. Impact fracture toughness properties of PA6/OBMFs nanocomposites	172
8.3.5. Dynamic mechanical analysis of PA6/OBMFs nanocomposites	175
8.4. Conclusions	177
Chapter 9: Conclusion and future work.....	179
9.1. Summary	179
9.2. Recommendations for future work	180
References:.....	182
Appendix A	206
Appendix B	209
Appendix C	212
Appendix D	215

Chapter 1: Introduction

1.1 Background

Operational discharge from oil and gas exploration industry, accidental spillage, or improperly disposed drilling wastes has serious detrimental effects on human and environment. When drilling muds/fluids and cuttings after oil & gas exploration process are disposed on the ground surface, the liquid fraction of chemicals starts seeping through the ground and eventually these chemicals destroy the living organisms in the ground and pollute the groundwater (Caenn et al., 2011). Consequently, oil-based muds (OBMs) and associated drill cuttings have become a major challenge in the industry for compliance with the requirements of zero discharge. Due to the European Union (EU) Waste Framework Directive (WFD), new legislations have been implemented in the EU member countries including United Kingdom for the recycling of wastes with a mission to prevent and reduce landfilling of waste (Mokhalalati et al., 2000) (Fijał et al., 2015).

Waste generated after drilling operation in oil and gas exploration industry is generally termed as drilling waste composed of used drilling muds or spent drilling muds and drill cuttings (Hill, 2007 and Veil, 2002). Spent drilling mud, drill cuttings and adhered oils are the key target ingredients to deal with drilling waste treatment operations in oil and gas exploration industry (Tuncan et al., 2000, Arce-Ortega et al., 2004). In early oil and gas operation industry, drilling wastes were discharged after the drilling operation directly to the landfill site or ocean which caused serious environmental pollution to the dumping site and its surrounding zones (Muschenheim and Milligan, 1996, Sadiq and Hussain, 2005, Sadiq et al., 2003). In 2008, the Waste Framework Directive 2008/98/EC, identified and declared certain specific ingredients in drilling mud waste as hazardous chemicals for the sake of environmental pollution control measures (Siddique et al., 2017, Chen et al., 2007). However, since the European Union (EU) Waste Framework Directive (WFD) in operation, drilling waste now cannot be disposed to landfill without different levels of treatment to meet the threshold limit of different chemicals including oil content and salinity to dispose to the landfill site (Robinson et al., 2009, Kogbara et al., 2016).

Historically, a wide range of treatment and disposal options are in practice now. However, a technical advancement of process optimisation to intensify the recycling and recovery of resources becomes an interesting area of research recently (ball et al., 2012). Although the separated liquids (water and oil condensates) are currently being reused in drilling mud preparation and in some cases, the oil is utilised to provide power for the other equipment on

the platform, it is important to note that, well conditions may vary and thus further analysis may be required to determine safest recycle or disposal options (Ormeloh, 2014, THERMTECH, 2012). In addition, there may be the need for supplementary treatment due to the heavy metal and large amount of salts present in the original drilling waste in certain cases (Holdway, 2002, Xu et al., 2018). This is imperative especially concerning the produced solids, which are currently being disposed of at landfill sites or recycled in the construction industry which may cause a serious threat to human life (El-Mahllawy and Osman, 2010, Pamukcu et al., 1990). Thermomechanical Cuttings Cleaner (TCC) - a latest technology to deal with drilling waste which is licensed to companies such as TWMA, Halliburton and Schlumberger to dispose solid residue after treating the drilling waste in landfill sites (THERMTECH, 2012).

Previous studies by Adegbotolu et al., (2014) and Shohel et al., (2018, 2019a, 2019b) focused on using the produced solids as reinforcement for polymer composites. However, this research delves further by assessing and improving on the operating mechanism of the TCC to efficiently produce the mineral powders (nanoclay) needed for use in the nanocomposite material industry. This will minimise the volume of drilling wastes disposed of at landfill sites and play a major role in reducing the carbon footprint of the oil and gas industry too.

1.2 Aim and objectives

The aim of this thesis is to develop a detailed understanding of the synergistic effects of different clay minerals that exist in OBMFs in influencing structural, morphological, rheological and thermo-mechanical behaviour of LDPE and PA6 nanocomposite materials.

The thesis objectives are:

- i. To conduct a critical literature review of existing drilling waste treatment technologies and their drawbacks as well as the state of the art in clays/polymeric nanocomposite.
- ii. To characterise OBM waste both in slurry and dry forms.
- iii. To develop LDPE/MMT and LDPE/Oil Based Mud Waste Slurry Nanocomposites and evaluate their crystallinity, thermal degradation behaviour, mechanical and rheological properties.
- iv. To manufacture and determine microstructural, mechanical and thermal degradation behaviour of reclaimed (thermally treated) oil-based mud fillers (OBMFs)/ LDPE nanocomposites.

- v. To manufacture and determine microstructural, mechanical and thermal degradation behaviour of reclaimed (thermally treated) oil-based mud fillers (OBMFs)/ PA6 nanocomposites

1.3 Methodology

A deep literature survey was followed by an extensive characterisation of the OBM waste as described in the project approach is shown on Figure 1.1. The focus of this study is to investigate the OBM slurry/OBMFs, a natural clay recovered from OBM waste, as a reinforcement for thermoplastic polymers. Due to the time limitation and necessity of in-depth investigation, one polar (PA6) and one non-polar (LDPE) is taken into consideration. Particular emphasis is given to polymer/clay compounding process, improvements in the nanoclay filler dispersion, evaluating interface compatibility, thorough morphological and structural analysis, thermal stability and degradation study. Different characterisation and mechanical testings were conducted to evaluate the performance of new materials developed.

Detailed investigations were carried out to evaluate the suitability of utilisation of OBM waste in both slurry and powder (thermally treated) forms as a reinforcement in LDPE matrix considering the structural, thermal and mechanical properties of LDPE/MMT as a benchmark material. Analysing and comparing different properties among LDPE/OBM slurry, LDPE/OBMFs and LDPE/MMT nanocomposites, OBMFs (thermally treated OBM waste) was taken in consideration to manufacture PA6/OBMFs nanocomposites to explore the effects of OBMFs in influencing filler dispersion, interface compatibility and thermo-mechanical properties of PA6 nanocomposites.

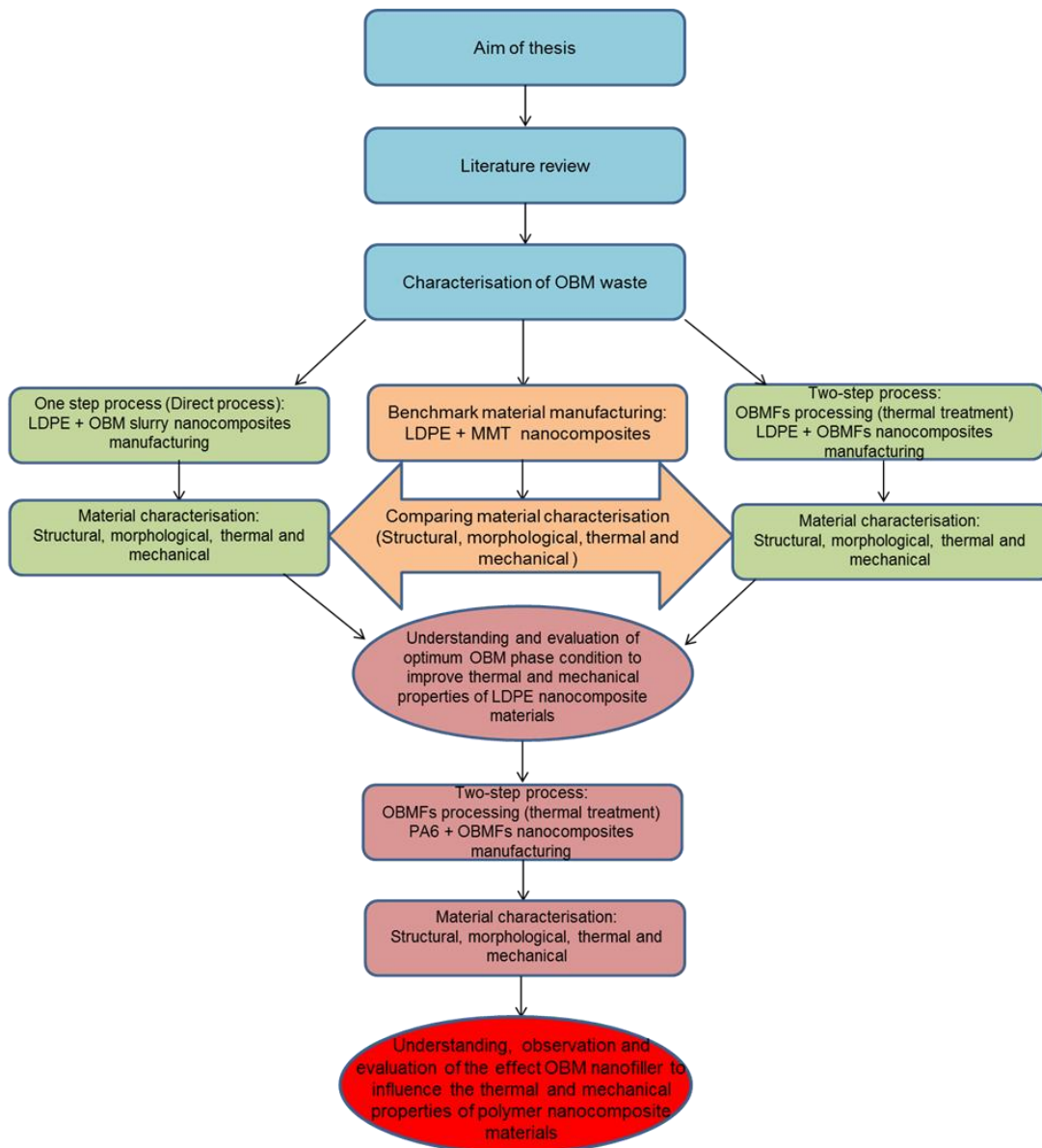


Figure 1.1 Methodology overview, workflow and critical analysis of the research showing the sample preparation and experimental procedures

1.4 Gap in knowledge and motivation for research

Existing drilling waste management techniques in oil and gas industry are facing a big challenge as these techniques hinder the economic robustness and very limited to protect the environmental pollution too. To meet the strict environmental regulations, a sustainable and effective waste management is a big demand now in oil and gas industry. Fortunately, advancement of waste treatment operations demonstrates improved clean-up operations in

oil and gas industry. Although these processes are successful in some extent to meet the discharge/disposal regulations, but in the long run these techniques may pass this pollutant from one stage to another stage or secondary level of environmental pollution. The potential solution of this global problem is either to destroy these hazardous chemicals completely which is a big challenge or to use/utilise them for beneficial uses. This recycling theme promotes a new window to turn the accumulated hazardous wastes in oil and gas industry into value added products.

The aim of this research is to utilise the oil-based mud (OBM) waste to convert into useful fillers for applications in engineering materials. To utilise this waste material which is considered a sink of pollutants, it is very important to understand the sources of drilling fluid wastes, chemical composition, and characterisation of these wastes to design an effective treatment process which helps to develop a safe polymer nanocomposite manufacturing process. Investigating literature on chemical composition of OBM wastes, it is clear that bentonite clay possesses a significant percentage of drilling fluid waste. In addition, initial characterisation of OBM waste confirms the presence of different clay minerals which have significant importance in developing new composite material. Clay/nanoclay is an important component in structural materials by improving the mechanical and thermal properties of polymer/clay nanocomposite materials which is comprehensively reported in literature. Although it is clearly evident that clay/nanoclay improves the mechanical and thermal properties of polymer/clay nanocomposite materials, but there is no information available in literature regarding how the recovered nanoclay from OBM waste influence the mechanical and thermal properties of polymer nanocomposite materials. The motivation of this study is to identify the influential factors affecting the mechanical and thermal properties of LDPE and PA6 matrix materials manufactured by utilising nanoclay fillers recovered from OBM waste.

1.5 Thesis structure

This report is divided into nine chapters highlighting experimental and analytical research performed. Chapter 1 presents briefly about the research background, aim and objectives, motivation and methodology for this work. Chapter 2 covers two sub-section: a) an overview of the literature that relates to the different aspects of OBM waste management/treatment techniques exist in oil and gas industry and the advantages and limitations of these techniques, the detrimental effect of this waste source on human and environment, characterisation and possible recycling/recoverable materials including clay minerals present in solid residue from OBM waste which is now discarded in landfill sites around the world; b) a literature survey on manufacturing, structure, morphology, rheology, thermal and

mechanical properties of different polymer clay nanocomposites. Chapter 3 highlights the structural, morphological, chemical, physical and thermal properties of spent OBM waste to understand and explore the adoptability in recycling option as nanofiller in polymer nanocomposite materials. Chapter 4 presented the potential opportunity to use OBM waste as nanofiller in LDPE matrix highlighting the influence of OBM waste in crystallinity and thermal degradation behaviour of novel LDPE/OBM slurry nanocomposites. Chapter 5 focuses on the effect of OBM slurry without any treatment on rheological and mechanical properties of LDPE/OBM slurry nanocomposites. Chapter 6 presents the thermal treatment of OBM waste to convert slurry in powder form (OBMFs) which is used as nanofiller in LDPE matrix. The effect of this OBMFs in influencing thermo-mechanical properties in LDPE matrix is highlighted in this chapter. Observing and evaluating different thermo-mechanical properties of LDPE/OBM slurry and LDPE/OBMFs nanocomposites compare to that of LDPE/MMT nanocomposites as a reference material, OBMFs is considered to use in PA6 polymer to identify the crystallinity and thermal degradation behaviour of PA6/OBMFs nanocomposites which is reported in Chapter 7. Chapter 8 highlights the effect of OBMFs in influencing different mechanical properties of PA6/OBMFs nanocomposites. Chapter 9 summarises the outcomes of different investigations and presents concluding remarks on these observations. At the end of this chapter, recommendations for future work propose highlighting the potential opportunities to further improve the overall properties of the nanocomposites.

Chapter 2: Literature Review

2.1 Introduction

In this chapter, two sub-sections are discussed in light of different sources of information reported in previous publications. First section is based on information available on different types of drilling mud and its function in drilling operation, pollutants associate with spent drilling waste especially with OBM waste, properties of spent OBM waste, OBM waste characterisation, developments in OBM waste management, different treatment techniques of spent OBM, challenges associated with these treatment systems and recycling or reclaiming opportunities of different clay minerals exist in spent OBM waste. Second section highlights the findings from previous publications regarding polymer clay-based nanocomposites. In this sub-section, the processing, structure, morphology and different properties of clay minerals and the effect of adding these clay minerals influencing different properties of polymer matrix is discussed. A summary of surveying different publications based on the above mentioned two sections is briefly presented at the end of this section.

2.2 Drilling mud waste

A drilling fluid is an essential part of drilling operation in oil and gas exploration operation to perform several functions such as removing and cleaning drill cuttings from the downhole, cooling and l

ubricating the drill bit, controlling the hydraulic pressure to protect well blowouts (Caenn et al., 2011; Fink 2015; Khodja et al., 2010). Although oil based mud (OBM) is environmentally hazardous, but due to its special features such as reliable shale inhibition, excellent lubricity, OBM is still an essential part of deep drilling in oil and gas exploration industries (Zhong et al., 2011; Liu et al., 2004; Gholami et al., 2018; Guancheng et al., 2016). This deep drilling operation intensifies the pollutants addition in OBM largely depends on geological conditions of oilfield which is considered a big concern for different stakeholders including spent OBM waste treatment services, local authorities, environmental activists and regulators involved in running waste framework directives (Veil, 2002; Force, 2009; Addy et al., 1984; Cranford and Gordon, 1991).

Neff et al., in 2000 reports that there are three types of drilling fluid used offshore whilst Rabia in 2002 argues that there are two types of drilling fluid. The difference in opinion stems

from Rabia in 2002 grouping oil-based mud (OBM) and synthetic based drilling muds (SBM) as subsets of non-aqueous drilling muds (NADM).

Therefore, drilling mud can generally be divided into two types based on the continuous phase present that carries mud constituents:

- a. Water-based muds (WBM)
- b. Non-aqueous drilling muds (NADM)

The choice of drilling fluid is dependent on the requirements of the well or area being drilled. Usually both WBMs and NADMs are used in drilling a well. WBMs are used to drill top sections of the well where pore pressure is low and NADM used for deeper sections where there are higher pressures or water-sensitive formations like shale (Tullow Oil, 2012).

Water based mud is composed of water mixed with bentonite clay and barite (to control mud weight) and other additives. The composition of a typical water-based mud is shown in Figure 2.1.

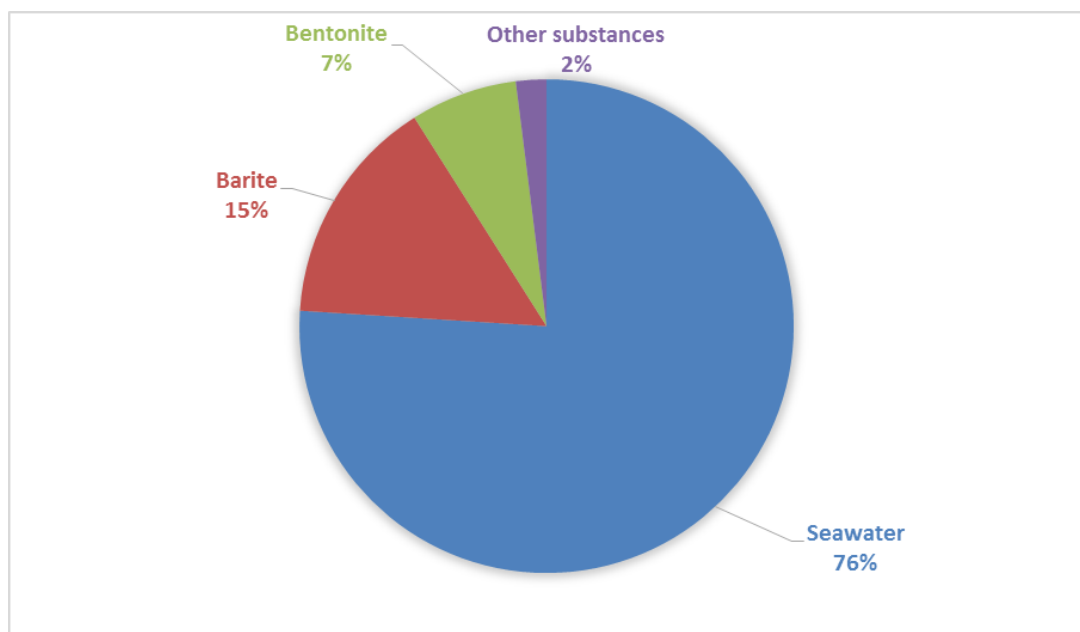


Figure 2.1 Water Based Mud Composition (Melton et al., 2003)

NADM is comprised of a *non-aqueous base fluid* such as diesel or mineral oil, water and other additives to obtain desired mud properties. The relative percentage of the various constituents of NADM is shown in Figure 2.2. They can also be subdivided into OBMs, Enhanced Mineral Oil-Based Mud (EMOBMs) and synthetic-based muds (SBMs).

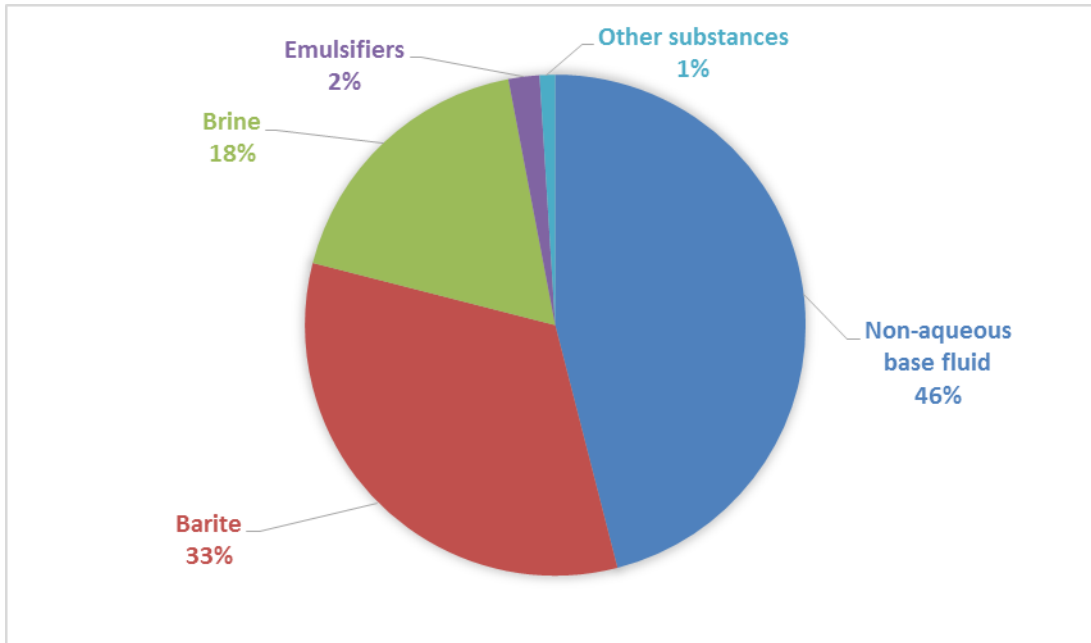


Figure 2.2 non-aqueous Drilling Mud compositions (Melton et al., 2003)

NADMs can be sub-divide into group I, II and III NADMs based on aromatic hydrocarbon concentrations as shown in Table 2.1.

Table 2. 1 NADM Classification Groups and Descriptions (KOH and TEH, 2011)

Group	Base Fluid	Aromatic Content	Aromatic (%)	PAH (%)
I	Diesel and conventional mineral oil Low toxicity	High	>5	>0.35
II	Enhanced Mineral oil Synthetics	Medium	0.5-5.0	0.001-0.35
III	(esters, olefins and paraffin)	Low to negligible	<0.5	<0.001

Drilling waste can be classified as shown in Table 2.2.

Table 2. 2 Types of Waste Discharges from Exploration and Production (Bashat, 2002)

Aqueous discharges	Solid waste	Atmospheric Emissions
<ul style="list-style-type: none">• Produced water	<ul style="list-style-type: none">• Tanking/piping sludge, waxes	<ul style="list-style-type: none">• Firefighting agents eg. Halons
<ul style="list-style-type: none">• Process water	<ul style="list-style-type: none">• Production chemicals	<ul style="list-style-type: none">• Refrigerants eg. CFCs
<ul style="list-style-type: none">• Hydro-test water	<ul style="list-style-type: none">• Industrial refuse	<ul style="list-style-type: none">• Vent gases
<ul style="list-style-type: none">• Contaminated rain/drainage water	<ul style="list-style-type: none">• Soil movements	<ul style="list-style-type: none">• Flare gases
<ul style="list-style-type: none">• Domestic sewage	<ul style="list-style-type: none">• Domestic refuse	<ul style="list-style-type: none">• Exhaust gases• Fugitive gases

In the oil and gas industry, the well drilling process produces two main types of waste;

- Drill Cuttings
- Used Drilling Fluid (Spent Mud)

The pressure applied to penetrate Oil and Gas reservoirs during drilling causes pieces of the rock being drilled to fall to the bottom of the well bore. These pieces, referred to as drill cuttings, clog the well if not carried out. Drilling fluid, also known as mud due to its consistency and appearance (Oil & Gas UK, 2015), is circulated in the well to transport the drill cuttings to surface. The composition of the drilling fluid enables it to perform this and other functional characteristics including cooling and lubricating the drill bit to reduce friction between the drill pipe and the well bore as well as controlling the formation pressures (Neff et al., 2000).

Drill cuttings can be categorised based on the drilling fluid they are dispersed in. They are oil-based, water-based and pseudo-oil-based drill cuttings. During exploratory drilling, coring method is employed to understand and collect geological information. In addition, analysis of drill cuttings gives important petrophysical data such as an indicator of the depth of the reservoir, oil and water saturations, porosity and permeability, morphology of cuttings and mineralogy of the rock being drilled.

They provide essential petrophysical information in the absence of cores, that helps characterise reservoirs. These include porosity, nuclear magnetic resonance (NMR), permeability and transverse relaxation time which is used to identify the formation characteristics during NMR measurements. This measurement is performed by determining

two phases such as polarisation and acquisition. The times are recorded while hydrogen atoms are aligned in the direction of a static magnetic field and also the resonance in a perpendicular direction of that static magnetic field. The decay of these two signals represents the transverse relaxation phase and the time difference is corresponding the transverse relaxation time (Denney, 2008).

Page et al. (2003) studied data from core samples, reporting that the cuttings particle size from the North Sea ranged from 10 μm to 2000 μm whilst cuttings from North West Hutton, United Kingdom (UK) ranged between 13 μm to 500 μm . The study also showed that cuttings analysed were composed of claystone, sandstone, siltstone, limestone, mudstone and shale. They also contained high concentrations of Quartz and barite. The presence of inorganic salts and halides, from drilling mud, were detected from the study. Saasen et al. (2008) also carried out research on the characterisation of simulated drill cuttings that showed particles ranging from 1 μm to 15 μm composed of mainly dolomite; determined with the use of Raman spectroscopy.

2.3 Characteristics of drilling wastes

In 2004, World Oil's categorised drilling fluids into nine distinct types including dispersed freshwater, non-dispersed fresh water, saltwater, oil-based, synthetic-based, air, mist, foam, and gasified drilling fluid systems (SPE International; Drilling fluid types, 2015, Fink, 2015). These drilling fluids can be broadly classified as either liquid or pneumatic (Azar and Samuel, 2007). Drilling fluid selection in a drilling operation depends mainly on the geological formation information of the wellbore area. However, drilling fluids should possess various physical properties, such as thixotropy which represents time dependant shear thinning property and rheology corresponding the flow property of a matter to make the drilling operation economical and sustainable (Besq et al., 2003). After the drilling operation, accumulated drill cuttings are suspended, assimilated, or dissolved in the drilling fluids without affecting its physical properties (Zhou et al., 2016). These fluids may contain a wide variety of dissolved minerals, dissolved and dispersed oil compounds, salts, metal ions, naturally occurring radioactive materials (NORM) and dissolved gases. To meet the environmental regulations, these fluids may need to be treated to a satisfactory level before disposing them in landfill. To identify the concerning constituents present in waste stream and to design the effective treatment process, the accurate and detailed physical and chemical characterisations of wastes are necessary (Piszcz et al., 2014).

The physical composition of drilling wastes is mainly based on the type of drill cuttings produced. These cuttings are generally a reflection of the geological constituents of the sub-surface being drilled as well as the individual solid or chemical components originally contained in the drilling fluid (Melton et al., 2000). In 1996, drilling operation was estimated to accumulate 7 million m³ drill cuttings in North Sea between the years 1964 and 1993 and was projected to 12 million m³ by 2000. Although the sources and compositions of wastes vary from site to site, their behaviour towards biological activities, cohesion with oil rich silts remain the same in nature. In a typical drill cutting pile, the pile is assumed to compose of 20-60% water, a bulk density of 1.6-2.3 g/cm³, and a particle size ranging from 10µm to 2 cm (Breuer et al., 2004), (Breuer et al., 2008). Hudgins (Hudgins and Charles, 1994) reported the most comprehensive study to date available in open literature covering ten operating companies and six chemical suppliers in North Sea that obtained data (see Figure 2.3) on the specific types and quantities of chemicals used in their operation and identified the properties of these chemicals. The survey also presented the discharge quantities and concentrations of chemicals during exploration and production activities performed by these companies in the North Sea. However, based on the Hudgins (Hudgins and Charles, 1994) survey results it can be summarised that the WBM accumulated more than three times the volume of discharge compare to OBM. It also noticed that the weighting agents, salinity, and bentonites chemicals accumulated about 90% of the total WBM discharge.

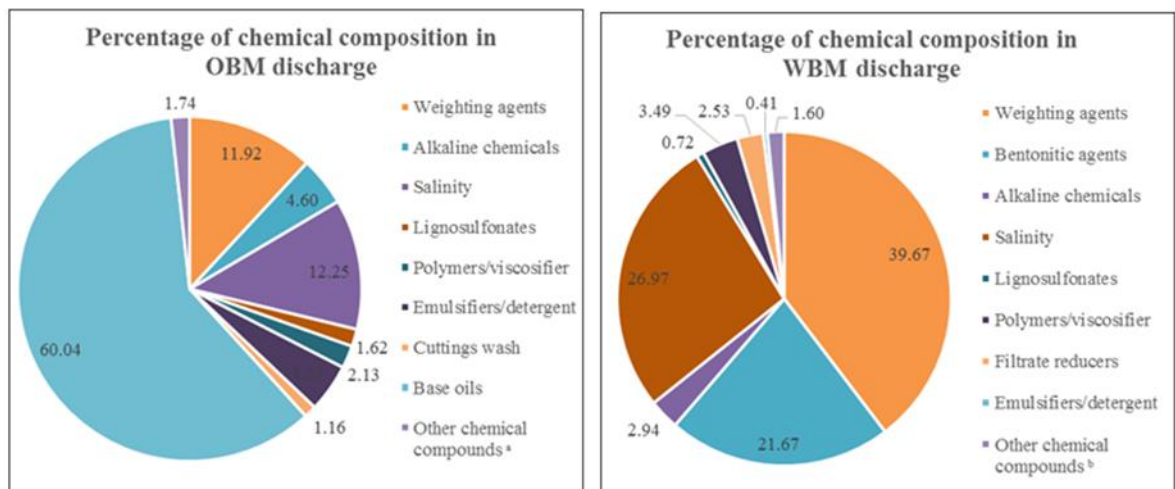


Figure 2.3 Percentage of individual chemical constituents present in OBM and WBM discharge adapted from Hudgins (Hudgins and Charles, 1994)

Note: a) Bentonitic agents, lost circulation, lignites, filtrate reducers, gilsonite, wetting agents, and thinning agents. b) Lost circulation, lignites, gilsonite, defoamers, biocides, corrosion

inhibitors, scale inhibitors, drilling lubricants, pipe-release agents, oxygen scavengers, shale inhibitors, and thinning agents.

It can be concluded by highlighting that about 53% of chemicals that are used in drilling operation are discharged as wastes and thus cause the pollutants burden in the environment (Hudgins and Charles, 1994) (Marsh, 2003).

The chemical composition of drill cuttings at the time of disposal is an indication of the drilled sub-surface strata and concentration of the chemical components of the drilling fluid that remain attached to the cuttings. The temporal trends towards drilling activities provide important information on the long-term effects of drill cutting discharges on geochemical and hydrogeological conditions (Phillips et al., 1998). Findings from different groups confirm the presence of certain metals in drill cuttings and their potential effect on the environment. Among these metals Cd, Cr, Ni, As, Co, Cu, Pb, V, Zn, Al, Ba, Fe, Mn are predominant in drill cuttings (Grant and Briggs, 2002) (Pozebon et al., 2005).

During the period of 1981-1986, the average annual discharge of oil on cuttings to the Norwegian Continental Shelf (NCS) was 1940 tons and that was eliminated gradually by implementing different directives such as OSPAR Commission in OSPAR regions. In addition to oil on cuttings discharge, the amount of produced water (PW) discharge has increased significantly due to the well ageing and also the rising number of oil and gas exploration and production fields. Large volume of OBM cuttings and SBM cuttings piled up in the seafloor before the regulations implemented in 1993/1996. It was estimated that about 45,000 m³, a height of around 25m, and a footprint of more than 20,000 m² cutting piles are still present in the northern and central part of the North Sea. About 79 large (>5000 m³) and 66 small (<5000 m³) cutting piles have been identified in United Kingdom Continental Shelf (UKCS) and NCS. Further, a significant concentration of total hydrocarbons (10,000 to 600,000 mg/kg) exists in the North Sea piles (Bakke et al., 2013).

However, even WBM cuttings with less hydrocarbon content may seriously affect benthic fauna by elevating oxygen consumption in sediments. The risk of drilling waste associated with WBM cuttings discharge to the ecosystem is presently considered low, but this statement cannot be verified from the published literature. However, the variation in the amount of drilling fluid that remains adhered to the drill cuttings at the time of disposal is influenced by the size of the cuttings. The smaller the size of cuttings, the harder it is to separate it from the drilling fluid. In addition to these metals derived from the drilling fluid and geologic formation being drilled, cuttings may also contain some petroleum hydrocarbons closely linked to that of the reservoir rock. Phillips et al (1998) has completed a study over nine years period to evaluate temporal trends of drilling activities and their effects on geochemical conditions. In that study they compared the elemental composition of drilling

mud and drilling mud waste in dry form and thus highlight certain metals concentrations transferred to the background sediment concentrations(Phillips et al., 1998).

Table 2. 3 Concentration of metals in Water Based Mud and Drill Cuttings from two offshore platforms in Southern California (Phillip et al., 1998).

Metal	Platform 1		Platform 2	
	Drilling Fluid	Cuttings	Drilling Fluid	Cuttings
Barium	53,900	15,084	12,500	1,180
Silver	0.37	0.5	0.39	0.63
Arsenic	10	10	9.3	13
Cadmium	1.17	2.89	1.75	3.62
Chromium	91	104	84	94
Copper	24	70	24	56
Mercury	0.09	0.07	0.06	0.04
Nickel	39	47	42	17
Lead	23	356	40	32
Vanadium	76	100	46	---
Zinc	167	664	235	972

Water based muds (WBM), with typical composition shown in Figure 2.1, which were the earliest drilling mud had fresh water or sea water as the continuous phase with clay and a weighting agent being the main constituents (Neff, 2005). They are relatively less expensive and about 80% of all wells are drilled using WBM (SPE International. Drilling fluid types, 2015).

In Table 2.3 shows a comparison of metal contaminants profile in water-based mud waste from two platforms in southern California. Barite or alternative weighting material, viscosifier, typically bentonite and different salts are generally more abundant than the other additives. Other additives may be included to improve or alter the properties of the WBM depending on the well type and technical performance desired due to anticipated well conditions. Nonetheless, these additives are not in concentrated elevations and are generally considered less toxic.

In the 1960s, oil-based muds (OBM) with typical composition, as shown in Figure 2.2 have been introduced particularly to address drilling problems encountered with using WBMs (SPE

International. Drilling fluid types. 2015). However, they are similar to WBMs in terms of the main constituents with the only exception being the formulation of the continuous phase with refined petroleum products such as diesel. One of the major advantages of using OBMs over WBMs is its ability to inhibit most shales and this is due to the formulation of OBMs with calcium chloride brine (SPE International. Drilling fluid types. 2015). Similarly, barite and bentonite are also major constituents of OBMs and provide the functional properties as with WBMs. Again, other additives are included in OBMs based on the desired performance of the mud and anticipated well conditions.

However, highly effective, the use of diesel given its high aromatic compound content gradually phased out as its disposal offshore was banned in most countries. Although this led to the development of Low Toxicity Mineral Oils (LTMOs) with significantly reduced aromatic compound content, strict regulations regarding discharge of cuttings coated with LTMOs led to the development of synthetic based muds (SBMs) (HSE, 2000). SBMs only differ from OBMs due to the use of oils not directly derived from crude as the base fluid. They are synthesised chemical compounds and may be in the form of organic esters, ether, acetyl, olefins or a mixture of any two (Neff, 2005). Similar to OBMs, SBMs also contain barite, clay, water and other additives and are rather simple in composition. Even though SBMs are more biodegradable and considered less toxic as compared to the OBMs, they are usually recycled and not disposed of into the environment due to their high cost. At their end of life however, they are usually re-injected and where this option may not be technically feasible, they are transported to an onshore site for further treatment before disposal; depending on what federal regulations permit (Jacques Whitford Stantec Limited, 2009). Cuttings may also have a similar chemical composition to the type of pneumatic drilling fluid used.

2.4 Environmentally concerned constituents in drilling waste

The American Petroleum Institute (API) reports that about 150 million barrels of drilling waste was generated from exploration and production operations in 1995. API further states that 1.21 barrels of waste is generated for every foot drilled. Ormeloh (2014) notes that between 2006 to 2009 approximately 220 tons per year of oily drilling waste was produced. Over 50% of this amount was treated onshore. In 2010, there was a 26% increase in the amount of cuttings and mud produced; this was attributed to injection well problems and the use of OBM for drilling. Increasingly, more OBM is used for wells due to the need to drill longer and deeper resulting in oilier waste production.

The trend of increased oil and gas waste is shown in Figure 2.4 using data from the Oil and Gas UK (2015) Environmental Report 2015 that reveals an 80% increase in the amount of

treated OBM cuttings discharged from offshore activity from 2013 to 2014 (as shown in Figure 2.5), although there was a general reduction in the oil price. There was however, a decline in the amount of WBM cuttings discharged from offshore installations.

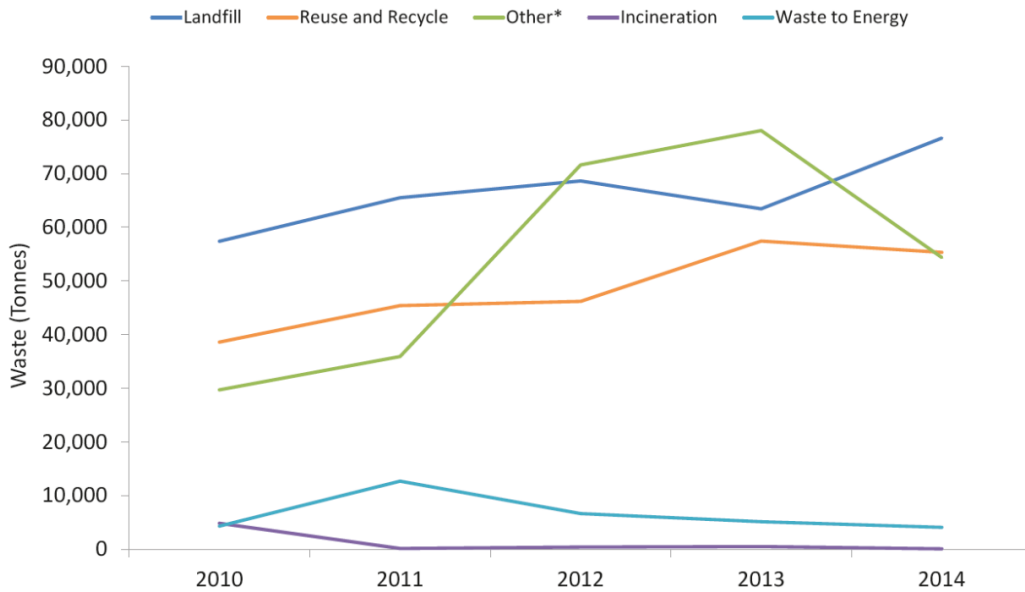


Figure 2.4 Waste Generated Offshore (Oil & Gas UK 2015)

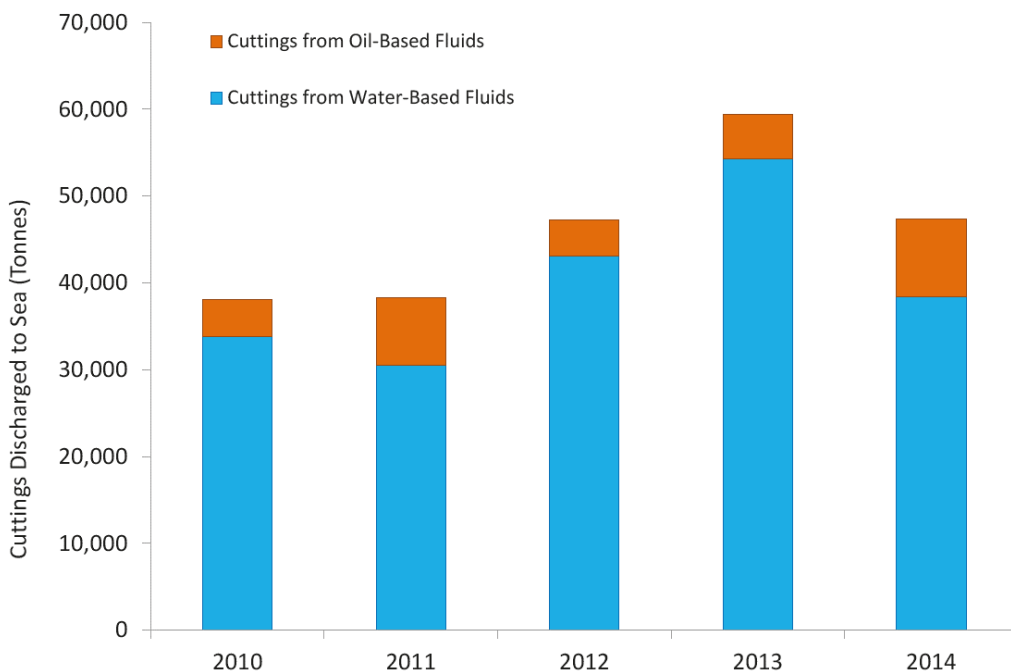


Figure 2.5 Cuttings Discharged to Sea (Oil & Gas UK 2015)

The report also showed that there has been a general increase in the amount of drilling waste recycled and reused in the UK; with a slump in 2014 as shown in Figure 2.4 waste generated offshore. This may be attributed to increased costs of operating in the oil industry due to low oil prices.

An improvement in the monitoring mechanisms of oil and gas waste could be attributed to the increase in oil contaminated cuttings in the UK in 2014. New players in the oil and gas industry such as Ghana currently do not actively monitor and measure levels of waste produced.

SBMs usually contain less than 0.001% of PAHs and OBMs containing diesel or mineral oil as a base fluid contain about 5% to 10% PAHs diesel oil and 0.35% in mineral oil (BERNIER et al., 2003). The PAHs present in OBMS with diesel and mineral oil as base fluids have the following toxic pollutants-fluorine, naphthalene, and phenanthrene, and non-conventional pollutants such as alkylated benzene and biphenyls (USEPA 2000).

Lichtenberg et al. (1988) also adds that hydrocarbons increase the toxicity of both synthetic and oil-based muds. He refers to work carried out by Kelly et al. (1987) stating that indicates the increase in toxicity of drilling fluid by the addition of mineral oil. He further refers to a study by Gaetz et al. (1986) which reports the correlation between increase in petroleum hydrocarbons and toxicity to mysids, a type of crustacean resembling shrimp which is sensitive to drilling muds. Lichtenberg et al. (1988) concludes by stating that factors such as source, constituents and age of the drilling fluid tested contribute to the toxicity of drilling fluids.

Further investigations into the toxicity of OBM on *Mara* and *Microtox* (bacteria), *Skeletonema costatum* (algae) and *Acarti tonsa* (crustaceans) was carried out by Aquateam et al. (2014). It revealed that leachate (water that drains through soil or landfill and leaches out some of its composition) stifled growth of algae. The toxic effect of the leachate on algae was attributed to the presence of copper. However, it was less toxic to bacteria and lower for crustaceans. It was concluded that a discharge of OBM drill cuttings is moderately toxic to algae and less toxic to bacteria and crustaceans.

During the drilling process, mud suspends drill cuttings during drilling operations. Oil present in mud contaminates cuttings; these cuttings have to be cleaned or treated to meet regulations set for disposal and reuse of drilling mud and cuttings.

Drill cuttings, as shown in Figure 2.6 are fragments of rock removed from the wellbore by the drill bit. During drilling, mud is circulated downhole through drill pipe and up through the annulus of the wellbore to maintain hydrostatic pressure and clean the hole, as shown in

Figure 2.7. They have variable physical and chemical characteristics depending on the rock formation that is drilled. The cuttings size ranges from clay to gravel (Reddoch, 2001)



Scale in cm

Figure 2.6 Drill cuttings in 1 cm scale (Colliver and Carter, 2000)

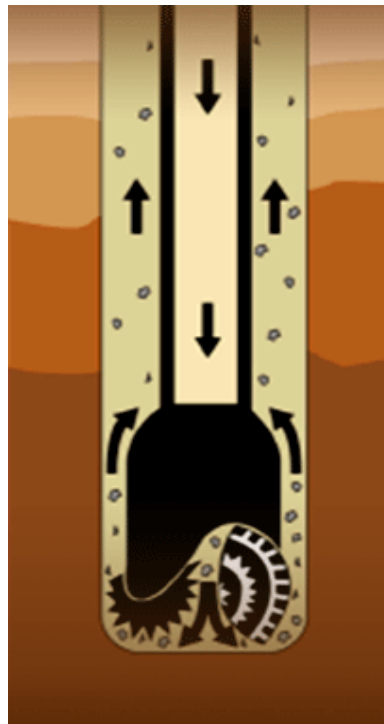


Figure 2.7 Cuttings Movement in Drilling Mud (Oil & Gas UK, 2015)

Soil contamination is hazardous to health and environment through its action on surface waters, ground waters and vegetation (phytotoxicity, bioaccumulation). Oil and gas industries, like other process industries, have a detrimental effect on environment (Khodja, 2010). The hazardous effect of the environmentally significant constituents in the produced drilling wastes is predominantly dependent on each constituent, its concentration at exposure, biotic environment at point of discharge and the duration of exposure.

The typical type of drilling wastes and their potential constituents are (Onwukwe and Nwakaudu, 2012):

- WBM cuttings: Heavy metals, inorganic salts, biocides, hydrocarbons
- OBM cuttings: Heavy metals, inorganic salts, hydrocarbons, solid/cuttings
- Spent OBM: Heavy metals, inorganic salts, hydrocarbons, solid/cuttings, BOD, surfactants
- Spent WBM: Metals including heavy metals, inorganic salts, hydrocarbons, biocides, hydrocarbons, solid/cuttings, BOD,
- Waste lubricants: Heavy metals, organic compounds.

Some of the metals are suspected to be present in concentrations significantly higher than the naturally occurring concentrations of the sediments, which make the disposal of these wastes a critical environmental concern (Onwukwe and Nwakaudu, 2012) (Grant and Briggs, 2002). Arsenic, nickel, copper, chromium, zinc, anthracene, diuron, fluoranthene, naphthalene, phenanthrene, and pyrene are considered as environmentally significant chemicals according to the literature (Pozebon et al., 2005; Bakke et al., 2013; Khodja et al., 2010 and Bignert et al., 2004).

Although the amount of drilling fluid constituents is very low, most of them especially heavy metals have a chronic effect on environment. The pollutants may nowadays be categorised in two different groups of pollutants: List I and List II as shown on Table 2.4 according to European Council Directive 76/464/EEC (DIRECTIVE HAT, 1976). List I group are substances, which are toxic, persistent, and possess the bioaccumulation properties while List II is a group of chemicals, which have deleterious effect on the aquatic environment. However, list II pollutants can be confined to a given area and also the pollutants concentration varies based on the characteristics and location of the water into which the pollutants are discharged.

Table 2. 4 List I and II pollutants in environment (DIRECTIVE HAT, 1976)

Type of pollutants	Members of pollutant groups
List I	<p>Organohalogen compounds and substances</p> <p>Organophosphorus compounds</p> <p>Organotin compounds</p> <p>Carcinogenic substances</p> <p>Mercury and its compounds*</p> <p>Cadmium and its compounds*</p> <p>Persistent mineral oils and hydrocarbons of petroleum origin</p> <p>Persistent synthetic substances</p>
List II	<p>Certain metals, metalloids, and their compounds: 1) Zinc 2) Copper* 3) Nickel* 4) Chromium (Cr(VI)*)</p> <p>5) Lead* 6) Selenium* 7) Arsenic* 8) Antimony* 9) Molybdenum 10) Titanium 11) Tin* 12) Barium</p> <p>13) Beryllium 14) Boron 15) Uranium 16) Vanadium 17) Cobalt 18) Thallium* 19) Tellurium* 20) Silver</p> <p>Biocides and their derivatives</p> <p>Toxic or persistent organic compounds of silicon and its substances</p> <p>Inorganic compounds of phosphorus and elemental phosphorus</p> <p>Non persistent mineral oils and hydrocarbons of petroleum origin</p> <p>Cyanides and fluorides</p> <p>Substances causing oxygen imbalance such as ammonia, nitrites</p>

*: Hazardous waste classified in according to Directive 2008/98/EC

In 2008, the Waste Framework Directive 2008/98/EC brought legal changes to the list of waste and hazardous waste criteria based on the source and composition of wastes (Parliament E. Directive, 2008). In this amendment the source of waste is identified into 20

chapters (from 01 to 20) and the different types of waste in the list are fully defined by the six-digit code (first two digits is chapter heading and the rest four digits for identifying sub-groups). Based on this Commission Decision, environmentally significant and hazardous elements or compounds which are present in drilling fluid wastes are denoted by * mark in Table 2.4 (EUROPEAN COMMISSION, 2014).

In addition, country specific requirements for discharge of drilling fluids and cuttings also do play a role in environmental protection. For instance, in the United Kingdom the OSPAR2000/3 discharge regulation comes into play and compliance requires limit of less than 1% oil on cuttings and do advice on when to inject cuttings or return to shore and oil recovery. The OSPAR2000/3 regulation does not permit discharge of synthetic based mud (SBM) cuttings offshore (DIRECTIVE HAT, 1976 and OSPAR Commission, 2015). However, Neff et al. (2000) argues that some of these metals (barium, chromium, lead and zinc) are likely to be present in concentrations significantly higher than the naturally occurring concentrations of the sediments thus disposal of wastes containing these is of critical environmental concern.

Table 2.5 Elemental composition of typical water-based drilling fluid constituents (mg/Kg) (Onwukwe and Nwakaudu, 2012)

Element	Water	Cutting	Barite	Clay	Lignite	Caustic
Aluminium	0.30	40400	40400	88600	6700	0.01
Arsenic	0.00	3.90	34	3.90	10.10	0.04
Barium	0.10	158.00	590000	640	640	0.26
Calcium	15.0	240000	7900	4700	16100	5400
Cadmium	0.00	0.08	6.00	0.50	0.20	0.00
Chromium	0.00	183.00	183.00	8.02	65.30	0.00
Cobalt	0.00	2.90	3.80	2.90	5	0.00
Copper	0.00	22.00	49	8.18	22.90	0.04
Iron	0.50	21900	21950	37500	7220	0.04
Lead	0.00	37.00	685	27.10	5.40	0.00
Magnesium	4.00	23300	3900	69800	5040	17800
Mercury	0.00	0.12	4.10	0.12	0.20	4
Nickel	0.00	15.00	3.00	15	11.60	0.09
Potassium	2.20	13500	660	2400	460	51400
Silicon	7.00	206000	70200	271000	2390	339
Sodium	6.00	3040.00	3040	11000	2400	500000
Strontium	0.07	312.00	540	60.50	1030	105

Although the concentration of these chemicals of concern (COCs) could be low, and toxicity considered negligible, accumulation and further increase in concentration may occur gradually up the food chain (Rana, 2008). The source of this waste stream is not necessarily coming from the downhole in drilling operation, but the drilling fluid itself a source of contaminants including different metals. Table 2.5 shows a typical composition of water-based mud highlighting different metals content. Moseley (1983) performed an indepth study to address the possibility to restore/disposal of drilling mud pits and produced water to land and their possible effects on soils, plants and surface/ground water. Part of that study was to identify individual components of water based mud and the elemental composition of those constituents in formulation water based mud. The concentrations of different pollutants including metals were further presented in tabular form by Onwukwe and Nwakaudu (2012). This eventually leads to an increase in toxicity. A case study on Lake Erie by Clark (2002) and reported the accumulation of toxic COCs and increase in toxicity up the food chain as part of the environmental impacts of drilling fluids and cuttings disposal.

The increase in toxicity up the food chain is of critical concern as it poses serious threats especially to humans. Even at very low levels, ingestion of COCs such as lead can have dire consequences. Research by the U.S. EPA suggests that characteristic neurobehavioral development of children and variation in the levels of particular blood enzymes in humans may be as a result of the presence of lead in very miniscule concentrations in the blood (Rana, 2008). Again, the presence of certain polycyclic aromatic hydrocarbons (PAHs) and COCs including but not limited to barium, chromium and mercury, have carcinogenic effects on humans and other negative impacts such as irritation to skin and eyes as well as damage to brain and nervous system (Rana, 2008).

Drilling operation in oil and gas exploration industry poses a significant source of chemical exposure and subsequent pollution risk for environment (Ismail et al., 2016 and Steinsvåg et al., 2008). Generation of drilling wastes, their chemical composition and different detrimental effects of these constituents on environment is discussed in the above section. To meet the tight regulations and strict environmental standard for waste disposal, oil and gas industry is facing a numerous challenges in technological development to ensure a clean and safe environment. Historically a wide range of biological and non-biological methods have been introduced for the treatment of drilling wastes such as composting/biopiling, land farming, land treatment, bioaugmented landfarming, burial pit, landfills, bioreactors, vermiculture, chemical solidification, thermal desorption and incineration.

Along with the aforementioned techniques, some other applications are economically beneficial such as, road spreading, use as filler in concrete, restoration of wetlands, and using drilling wastes as fuel. To select the best available technology for drilling waste management, a few significant factors have to be considered: cost, suitability with the local environment, safety aspects, and the relevant regulatory directives or framework (Ball et al., 2012). All these treatment measures mentioned above is enormously reported in the literature whereas this research work focuses on utilisation of constituents present in OBM waste rather treating them and thus increasing the pollutants load in the environment. Another aspect of this work is to encapsulate these pollutants in recyclable polymer matrix. Since clay minerals are a major part of this waste, it would be useful to understand the effect of clay minerals in influencing different properties of materials such as morphological, structural, thermal, mechanical and rheological properties. The effect of clay minerals in influencing different properties of LDPE and PA6 polymer is discussed briefly in the next section.

2.5 Clay nanoplatelet and its influence in polymer/clay nanocomposites

The possibility of using clay minerals in Polymer matrix was first reported in literature in 1961 (Gilman, 1999). Since then, several research groups worldwide are actively performing research to develop fundamental knowledge in utilising this promising layered silicate in nanocomposites (Messersmith and Giannelis, 1995 and LeBaron et al., 1999). However, it is important to understand the structure and chemistry of clay platelets to achieve incorporation of the layered silicates in polymer matrix (Gilman, 1999). The following section describes briefly the structure of different clay minerals including the morphology, different manufacturing processes and the effect of this clay in influencing thermo-mechanical properties of polymer nanocomposites.

2.5.1 Clay nanoplatelets

The term 'clay' refers to naturally occurring phyllosilicates which shows plasticity in wet condition and turns into hard material upon drying or firing (Guggenheim and Martin, 1995). Due to this interesting characteristic, clay is used in architecture, industry and agriculture for decades (Murray, 1991, Bergaya and Lagaly 2006). However, these clay minerals can be divided in four groups based on their layered structure. These major groups including their sub-groups and general formula are presented as below.

- Kaolinite ($\text{Al}_2\text{Si}_2\text{O}_5(\text{OH})_4$): kaolinite, dickite, nacrite.
- Montmorillonite or smectite $(\text{Ca}, \text{Na}, \text{H})(\text{Al}, \text{Mg}, \text{Fe}, \text{Zn})_2 (\text{Si}, \text{Al})_4\text{O}_{10}(\text{OH})_2\text{-XH}_2\text{O}$: montmorillonite, pyrophyllite, talc, vermiculite, sauconite, saponite, notronite.
- Illite $(\text{K}, \text{H})\text{Al}_2 (\text{Si}, \text{Al})_4 \text{O}_{10}(\text{OH})_2\text{-XH}_2\text{O}$: illite
- Chlorite: amesite $((\text{Mg}, \text{Fe})_4\text{Al}_4\text{Si}_2\text{O}_{10}(\text{OH})_8)$
 - Chamosite $((\text{Fe}, \text{Mg})_3\text{Fe}_3 \text{AlSi}_3\text{O}_{10}(\text{OH})_8)$
 - Cookeite $(\text{LiAl}_5\text{Si}_3\text{O}_{10}(\text{OH})_8)$
 - Nimite $((\text{Ni}, \text{Mg}, \text{Fe}, \text{Al})_6\text{AlSi}_3\text{O}_{10}(\text{OH})_8)$

The elementary structural characteristics of clay minerals are distinguished by the structure of silica tetrahedron and aluminium octahedral (Uddin, 2008).

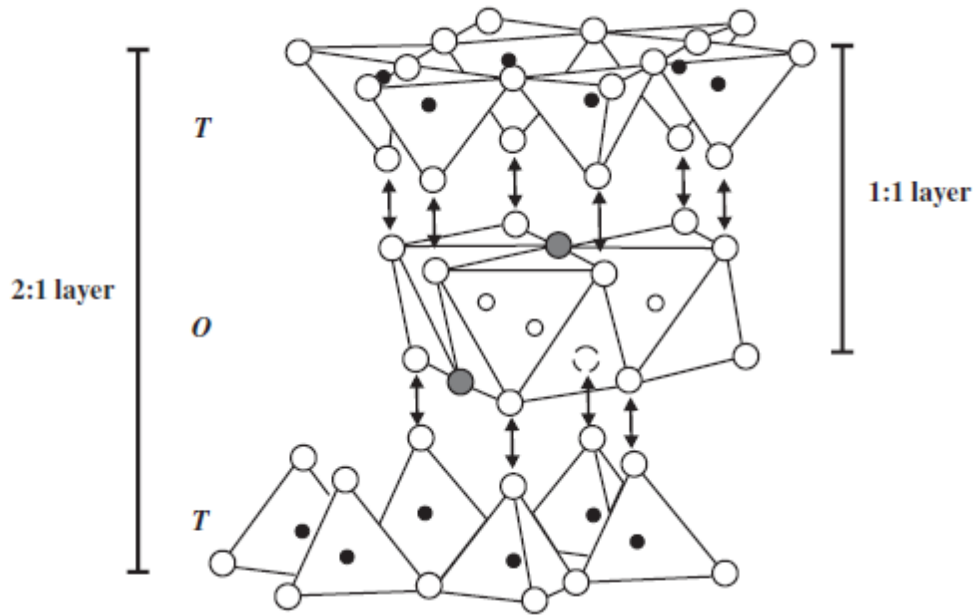


Figure 2.8 Presentation of 3d structure of tetrahedral and octahedral sheets forming 1:1 and 2:1 layer clay (Christidis, 2011)

Considering the arrangement of these tetrahedral and octahedral sheets, different clay minerals can be described differently such as 1: 1 clay mineral has one tetrahedral and one octahedral sheet per clay layers whereas 2:1 clay mineral has one octahedral sheet sandwiched between two tetrahedral sheets (e.g. montmorillonite sheet structure is 2:1) (Christidis, 2011 and Uddin, 2008).

Different clay minerals possess different morphology and form different structure which can be identified in qualitative and quantitative measures using scanning electron microscopy (SEM) and X-ray diffraction (XRD) analysis respectively. Christidis (2011) published an article highlighting different versatile nature of clays. He addressed the relation between physical properties such as particle size and shape, chemical characteristics, hydration and swelling properties, rheology and plasticity properties, colour and interactions with organic and inorganic compounds with the performances of this clay in different industrial applications. Four clay materials were considered in that study including kaolins, bentonites, fibrous clays and common clays and shales. A comparison of structures of few clay minerals noticeable in SEM images as shown in Figure 2.9. Figure 2.9 (a) shows a typical triclinic kaolinite mineral with pseudo-hexagonal crystals. In nature, halloysite clay minerals present in various forms and shows different morphologies such as spheres, tubes, oblate spheroids, plates and irregular shapes. Figure 2.9 (b) (c) shows tubular and spheroidal crystals of halloysite clay minerals. Montmorillonite is a sub group of smectite clays with 2:1 layer silicates structure. Generally, smectites form small crystals (less than 0.5 μm) in size and

found in different shapes such as subhedral, euhedral, lath and ribbon crystallites. Figure 2.9 (d) shows the subhedral montmorillonite crystal structure.

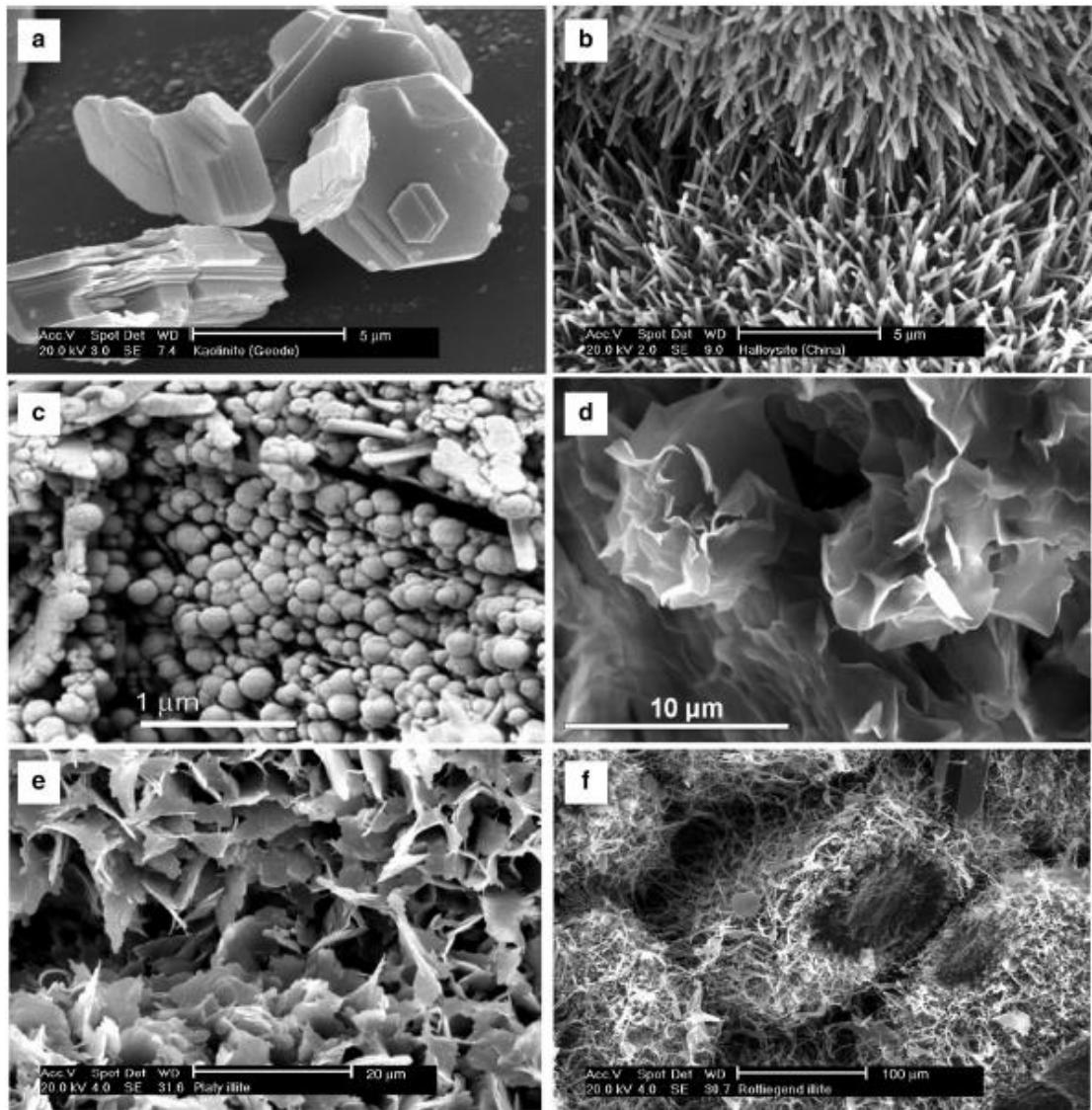


Figure 2.9 SEM images of: (a) kaolinite; (b) tubular crystals of halloysite; (c) spheroidal crystals of halloysite; (d) wavy subhedral montmorillonite crystals; (e) flaky illite crystals and (f) fibrous illite (Christidis, 2011)

Illite is a sub group of mica group which is found in platy, fibrous and lath-like crystals. Figure 2.9 (e) and (f) shows flaky and similar to fibrous crystal structures of illite clay minerals (Christidis, 2011). An in-depth qualitative analysis of petroleum sludge was performed by Andrade et al. (2009). The key findings from the study confirmed the presence of irregular sizes of dry oily petroleum sludge by scanning electron microscopy (SEM) analysis. Moreover, smaller sized layered platelets were also highlighted in that study which is attributed to bentonite clay. The existing larger particles in dry oily petroleum sludge are

suggested to be barite, calcite, sandstone and quartz which were manifested by the findings from other study performed by Wang et al. (2012) and Bin Merdhah (2010).

The area, length, thickness and volume are the key parameters to assess the mechanisms of crystal growth of extremely small phyllosilicate particles. Transmission electron microscopy identifies the compositional fundamental particles which are usually 1-3 nm in completely dispersed clay minerals (Nadeau, 1985). The transmission electron microscopy (TEM) provides simultaneously three fundamental types of information in analysing clay minerals: a) textural information including image processing up to atomic level; b) developing selected area electron diffraction (SAED) which describes the crystal structures of minerals and c) applying energy dispersive spectroscopic (EDS) techniques to identify the quantitative analysis of chemical data in a specific area of clay mineral (Lázaro, 2007).

In Figure 2.10, an attempt to quantify the physical dimensions of completely dispersed fundamental particles in clay minerals is presented. Li et al. (2015) highlighted the morphology of naturally crystallised kaolinite with a hexagonal sheet parallel to (001) which is presented in Figure 2.10 (a). Lázaro published an article in 2015 emphasising the aspect of geological and technological importance of two clay minerals- halloysite and kaolinite. Kaolinite and halloysite have similar structure, composition and genesis and both are dioctahedral 1:1 layer silicates.

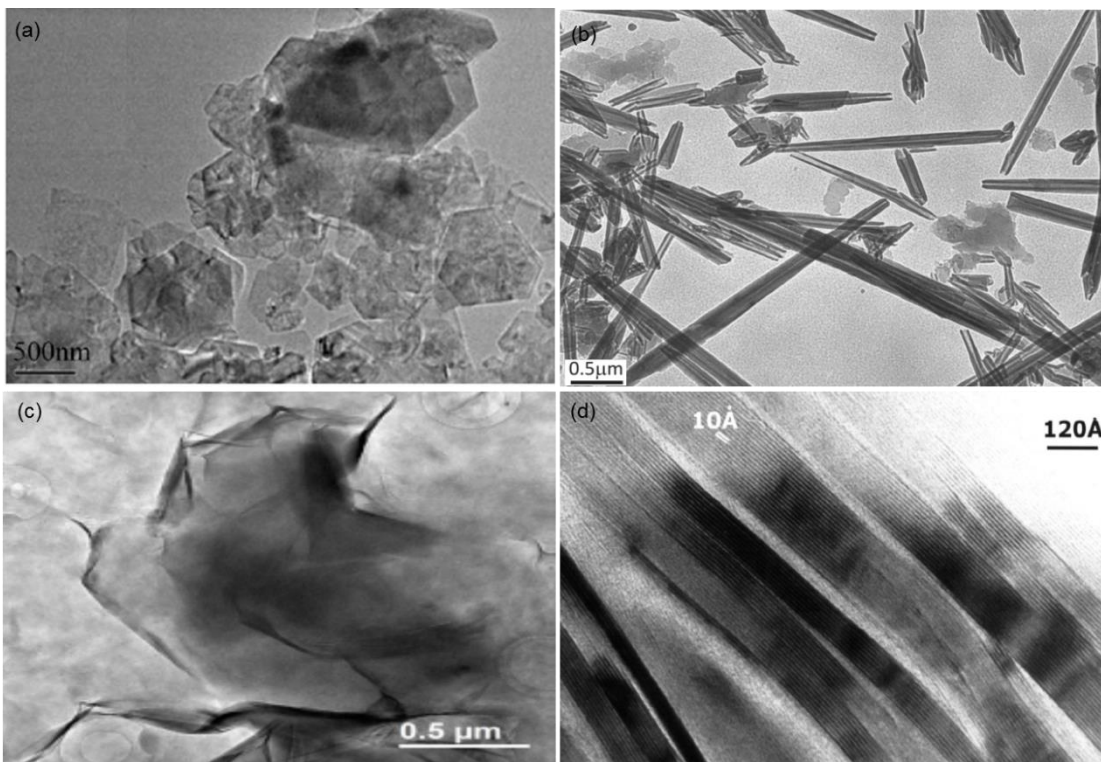


Figure 2.10 TEM micrographs of: (a) kaolinite; (b) tubular crystals of halloysite; (c) wavy subhedral montmorillonite crystals; (d) illite crystals

However, halloysite has two forms- hydrous form (10Å) and less hydrous form (7Å). There are mainly three different types of halloysite morphology is readily reported in the literature: spheroidal, tubular and plate (Adamo et al., 2001 and Niu, 2016). Tubular is the predominant morphology of halloysite and these tubules can be long and thin, short and stubby. A typical TEM micrograph of long tubular halloysite is reported by Lázaro in 2015 which is presented in Figure 2.10 (b).

Krupskaya et al. (2017) investigated the mechanism in changing montmorillonite structure with the change of bentonites properties under thermo-chemical treatment. In this investigation, natural samples from the Tagansoye deposit was analysed and the size of laminar montmorillonite particles was 1-2 µm which was reported in the literature and the TEM micrographs of MMT from Tagansoye deposit is presented in Figure 2.10 (c).

Lázaro (2007) reported the illitization process describing the sequential smectite to illite development as a function of burial depth in the tertiary sediments in the Gulf coast of the United States. The alteration and dissolution of different phases and crystallisation of dioctahedral clays were analysed at angstrom and nanometer scale level which was highlighted in that report. The report published in details information on the illitization sequence in a hydrothermal alteration including identifying lattice-fringe TEM image of illite crystals which is presented here in Figure 2.10 (d).

Size and composition are the key elements in identifying the characteristics of clay minerals especially when it recovers from any waste source and exist in complex phases. To identify the clay minerals and its behaviour, quantitative analysis of clay minerals is the first step to develop the mineralogical profile (Ouhadi and Yong, 2003). Although optical microscopy is readily used to identify sands and coarse size crystalline materials, X-ray powder diffraction is the most reliable technique in identifying the mineralogy of clay materials (Poppe et al., 2001 and Hillier, 2000). Kłosek-Wawrzyn et al. (2013) analysed the sintering behaviour of clay materials which was a big challenge due to the complex mineralogical composition in clay materials transforming phase conditions during sintering. XRD technique was used in that study to identify the microstructure of clay minerals especially targeting the kaolinite clay minerals. The performed XRD analysis highlighting the kaolinite powder consisted of kaolinite, quartz and a small amount of illite phase of clay minerals is presented in Figure 2.11 (a).

Falcón et al. (2015) developed anticorrosion coatings utilising halloysite nanotubes. The structural changes in halloysite nanotubes after treatment with 2 mol/L sulfuric acid for 6 hours were evaluated with the samples without treatment. The XRD patterns for both samples were compared overlaying the peaks which are presented in Figure 2.11 (b).

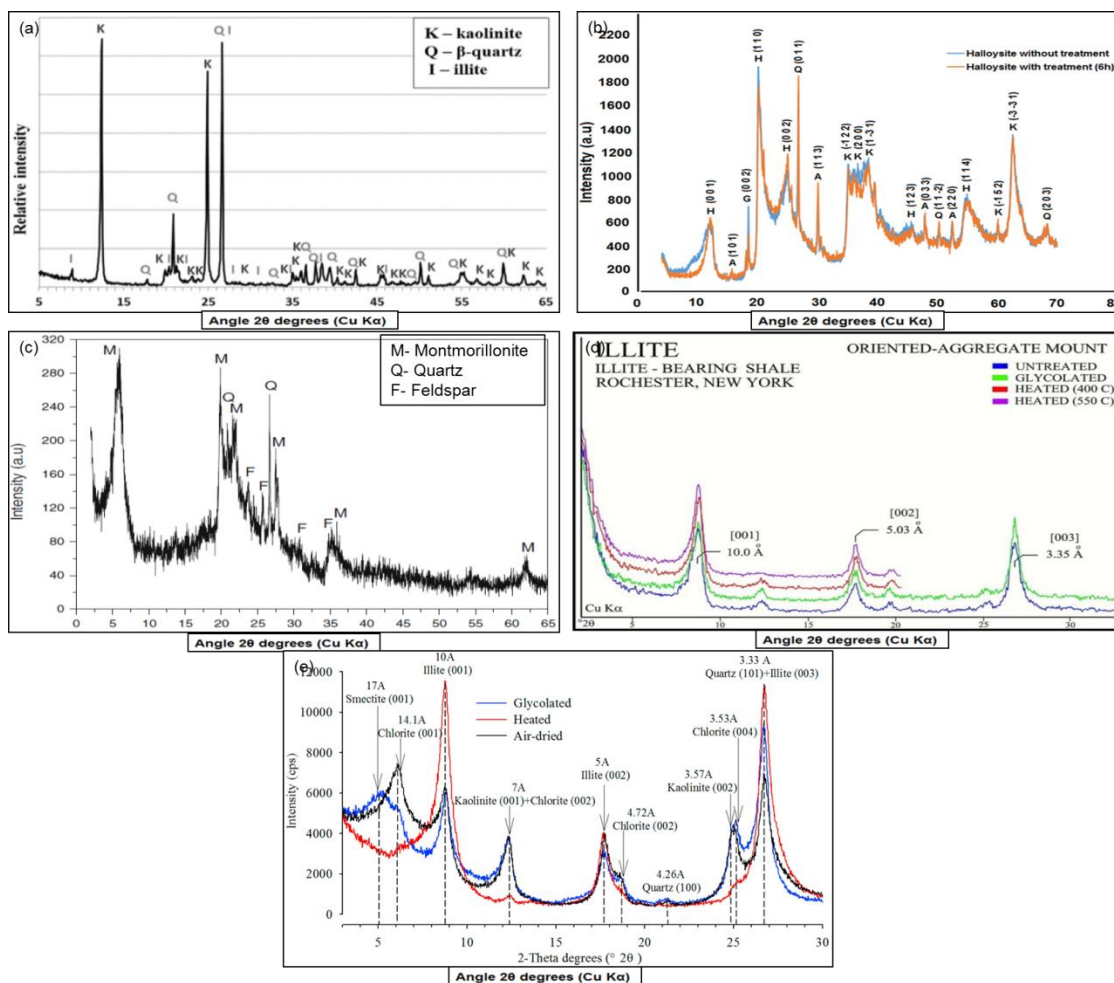


Figure 2.11 XRD pattern of: (a) kaolinite (Kłosek-Wawrzyn et al. 2013); (b) halloysite (Falcón et al. 2015); (c) montmorillonite (Djowe et al. 2013); (d) illite (Poppe et al. 2001) and (e) different clay minerals under different phase condition (Zhao et al., 2018)

Figure 2.11 (b) shows the XRD patterns of halloysite nanotubes with containing a small amount of alunite, quartz, kaolinite and gibbsite as impurities. The natural halloysite shows a sharp peak at 20.1° along 2θ axis which is a characteristic peak of tubular halloysite.

Djowe et al. (2013) performed surface treatment of smectite clay by using non-thermal gliding arc plasma at atmospheric pressure. XRD analysis was carried out to evaluate the effect of treatment on the crystalline and textural properties of the materials. The XRD patterns of this material revealed the presence of calcium montmorillonite (d space = 14.86 nm) with a small amount of quartz and feldspar as impurities which is also presented in Figure 2.11 (c). U.S. Department of the Interior, U.S. Geological Survey (Poppe et al., 2001) published a laboratory manual for X-ray powder diffraction to identify size and composition of different clay minerals in sediments. In that report, illite is mentioned as a group name of clay which consists of non-expanding dioctahedral micaceous minerals. Members of this clay groups are characterised by 10-angstrom 001 and a 3.3-angstrom 003 peaks which remain

unchanged by ethylene glycol or glycerol solvation, followed by potassium saturation and apply heat to 550°C. The XRD patterns of illite clay minerals in raw condition and under two different standard treatment conditions were highlighted in that report which is presented in Figure 2.11 (d). Zhao et al. (2018) studied the naturally alteration processes of fluvial sediments deposited since the Holocene. In that study, XRD data were analysed for all samples in three stages: a) air drying at room temperature; b) ethylene glycol saturated at 60°C for 12h and c) heating the samples at 490°C for 2h. The changes in XRD patterns of different clay minerals under these three experimental conditions were highlighted which is presented in Figure 2.11 (e). Several research groups presented different minerals content in petroleum sludge by XRD and ATR-FTIR analysis. The XRD pattern in certain peaks at 2-theta data confirmed the presence of barite ($2\theta = 26.2^\circ(26^\circ), 29.1^\circ(29^\circ), 31.9^\circ$ and 43.5°), quartz ($2\theta = 21.5, 23$ and 26.0°), zinc oxide ($30-40^\circ$), montmorillonite ($6^\circ, 9^\circ, 12^\circ, 14^\circ, 18^\circ, 27^\circ, 30^\circ, 61^\circ$), bentonite ($6^\circ, 9^\circ, 12^\circ, 14.8^\circ, 18^\circ, 27^\circ, 30^\circ, 61^\circ$), Magnetite oxide (35.5°) and calcite ($29.6^\circ, 39^\circ$). such as ($2\theta = 26.2^\circ (26^\circ), 29.1^\circ (29^\circ), 31.9^\circ$ and 43.5°). In addition, the band peaks at 1166 cm^{-1} in their attenuated total reflection-fourier transform infra-red (ATR-FTIR) study also confirmed the presence of Si-O stretching of quartz and the spectra bands at 1124 cm^{-1} and 1014 cm^{-1} highlighted the presence of montmorillonite (Adegbotulu, 2016 and Pendleton, 2014).

2.5.2 Polymer clay nanocomposites

Many industries including aerospace, automobile, civil infrastructures, sports, and marine are incredibly increasing their uses of nanocomposite materials because of these nanocomposites are better in their high performance and light weight applications than any other materials. Recently the use of nanoclays as fillers in polymers is receiving an increased interest due to their influential effect of improving different properties including mechanical (Luo and Daniel, 2003), thermal stability (Meneghetti and Qutubuddin, 2006), gas barrier (Cui et al., 2015), chemical and solvent resistant (Hu et al., 2014), flame retardant (Zhao et al., 2005) and impact resistant properties (Chen and Evans, 2009). These unique characteristics make these composite materials to take into consideration for using them in large bridge structures, wing blades, offshore platforms, engine machinery, electronic goods, and medical devices (Silva et al., 2013; Pereira and Martins, 2014 and Horrocks et al., 2001). A composite material is a heterogeneous mixture of two or more materials combine into one material to avoid the limitations of individual materials and also to favour the individual advantages (Hollaway and Teng, 2008). However, composite materials have some key disadvantages such as anisotropic properties, low through-thickness mechanical properties,

poor impact damage tolerance, and poor flammability properties because of the presence of polymer or organic substances (Advani et al., 2003).

Polymers are flammable and generate smokes and toxic gases under fire condition which hinders polymer materials usage in different applications (Morgan and Wilkie, 2007; Bourbigot et al., 2006 and Higginbotham et al., 2009). since the application of nanocomposite materials is increasing day by day, a safe and sustainable nanocomposite materials development is a demand now which is expected to be thermally stable and less flammable (Pashaei and Hosseinzadeh, 2016 and Bao et al., 2012). Development of new improved flame retardants are always an interesting area of research which has a tremendous commercial value, but the drawbacks associated with these improved materials are also be considered seriously as most of these flame retardants damage the other properties of materials including viscosity, reactivity, environmentally hazardous, physical and mechanical properties of final product (Weil and Levchik, 2008; Kandola et al., 1996 and Laoutid et al., 2009).

To avoid these difficulties, introducing nano scale reinforcement and flame-retardant materials such as nanoclays, carbon based nanomaterials etc in polymer matrix is considered as an alternative measures (Horrocks et al., 2001; Samyn et al., 2008 and Kiliaris and Papaspyrides, 2010).

Toyota Central Research & Development Labs is the pioneer to introduce polymer clay nanocomposite (PCN) where researchers were able to disperse clay platelets randomly and homogenously in polymer matrix. In 1985, this lab first introduced PCN which was commercialised as car equipment in 1989 (Okada and Usuki, 2006). In 1997, Gilman found revolutionary fire retardancy in new class of materials, organic-inorganic nanocomposites (Gilman et al., 1997 and Kashiwagi et al., 1997). Vaia and Giannelis (1997) published a ground-breaking report on different factors essentially influence the melt intercalation process for polymer-clay nanocomposite manufacturing. According to their findings, the most influential factors are: layered silicates functionalisation, anneal temperature, molecular weight of polymer matrix material and the polar interactions between layered silicates and polymers. However, to functionalise the silicate layers it is essential to understand the polar interactions between polymers and interlayers in clay structure and replacing the cationic groups in clay surface with the cationic head group of the surfactant leaving the organic tail radiating away from the clay surface. Alexander and Dubois (2000) reported that the effect of packing density and the polymer chain length in influencing the polymer chains to lay either parallel or tilted paraffinic arrangement which is shown in a schematic diagram in Figure 2.12 extracted from that report.

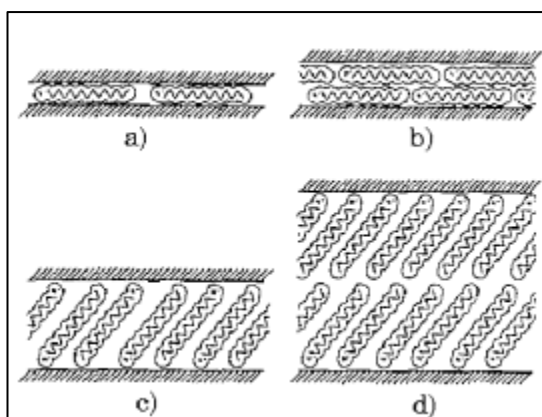


Figure 2.12 Alkyl chain sandwiched in layered silicates forming: a) lateral monolayer; b) lateral bilayer; c) paraffinic mono layer and d) paraffinic bilayer (Alexandre and Dubois, 2000)

When the interlayer packing density and the chain length decreases, the chains form a disordered, liquid-like structure due to the increase of *gauche/trans* conformer ratio which is presented in Figure 2.13.

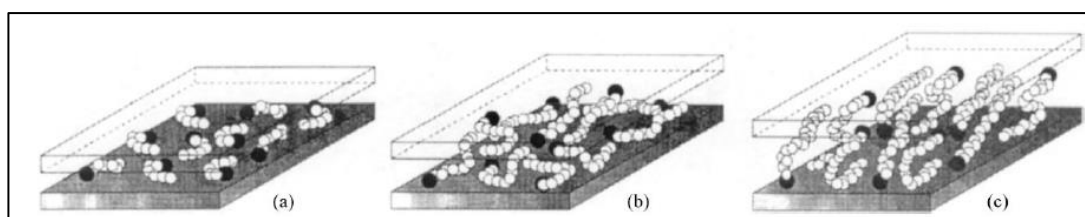


Figure 2.13 Alkyl chain aggregation model: a) lateral monolayer of short alkyl chain; b) lateral bilayer with in-plane disorder; and c) internal order increment by the formed internal chain aggregation. (Alexandre and Dubois, 2000)

The thickness of layered silicate is usually 1 nm and possesses high aspect ratio in the range of 10-1000. A few weight percentages of layered silicate offer a wide range of thermo-mechanical properties improvement in polymer matrix. The main challenge to achieve the properties improvement is uniform dispersion of clay platelets throughout the polymer matrix which creates the difference between different properties in conventional composites and nanocomposites (Pavlidou and Papaspyrides, 2008; Krishnamoorti et al., 1997 and Vaia et al., 1999). The interfacial interactions between polymers and layered silicate dictate the type of polymer/layered silicate (PLS) nanocomposites manufactured (Ray and Okamoto, 2003 and Usuki et al., 1993). Ray and Okamoto (2003) discussed three types of PLS nanocomposites in their report such as (a) intercalated nanocomposites; (b) flocculated nanocomposites and (c) exfoliated nanocomposites.

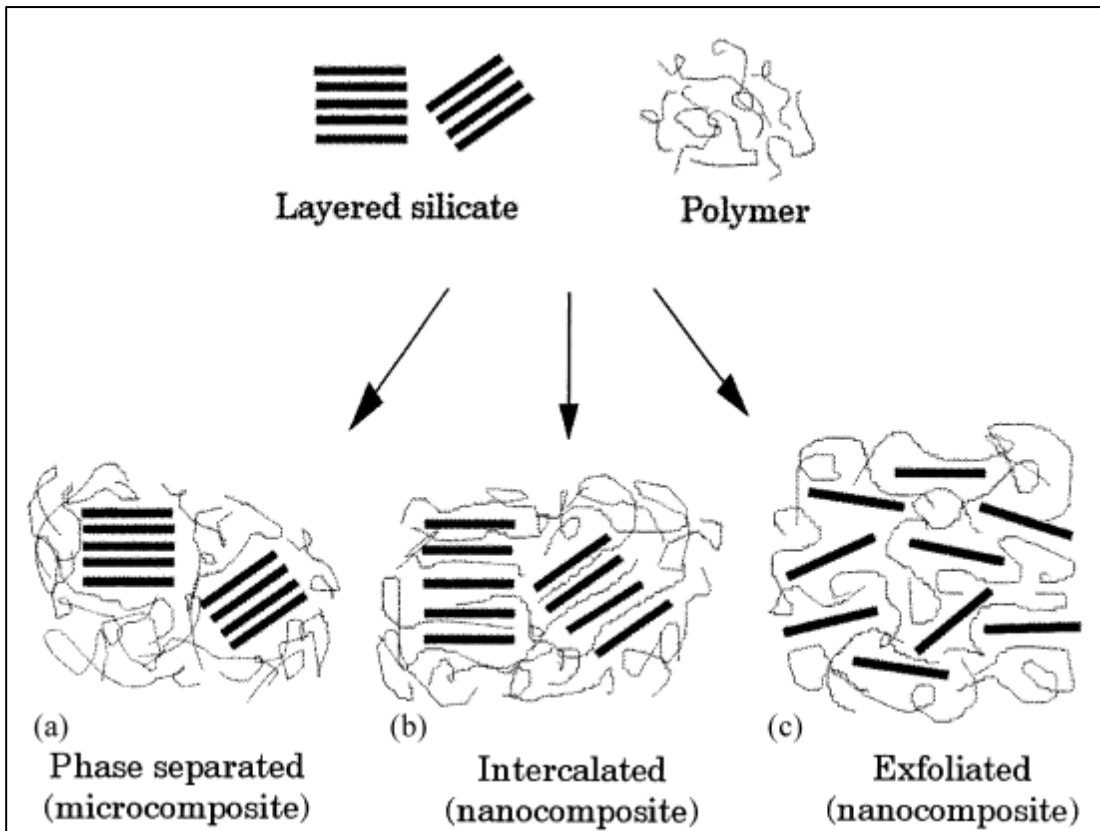


Figure 2.14 Schematic presentation of different polymer/layered silicates nanocomposites (Ray and Okamoto, 2003)

Micro-sized filler such as clay reinforced polymers were manufactured by breaking down clay aggregates to improve properties in polymer/clay composite materials over decades. Improvement of different properties is limited to achieve in this system due to the less interaction between clay platelets and polymer chains which is shown in Figure 2.14 (a) and 2.15. The weak interlayer bonding in clay stack may act as damage initiation sites in applications (Gao, 2004, and Priolo et al., 2010).

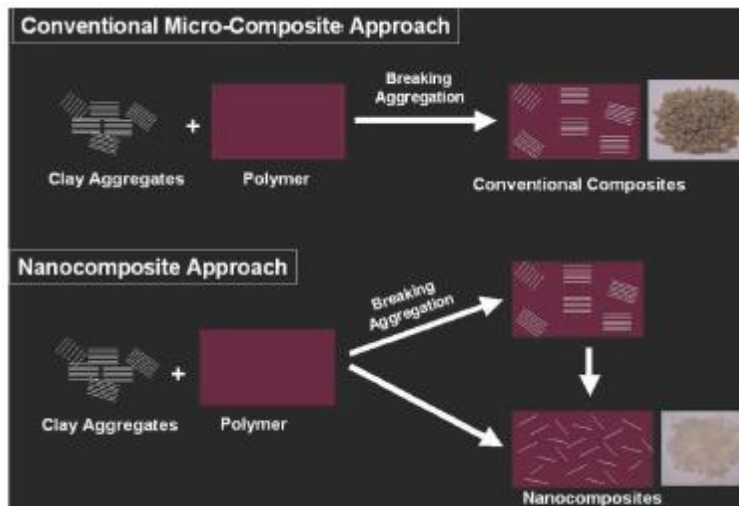


Figure 2.15 Schematic illustrations of conventional micro and nanoscale manufacturing approach (Gao, 2004)

Intercalated nanocomposites are formed when a few of polymer chains are inserted in silicate layers in a regular fashion which is presented schematically in Figure 2.14 (b). Flocculated nanocomposites are also come under this type of nanocomposite where silicate layers are flocculated due to the hydroxylated edge to edge interactions among silicate layers. Exfoliated nanocomposites are nanocomposites where clay layers are separated in polymer matrix leaving the average distances among the interlayers. Generally, to achieve exfoliation less amount of clay is needed compare to the clay content is needed to form intercalation. The exfoliation structure of clay platelets is schematically presented in Figure 2.14 (c).

2.6 Preparation of polymer clay nanocomposites

There are two popular polymer/clay manufacturing techniques have been reported in different literatures (Hussain et al., 2006, Wang et al., 2004 and Rao and Pochan, 2007): melt processing and solution processing. However, in-situ polymerisation and template synthesis techniques are highlighted in literature too. These processes are briefly discussed in the following sections.

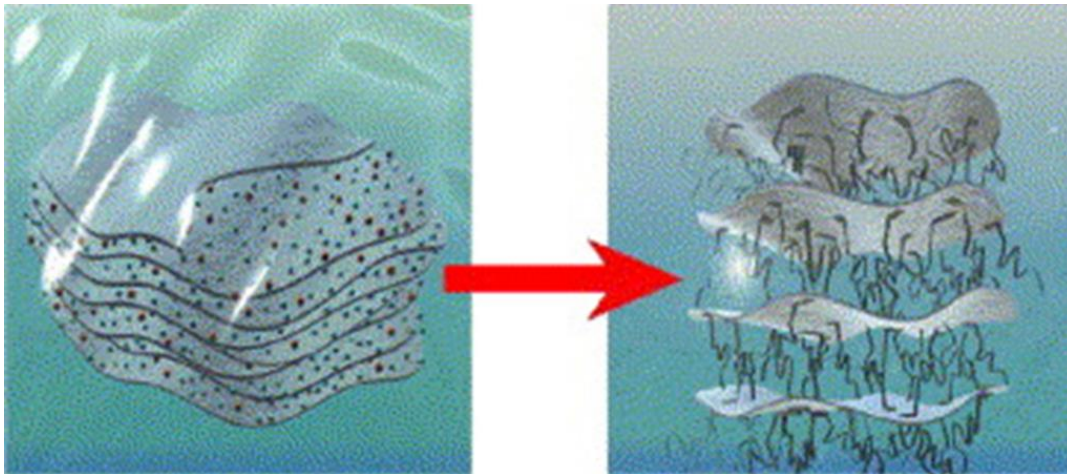


Figure 2.16 Schematic illustration of clay platelets expansion to improve interaction between polymer chains and clay platelets (Fischer, 2003)

2.6.1 Solution processing

Solution blending is a two-step process; first, solvent is selected carefully where polymer can easily be dissolved in that solvent. In second step, clay is dispersed in the same solvent. Finally, the dispersed clay solution is mixed with polymer/solvent solution. This mixed solution is allowed to leave for a subsequent period of time to homogenize the solution and to intensify the evaporation of solvent from the mixed solution. A schematic presentation of this process is published by Gou et al. in 2012. The mechanism in this process is that the soluble polymer will replace the solvent which is placed between the interlayers in clay during the clay swells up in solvent. This process produces hybrids with nanoscale morphology.

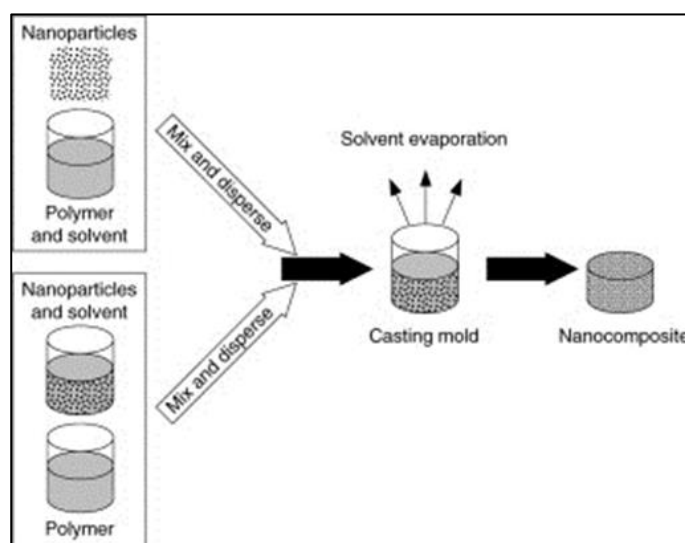


Figure 2.17 A schematic illustration of solution processing (Gou et al., 2012)

This method becomes popular in manufacturing water-soluble polymers. Among the most reported solution blending process of polymer composites in literature including polyvinyl alcohol (PVOH) (Ogata et al., 1997 and Greenland, 1963), polyvinyl pyrrolidone (PVP) (Francis, 1973 and Levy and Francis, 1975), polyethylene oxide (PEO) (Ogata et al., 1997; Aranda and Ruiz-Hitzky, 1992 and Shen et al., 2002), polyethylene vinyl alcohol (PVA)(Carrado et al., 1996 and Clegg and Breen, 2014), polyacrylic acid (PAA) (Tran et al., 2005 and Natkański et al., 2012). Several non-water-soluble polymers are reported in literature too, such as high-density polyethylene (HDPE)/carbon nanotube (CNT) nanocomposites synthesised by Kodjie et al. (2006) and polylactic acid (PLA) by Lim et al. (2008).

2.6.2 *In-situ* polymerisation

In-situ polymerisation is one of the polymerisation techniques where monomer and catalyst takes place inside the gallery space of filling materials such as clay, carbon-based particles etc. However, the platelets in case of clay filler are swelled and change in dispersion characteristics of clay platelets in polymer matrix.

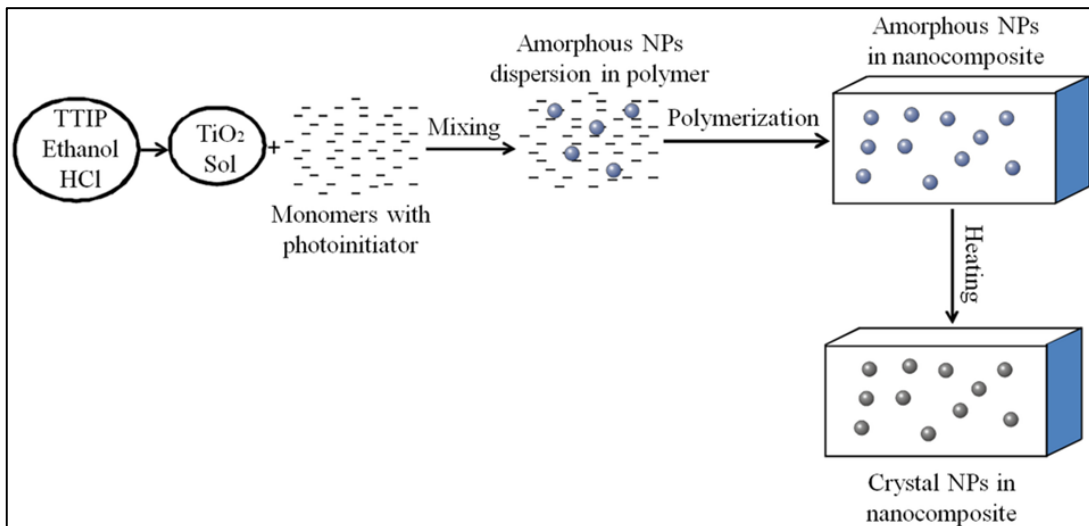


Figure 2.18 A schematic illustration of *In-situ* polymerisation process (Guo et al., 2014)

This technique is reported to be an effective way to exfoliate clay platelets in polymer (Zapata et al., 2008). Figure 2.18 shows a schematic illustration of *in-situ* process which is followed by Guo et al. in 2014 to manufacture nanocomposites tuning by adding TiO₂ nanoparticles.

This process has certain advantages including one step synthesis process ensuring better compatibility between clay platelets and polymer and enhancing clay dispersity in polymer matrix. Generally, adding organically modified clays in monomer in presence of an appropriate initiator under a specific environment is the basic polymerisation process to carry out *In-situ* polymerisation. However, selecting initiator and system environment is polymer and nanomaterials specific. Sun and Garces (2002) reported a novel approach of manufacturing high-performance polypropylene-clay nanocomposites by *In-situ* polymerisation where external activators, high pressure and high temperature are not needed. This process can be applied to other polyolefin-clay nanocomposites according to their claim.

2.6.3 Template synthesis

Template synthesis process is similar to the *in-situ* polymerisation process. The only difference between these two processes is that in template synthesis process, clays are synthesised in the presence of a polymer solution. Clay minerals have been studied extensively including as host matrices of different organic materials. This process is useful to synthesise nanocomposites with superior electrical properties where electroactive polymers intercalates to the porous inorganic materials (Fernández-Saavedra et al., 2009).

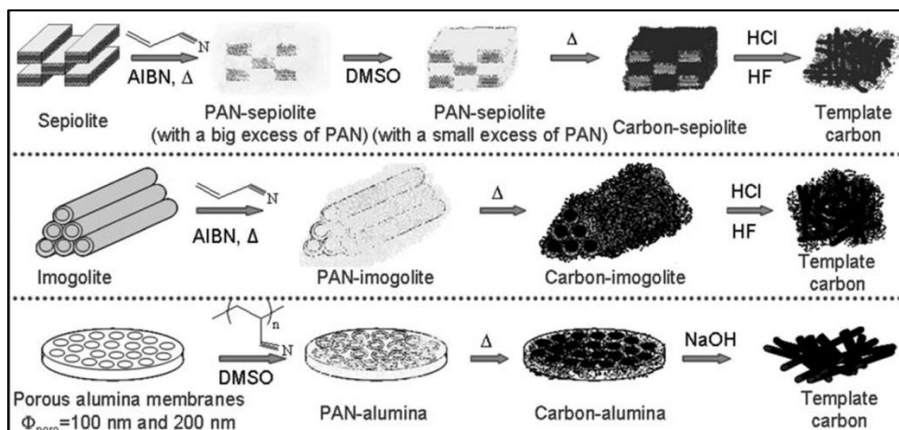


Figure 2.19 A schematic illustration of template synthesis process of PAN-inorganic nanocomposites (Fernández-Saavedra et al., 2009)

One of the important features of this type of nanocomposites is that large amounts of polymer are needed and highest degree of filler dispersion can be achieved by following this technique. Figure 2.19 shows a schematic illustration of template synthesis process of polyacrylonitrile (PAN)-inorganic nanocomposites (Fernández-Saavedra et al., 2009).

2.6.4 Melt processing

Melt blending is an interesting manufacturing process of thermoplastics and elastomeric nanocomposites due to its ease of application and economically viable. In a simple way, melt compounding can be described as a composite/nanocomposite manufacturing process where polymer is melt and combined with the target amount of fillers such as clay using Banbury or extruder (Bilotti et al., 2008). It is a common practice to apply shearing force in heating zones to produce nanocomposite compounds. Melt blending has a number of advantages over the other conventional nanocomposite manufacturing process such as this process is environmentally benign as it does not need any solvent which is needed in solution blending process and *in-situ* polymerisation process. However, controlling the dispersion of platelets in polymer solution is not always achievable or reproducible in *in-situ* polymerisation process (Rane et al., 2018). Considering different aspects of this manufacturing technique such as the suitability of this process in industrial scale operation, environmentally safe and economically sustainable- this process has become popular and reliable in both in industry and in research community.

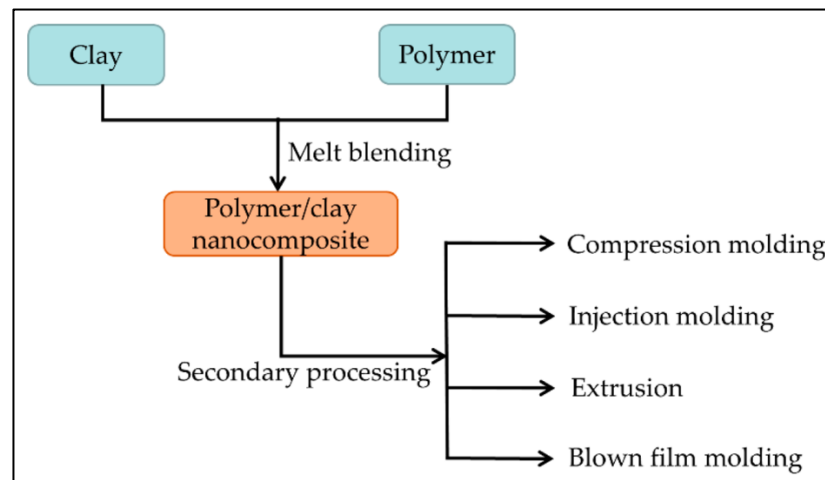


Figure 2.20 A schematic illustration of melt compounding process (Guo et al., 2018)

After presenting briefly the data observed by different research groups and published in literature, it can now be concluded that different clay minerals possess different chemical composition, structures and morphology. The effect of using these different kinds of clay on thermal and mechanical properties of polymer nanocomposites varies due to the characteristics of different types of clay is different. Various types of manufacturing processes of polymer-clay nanocomposites are described briefly too. The following section describes the addition of clay in influencing the crystallinity, thermal and mechanical properties of LDPE and PA6 polymer matrices.

2.7 LDPE clay nanocomposites

The morphological structure, chemistry and physical characteristics of clay influence the thermal, mechanical and rheological properties of polymer/clay nanocomposites (Nguyen and Baird, 2006 and Xu et al., 2006). All these characteristics play a major role dictating the interfacial adhesion between clay platelets and polymer matrix (Zare, 2016, Borse and Kamal, 2006). High interfacial area with strong interaction between clay and polymer ensures better thermal, mechanical and rheological properties of nanocomposites compare to those of conventional composites (Grigoriadi et al., 2013 and Masenelli-Varlot et al., 2007). This interfacial adhesion is directly linked with polarity of clay platelets and polymers. There is a very negligible or no interaction between polar clay platelets and non-polar polymer such as polyethylene (PE), polypropylene (PP) which is highlighted in different literature (Grigoriadi et al., 2013 and Giannakas et al., 2009).

Several research groups have reported the thermal stability behaviour of polyethylene clay nanocomposites in different research articles. Xie et al. (2012) have reported the thermal stability by analyzing the thermogravimetric analysis (TGA) curves (under nitrogen gas condition) of their LDPE/OMMT nanocomposite specimens. The onset degradation temperature of the nanocomposite specimens of only 0.5 wt% have increased by a considerable 23 °C for organically modified montmorillonite (OMMT) compared to that of neat LDPE. Morawiec et al. (2005) have also performed thermogravimetric analysis (TGA) on their samples which were conducted under nitrogen atmosphere and in an air atmosphere. Based on the TGA curves, Morawiec et al. (2005) have concluded that the presence of filler did not significantly improve the thermal stability in a nitrogen atmosphere since decomposition temperature and peak intensity have all been recorded to be relatively consistent. More research on the thermal properties of organoclay/polymer nanocomposites carried out by Attaran et al. (2015) have reported no notable change in the nucleation activity between neat LDPE and LDPE/OMMT 6 wt% specimens from their differential scanning calorimetry (DSC) analysis. Hemati and Garmabi (2011) have observed improved thermal stability of their LDPE/ linear low density polyethylene (LLDPE)/nanocomposites in the air and nitrogen atmosphere and observed a weight loss at a lower temperature due to the decomposition of the organic modifier.

There are numerous results published in literature highlighting mix of opinions based on the research findings. Zhang and Sundararaj (2006) published an article claiming that all mechanical properties including ductility of LLDPE/ poly(ethyl methacrylate) (PEMA)/clay nanocomposites increase with clay loading. The improvement in interfacial adhesion among LLDPE, PEMA and clay due to the enhanced miscibility between LLDPE and PEMA is

emphasised for the improvement of mechanical properties especially for the improvement in ductility. It is a common practice now to add compatibiliser such as ethylene-vinyl acetate (EVA) copolymer (Dadfar et al., 2011), low molecular weight oxidized polyethylenes (Durmuş et al., 2007), maleic anhydride grafted polyethylene (PEMA) (Parija et al., 2007), zinc-neutralized carboxylate ionomer (Sánchez-Valdes et al., 2006), Oxidized Wax (Geethamma and Luyt, 2008) to improve different properties including thermal, mechanical, toughness and barrier properties.

2.8 PA6- clay nanocomposites

The application of layered aluminosilicate as fillers in polyamide nanocomposites has received attention in recent years. PA6- layered-silicates have been studied over years due to its unique properties to reduce flammability, increasing heat resistance, exhibit higher tensile strength, improving tensile modulus, increasing flexural strength and also improving flexural modulus (Fornes and Paul, 2003; Bourbigot et al., 2002, Njuguna et al., 2008, Morgan and Gilman, 2003 and Bourbigot and Duquesne, 2007). The continuous improvement of these achievements has attracted researchers to scale up certain properties such as thermal stability, flame retardancy, ablation and barrier resistance in the composite material to increase the application of this material as advanced structural material in different industries including automotive and space industries (Leszczyńska et al., 2007a; Leszczyńska et al., 2007b; Seymour and Kirshenbaum, 1986 and Qin et al., 2003). The advancement of these properties largely depends upon the nanomorphology of this filler into the polymer chain as this morphology related to the chemical structure of the filler which is source of origin and surface modification dependent (Pavlidou and Papaspyrides, 2008 and Dennis et al., 2001).

In semicrystalline polymers such as PA6, two interphases which act as immobilised fraction are highlighted. One is present between the amorphous fraction and crystal fraction in the polymer and the other exists between the inorganic filler and polymer matrix. These interphases generate rigid amorphous fraction (RAF) which act between crystal and amorphous phase as a result of evolving immobilisation of a polyamide chain due to crystal (Schick, 2009 and Schick et al., 2001). The addition of clay particles in the PA6 nanocomposites can increase the growth rate of these crystals (α or γ form). However, increasing the clay content beyond a certain level retards the rate of crystallisation which plays the main role in thermodynamic stability of the material (Fornes and Paul, 2003 and Wu and Wu, 2002).

Shishan et al. (2004) reported that the modulus, bending strength and heat distortion temperature of PA6/MMT nanocomposites increased with increasing clay content but decreased the tensile strength with the addition of MMT more than 4.3 wt%. Tjong et al. (2002) highlighted the improved strength and the stiffness of PA6/MMT nanocomposites at the expense of tensile ductility.

The bulk mechanical properties were studied by Liu et al. (2011) that PA6 with 3 wt% MMTs exhibited the best performance in tensile strength and flexural strength. It was also found in their study that higher loading of MMT in PA6 matrix-initiated agglomeration and leading to a decrease in tensile and flexural strength tests. Borse and Kamal (2006) presented the effect of different organophilic treatment of MMT surfaces, residence time and mixing efficiency during extrusion process on mechanical properties of PA6/clay nanocomposites. Interesting findings were highlighted in their report that longer residence time and higher mixing efficiency during extrusion process produced the highest degrees of exfoliation and enhanced the mechanical properties of PA6/clay nanocomposites.

In addition to clay loading in polymer, the source of clay minerals also plays an important role in influencing properties in nanocomposite materials (Uddin, 2008 and Carretero and Pozo, 2009). Considering the different aspects of clay mineral sources and potential applications in influencing the mechanical and thermal properties in nanocomposite materials, The Centre for Advanced Engineering Materials at Robert Gordon University has initiated an investigation on how the reclaimed layered silicate from oil-based mud (OBM) waste influence the properties in engineering nanocomposite materials. It is also important to mention here that this research group has aimed to investigate the relation between the change in amorphosity and crystallinity of polymer chain due to the addition of these OBMFs in nanocomposite and the variation in properties of material mainly thermal property of material. These OBMFs behave in a similar manner as other inorganic particles which often act as nucleating agents in polymer nanocomposites and sometimes cause the retardation of crystallisation in the structure. Since the large surface of the nanofiller is contributing the greater interphases between filler and polymer matrix, it is believed that the properties of the materials are significantly influenced by this interaction between interphases (Wurm et al., 2010).

2.9 Conclusion

The accumulated drilling fluid wastes in oil and gas industry is different in every operation site. The variations in drilling operations including using drilling fluid with different compositions and the variations in geological conditions make these waste streams so

diverse that there is not any standard drilling fluid waste profile tool to identify the composition and character of the wastes. The scenario is even more complex in offshore drilling operation as the unique sediment characteristics, benthic community, and hydrodynamic regime also influence the drilling waste characteristics.

To design a sustainable and viable drilling waste management plan/model, the first step is to identify the composition and nature of the pollutants in the wastes. Based on this information different waste treatment plan can be placed in operation such as, thermal treatment, thermo-mechanical treatment, biological treatment, encapsulation of pollutants. To meet the current strict environmental regulations with respect to disposal of this waste or to recycle or recover valuable components such as certain metals, identification of drilling waste composition and characterisation analysis is the obvious first step to move forward to the next stages. However, the environment is still facing the biggest challenge - are these treatment measures capable of producing pollutants free or environmentally safe discharge or producing pollutants free or eco-friendly solid waste? The solution might be very difficult as these treatment processes involve space requirements, duration of treatment operation, operational cost, investment cost, monitoring requirement, expertise etc. These obligations open up a new era of research to use this waste as a raw material to make valuable products rather than incurring burden to the environment. This literature review highlighted the problems associated with OBM waste, the draining route of potential engineering valuable compounds in waste to landfill site and the possible solution of turning waste into valuable products as filler in engineering nanocomposite material.

The key findings of the literature review are

- Drilling mud and its functions in oil and gas exploration industries are discussed here. Although OBM waste is considered as a hazardous waste, but due to its unique functionality in drilling operation which makes OBM as an essential material in drilling operation. However, accumulated of this hazardous OBM waste discharged on site for decades due to the lack of law enforcement and knowledge of detrimental effects of this waste to the environment. The data of Drilling waste generation and the discharged waste in the sea was presented in this review in light of information available in literature.
- The recoverable useful compounds including different clay minerals were highlighted in this chapter by presenting OBM waste characterisation. Focusing OBM waste as a potential source of useful clay minerals, the technological future of using these clay minerals was discussed especially as a filler in nanocomposite manufacturing.

- The effects of different clay minerals on influencing morphological, structural, rheological, thermal and mechanical properties of different polymer/clay nanocomposites were presented.
- The potential utilisation of OBM waste as a source of nanoclay in developing polymer nanocomposites manufacturing was highlighted and supported by the literature findings of using clay minerals in polymer matrices to improve different thermo-mechanical properties.
- The recycling option of different nanocomposites were mentioned which may save the limited resources in the long run.

This research project will scrutinise this and assist towards the development of introducing nanoclay recovered from oil-based drilling fluid, which is also called Oil Based Mud (OBM) waste from oil and gas industries into nanocomposites with better mechanical and thermal properties.

Chapter 3: Thermal Treatment Process and Characterisation of Oil Based Mud Waste

3.1. Introduction

A drilling fluid is an essential part of drilling operation in oil and gas industry to perform certain functions such as removing and cleaning drill cuttings from the downhole, cooling and lubricating the drill bit, controlling the hydraulic pressure to protect well blowouts (Caenn et al., 2011; Fink, 2015; Khodja et al., 2010). Among different drilling fluids, (OBM) is preferable material, especially where reliable shale inhibition and excellent lubricity is needed (Patel et al., 2007). This drilling fluid predominantly OBM which is used in deep drilling operation ended up with a large number of pollutants introducing in drilling fluids addressing a big concern for the oil and gas industry and government regulators (Veil, 2002; Force, 2009).

However, Gbadebo et al. (2010) investigated the elements presents in both oil based and water based mud using atomic absorbtion spectrophotometry and the content of Fe, Ca, Mg, Cr, Pb, Mn and Ni were reported in that study. Another study performed by Adegbotolu et al. (2014) also highlighted the presence of heavy and trace metals using inductively coupled plasma optical emission spectroscopy (ICP-OES) analysis of oil-based drilling fluid and cuttings. To investigate the thixotropy nature of OBM waste, rheology measurements are essential. A number of studies have been reported in the literature including Taiwo and Otolorin (2009) and McCosh et al. (2009) and the findings from these studies highlighted the incremental viscosity of OBM waste comparing the viscosity of fresh OBM due to the addition of fine solids from the low density cutting of the formation which trap water to form gels which causes the lowering of the free oil/water ratio (OWR) in the given sample.

Considering the information scarcity in literature, this study focusses onto characterisation of oil-based drilling fluid waste and builds on our previous studies and investigations, this study provides a comprehensive chemical, thermal and rheological analysis of the oil-based mud waste in North Sea Region (Adegbotolu et al., 2014 and Siddique et al., 2017). It is expected that the characterisation of this used oil-based drilling fluid gives indications of method suitability or the effective level of treatment needed to design a sustainable solid waste management measure in oil and gas industry. The microscopy, chemical and elemental analysis, calorimetry, thermogravimetry, spectroscopy, energy dispersive X-ray analysis (EDXA) and X-ray diffraction were carried out to evaluate the thermo-chemical characteristics of the OBM waste. The overview on opportunity and challenges in converting

this OBM waste to a source of recovered resources and utilisation as primary and secondary raw materials are discussed and conclusions drawn.

3.2. Experiment

3.2.1. Materials and samples preparation

The OBM waste was donated by a local oil and gas service company in Aberdeen, UK. Tetrachloroethylene (TCE) was purchased from Sigma Aldrich, UK, and degassed deionised water, metal stock solutions in nitric acid (10,000ppm) and hydrochloric acid were obtained from Fisher Scientific Ltd, UK.

To characterise the solid content in this OBM slurry, the petroleum hydrocarbon was eliminated by using thermal treatment process. To obtain the solid residue, the OBM slurry is heated sporadically by following the stages: 50°C for 12 hours (1st heating) followed by 80°C for a further 12 hours (2nd heating); finally, the residue is heated at 700°C for 12 hours (3rd heating). To facilitate to carry out different analysis, this solid residue was crushed into smaller pieces using a grinder followed by a further size reduction to produce powder by using IKA UltraTurrax ball mill.

The montmorillonite (MMT), K10 was supplied by Sigma-Aldrich, UK which used as a reference material to compare different characteristics between MMT and OBM powder.

3.2.2. Structural and morphology analysis

Scanning electron microscope (SEM) was performed using a JEOL JSM-7400F instrument with a magnification of 10000X, 8.0 mm working distance (WD) and accelerating potential of 5.0 kV. The samples were coated with gold and palladium using sputter deposition for 2 minutes prior to the analysis.

Attenuated total reflectance- fourier transform infrared (ATR-FTIR) spectroscopy was carried out for 32 scans between 4000-400 cm^{-1} with a resolution of 4 cm^{-1} . A blank measurement was taken to minimise the influence of water vapour and carbon dioxide from the atmosphere. The air background was collected and then the sample spectra was collected and saved. The dry drilling waste sample was placed between the ATR stage and the diamond.

Mineralogical composition for both OBM powder and MMT was determined by X-ray diffraction (XRD) using a Siemens D5000 diffractometer with Cu K α radiation ($\lambda = 0.15406$ nm) in the range of 3-60° and 0.1° 2 θ step size and scanning speed was 0.02°/s. The diffraction details and relative intensities were obtained and compared by using Rietveld refinement software.

3.2.3. Element analysis

Elemental compositional analysis was carried over using spent drilling fluids supplied by a local company in Aberdeen, UK. The samples were replicated two times to make the results more analytically acceptable and reproducible. This analysis can be divided in two sections; a) sample digestion procedure and b) sample analysis using inductively coupled plasma optical emission spectrometry (ICP-OES) instrument. To determine the elemental composition of dry OBM waste, energy dispersive x-ray analysis (EDXA) (Oxford Instruments INCA Energy) was carried out.

The ICP-OES analysis was performed following the same procedure followed by Adegbotolu (2016). The following operation parameters of Power: 1500 Watts, frequency: 40.68 MHz, nebulizer flow: 0.60 L/min, Argon plasma flow: 15 L/min, Argon auxiliary Flow: 0.2 L/min, Argon pump rate: 2.0 mL/min were followed. 0.5g of sample was digested using an aqua regia-microwave digestion procedure for 30minutes. An Optima 2100 DV ICP-OES system was used to carry out the analyses. A 100mg/l multi-element standard was prepared and used to prepare the standards calibration of range 0.5mg/l to 5mg/l. The elements in multi-element standard were Heavy metals: The concentrations of alkaline earth metals (Mg, Ca, Ba), alkali metals (Na, K), transition metals (V, Cr, Mn, Fe, Ni, Cu, Zn, Cd), post-transition metals (Al, Pb), metalloids (Si, As), polyatomic non-metals (P, S), and actinide (U), The acid extract was analysed for the selected elements using ICPOES. The analytical results obtained were compared against OSPAR threshold guidelines.

Sample digestion procedure is a step by step process where the drilling fluid sample (0.5 g) was transferred to Teflon beakers, followed by adding 8 mL of HNO₃ in the beakers. Digestion was performed in triplicate for drilling fluid sample. They were kept in a closed system in a microwave oven (ETOH) for 15 min on the temperature ramp (13.33°C/min) until to reach at 200°C. The samples were kept in the same temperature environment in the digester for an additional 15 minutes for completing the samples digestion process.

After digestion, all extracts were filtered through Whatman 1, 542 (Hardened Ashless) filter paper and transferred to 50 mL volumetric flasks (Fisher Scientific), filling with deionised

water. Glassware was cleaned and decontaminated in a 5% nitric acid solution for 24 h and then rinsed with deionised water.

3.2.4. Thermal analysis

TA Q100 instrument under a nitrogen environment was used for performing Differential Scanning Calorimetry (DSC) thermal analysis by following heat-cool-heat procedure with the temperature ramp of 10°C/min from -20°C to 250°C. The TA Q500 instrument was used to perform Thermogravimetric Analysis (TGA) to identify the degradation and decomposition nature of the materials. The temperature was set on ramp mode from room temperature (15°C) to 1000°C at a rate of 10°C/minute.

3.3. Result and discussion

3.3.1. Morphology study

In Figure 3.1, the micrograph shows the tightly stacked platelets of montmorillonite and OBM waste powder with size ranges up to 1000nm.

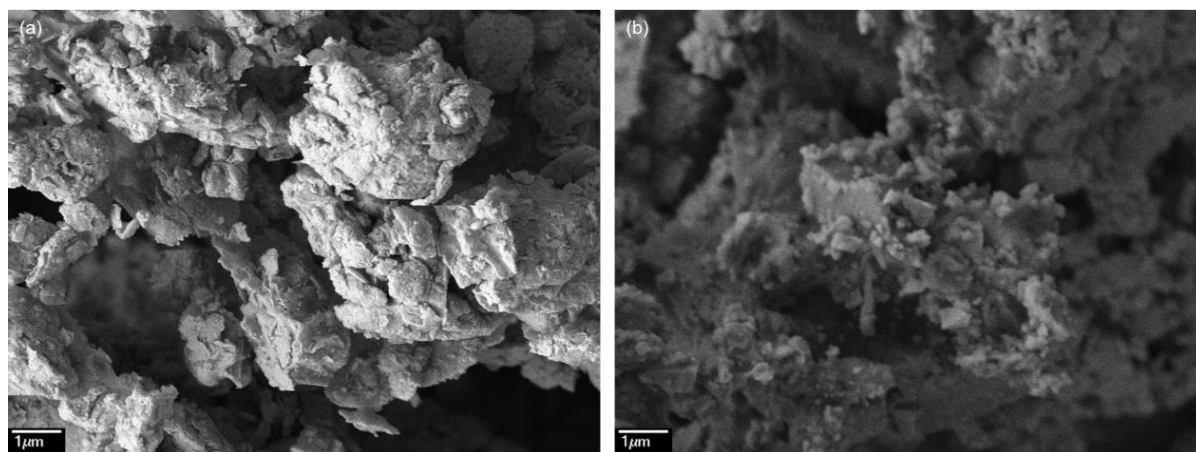


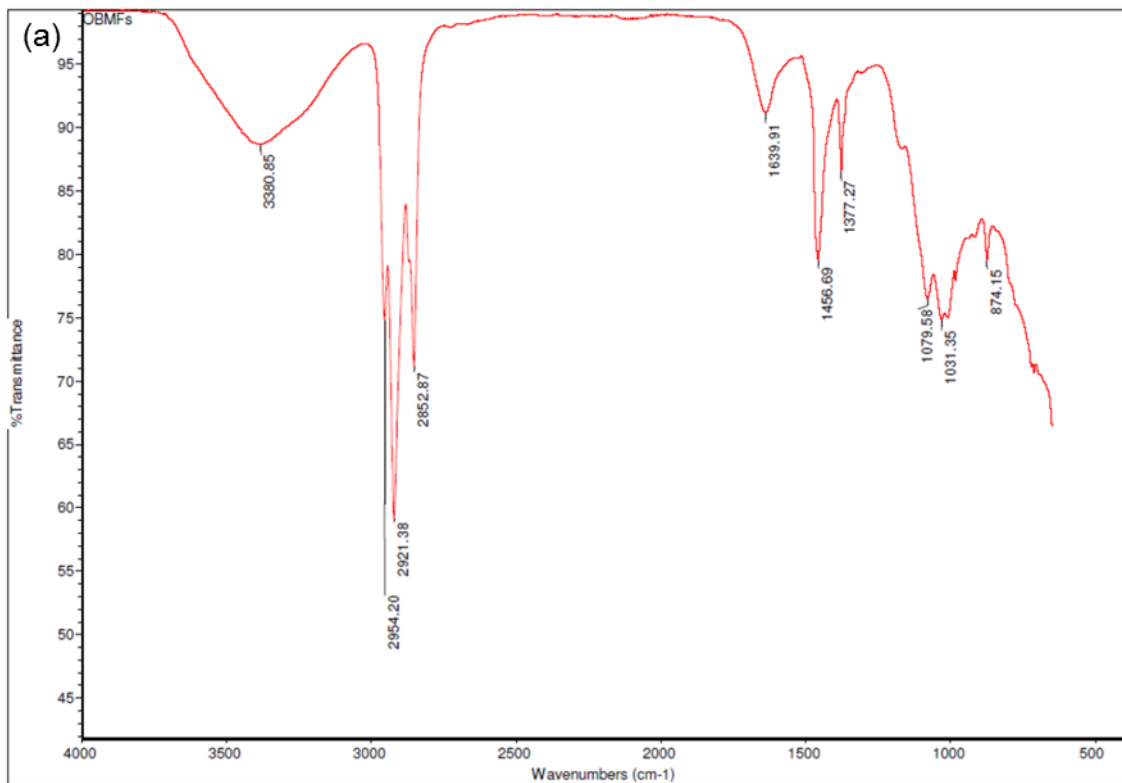
Figure 3.1 SEM images of (a) Montmorillonite as a reference material and (b) OBM waste dry powder

The SEM micrographs were used to investigate the morphological representation of different clay minerals present in OBM waste which is compared with that of standard montmorillonite sample supplied by Sigma-Aldrich. Both micrographs represent the platelet structure of MMT

(a) and OBMFs (b). However, OBM shows tightly stacked the platelets with variant sizes of platelets with different shapes whereas montmorillonite shows regular platelet shapes with uniform structure. It can articulate here that different clay minerals may influence the structure and shape of the platelets present in OBM waste. Detail morphology will be discussed in the next study where different clay minerals can be identified by observing the structure and shape of different platelets present in OBM waste.

3.3.2. Chemical structure analysis

The resulting spectra from ATR-FTIR analysis of OBM waste slurry and its solid contents are presented in Figure 3.2. and Appendix A.



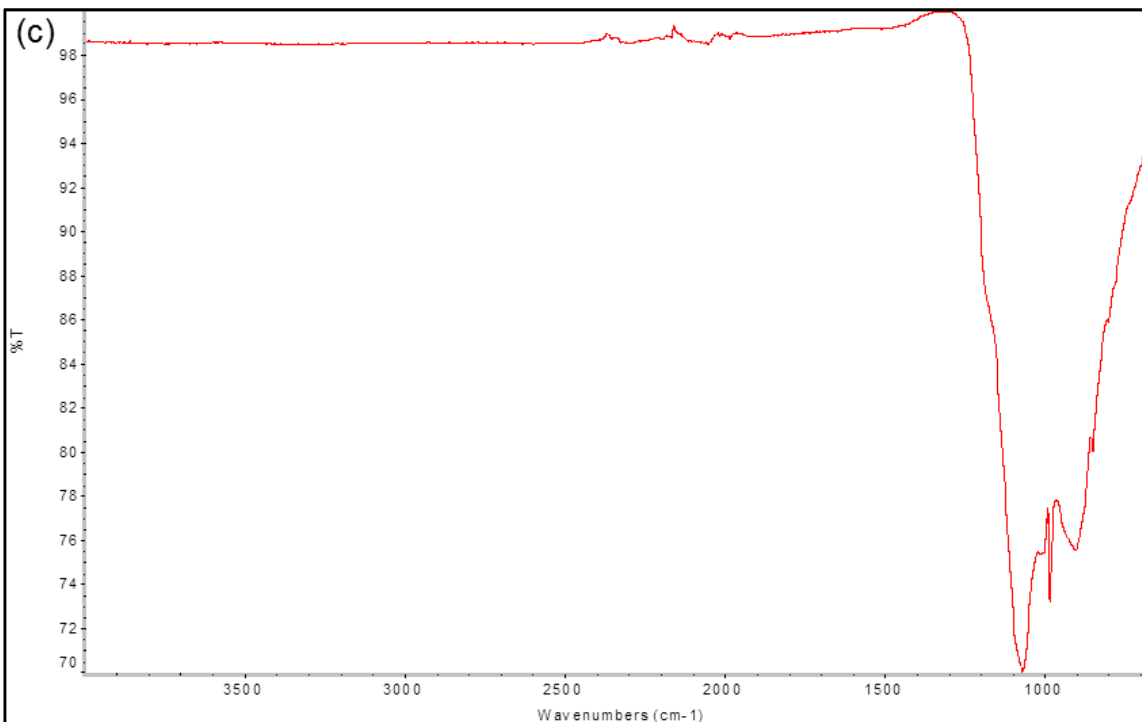
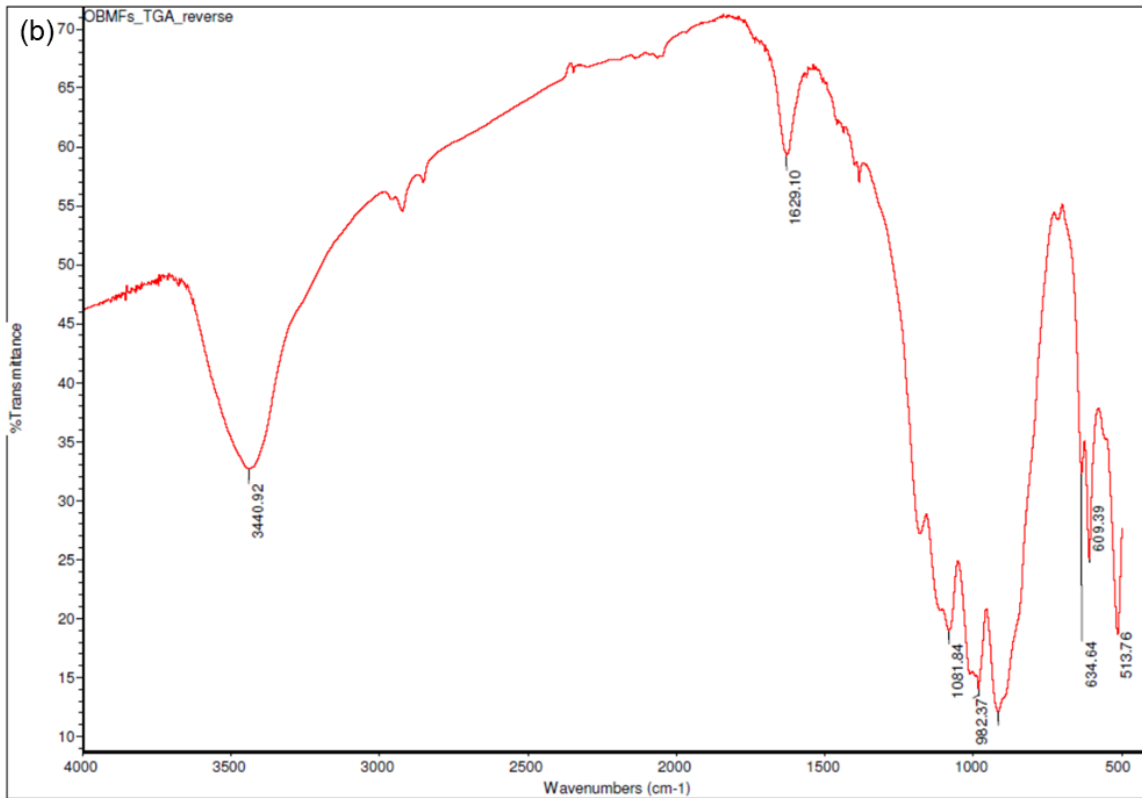


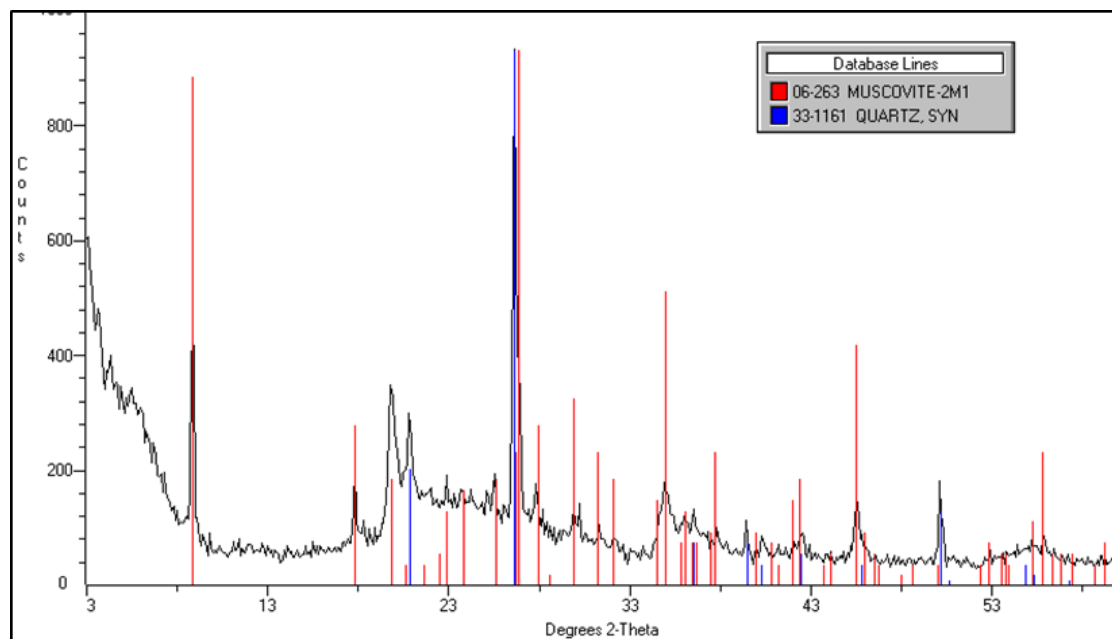
Figure 3.2 ATR-FTIR full scale spectra of (a) OBM waste slurry; (b) OBM waste residue after TGA analysis and (c) OBM waste dry powder

Figure 3.2 (a) shows different OH bending presence in OBM slurry which corresponds to the hydrocarbon presence in the substance. Figure 3.2 (b) and (c) represents different peaks

corresponding to different chemical bonds in OBM waste after TGA and in OBM waste powder. A broad band near 3380 cm^{-1} corresponds to the H-O-H vibrations of adsorbed water. The clay minerals in OBM waste show Si-O stretching and bending as well as OH bending absorptions in the range of $1300\text{-}400\text{ cm}^{-1}$. Variations in the layers arrangements are reflected in the shape and positions of the bands. Strong band peaks at $1120\text{-}1000\text{ cm}^{-1}$ corresponds to the Si-O stretching vibrations of kaolinite and dickite. The main Si-O band peak corresponds to chrysotile is observed at a lower frequency of 980 cm^{-1} . The band peak at 1080 cm^{-1} represents the montmorillonite whereas the band peak at 980 cm^{-1} corresponds to the saponite minerals in OBM waste. The band peaks in the region of $980\text{-}900\text{ cm}^{-1}$ represents the dioctahedral minerals while the band in the region of $700\text{-}600\text{ cm}^{-1}$ range corresponds to the trioctahedral minerals. The band peak at 600 cm^{-1} represents the presence of Mg^3OH . The peak at 916 cm^{-1} reflects the partial substitution of octahedral Al by Mg in montmorillonite. Band spectra profile published in the literature is very helpful to identify different clay minerals present in OBM waste (Madejova, 2003). This clearly exceeds the OSPAR regulation of 1%w/w for drill mud/cuttings (Al-Ansary and Al-Tabbaa 2007).

3.3.3. Mineral composition analysis

Mineralogical analysis for OBM waste showed that it is essentially dominant by muscovite, barite, montmorillonite and quartz. However, a trace amount of kaolinite, meionite, halloysite, aluminium, silicon chlorite and anorthite are also present in OBM waste.



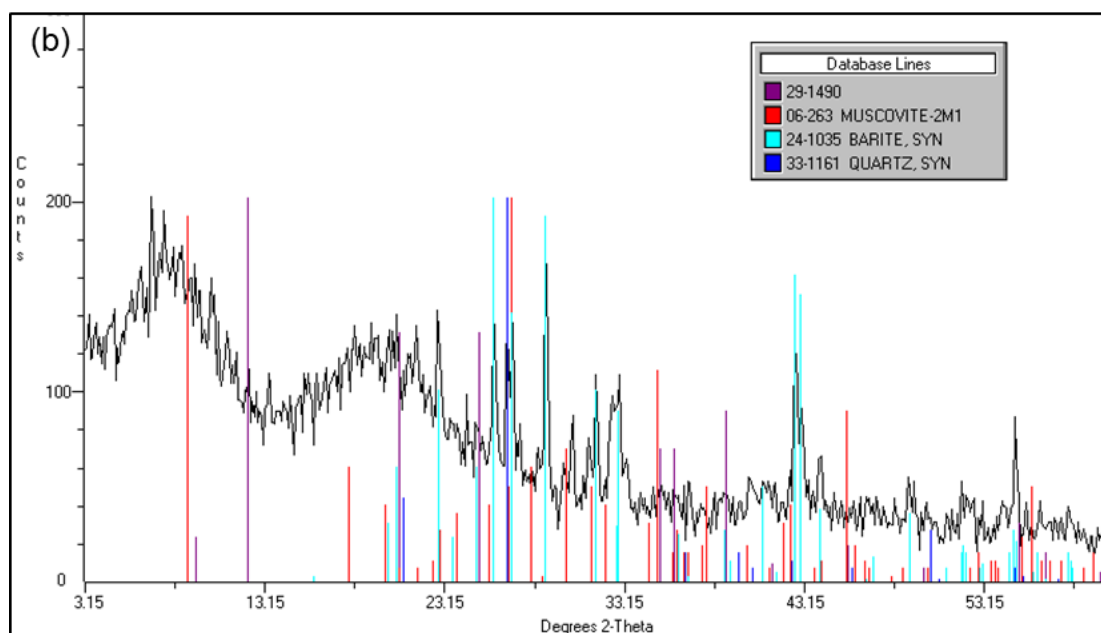


Figure 3.3 WAXD patterns of (a) MMT and (b) OBM waste

XRD patterns of OBM sample in air dried state compared the XRD patterns of Montmorillonite as a reference which indicated the presence of sharp montmorillonite peaks in OBM waste. The diffraction peaks at 29-1490 in Figure 3.3 corresponded to the sets in JCPDS cards and confirmed the presence of montmorillonite by using Rietveld refinement software. The d_{001} spacing was calculated using Bragg's law $n\lambda = 2d \sin\theta$ where λ is the wavelength of X-ray radiation used in the analysis, d corresponds the distance between diffraction lattice planes and θ is the half diffraction angle. For OBM waste a diffraction peak at $2\theta = 6.700^\circ$ was observed which corresponded to a d -spacing of 13.2\AA .

3.3.4. Elemental analysis

Calibration was performed for metal analysis using standard $10,000 \text{ mg L}^{-1}$ solution supplied by Fisher Scientific, UK. Table 3.1 highlighted the recovered elements present in OBM waste. Sample analysis were performed only when the r^2 of the calibration curve was higher than 0.999. The concentrations of alkaline earth metals (Mg, Ca, Ba), alkali metals (Na, K), transition metals (V, Cr, Mn, Fe, Ni, Cu, Zn, Cd), post-transition metals (Al, Pb), metalloids (Si, As), polyatomic non-metals (P, S), and actinide (U) in the extracts were determined by using PerkinElmer Optima 8000 ICP-OES instrument.

Table 3. 1 Elemental analysis of raw OBM waste using ICP-OES

Elements	Concentration ($\mu\text{g/g}$)		Mean	$\pm\text{SD}$
	Sample 1-1	Sample 1-2		
Ba	174	108	141	46
Ca	82241	89799	86020	3779
Na	77	79	78	2
Fe	337	356	346	13
Al	174	177	176	2
Mg	46	48	47	1
K	55	49	52	4
Mn	365	379	372	10
V	26	27	27	0
Ni	19	20	19	1
As	0	0	0	0
Cr	39	44	42	3
Cd	0	0	0	0
Zn	256	278	267	15
Cu	47	46	47	0
Pb	138	146	142	6
Si	51	59	53	4
P	108	114	111	4
S	4694	4931	4813	168
U	199	217	208	12

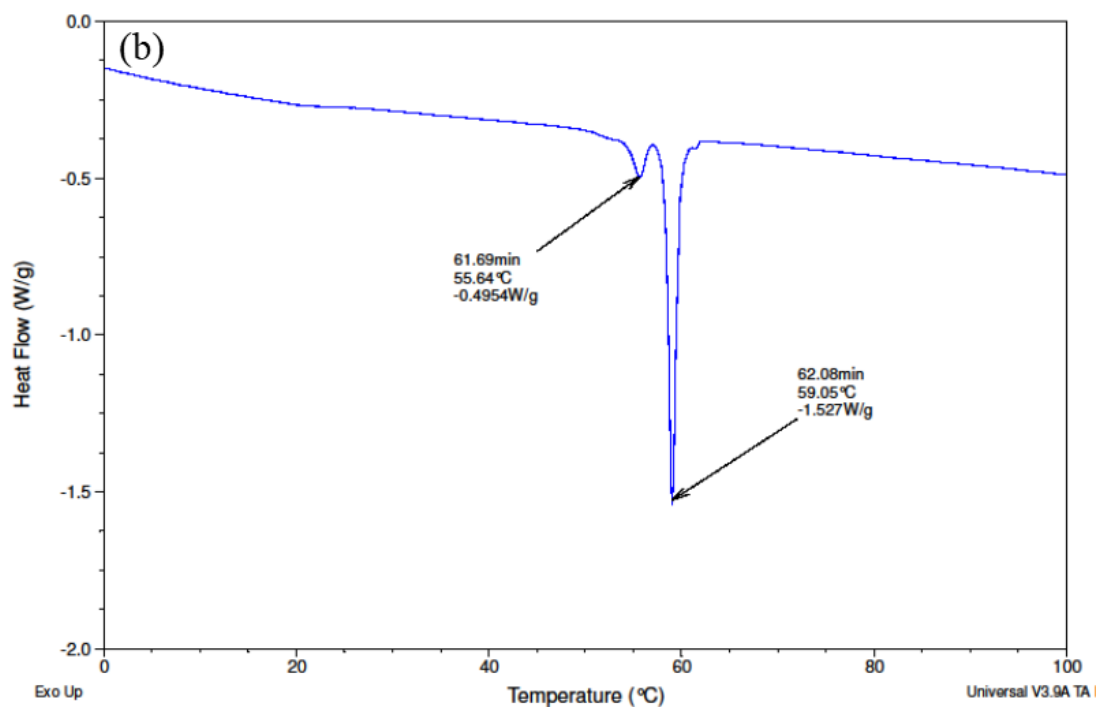
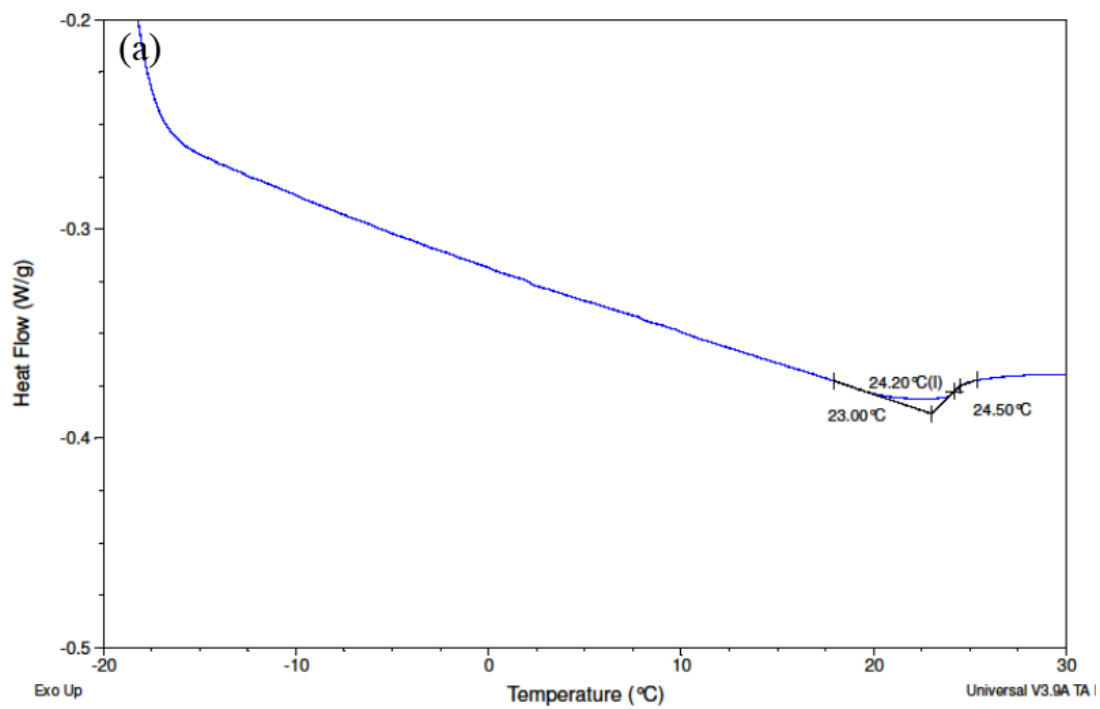
EDXA was carried out to determine the elemental composition of dry OBM waste which is presented below.

Table 3. 2 EDXA of OBM waste powder

Element	Weight%
O	29.12
Na	0.59
Al	1.4
Si	4.49
S	9.95
Cl	2.49
K	0.31
Ca	6.32
Fe	0.86
Ba	44.47
Totals	100

3.3.5. Thermal properties

In order to investigate the thermal degradation behaviour of OBM waste, non-isothermal measurements were taken by using DSC instrument and the results are shown in Figure 3.4.



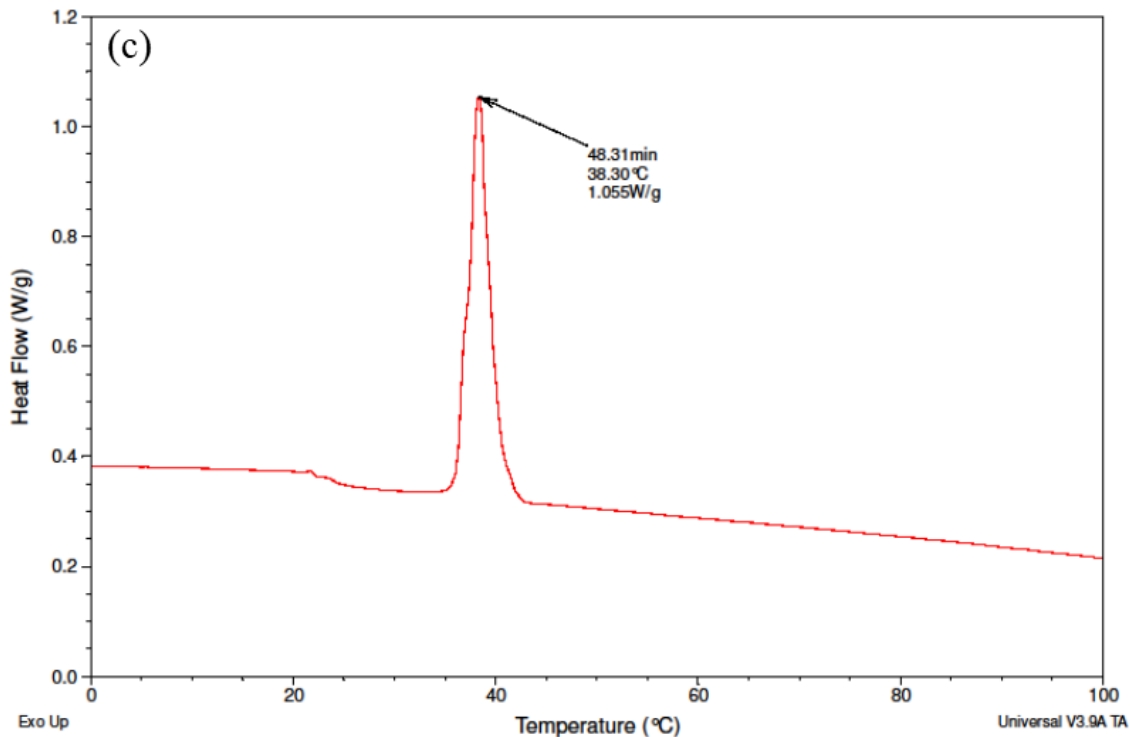
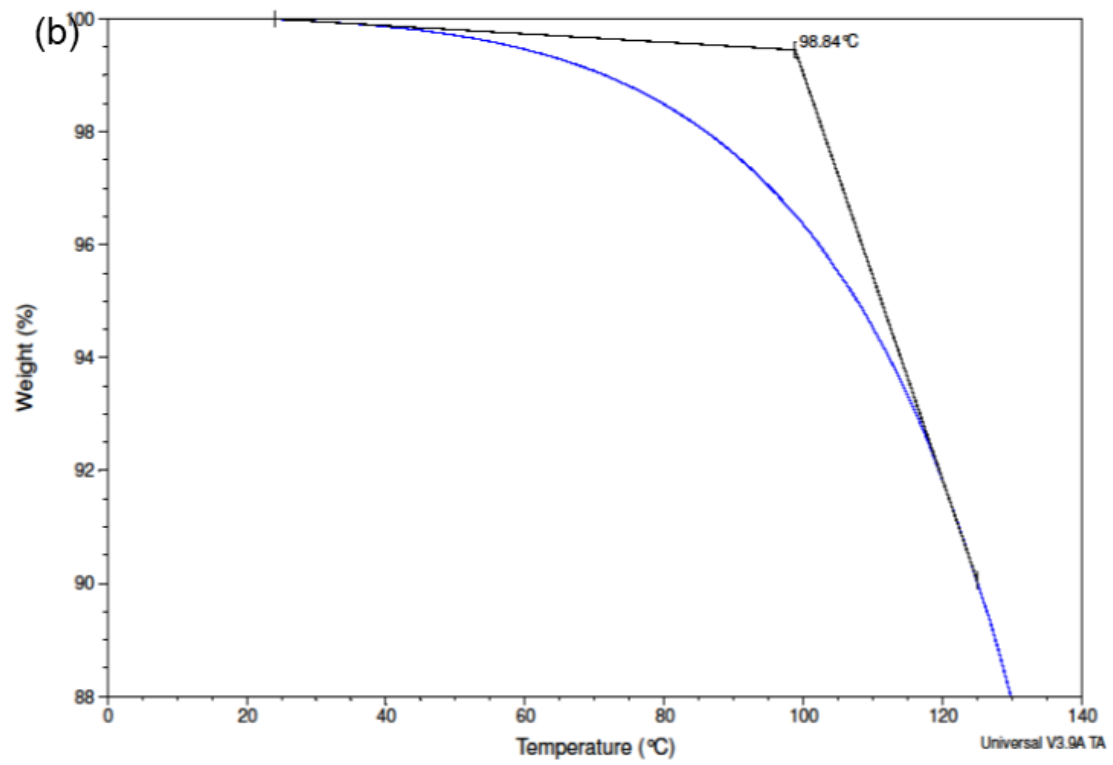
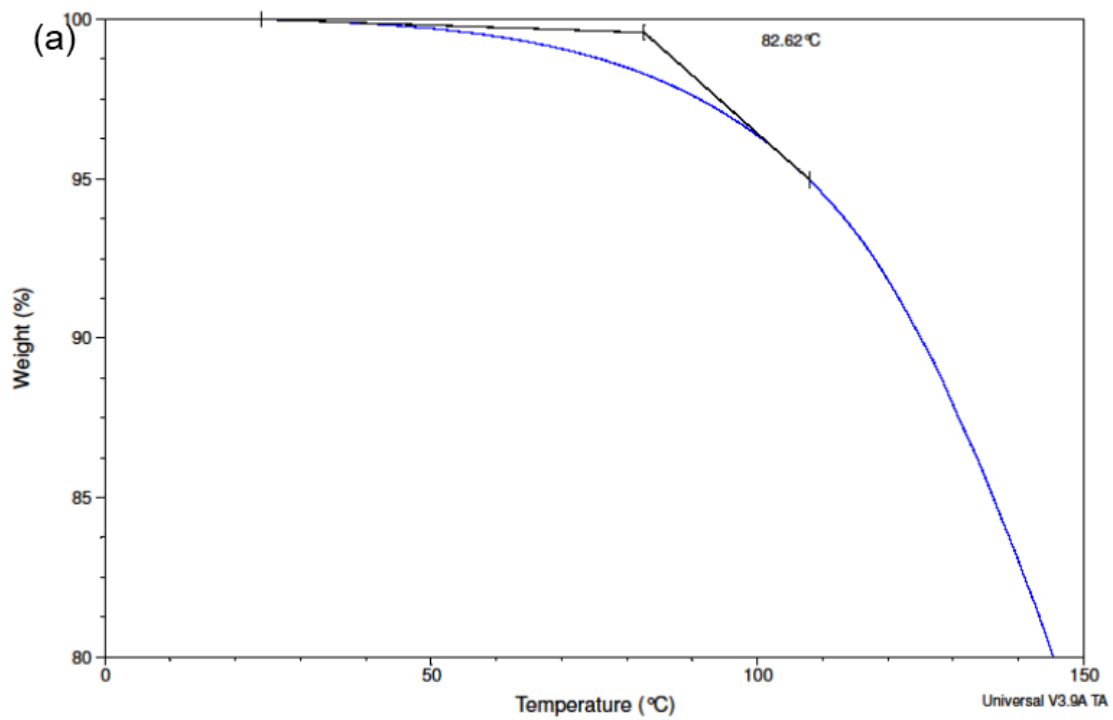


Figure 3.4 DSC thermograms of OBM waste at (a) glass transition temperature (T_g); (b) melting temperature (T_m) and (c) crystallisation temperature (T_c)

Comparing different thermograms in Figure 3.4 (b) there are two peaks present in melting temperature at 56.64°C and 59.05°C . It can be attributed here that the first peak at 56.64°C corresponds to the γ crystal phase whereas the peak at 59.05°C is the representative of α phase crystals. It is important to notice here that the crystal phase is dominant in this OBM waste which is thermodynamically stronger than γ phase crystals. This observation is also established by the amount of residue recovered after TGA study. Figure 3.4 (a) and Figure 3.4 (c) shows the glass transition temperature (T_g) and crystallisation temperature (T_c) of OBM waste respectively.

The thermal degradation of OBM waste has been analysed in N_2 environment using TA instrument TGA Q500. Onset degradation of the sample in different stages are presented in Figure 3. 5.



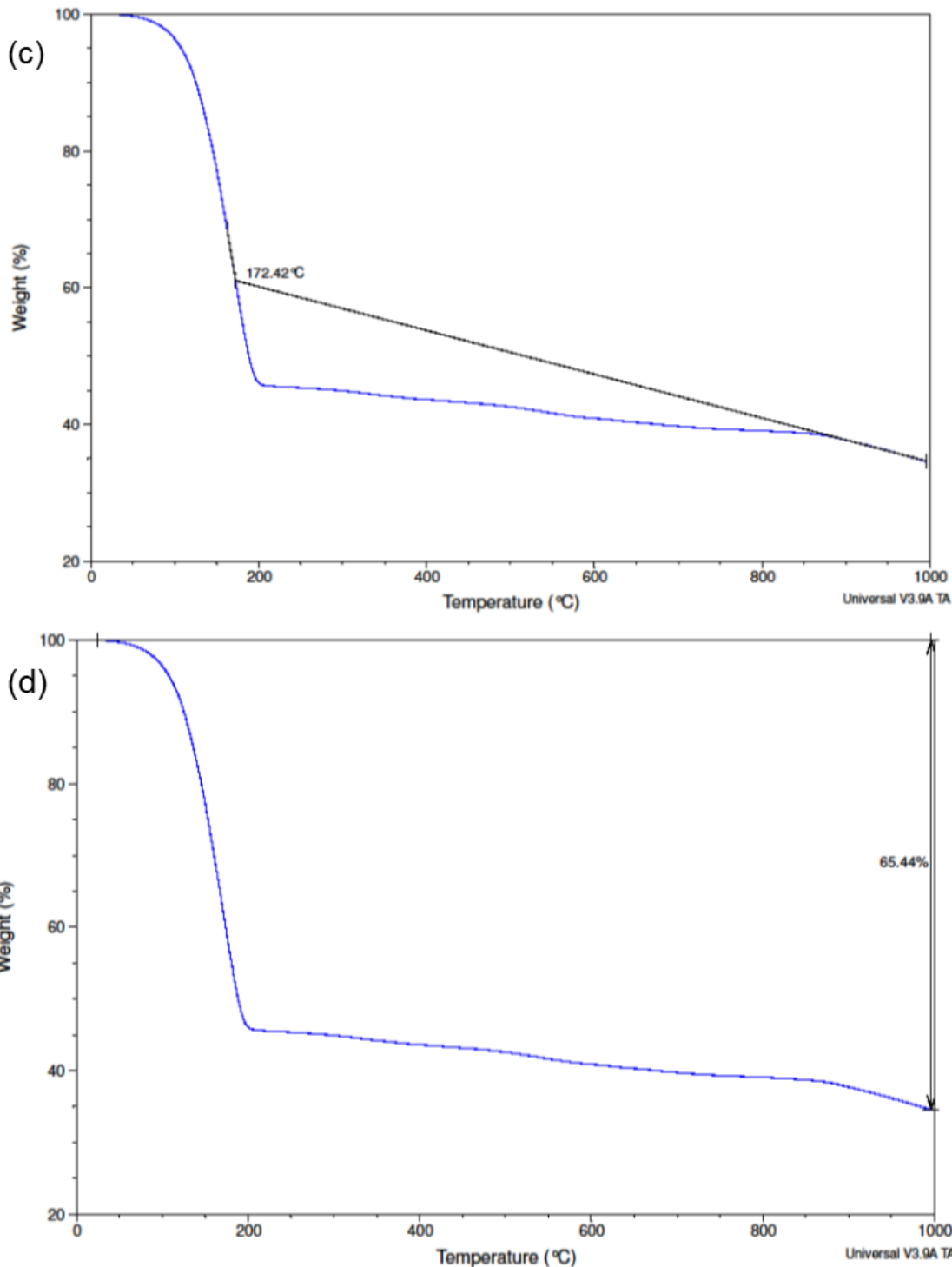


Figure 3.5 TGA thermograms of OBM waste at (a) onset degradation at 5% weight loss; (b) onset degradation at 10% weight loss; (c) onset degradation at 65% weight loss and (d) residue at 1000°C

Figure 3.5 (a), (b) and (c) shows the onset degradation of OBM waste at different stages such as 5%, 10% and 65% weight loss respectively. Figure 3.5 (d) shows the weight % of residue left after 1000°C. Since this OBM waste is a complex mix of organic and inorganic

substances, the thermograms associated with the endothermic reaction of any specific materials/minerals is very difficult to establish. However, Table 4 shows the potential thermograms peaks associated with different clay minerals.

Table 3.3 Endothermic reactions of different clay minerals at different temperature stages at TGA (Grim and Rowland, 1942)

Clay minerals	Reaction temperature profile
Quartz	endothermic reaction at 565°C, 870°C
Goethite	endothermic reaction at 450°C
Limonite	endothermic reaction at 350°C
Gibbsite	endothermic reaction at 350°C
Diaspore	endothermic reaction at 550°-570°C
Kaolinite	endothermic reaction at 550-600°C
Halloysite, Kaolinite and Illite	endothermic reaction at 500-650°C
Illites	endothermic reaction at 100-200°C, 500-650°C and about 900°C
Montmorillonite	endothermic reaction at 100-250°C, 600-700°C and about 900°C
Brucite	endothermic reaction at 425-475°C
Hydrated halloysite	endothermic reaction same as kaolinite with an additional reaction at 100-125°C

3.5. Conclusions

This study, however, on characterisation of the OBM waste is limited to certain wells in North Sea region compare to the waste generated millions of tonnes every year worldwide. Findings from different characterisation including morphology study, chemical and mineralogical study and thermal study it can be concluded that this waste is associated with critical raw materials for different industrial applications, environmentally significant materials including heavy metals and potentially nanoclay as a green filler in nanocomposite manufacturing to improve mechanical, thermal, gas barrier and flame-retardant properties.

Chapter 4: The Crystallinity and Thermal Degradation Behaviour of LDPE/Oil Based Mud Waste Slurry Nanocomposites

4.1. Introduction

Sustainable waste management in oil and gas industries represents the rational recovery or uses of resources, ensure health and safety and thus improvement of life quality, protection of eco-systems and to convert waste into valuable products (Elektorowicz and Habibi, 2005; Maloney and Yoxtheimer, 2012; Smith et al., 2003; LaGrega et al., 2010; Knight et al., 1999; Colborn et al., 2011; Binnemans et al., 2015). Spent drilling fluids, also known as mud predominantly OBM is one of the main sources of waste stream in oil and gas industry (Onwukwe and Nwakaudu, 2012; Hickenbottom et al., 2013; Rightmire, 1984; Susich and Schwenne, 2004 and Ismail et al., 2017).

The OBM waste slurry is generally composed of clay minerals including metals in a strong suspended solid phase condition. This suspended clay slurry has been selected in this study as reinforcement in LDPE matrix not only because it improves the thermal stability, but in an aspect of valorising an unwanted and unexploited waste discarded at landfill site as an existing practice in oil and gas industry. This article highlights other properties of OBM waste and delivers the potential opportunity of utilising this OBM waste as nanofiller in developing and manufacturing novel nanocomposite materials.

4.2. Materials and experimental details

4.2.1. Materials and samples preparation

The OBM waste slurry was donated by a local oil and gas service company in Aberdeen, UK. To characterise the solid content in this OBM slurry and to use this OBM powder as filler in nanocomposite, the thermal treatment was performed as mentioned in section 3.2.1.

Lupolen 1800S (trade name of LDPE, manufactured by Lyondellbasell industries Ltd) was supplied by Northern Polymers and Plastics Ltd, UK. It has a melting point of 106°C and a V-2 rating in accordance to UL 94 (vertical burning test) at 1.6 mm thickness. The montmorillonite (MMT), K10 was supplied by Sigma-Aldrich, UK which used as a reference material to evaluate characteristics between MMT and OBM nanofiller.

4.2.2. LDPE/OBM slurry and LDPE/MMT nanocomposite manufacturing process

LDPE pellets and MMT were dried at 90°C overnight prior to melt compounding. Moisture free LDPE (oven dried at 90°C for 12 hours) mixed with slurry prior to melt compounding. The weighed OBM slurry was mixed with LDPE pellets with glass stirrer in beakers under the fumehood and left there for 30 mins to facilitate mixing OBM slurry with pellets and to evaporate the low volatile chemical contents in OBM slurry.

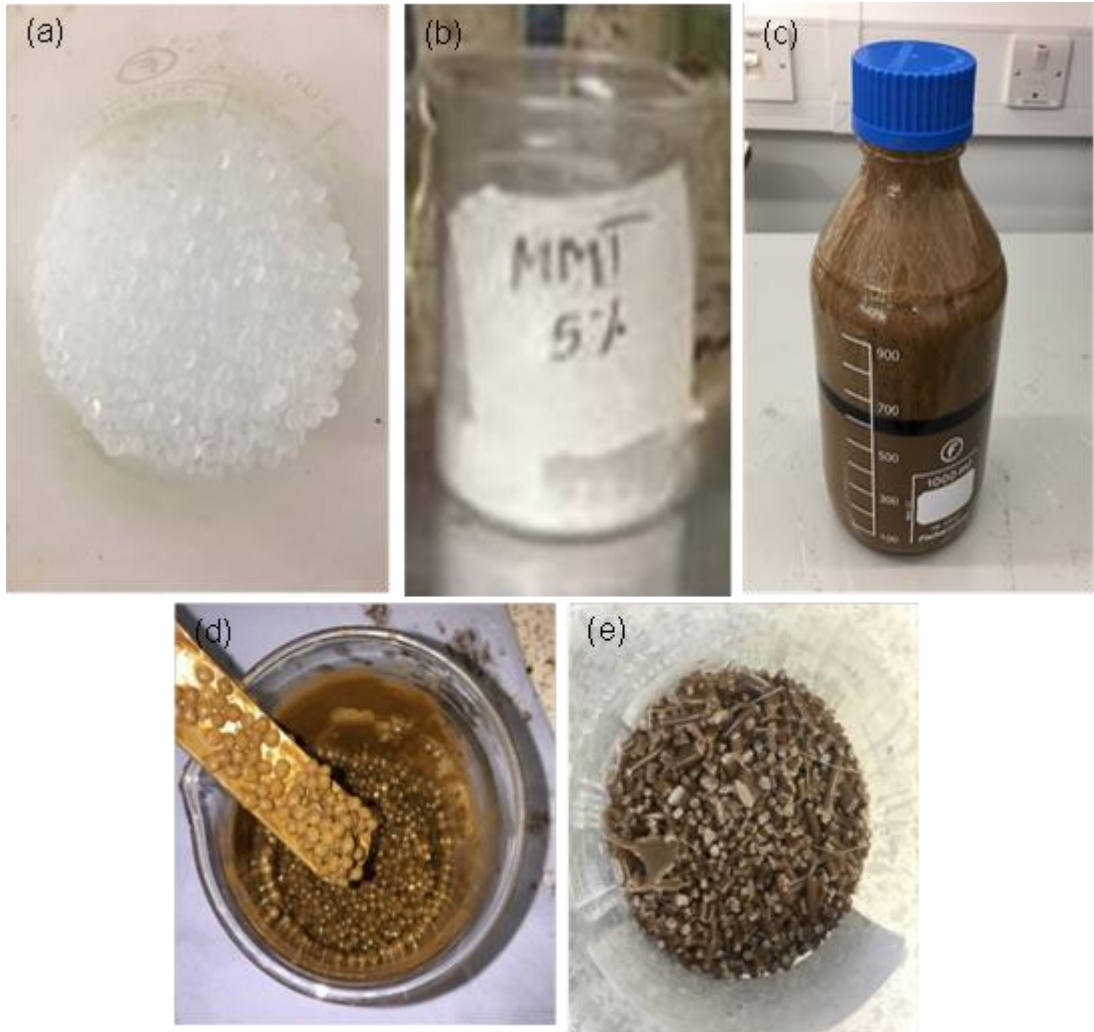


Figure 4.1 Manufacturing of LDPE/MMT and LDPE/OBM slurry nanocomposites using (a) LDPE pellets; (b) MMT filler; (c) OBM slurry; (d) uniform mixing of LDPE and OBM slurry; and (e) LDPE/OBM slurry compounds in pellet forms after extrusion

LDPE pellets mixed with MMT clay in a tumbler mixer before manufacturing the compounds. OBM slurry and MMT direct mixed with LDPE in a different weight percentage as shown in Figure 4.1 different compounds were prepared such as 0, 2.5, 5, 7.5 and 10 wt% of filler in a respective wt% of LDPE pellets to make 100 wt% raw compounds of LDPE/MMT and

LDPE/OBM slurry nanocomposites as required. Since the clay minerals including other chemical substances remain in suspended condition, the % of filler loading is considered as the weight of slurry which is mixed of solid and liquid phases. The raw mixture of LDPE/MMT and LDPE/OBM slurry were compounded using a twin-screw extruder (TwinTech extrusion Ltd.) at 60 RPM over five different heating zones: 1st zone (120°C), 2nd zone (200°C), 3rd zone (210°C), 4th zone (200°C) and die/5th zone (200°C). The compounded strands were sized into pellet form by using a pelletiser which were then injection moulded into a dog-bone and bar mould (dual cavity) using the barrel temperature at 230°C with a moulding pressure of 10 bar to manufacture nanocomposite materials for different tests and analysis.

4.2.3. Structural and morphology analysis

Scanning electron microscope (SEM) was performed using a JEOL JSM-7400F instrument with a magnification of 25000X, 8.0 mm working distance (WD) and accelerating potential of 5.0 kV. The samples were coated with gold and palladium using sputter deposition for 2 minutes prior to the analysis.

The ATR-FTIR characterisation method used in this chapter is described in chapter 3.2.2. Mineralogical composition for OBM powder, MMT and LDPE/OBMFs nanocomposites was determined by following the same method described in chapter 3.2.2.

4.2.4. Element analysis

To determine the elemental composition of dry OBM waste, LDPE/OBM slurry nanocomposites and LDPE/MMT nanocomposites, energy dispersive x-ray analysis (EDXA) (Oxford Instruments INCA Energy) was carried out. To determine the inorganic elements including heavy metals exist in dry OBM slurry powder, LDPE/MMT and LDPE/OBM slurry nanocomposites, an investigation carried out using Malvern Panalytical XRF spectrometers.

4.2.5. Thermal analysis

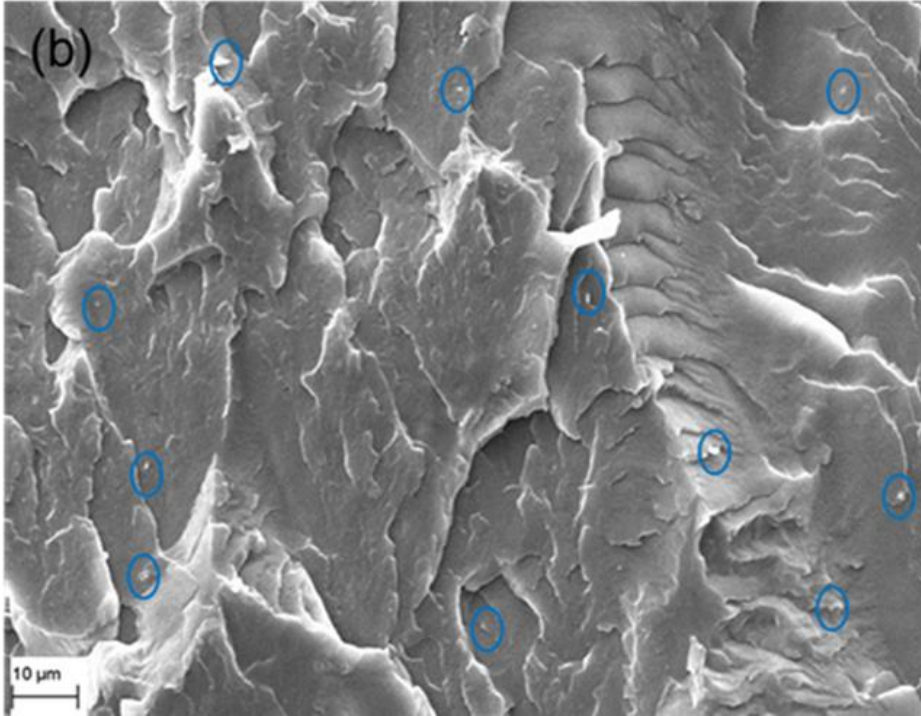
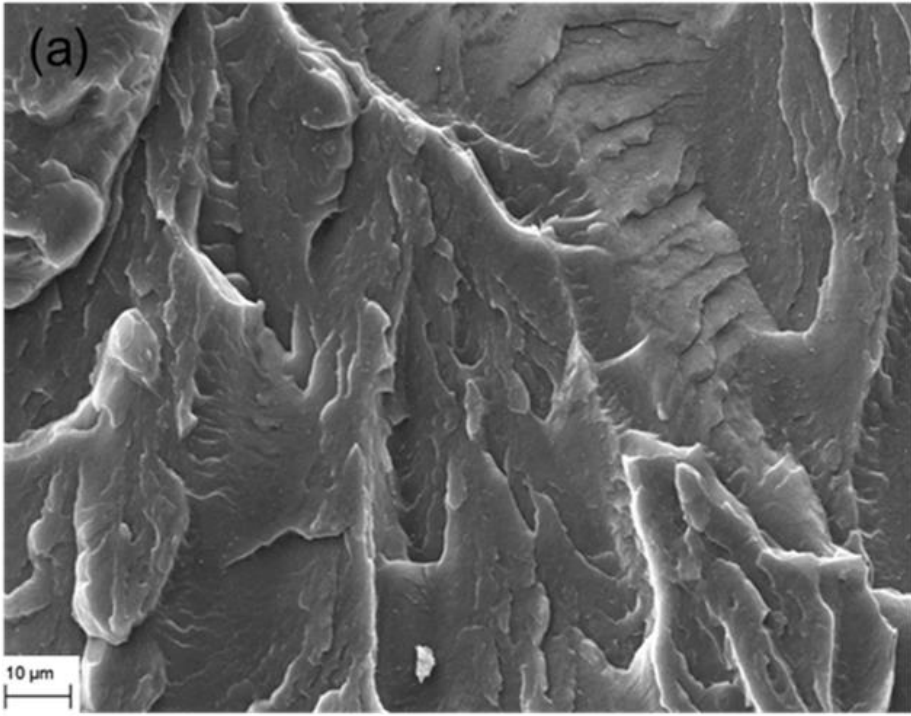
The thermal analysis including DSC and TGA method used in this chapter is described in chapter 3.2.4.

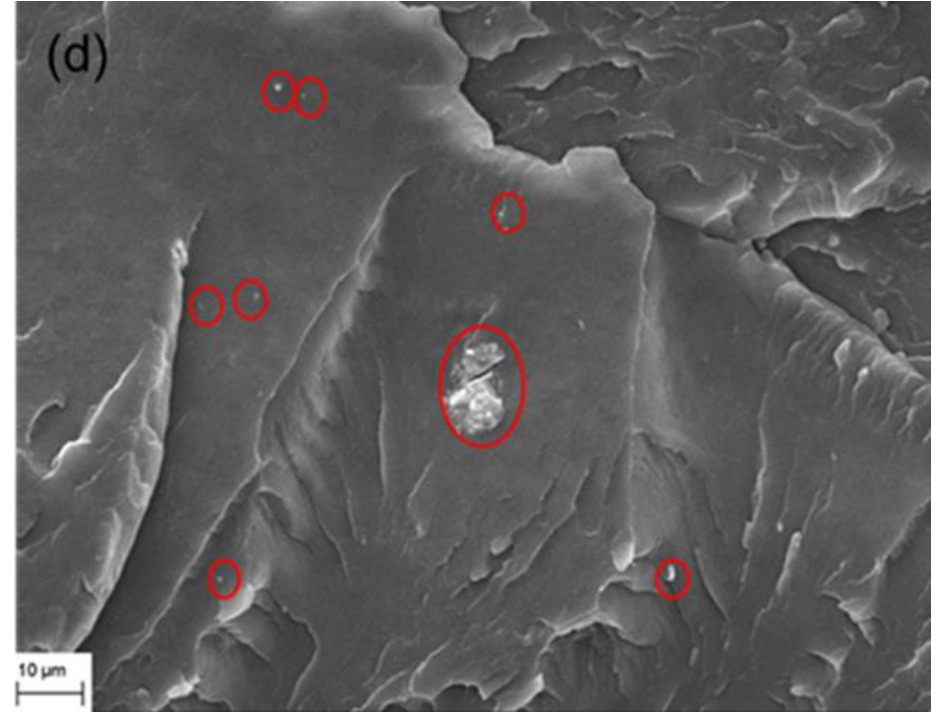
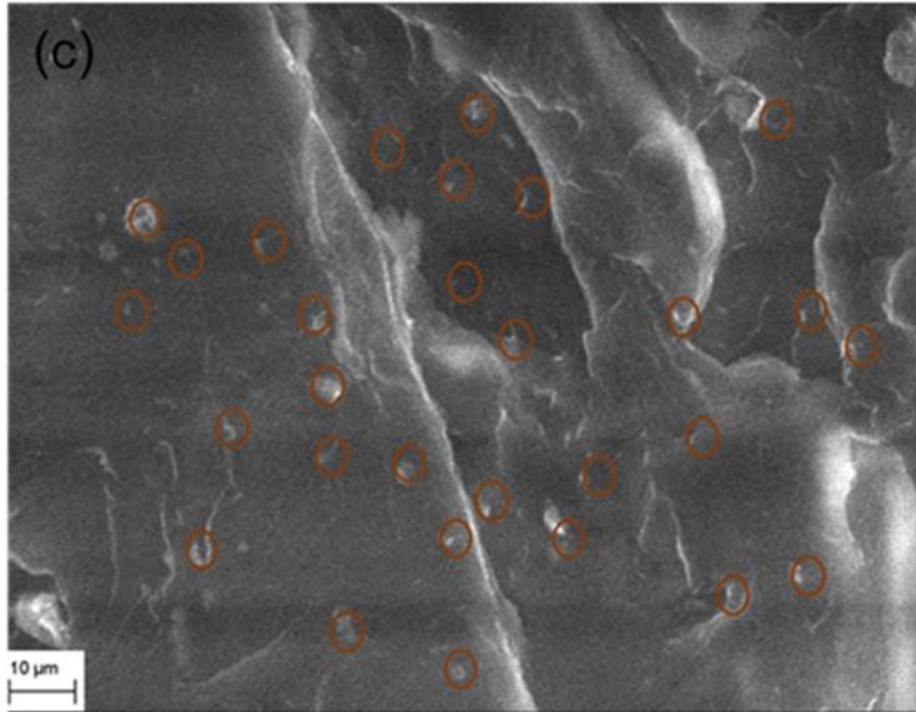
4.3. Result and discussion

4.3.1. Morphology study

In Figure 3.1 in previous chapter shows the tightly stacked micrographs of clay platelets of montmorillonite and OBM waste powder with size ranges up to 1000nm.

The SEM micrographs were used to investigate the morphological representation of different clay minerals present in OBM waste which is compared with that of standard montmorillonite sample supplied by Sigma-Aldrich. Both micrographs represent the platelet structure. However, OBM shows tightly stacked the platelets with variant sizes of platelets with different shapes whereas montmorillonite shows regular platelet shapes with uniform structure. It can articulate here that different clay minerals may influence the structure and shape of the platelets present in OBM waste.





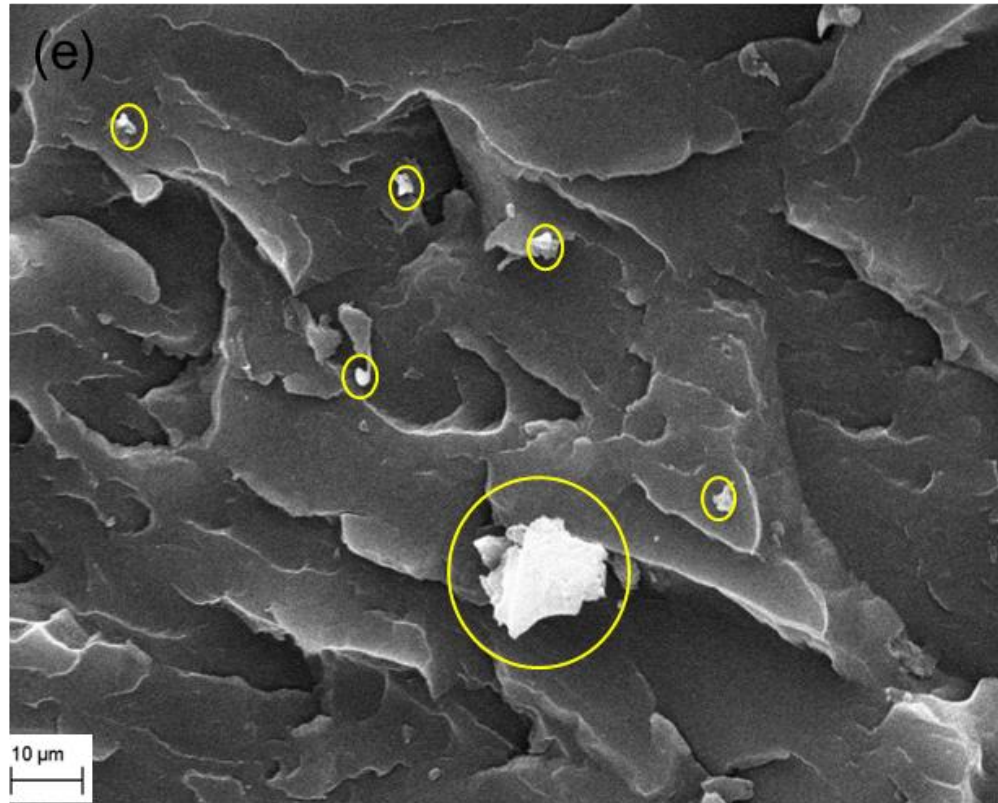
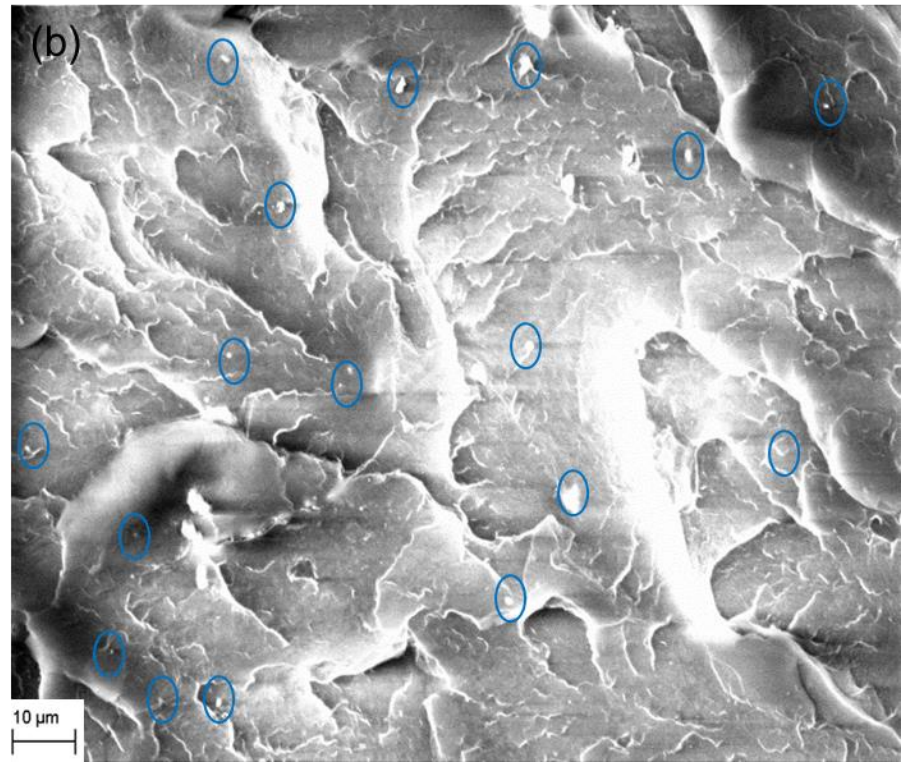
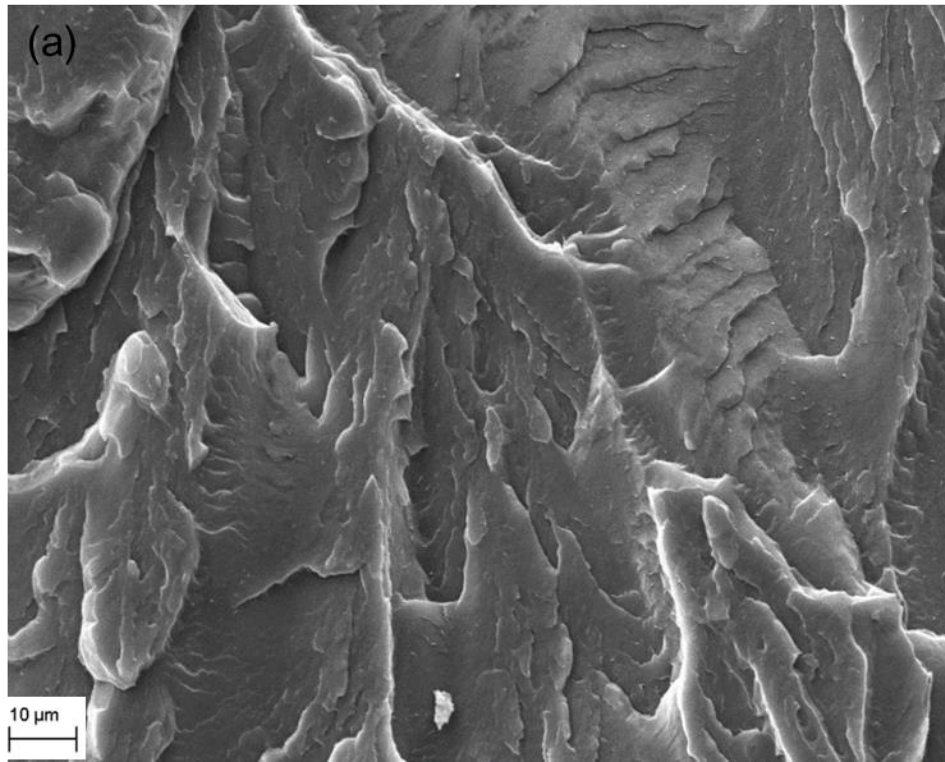
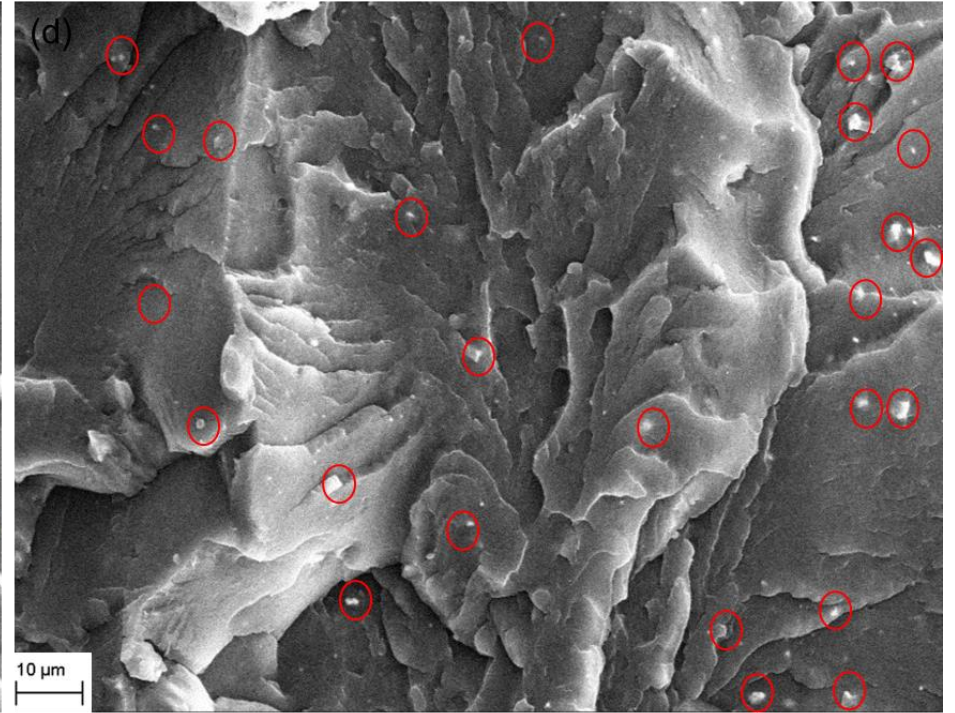
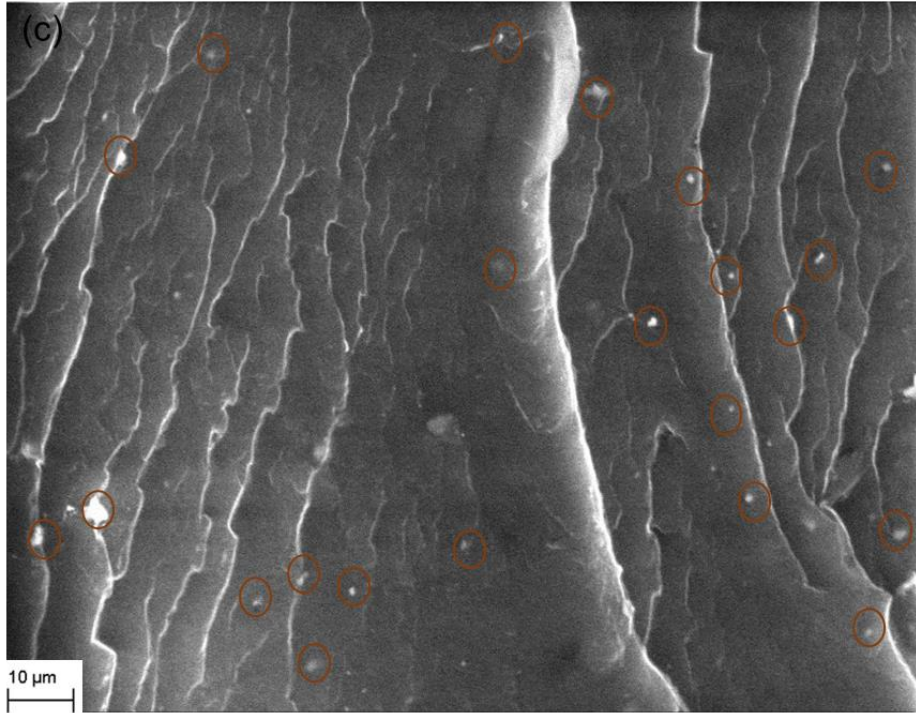


Figure 4.2 SEM images of (a) neat LDPE; (b) LDPE with 2.5 wt% MMT; (c) LDPE with 5.0 wt% MMT; (d) LDPE with 7.5 wt% MMT and (e) LDPE with 10.0 wt% MMT





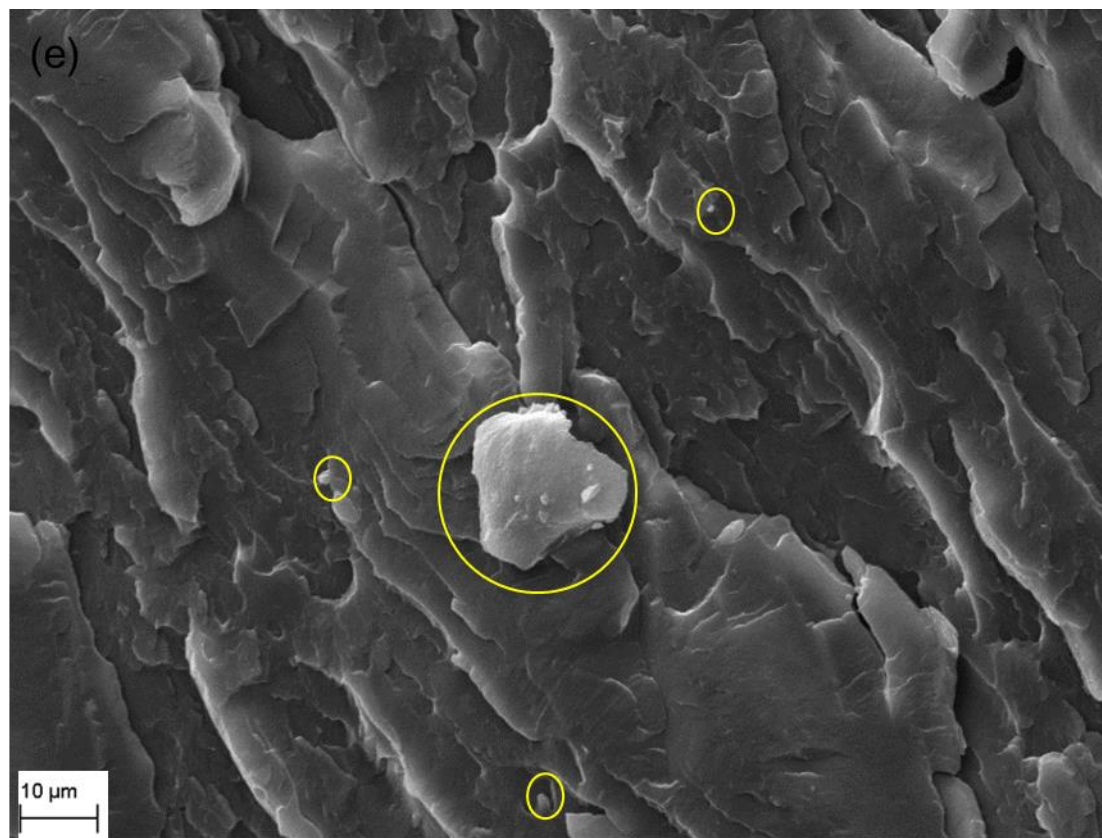


Figure 4.3 SEM images of (a) neat LDPE; (b) LDPE with 2.5 wt% OBM slurry; (c) LDPE with 5.0 wt% OBM slurry; (d) LDPE with 7.5 wt% OBM slurry and (e) LDPE with 10.0 wt% OBM slurry

To identify the surface topography of reclaimed clay from oil-based mud waste reinforced LDPE nanocomposites, montmorillonite reinforced LDPE nanocomposites are considered as a standard benchmark sample. It is noticeable in Figure 4.3 that the OBM clay platelets are better distributed in polymer matrix compare to MMT clay platelets are distributed in LDPE matrix in Figure 4.2. The interfacial adhesion between clay platelets and polymer matrix is stronger in LDPE/OBM slurry nanocomposites compare to the adhesion between montmorillonite and LDPE matrix. This is predominantly noticeable in samples with higher filler content such as LDPE with 7.5 and 10 wt% filler nanocomposites show strong physical contact between filler and polymer matrix. From the morphological observation it can be concluded here that OBM slurry is distributed evenly throughout the polymer matrix and following the regular gap between platelets in LDPE with 2.5, 5 and 7.5 wt% OBM slurry nanocomposites. It can be highlighted here that the interfacial gap between platelets and LDPE matrix is lesser in LDPE/OBM slurry nanocomposites compare to that in LDPE/MMT nanocomposites. This observation leads to articulate the superior interfacial adhesion mechanism between OBM slurry and LDPE matrix compare to the adhesion mechanism in LDPE/MMT nanocomposites.

4.3.2. Chemical structure analysis

The ATR-FTIR spectrum analysis of neat LDPE, LDPE/MMT nanocomposites and LDPE/OBM slurry nanocomposites have been carried out and the resulting spectra are overlayed and presented in Figure 4.4 and Figure 4.5. The spectra of neat LDPE, LDPE/MMT nanocomposites and LDPE/OBM slurry nanocomposites are stacked and presented in **Figure B1** and **B2** at Appendix B.

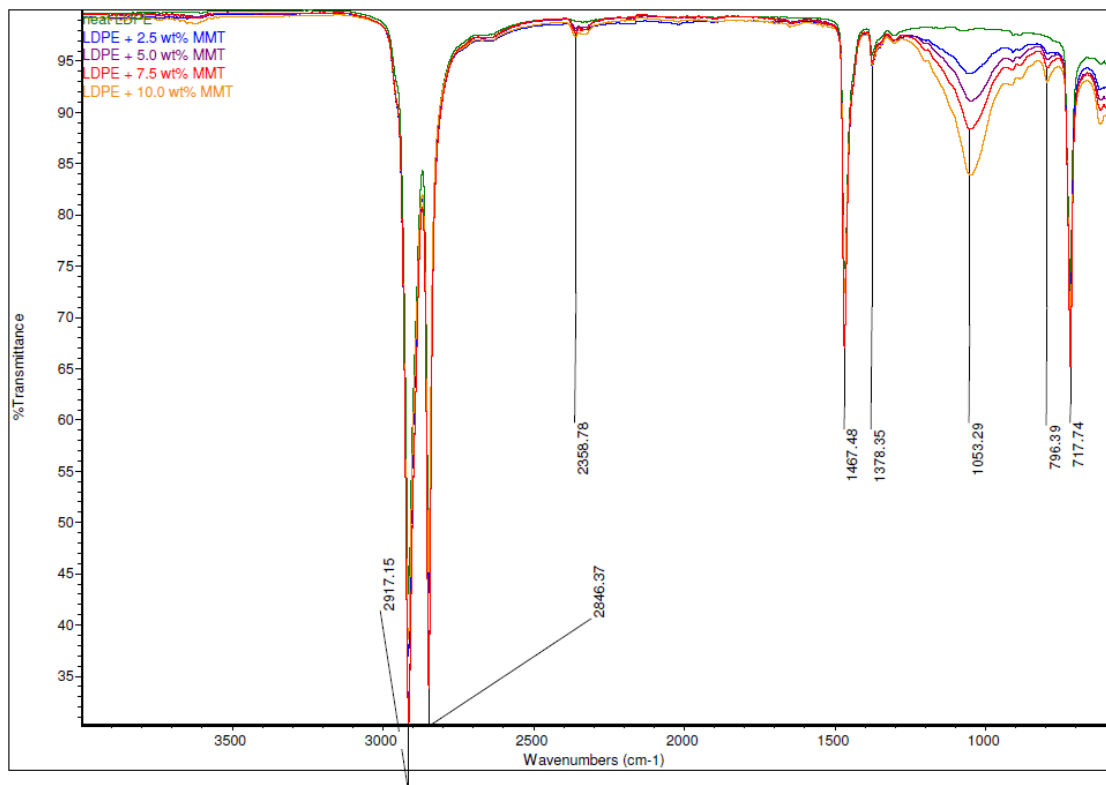


Figure 4.4 Comparison of ATR-FTIR common scale spectra of LDPE and LDPE/MMT nanocomposites

The absorption bands due to structural OH and Si-O groups play an important role to identify different clay minerals present in LDPE/OBM slurry and LDPE/MMT nanocomposites. The chemical structure of LDPE and LDPE/MMT nanocomposites were identified by using ATR-FTIR which represents the IR transmittance peaks at 1053.29 cm^{-1} corresponding to montmorillonite in Figure 4.4 (Madejova, 2003), (Nayak and Singh, 2007).

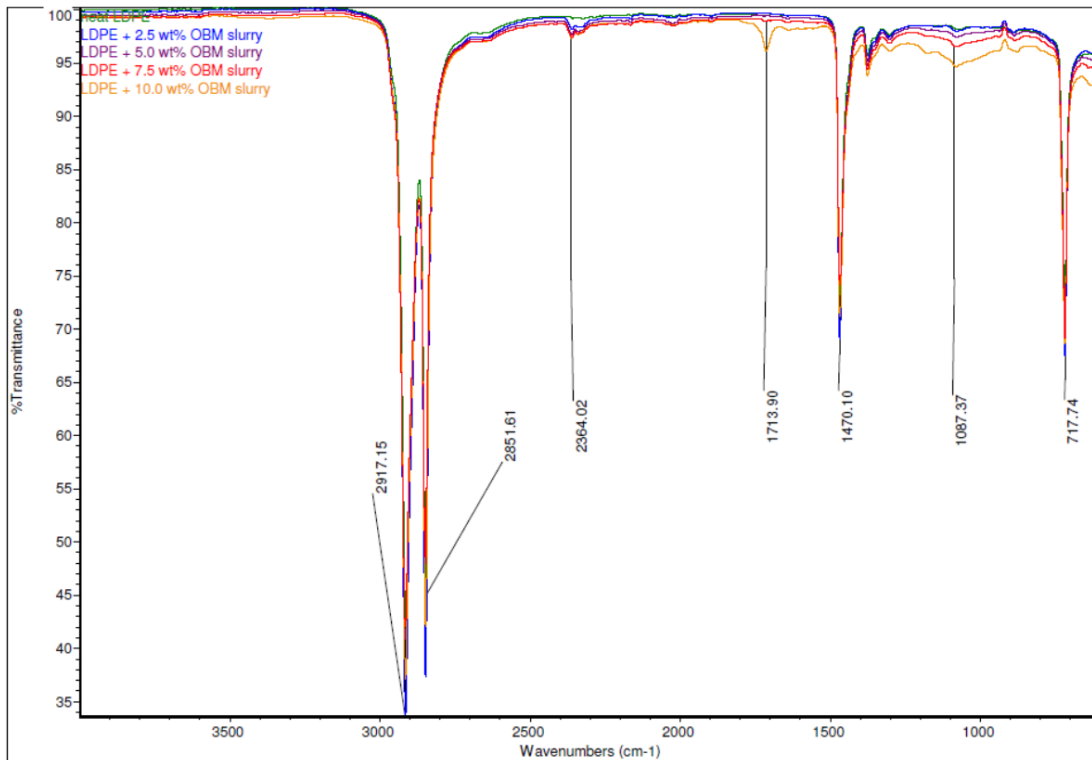


Figure 4.5 Comparison of ATR-FTIR common scale spectra of LDPE and LDPE/OBM slurry nanocomposites

In Figure 4.5, there are three peaks at 2364.02 cm^{-1} , 1713.90 cm^{-1} and 1087.37 cm^{-1} are clearly noticeable. The presence of band at 2364.02 cm^{-1} indicates the possibility of the presence of illite (Nayak and Singh, 2007). The peak at 1087.37 cm^{-1} represents the stretching of Si-O which indicates the presence of Kaolinite (Siddique et al., 2019b) (Nayak and Singh, 2007). The infrared absorption band at 1713.90 cm^{-1} corresponds to silica-aluminium and aluminosilicates present in the nanocomposites (Djomgoue and Njopwouo, 2013).

4.3.3. Mineral composition analysis

Mineralogical analysis for OBM waste showed that it is essentially dominant by muscovite, barite, montmorillonite and quartz. However, a trace amount of kaolinite, meionite, halloysite, aluminium, silicon chlorite and anorthite are also present in OBM waste which is shown in Figure 4.6 (a) (b).

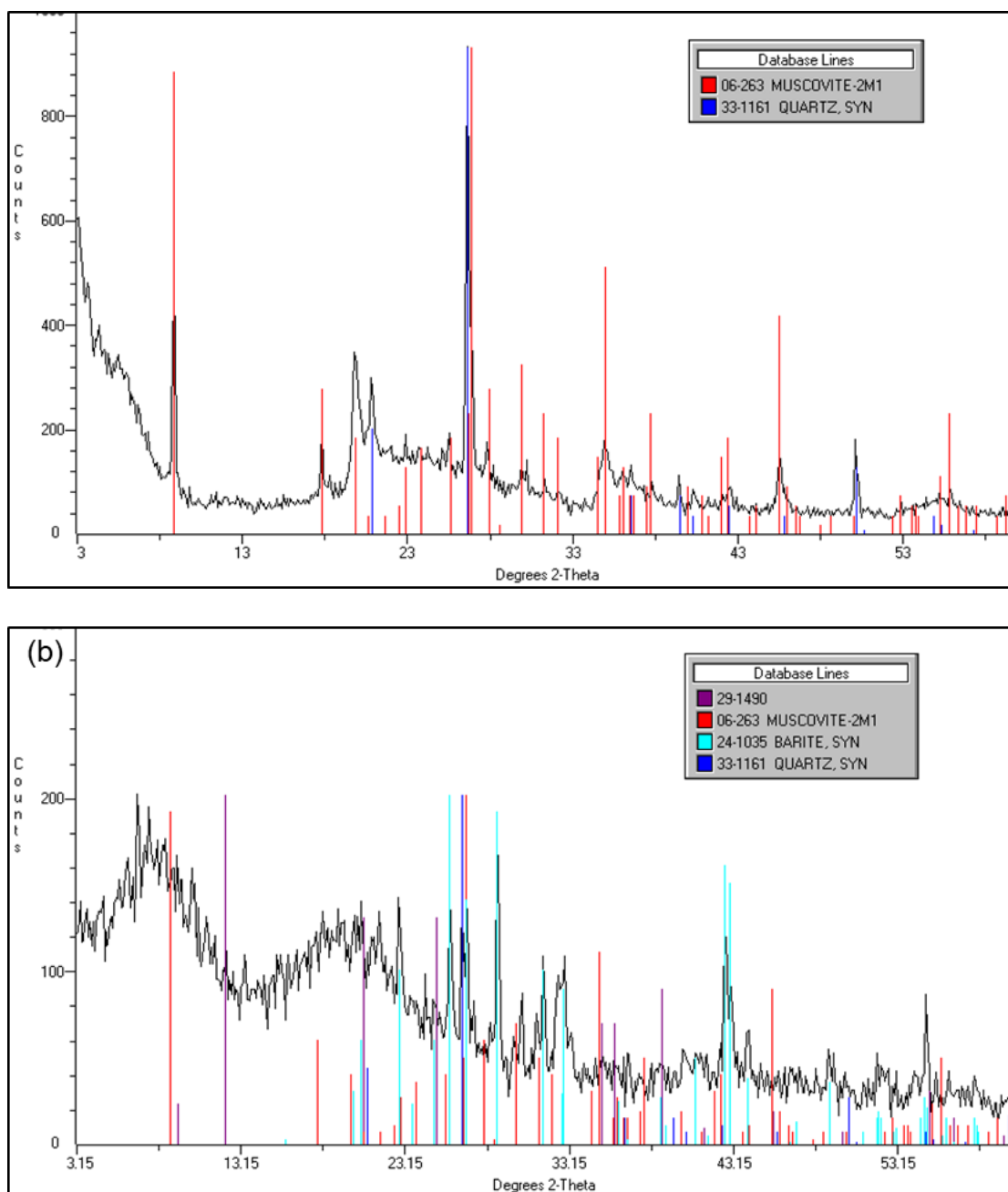


Figure 4.6 WAXD patterns of (a) MMT and (b) OBM waste

XRD patterns of OBM sample in air dried state compared the XRD patterns of Montmorillonite as a reference which indicated the presence of sharp montmorillonite peaks in OBM waste. The diffraction peaks at 29-1490 in Figure 4.6 (a) (b) corresponded to the sets in JCPDS cards and confirmed the presence of montmorillonite by using Rietveld refinement software.

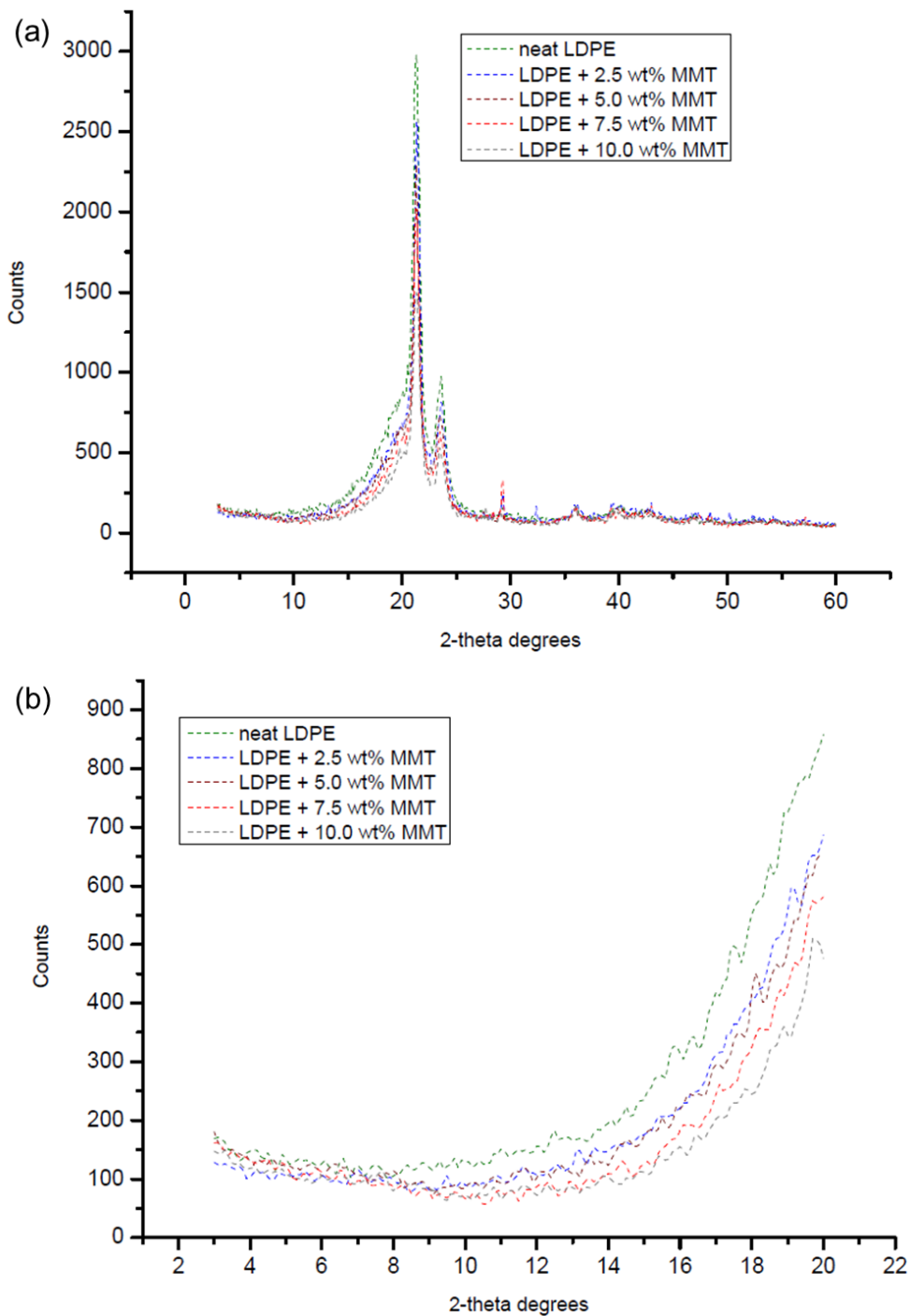
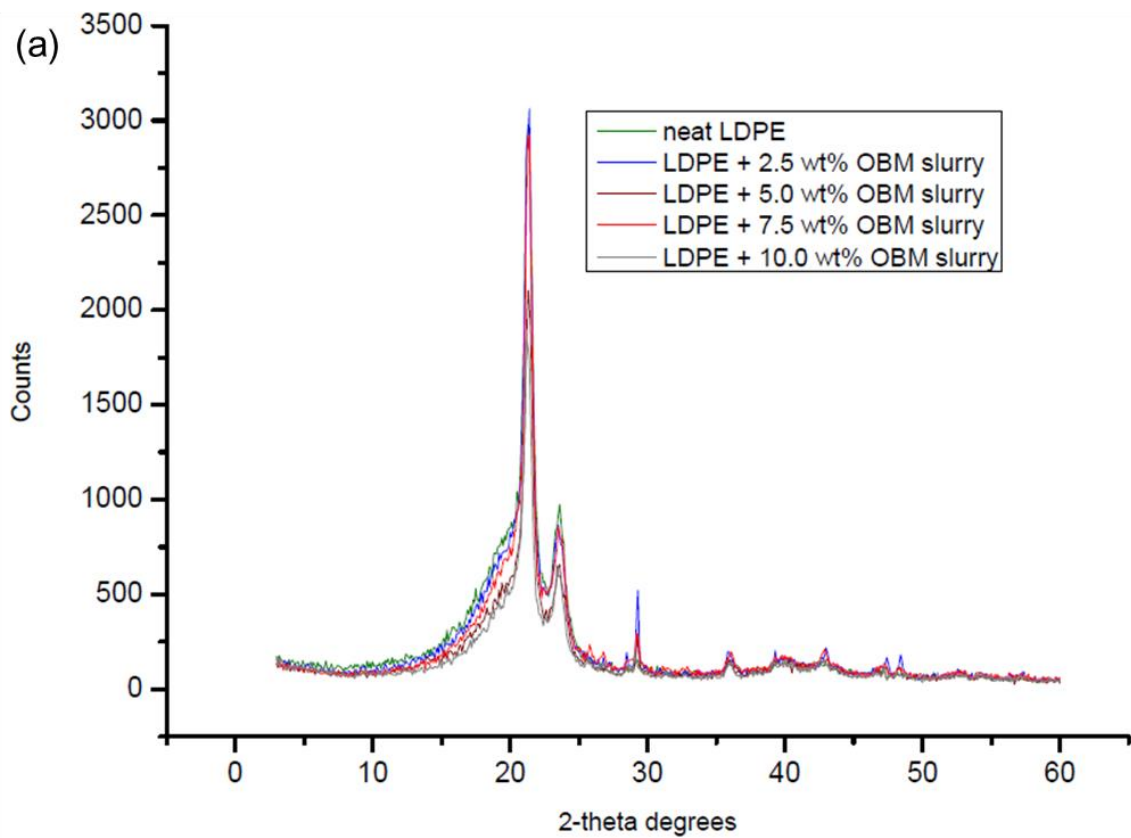


Figure 4.7 Different XRD patterns of LDPE and LDPE/MMT nanocomposites at (a) WAXD; (b) SAXD

The d_{001} spacing was calculated using Bragg's law $n\lambda = 2d \sin\theta$, where λ is the wavelength of X-ray radiation used in the analysis, d corresponds the distance between diffraction lattice planes and θ is the half diffraction angle. For MMT and OBM slurry waste, a diffraction peak at $2\theta = 6.700^\circ$ was observed which corresponded to a d -spacing of 12.62 Å and 13.2Å respectively.

The XRD analyses are illustrated in Figure 4.7 (a) (b) and Figure 4.8 (a) (b) addressing the diffractograms at (a) wide angle X-ray diffraction (WAXD); and (b) small angle X-ray diffraction of LDPE/MMT and LDPE/OBM slurry nanocomposites respectively. In Figure 4.7, XRD patterns of LDPE and LDPE/MMT nanocomposites are presented. A clear shift of the diffraction peaks of the planes (001) of MMT towards lower angles for the LDPE/MMT nanocomposites is noted. The basal spacing of MMT increases with different nanocomposites in different ratios. Using Bragg's law $n\lambda = 2d\sin\theta$, where λ is the wavelength of the X-ray radiation applied in the experiment, d corresponds to the distance between diffraction lattice plane and θ is the half of the diffraction angle.



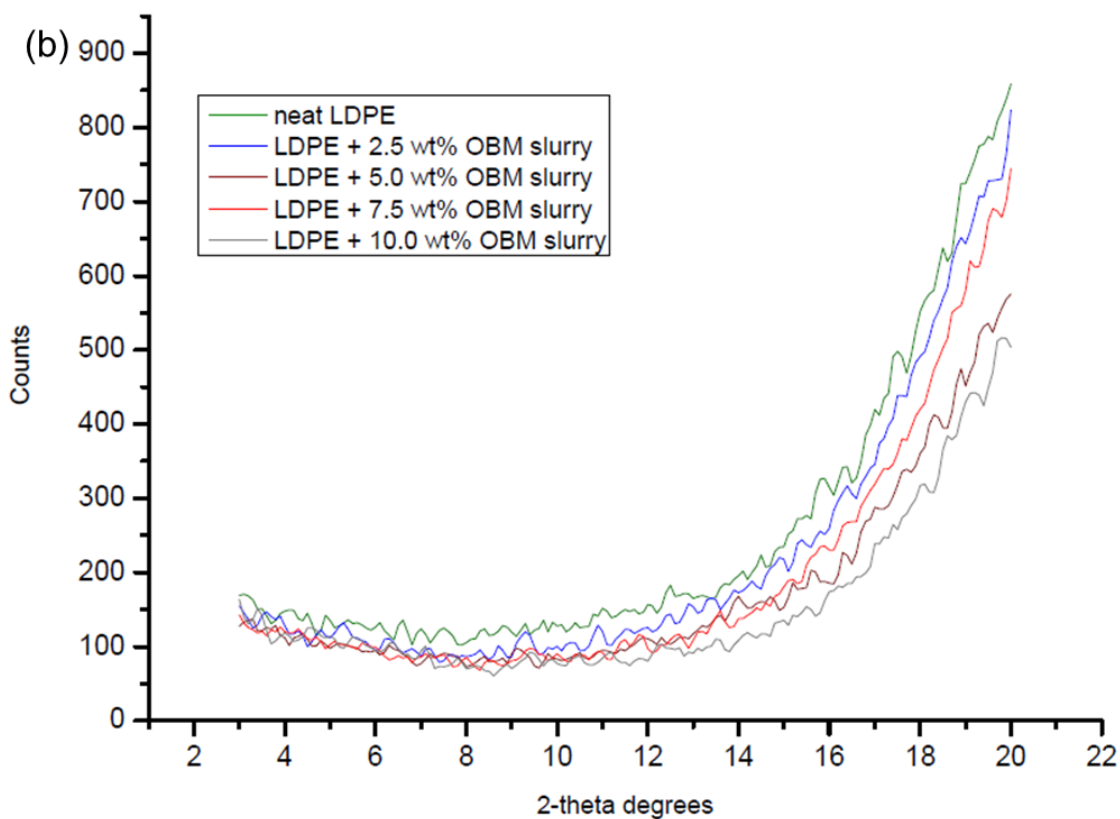


Figure 4.8 Different XRD patterns of LDPE and LDPE/OBM slurry nanocomposites at (a) WAXD; (b) SAXD

The diffraction peak of MMT was observed at $2\theta = 11.40^\circ$ which corresponds to a d -spacing of 7.75 \AA . The d -spacings of LDPE with 2.5 wt% and 5 wt% MMT nanocomposites were identified at 10.6° and 10.2° which corresponds to the value of 8.34 \AA and 8.67 \AA , respectively. However, the d -spacings of LDPE with 7.5 wt% and 10 wt% MMT nanocomposites were analysed at 9.3° and 8.6° which corresponds to the value of 9.50 \AA and 10.27 \AA , respectively. Moreover, the diffraction peak of OBM slurry (dry powder) was observed at $2\theta = 12.40^\circ$ which corresponds to a d -spacing of 7.13 \AA . The d -spacings of LDPE with 2.5 wt% and 5 wt% OBM slurry nanocomposites were identified at 10.9° and 9.7° which corresponds to the value of 8.11 \AA and 9.11 \AA , respectively. However, the d -spacings of LDPE with 7.5 wt% and 10 wt% OBM slurry nanocomposites were identified at 9.1° and 8.2° which corresponds to the value of 9.71 \AA and 10.77 \AA , respectively. Considering the XRD data obtained in this investigation, it can be inferred that OBM slurry showed better delamination (higher basal spacing) compare to that of MMT in LDPE matrix.

4.3.4. Elemental analysis

EDXA was carried out to determine the elemental composition of dry OBM waste, neat LDPE, LDPE/MMT and LDPE/OBM slurry nanocomposites which is presented in Table 4.1.

Table 4.1 EDXA of OBM waste powder, neat LDPE, LDPE/MMT and LDPE/OBM slurry nanocomposites

Element	OBM clay (Dry)	Neat LDPE	LDPE + 2.5 wt% MMT	LDPE + 2.5 wt% OBM slurry	LDPE + 5.0 wt% MMT	LDPE + 5.0 wt% OBM slurry	LDPE + 7.5 wt% MMT	LDPE + 7.5 wt% OBM slurry	LDPE + 10.0 wt% MMT	LDPE + 10.0 wt% OBM slurry
C	-	98.12	96.27	96.95	94.65	97.04	91.26	97.20	88.26	97.36
O	55.3	1.88	3.13	2.79	4.56	2.58	7.47	2.44	10.12	2.20
Na	1.06	-	0.09	-	-	-	-	-	-	-
Mg	0.53	-	-	-	-	-	-	-	0.05	-
Al	2.78	-	0.12	-	0.15	0.10	0.26	0.12	0.32	0.16
Si	9.92	-	0.39	0.11	0.59	0.13	0.95	0.09	1.19	0.09
S	5.74	-	-	-	-	-	-	-	-	-
Cl	3.61	-	-	0.06	-	-	-	-	-	0.05
K	0.4	-	-	-	-	-	-	-	-	-
Ca	10.4	-	-	0.09	-	0.10	-	0.09	-	0.09
Mn	3	-	-	-	-	-	-	-	-	-
Fe	1.99	-	-	-	0.05	-	0.06	-	0.06	-
Ba	1.61	-	-	-	-	0.05	-	0.06	-	0.05
Totals	6.63	100	100	100	100	100	100	100	100	100

The XRF chemical composition of OBM slurry powder, neat LDPE, LDPE/MMT and LDPE/OBM slurry nanocomposites is presented in Table 4.2.

Table 4. 2 XRF analysis of OBM waste powder, neat LDPE, LDPE/MMT and LDPE/OBM slurry nanocomposites

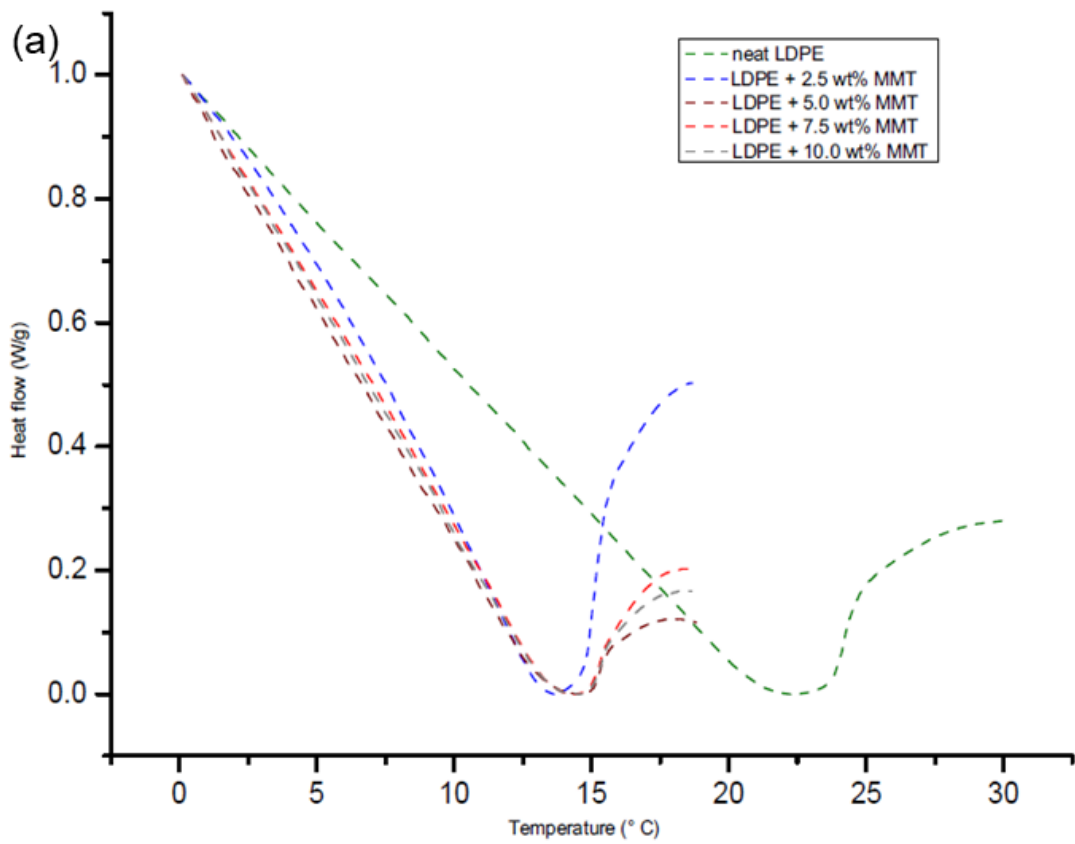
Element	OBM	neatLDPE	LDPE + 2.5 wt% MMT	LDPE + 2.5 wt% OBM slurry	LDPE + 5.0 wt% MMT	LDPE + 5.0 wt% OBM slurry	LDPE + 7.5 wt% MMT	LDPE + 7.5 wt% OBM slurry	LDPE + 10.0 wt% MMT	LDPE + 10.0 wt% OBM slurry
	100.0									
Sum	0	0.45	3.12	1.99	4.43	3.44	6.82	6.02	5.65	8.45
CaO	15.11	0.14	0.37	0.52	0.31	0.86	0.48	1.49	0.43	2.05
P ₂ O ₅	-	0.23	0.33	0.31	0.37	0.34	0.39	0.34	0.40	0.33
Al ₂ O ₃	6.06	-	0.17	-	0.25	-	0.42	-	0.34	-
As	0.12	-	-	-	-	-	-	-	-	-
Ba	27.41	-	-	0.22	-	0.48	-	1.07	-	1.52
Cl	3.37	-	0.03	0.08	0.03	0.13	0.04	0.22	0.03	0.27
Fe ₂ O ₃	3.71	-	0.85	0.31	1.36	0.56	1.90	0.95	1.52	1.25
K ₂ O	0.65	-	-	-	-	-	-	-	-	-
MgO	0.83	-	-	-	-	-	-	-	-	-
MnO	3.35	-	-	0.25	-	0.50	-	0.94	-	1.21
Na ₂ O	0.57	-	-	-	-	-	-	-	-	-
SiO ₂	22.18	-	1.25	0.11	1.89	0.22	3.29	0.36	2.69	0.47
SO ₃	15.63	-	-	-	-	0.19	-	0.34	-	0.47
Sr	0.55	-	-	-	-	-	-	0.11	-	0.15
TiO ₂	0.23	-	-	-	-	-	-	-	-	0.48
Zn	-	-	-	-	-	-	-	-	-	-
Cu	0.01	0.01	0.01	0.01	0.01	-	0.01	0.04	0.01	0.03
other										
s	0.22	0.08	0.10	0.17	0.22	0.17	0.30	0.19	0.23	0.23

XRF analysis confirmed that BaSO₄, SiO₂, Al₂O₃, CaO and Fe₂O₃ were found to be major constituents of OBM slurry (dry powder). Silicon dioxides, iron oxides, alumina, barium sulphate, calcium oxides and manganese oxides are known to be the hardest substances.

The presence of these hard substances in OBM powder suggested that this slurry can be used as a particulate reinforcement in polymer matrix.

4.3.5. Thermal properties

To investigate the thermal degradation behaviour of OBM waste, non-isothermal measurements were taken by using DSC instrument and the results were shown in Figure 3.4 in previous chapter.



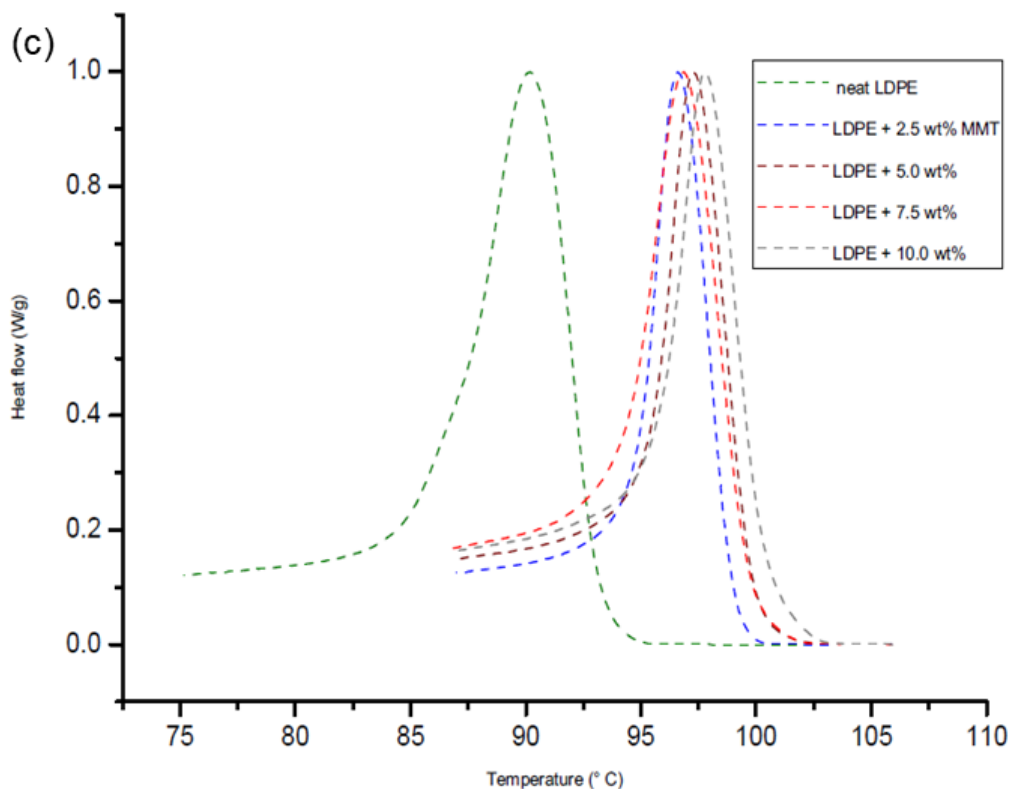
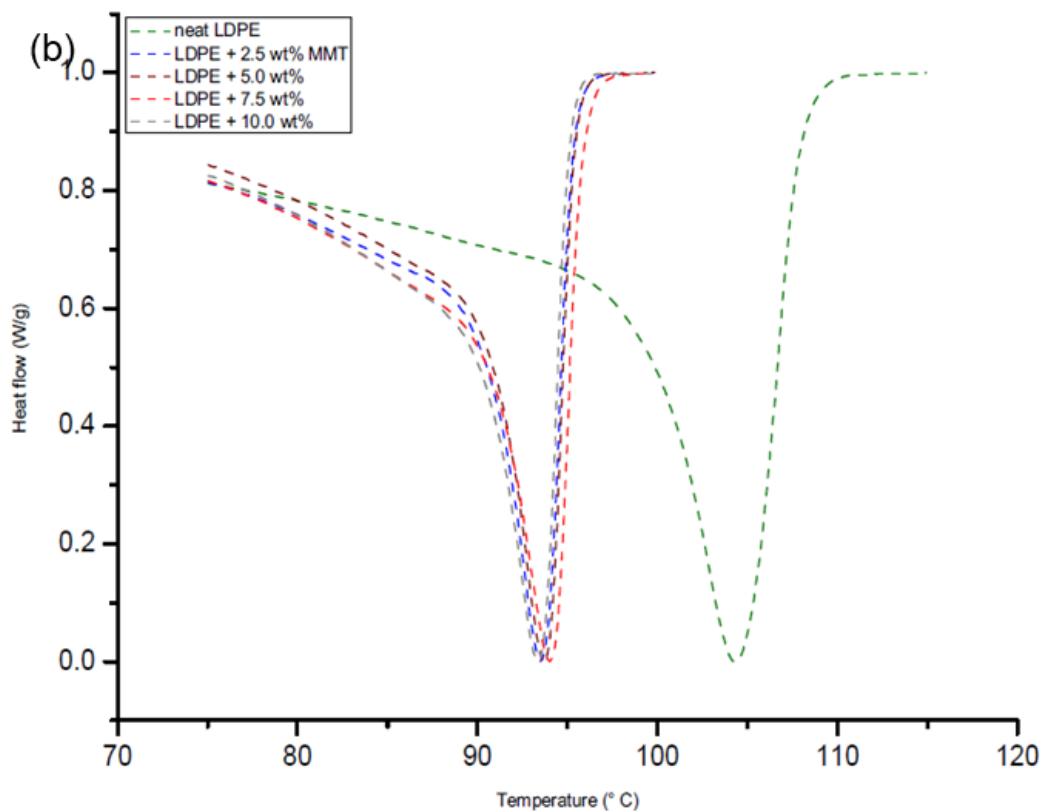
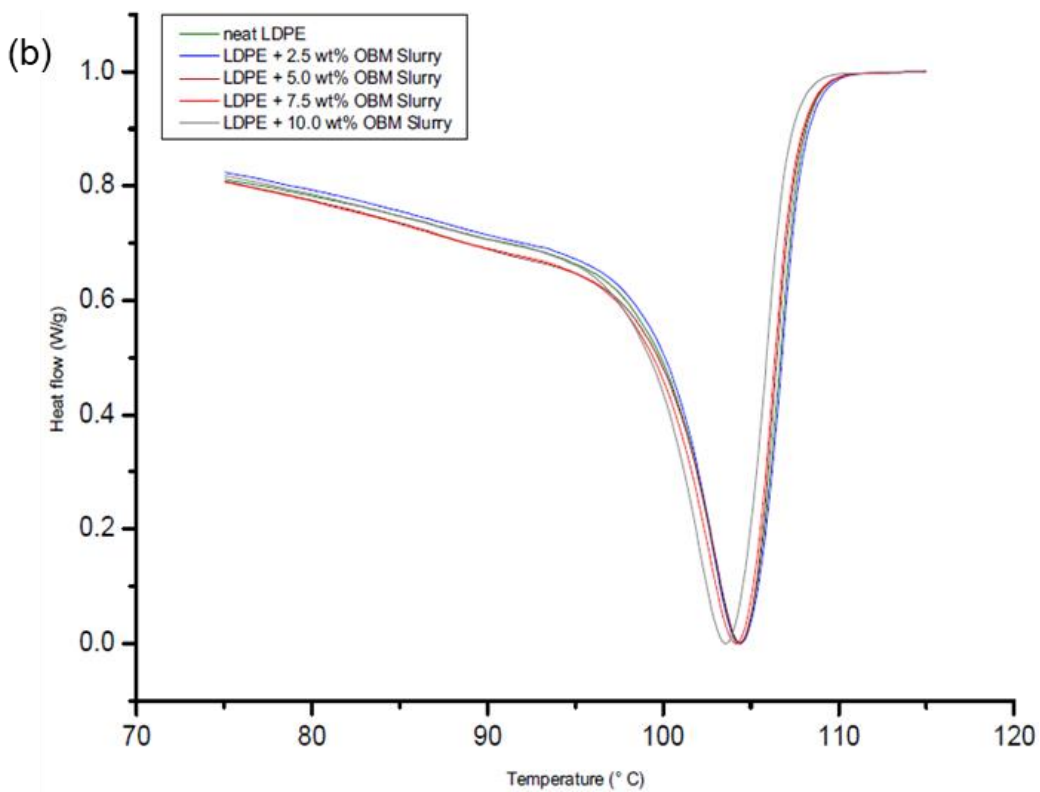
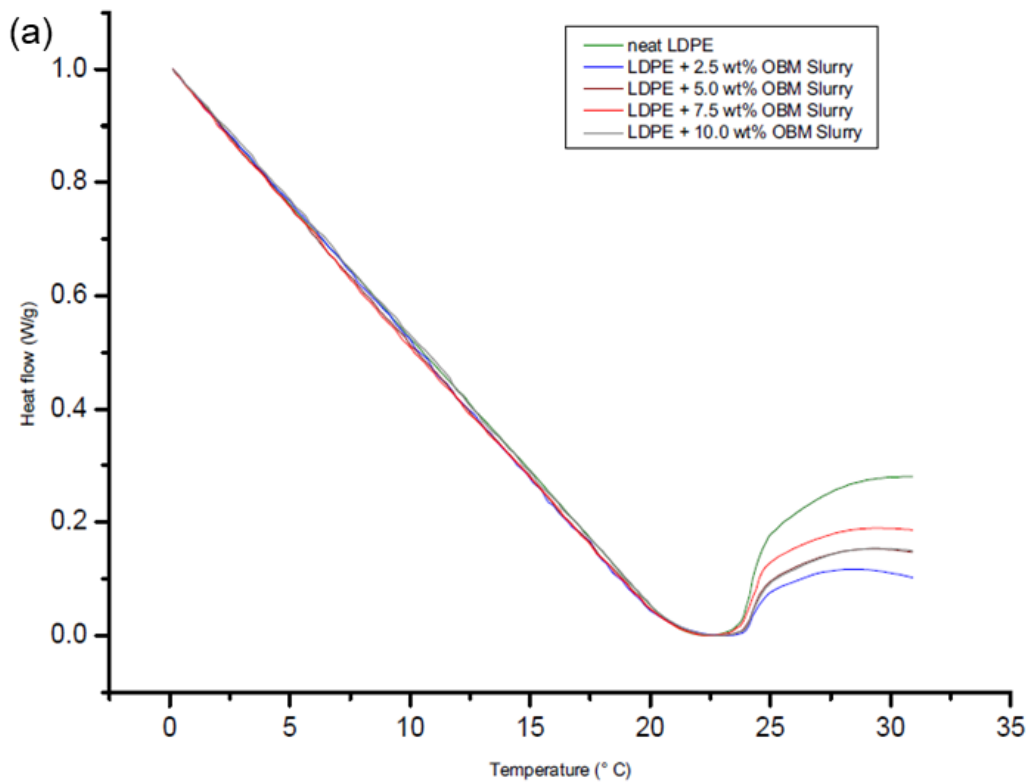


Figure 4.9 DSC thermograms of LDPE and LDPE/MMT nanocomposites at (a) glass transition temperature (T_g); (b) melting temperature (T_m) and (c) crystallisation temperature (T_c)

To identify the influence of OBM slurry on the thermal degradation behaviour of LDPE/OBM slurry nanocomposites, non-isothermal DSC studies were conducted. Investigation on the thermal degradation behaviour of LDPE/MMT nanocomposites considered as a benchmark standard.

Analysing the DSC thermograms in Figure 4.9 (a), it can be highlighted that there are not any significant changes in the glass transition temperature (T_g) of LDPE/MMT nanocomposite materials, but this T_g is lower than the T_g of neat LDPE. However, there are not any significant changes among the T_g of neat LDPE and LDPE/OBM slurry nanocomposites which is shown in Figure 4.10. The same trend is noticeable in comparing the thermograms between LDPE/MMT and LDPE/OBM slurry nanocomposites. The melting point remains almost same for neat LDPE and LDPE/OBM slurry nanocomposites whereas the addition of MMT filler lowered the melting point of LDPE/MMT nanocomposites.



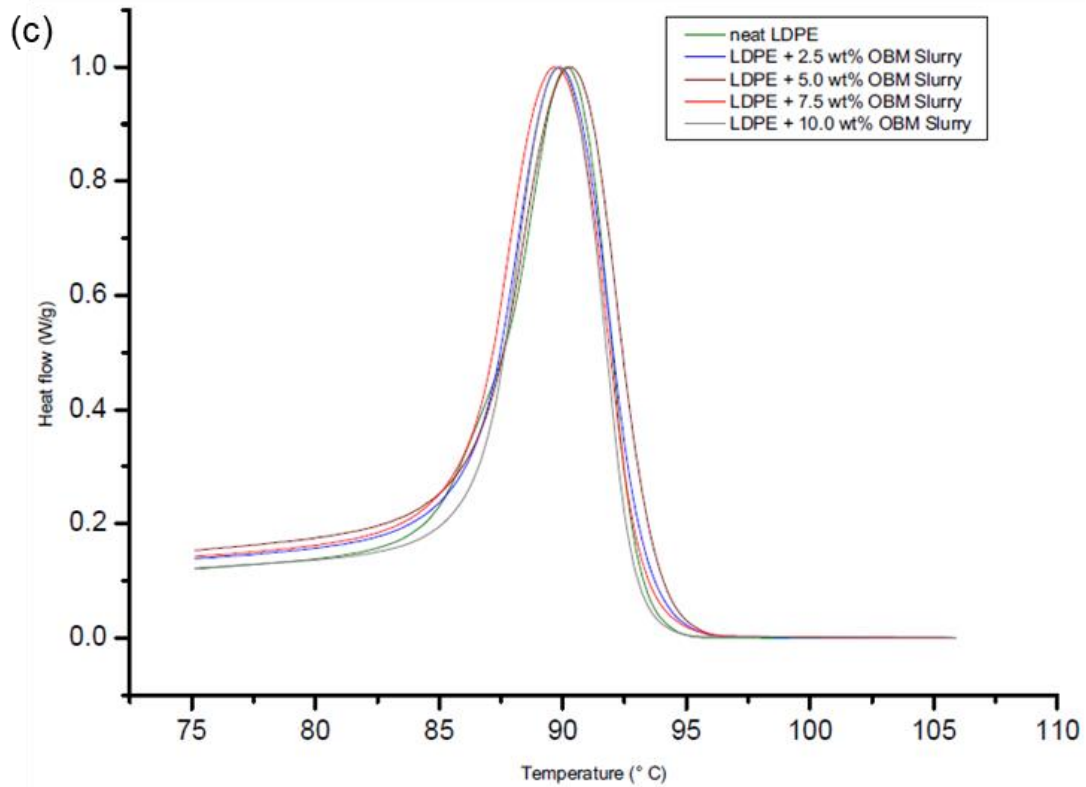


Figure 4.10 DSC thermograms of LDPE and LDPE/OBM slurry nanocomposites at (a) glass transition temperature (T_g); (b) melting temperature (T_m) and (c) crystallisation temperature (T_c)

Considering the heat capacity value from the melting thermograms in Figure 4.9 and Figure 4.10, the % of crystallinity can be identified using the following equation:

$$\% \text{ of crystallinity} = [\Delta H_m - \Delta H_c] / \Delta H_m^0 * 100\% \quad (4.1)$$

Where ΔH_m is the heat of melting, ΔH_c the heat of cold crystallisation which is 0 in this experiment ($\Delta H_c=0$ in this case) due to the absence of cold crystallisation phase in this experiment, and ΔH_m^0 is a reference value if the polymer were 100% crystalline. All the units are in J/g and the value of ΔH_m^0 is 293 J/g (Siddique et al., 2019b). The % of crystallinity value of LDPE, LDPE/MMT and LDPE/OBM slurry nanocomposites are presented in Table 4.3.

It is noticeable that there is a decreasing trend of % of crystallinity in nanocomposites with higher (more than 5 wt%) filler contents. However, there is an indication of increasing % of crystallinity in nanocomposites with lower (less than 5 wt%) filler contents. This decreasing trend in nanocomposites with higher wt% filler contents can be explained by the interruption

caused by this filler in LDPE matrix, which hinders the motion of the polymer chain segments and inhibit crystal growth.

Table 4.3 Structural composition and thermal properties details of neat LDPE, LDPE/MMT and LDPE/OBM slurry nanocomposites

Material	% of crystallinity	RAF= 1- MAF-CF	MAF ($\Delta C_p / \Delta C_{p(am)}$)	Specific heat capacity (C_p) JK ⁻¹ kg ⁻¹
Neat LDPE	16.16	0.10	0.74	3349
LDPE+2.5 wt% MMT	17.25	0.31	0.52	3063
LDPE+5.0 wt% MMT	17.98	0.30	0.52	2975
LDPE+7.5 wt% MMT	14.76	0.47	0.38	2234
LDPE+10.0 wt% MMT	12.46	0.49	0.39	2409
LDPE+2.5 wt% OBM slurry	17.17	0.33	0.50	3394
LDPE+5.0 wt% OBM slurry	13.94	0.32	0.55	2871
LDPE+7.5 wt% OBM slurry	15.65	0.17	0.67	3246
LDPE+10.0 wt% OBM slurry	13.56	0.32	0.54	2801

The specific heat capacity value of LDPE, LDPE/MMT and LDPE/OBM slurry nanocomposites have been identified by analysing the thermograms in Figure 4.9 (c) and Figure 4.10 (c). The specific heat capacity value can be determined by the following equations:

$$C_p = (\delta Q / \delta T) \quad (4.2)$$

$$C_p = (\delta Q / \delta t) \times (\delta t / \delta T) \quad (4.3)$$

Where C_p is the heat capacity in Joules per Kelvin (JK⁻¹), Q is heat energy in Joule and T is the temperature denoted as °C or K. $\delta Q / \delta t$ represents the heat flow and $\delta t / \delta T$ corresponds to

reciprocal heating rate (Siddique et al., 2019a). By using these two equations, the analysed specific heat capacities of neat LDPE, LDPE/MMT and LDPE/OBM slurry nanocomposites are identified, as presented in Table 4.3.

The heat capacity data presented in Table 4.3 shows the negative effects of clay minerals as filler in polymer matrix. However, LDPE with lower filler contents (2.5 and 5 wt%) showed higher specific heat capacity tendency compare to that of higher filler contents nanocomposites. There is a trend noticeable for both of these fillers that the nanocomposites with higher percentage filler contents (7.5 and 10 wt% in this case) indicated to act as a thermal conductive material. The heat capacity value decreases about 33% in LDPE with 7.5 wt% MMT nanocomposite whereas it is about 17% heat reduction in LDPE with 10 wt% OBM slurry nanocomposites.

It is important to identify the different phases exist in semi-crystalline polymer nanocomposites as this will dictate mechanical and thermal properties of the materials. Evaluating the heat capacity value, C_p in glass transition temperature, mobile amorphous fraction (MAF) can be identified by the following equation:

$$MAF = \Delta C_p / \Delta C_{p_{amp}} \quad (4.4)$$

Where $\Delta C_p / \Delta C_{p_{amp}}$ are the heat capacity increments at the glass transition temperature of LDPE and its nanocomposites and the pure amorphous LDPE polymer, respectively. Using the MAF value, rigid amorphous fraction (RAF) can also be identified by the following equation:

$$RAF = 1 - crystallinity - \Delta C_p / \Delta C_{p_{amp}} \quad (4.5)$$

Using the equations (4.4) and (4.5), the MAF and RAF values are identified and presented in Table 4.3.

It can be highlighted here that the RAF increases up to five times compare to RAF of neat LDPE by adding MMT fillers in LDPE matrix. There is an increasing trend of RAF noticeable with the increasing amount of MMT content in LDPE/MMT nanocomposites. However, the RAF increases about three times compare to the RAF of neat LDPE by adding OBM slurry in LDPE matrix. The RAF remains almost constant for different LDPE/OBM slurry nanocomposites which indicate there is no influence of filler amounts increasing the RAF in LDPE/OBM slurry nanocomposites.

The thermal degradation of OBM waste has been analysed in N_2 environment using TA instrument TGA Q500. Onset degradation of the sample in different stages is presented in Figure 3.5 in previous chapter.

Thermal degradation behaviour of LDPE/MMT and LDPE/OBM slurry nanocomposites has been studied under the same environmental condition and analysis method as the environmental condition and analysis method followed in identifying the thermal degradation behaviour of OBM slurry waste.

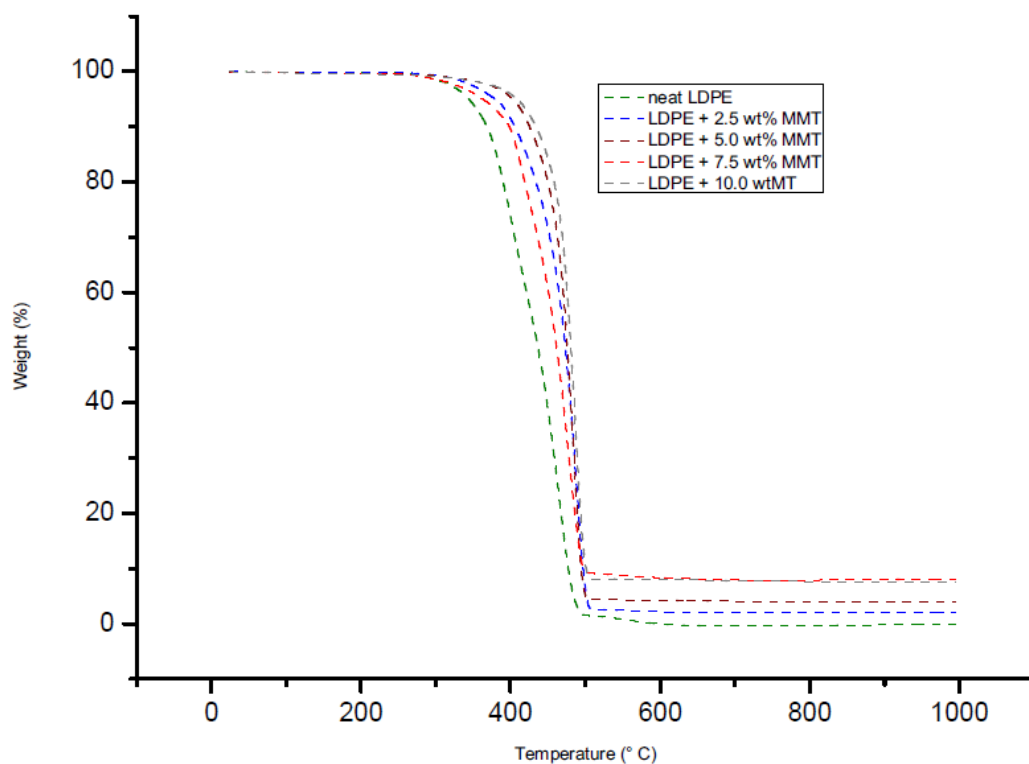


Figure 4.11 TGA thermograms of neat LDPE and LDPE/MMT nanocomposites

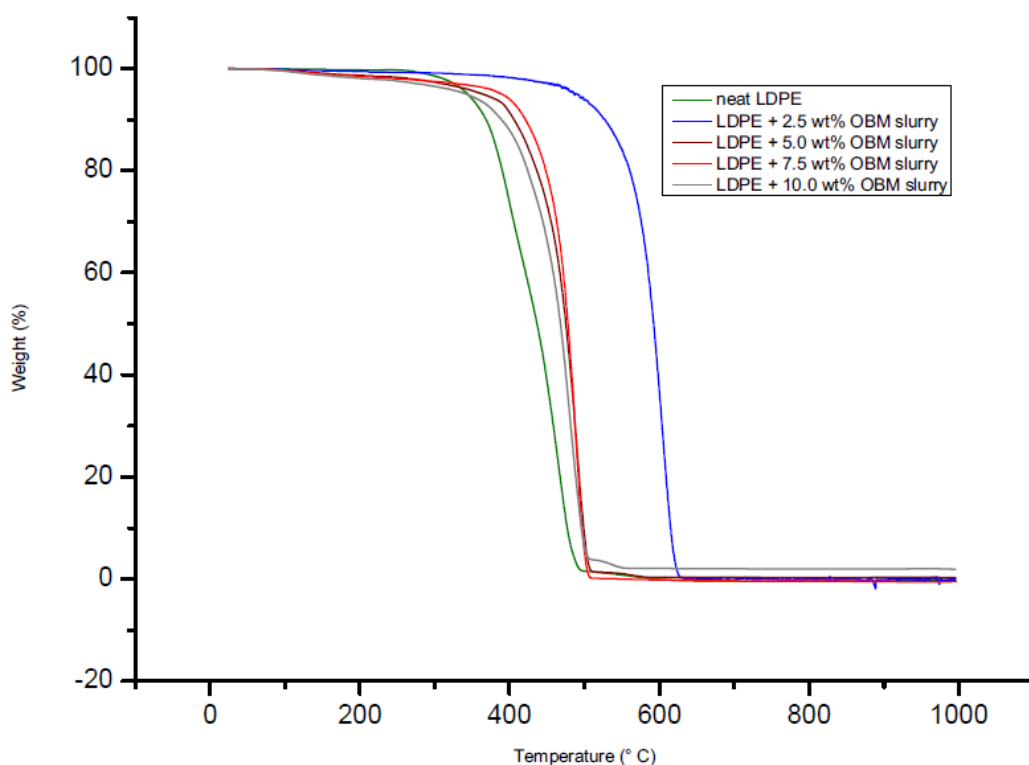


Figure 4. 12 TGA thermograms of neat LDPE and LDPE/OBM slurry nanocomposites

The degradation scenario of these materials at different heating stages are analysed and the key findings are presented in Table 4.4.

Table 4.4 TGA analysis at different decomposition stages of LDPE, LDPE/MMT and LDPE/OBM slurry nanocomposites

Material	T _{D5%} (°C)	T _{D10%} (°C)	D 1/2 Time	Residue (% wt) at 1000 °C
LDPE	381.27	407.39	45.03	0.15
LDPE+2.5 wt% MMT	329.75	368.91	45.05	1.98
LDPE+5.0 wt% MMT	373.12	399.83	45.16	3.99
LDPE+7.5 wt% MMT	316.85	350.93	44.06	7.93
LDPE+10.0 wt% MMT	373.81	401.36	45.84	7.65
LDPE+2.5 wt% OBM slurry	366.90	386.67	44.59	0.20
LDPE+5.0 wt% OBM slurry	370.09	365.39	45.44	0.37
LDPE+7.5 wt% OBM slurry	327.70	383.26	45.59	0.40
LDPE+10.0 wt% OBM slurry	350.07	333.77	44.64	1.97

The onset degradation temperature of neat LDPE, LDPE/MMT and LDPE/OBM slurry nanocomposites materials are presented at weight % losses of 5% and 10%. In all cases, the onset degradation temperature of nanocomposites is less than that of neat LDPE. There are not any significant changes in D1/2 time (the time needed to reach 50% degradation) which indicates the filler content may not have any influence on degradation time and the increase in filler contents in nanocomposites may intensify the heat flow which is shown elevated temperature in D1/2 time. It is also noticeable, for both nanocomposites, the residue remains after 1000° C increases with the incremental wt% of fillers in nanocomposites. There is a big difference in residue amount (in %) left after TGA in two nanocomposites indicates OBM slurry may have significant influence in decomposing LDPE matrix which might be an interesting area to explore in the future.

4.5. Conclusions

The possibility of manufacturing novel economically valuable engineering nanocomposite materials from OBM waste has been demonstrated. Observations from different characterisation including morphology study, chemical and mineralogical study and thermal study it can be concluded that this waste is associated with critical raw materials for different industrial applications, environmentally significant materials including heavy metals and potentially nanoclay as a green filler in nanocomposite manufacturing to improve mechanical, thermal, gas barrier and flame-retardant properties.

Chapter 5: Mechanical and Rheological Properties of LDPE/MMT and LDPE/Oil Based Mud Waste Slurry Nanocomposites

5.1. Introduction

The improvement of specific features such as mechanical, thermal, gas barrier, resistance to heat and flame in polymer matrices has led to an increasing interest of polymer nanocomposites research (Fu and Qutubuddin, 2001; Choudalakis and Gotsis, 2009; Lan and Pinnavaia, 1994; Cui et al., 2015 and Bhattacharya, 2016). The addition of layered clays even at very low concentration (< 7-8 wt%) in polymer matrices predominantly in several polar polymers such as polyamides, polylactic acid and poly (methyl methacrylate) improved the properties (Siddique et al., 2019a; Jahromi et al., 2016; Follain et al., 2016; Zhao et al., 2015; Nam et al., 2015; Dong et al., 2015; Scarfato et al., 2016 and Karaj-Abad et al., 2016). An effective polymer-clay affinity leads to strong polymer-clay interfacial adhesion which helps to disperse the clays by delaminating the nanoplatelets at nanoscale level (Zare, 2016 and Li et al., 2015). Although interfacial adhesion between polar polymers and clay platelets are successful in some extent, the interfacial adhesion between non-polar polymer such as polyethylene and clay platelets are still very poor and limited (Iqbal et al., 2016; Siddique et al., 2019b and Herrero et al., 2016). However, different researchers applied various techniques including utilising compatibilizers and coupling agents in nanocomposites manufacturing process (Hossen et al., 2015; Sánchez-Valdes et al., 2017; Ibarra-Alonso et al., 2015 and Samper-Madrigal et al., 2015). Considering the poor performances/results obtained from dispersing clay platelets into non-polar polymer matrices, an effective, and suitable to manufacturing, cheap and eco-friendly nanocomposites compounding/manufacturing technique is still an attractive area of research.

Traditionally, a range of biological and non-biological methods have been employed to treat the spent oil-based drilling fluid. All these methods are associated with cost, time and space requirement and environmentally hazardous. Considering these drawbacks to manage the environmentally hazardous waste and existing organically modified clay minerals, the authors initiated an investigation on how the reclaimed layered silicate from oil based mud (OBM) waste influence the properties in engineering nanocomposite materials. In chapter 4, depth structural, morphological and thermal investigations were carried out based on the results obtained from OBM waste slurry reinforced polymers. Different types of clay minerals such as muscovite, anorthite, montmorillonite, kaolinite etc remains in strong suspended

condition in the OBM waste slurry. It was anticipated that the cations exist in clay minerals layers were replaced by stronger cations in surfactant used in OBM formulation. It was hoping to utilise the organophilic nature of clay surfaces exist in OBM waste in its natural condition and to investigate the compatibility of this raw OBM slurry with polymer matrix. The present work is an extension of chapter 4 and focus on the effect of this novel filler in raw slurry condition without any treatment on rheological and mechanical properties of LDPE/OBM slurry nanocomposites.

5.2. Experimental

5.2.1. Materials and samples preparation

The materials and sample preparation method used in this chapter are described in section 4.2.1.

5.2.2. LDPE/OBM slurry nanocomposite manufacturing process

The manufacturing method of LDPE/MMT and LDPE/OBM slurry nanocomposites used in this study is described in section 4.2.2.

5.2.3. Morphology

The dispersion characteristics of MMT and OBM slurry clay platelets in LDPE matrix were analysed using a Zeiss EVO LS10 Scanning Electron Microscope (SEM) with a magnification of 1.0 KX, 8.5 mm working distance and 20.0 kV accelerating potential. The samples were fractured following a cryogenic sampling technique and were gold coated using sputter deposition for 2 minutes prior to fit in the equipment for observation.

5.2.4. Mechanical testing

Tensile tests were carried out by following ISO standard 527-3.28 5 specimens for each type of nanocomposites were tested. An Instron 3382 universal testing machine using with Bluehill 3 software were used to perform tensile test. The addition of montmorillonite and

OBM slurry fillers in the LDPE matrix resulted in changes the mechanical properties of LDPE/MMT and LDPE/OBM slurry nanocomposites. Array of different materials reinforced with different wt% of MMT and OBM slurry fillers are presented in Figure 5.1 (a) and (b) respectively. A set of five samples were tested and the average data is taken into account to identify the mechanical properties of each material.

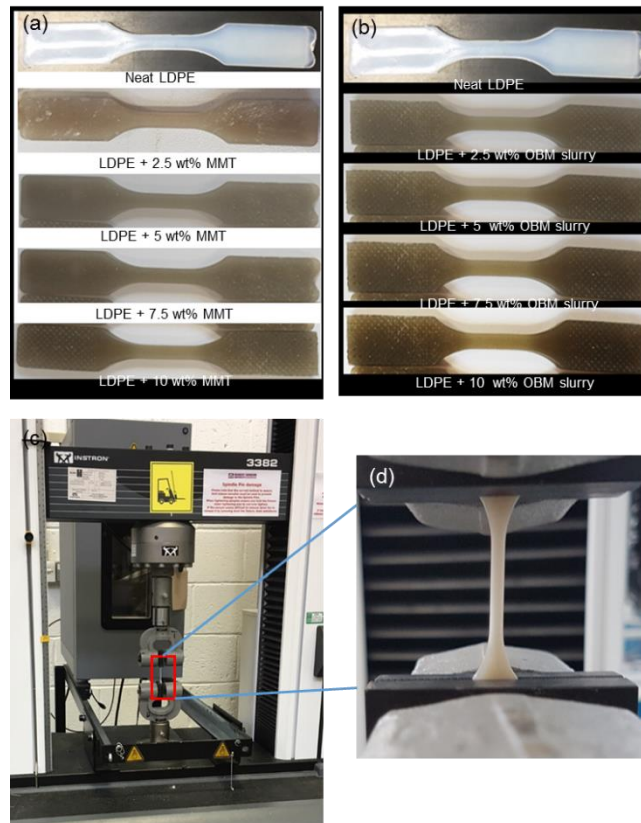


Figure 5.1 Array of tensile test specimen of (a) neat LDPE and LDPE/MMT nanocomposites; (b) neat LDPE and LDPE/OBM slurry nanocomposites and presentation of (c) tensile test set up and (d) observation of plastic deformation through the reduced area of sample

The dog-bone shaped samples were prepared according to ASTM method D-638. The tests were performed at constant strain rate of 2 mm/min and the data presented here is the average of 5 samples. Figure 5.1 (c) shows the equipment set up to perform tensile testing of materials. Figure 5.1 (d) shows the change in sample colour and also indicating the plastic deformation of sample while the sample under stress during test.

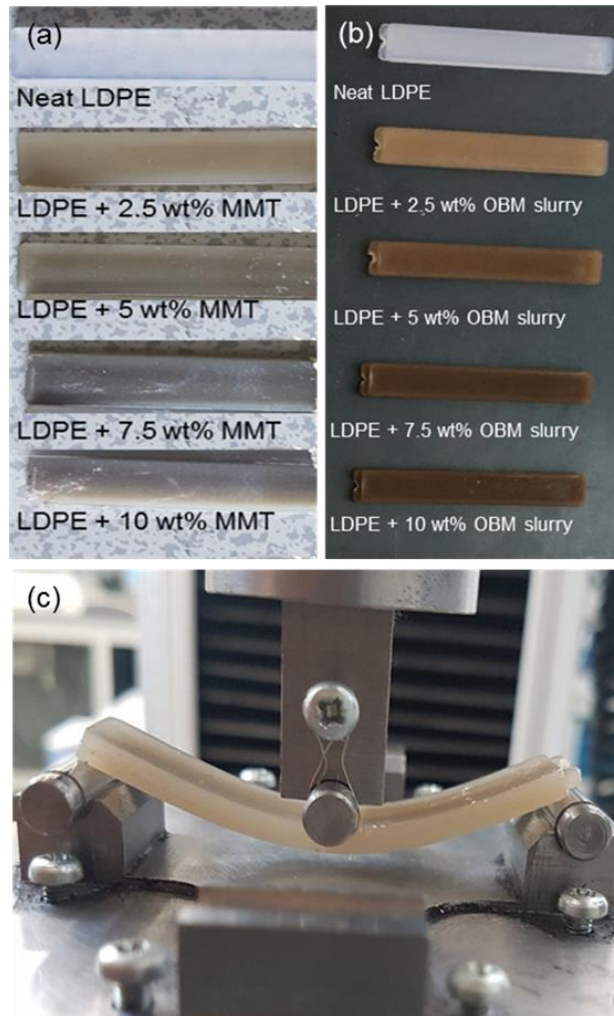


Figure 5.2 Array of 3-point bending test specimen of (a) neat LDPE and LDPE/MMT nanocomposites; (b) neat LDPE and LDPE/OBM slurry nanocomposites and (c) observation of 3-point bending test of sample

Flexural experiments were carried out according to ISO 14125 test standard. All tests were performed at a constant strain rate of 2 mm/min using the same equipment as for tensile test and the data calculated here is the average of 5 samples. Array of different materials reinforced with different wt% of MMT and OBM slurry fillers are presented in Figure 5.2 (a) and (b) respectively. A set of five samples were tested and the average data is taken into account to identify the flexural properties of each material.

5.2.5. Rheological characterisation

Rheological characterisation was performed using an oscillatory shear in Dynamic Stress Rheometer (AR 1000, TA Instruments) using parallel plate geometry of 8 mm diameter and at a gap of 3.1 mm. In all cases, samples were analysed to identify the viscoelastic

properties as a function of temperature. The temperature range used in this analysis was from 0 to 90°C, with a heating rate of 3°C /min. All the samples were scanned at a fixed frequency of 1 Hz, with a strain of 0.2%.

5.3. Results and discussion

5.3.1. Morphology study of LDPE/MMT and LDPE/OBM slurry nanocomposites

The SEM micrographs were used to analyse and compare the changes in morphological structure of MMT and OBM slurry in LDPE matrix. Figure 4.2 and Figure 4.3 in the previous chapter shows the morphology of LDPE/MMT and LDPE/OBM slurry nanocomposites. The cavities and uneven surfaces appear in the images due to the cryogenic fractures of samples. A higher degree of filler dispersion is observed in LDPE/OBM slurry nanocomposite samples compare to the MMT dispersion in LDPE/MMT nanocomposites predominantly in higher filler content samples in Figure 4.2 (e) and Figure 4.3 (e). Figure 4.2 (d) and (e) show the tendency of MMT agglomeration in LDPE matrix whereas Figure 4.3 (d) and (e) show uniform distribution of OBM slurry in LDPE matrix.

5.3.2. Tensile properties of neat LDPE, LDPE/MMT and LDPE/OBM slurry nanocomposites

Observing stress-strain data from tensile test of LDPE/MMT and LDPE/OBM slurry nanocomposites in Figure 5.3, different mechanical properties were identified. The stress-strain graph (Figure 5.3) demonstrates the typical behaviour of LDPE material which shows an initial linear elastic region followed by a little drop in graph highlighting the non-linear transition to yield (Jordan et al., 2016). These yield points are apparent in both Figure 5.3 (a) and (b). It is noticeable in Figure 5.3 that similar behaviour is noticeable in strain softening followed by strain hardening stages in both LDPE/MMT and LDPE/OBM slurry nanocomposites.

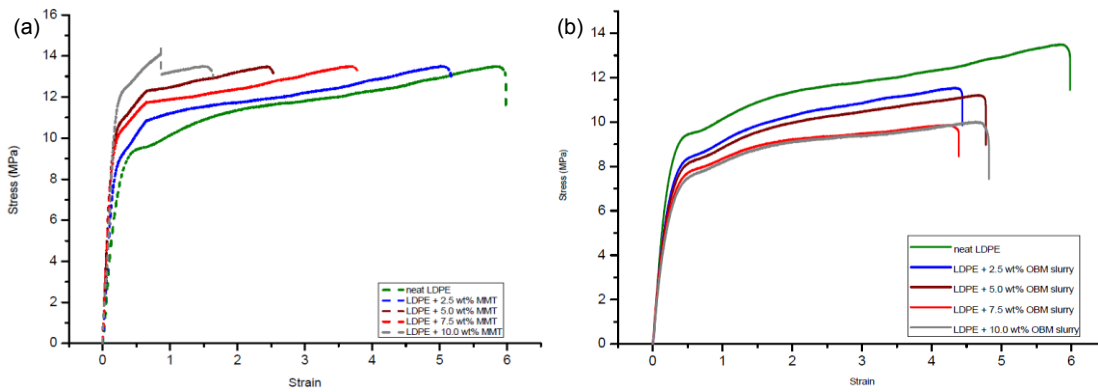


Figure 5.3 Stress-strain curves of (a) neat LDPE and LDPE/MMT and (b) neat LDPE and LDPE/OBM slurry nanocomposites

For 7.5 to 10 wt% MMT loading, there is a sharp increase in tensile strength which is noticeable in Figure 5.4 while only minor changes were observed on tensile strength for 0 to 7.5 wt% MMT loading.

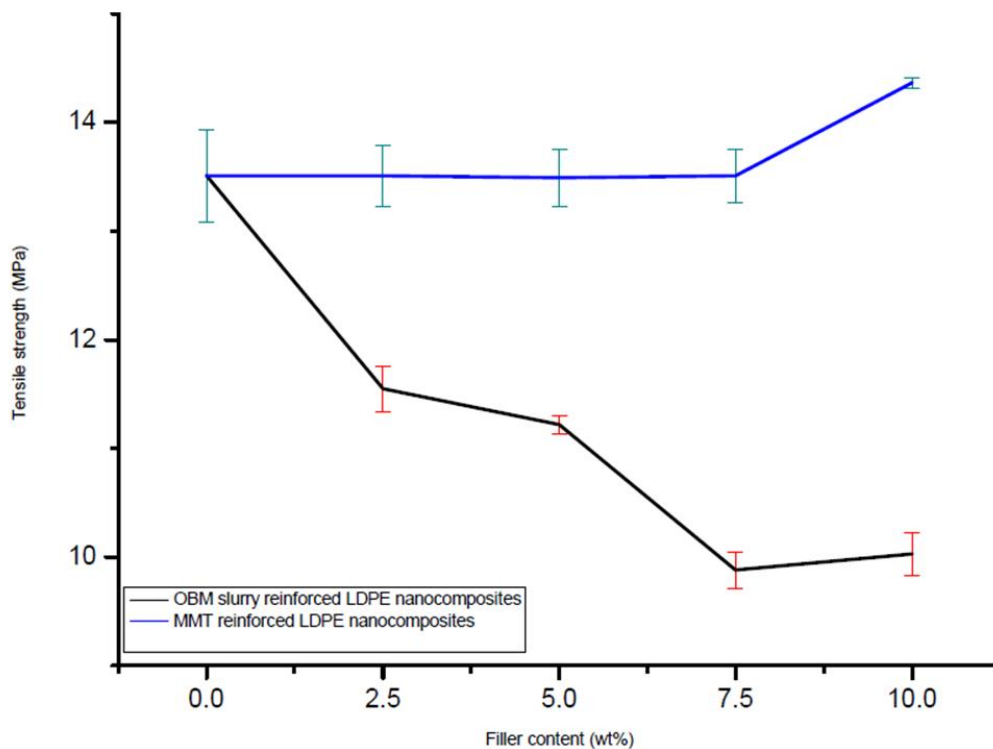


Figure 5.4 Comparison of tensile strength between LDPE/MMT and LDPE/OBM slurry nanocomposites considering tensile strength of neat LDPE as a baseline

However, the progressive decrease in tensile strength is highlighted in Figure 5.4 with the increasing of OBM slurry filler contents from 0 to 10 wt%. This could be explained by the decohesion between the matrix and OBM slurry nanoparticles under stress. This decohesion

generates a stress concentration through the void area between matrix and nanoparticles which accelerates the sample break.

However, the increase in MMT content from 0 to 10 wt% resulted in about 40% increase in Young's modulus whereas the increase in OBM slurry content from 0 to 10 wt% resulted in about 30% decrease in Young's modulus.

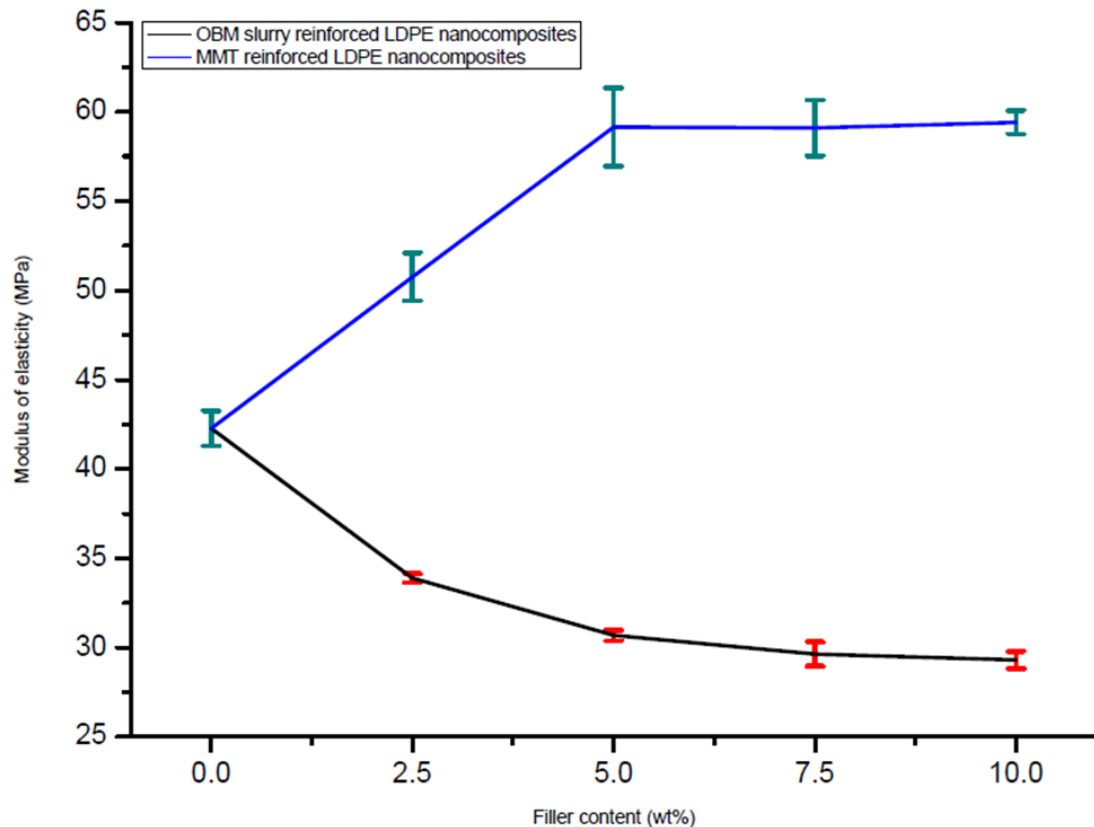


Figure 5.5 Comparison of modulus of elasticity in tension of neat LDPE, LDPE/MMT and LDPE/OBM slurry nanocomposites

A sharp increase in the modulus can be observed when MMT loading increases from 0 to 5 wt%. Beyond 5 wt% in MMT content, there are not any significant changes noticeable in Young's modulus in Figure 5.5. The opposite trend is evident for LDPE/OBM slurry nanocomposites. A sharp decrease in the modulus can be observed when OBM slurry loading increases from 0 to 5 wt%. From 5 to 10 wt% of OBM slurry loadings, there is not any significant changes in elastic modulus which is highlighted in Figure 5.5. The significant enhancement in the tensile modulus is noticeable with increasing the MMT content whereas a substantial decrease in tensile modulus is reported with the incremental loading of OBM slurry in LDPE matrix. It can be concluded that the addition of MMT improved the stiffness of LDPE matrix whereas the stiffness decreased with the addition of OBM slurry in LDPE

matrix. However, the percentage elongation at yield decreases with the increase of both MMT and OBM slurry filler contents.

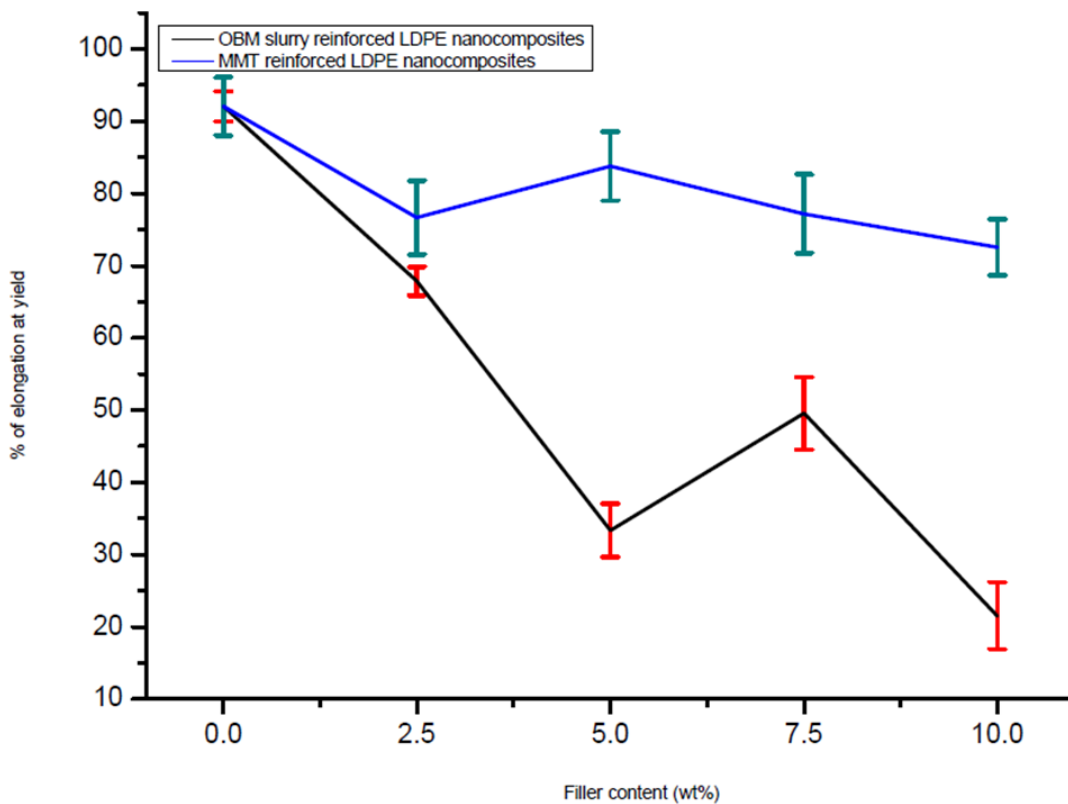


Figure 5.6 Comparison of percentage elongation at yield of neat LDPE, LDPE/MMT and LDPE/OBM slurry nanocomposites

There is a minor effect of ductile property in LDPE/MMT nanocomposites which is presented in Figure 5.6 due to the addition of MMT loading in LDPE matrix. Nonetheless, the percent elongation at yield in LDPE/OBM slurry nanocomposites decreases enormously due to addition of OBM slurry in LDPE matrix. It can be attributed to a reduction in deformability of interface between nanoparticles and matrix. From the morphology presented in Figure 4.3, the uniform distribution and dispersion of OBM slurry clay fillers intensifies the crack propagation through the cross section of the samples and thus resulting in reduced percent elongation in LDPE/OBM slurry nanocomposites. The faster crack propagation in LDPE/OBM slurry nanocomposites compare to that in LDPE/MMT nanocomposites is due to the close distances among the OBM slurry clay platelets which influences the sample fails quicker and under lower forces applied on the samples.

5.3.3. Flexural properties of neat LDPE, LDPE/MMT and LDPE/OBM slurry nanocomposites

The flexural stress-strain curves of neat LDPE, LDPE/MMT and LDPE/OBM slurry nanocomposites are shown in Figure 5.9.

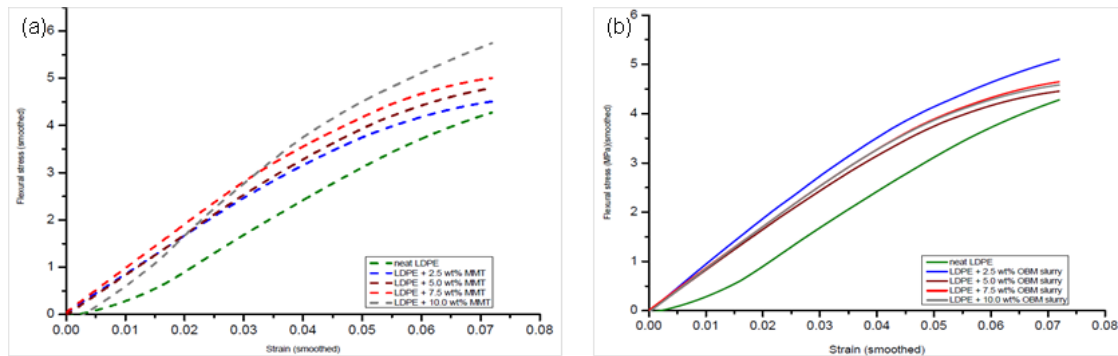


Figure 5.7 Flexural stress-strain curves from 3-point bend test of neat LDPE, LDPE/MMT and LDPE/OBM slurry nanocomposites

It is observed that the gradient of stress-strain curve in Figure 5.7 (a) increases with the incremental loading of MMT fillers in LDPE matrix. However, the gradient of stress-strain curve in Figure 5.7 (b), also showed higher for LDPE/OBM slurry nanocomposites compare to that of neat LDPE, but these incremental gradients in LDPE/OBM slurry nanocomposites are OBM slurry loadings independent. The constituents and the interface interactions are the key factors which dictate the flexural strength of fibre or nanoparticle reinforced nanocomposites. Homogeneity is another important factor which needs to be taken into account when interpreting flexural properties of materials. Since in flexural/bending test, the convex side of the sample is extended and the concave side is compressed, the degree of distribution of clay nanoplatelets into LDPE matrix plays main role in affecting the flexural properties.

The variation of flexural strength of LDPE/MMT and LDPE/OBM slurry nanocomposites reinforced with different weight (2.5, 5, 7.5 and 10) percentage of fillers is presented in Figure 5.8.

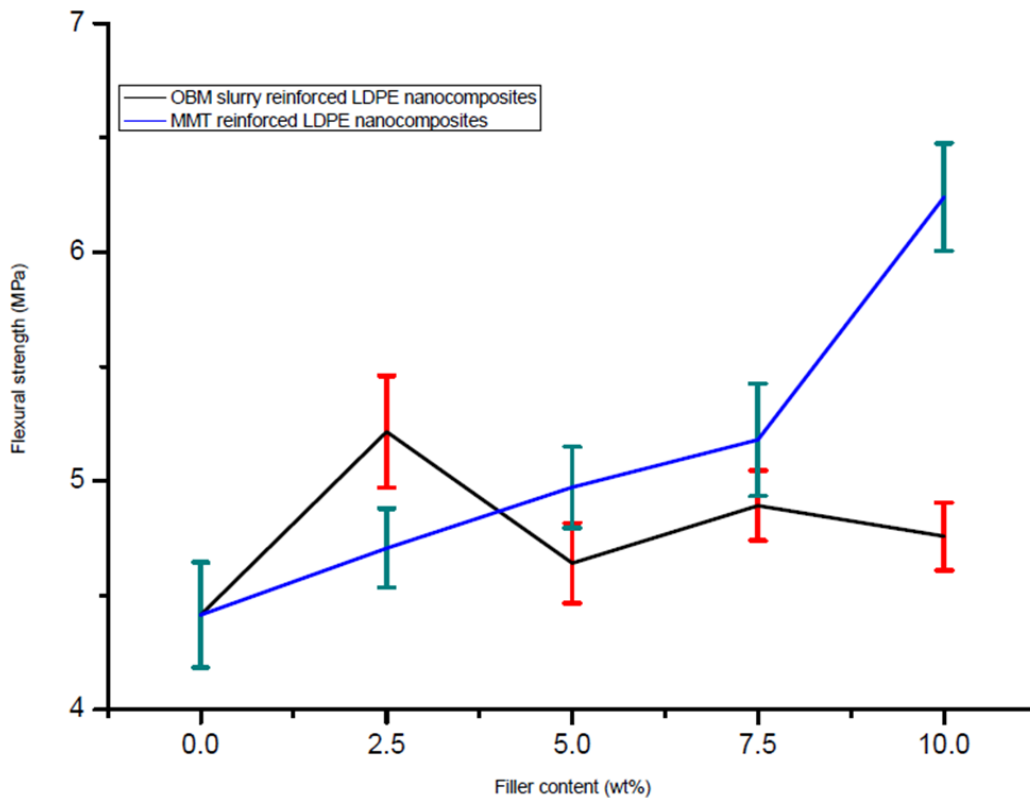


Figure 5.8 Comparison of flexural strength of neat LDPE, LDPE/MMT and LDPE/OBM slurry nanocomposites

In Figure 5.8, neat LDPE shows the lowest flexural strength which is considered as a reference point. There is a linear improvement of flexural strength is noticeable for LDPE/MMT nanocomposites. However, the flexural strength does not show any trend for LDPE/OBM slurry nanocomposites. The maximum flexural strength is evident for LDPE/MMT nanocomposites with 10 wt% MMT content. However, LDPE with 10 wt% OBM slurry nanocomposite shows the lowest flexural strength compared to the flexural strength of other LDPE/OBM slurry nanocomposites.

The flexural modulus of LDPE/MMT and LDPE/OBM slurry nanocomposites is shown on Figure 5.9.

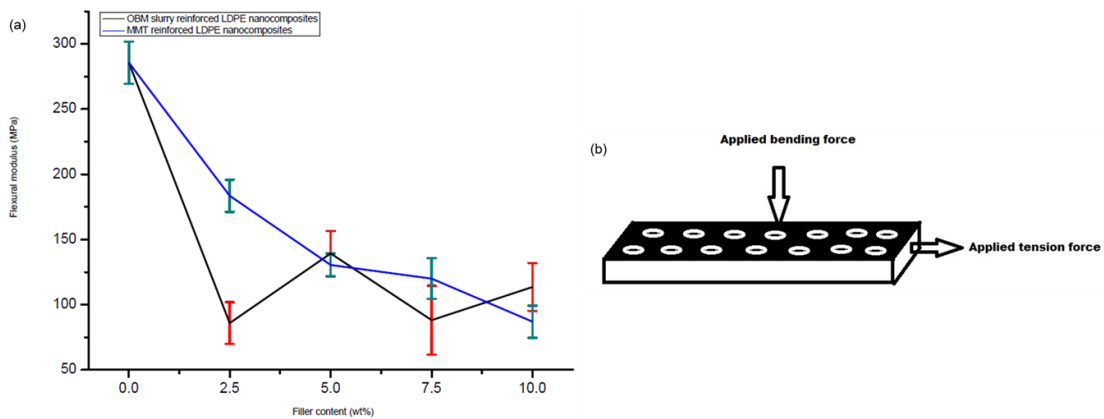


Figure 5. 9 (a) Comparison of modulus of elasticity in bending of neat LDPE, LDPE/MMT and LDPE/OBM slurry nanocomposites; (b) a schematic illustration of applied force in tension and bending test and the distribution of MMT and OBM slurry nanoplatelets through the sample

It was observed that the flexural modulus decreased steadily in LDPE/MMT nanocomposites from 0 wt% to 10 wt%, see Figure 5.9 (a). However, the decreasing trend in flexural modulus for LDPE/OBM slurry is not linear and it is not possible to correlate the effect of OBM slurry loading influencing the flexural modulus of LDPE/OBM slurry nanocomposites. Both tensile and flexural modulus decreases with the incremental load of OBM slurry in LDPE matrix. Although the tensile modulus of LDPE/MMT increases with the incremental loading of MMT in LDPE matrix, the flexural modulus of LDPE/MMT nanocomposites decreases with the MMT loading from 0 to 10 wt%.

The extent to which the reinforcing nanoplatelets influencing the modulus of materials depended directly on the thickness of the filler particles, dispersion and distribution pattern of nanoplatelets in polymer matrix and thus on the aspect ratio (Lee et al., 2010 and Halit, 2018). The nanomorphology, dispersion and distribution mechanism of OBM nanoplatelets in polymer matrix has already been reported recently by the authors (Siddique et al., 2019a and Siddique et al., 2019b). Further, in our previous studies, the improvement of thermal stability was evident and reported in literature. Although the improvement in thermal stability has been achieved utilising reclaimed clay from spent OBM waste, the effect of this novel filler on rheological and mechanical properties is unknown.

Based on the observations from these reported studies, it can be highlighted that the influence of interfacial interaction between polymer and clay governs the modulus property in the nanocomposites which also agrees with the findings by Lee et al. (2010). The large interfacial area provides better stress transfer at the interface between polymer and clay platelets. In Figure 5.9 (b), a schematic diagram illustrates the dispersion of clay platelets into polymer matrix. As the diameter of the white circle (demonstrating clay platelets) in

Figure 5.9 (b) is higher than its thickness, the interfacial area between polymer and clay platelets is higher in the longitudinal direction. Hence, higher tension load is needed to overcome the frictional force generated by the interfacial area between polymer and clay platelets. On the other hand, in 3-point bending test, bending/flexural force is applied through the width of the sample and at the middle of the beam. As the thickness of platelets is lower than its diameter, the frictional force at the interfacial area between clay and polymer is lower than the frictional force generated in the longitudinal direction. This statement satisfies the decreasing trend in flexural modulus for both LDPE/MMT and LDPE/OBM slurry nanocomposites.

5.3.4. Rheological characterisation of neat LDPE, LDPE/MMT and LDPE/OBM slurry nanocomposites

The rheological properties of neat LDPE, LDPE/MMT and LDPE/OBM slurry nanocomposites were studied using oscillating shear rheometer to investigate the accumulated percolated network of the fillers, which may influence the electrical and thermal conductivity of polymer nanocomposite materials. This technique is a very effective identifying the filler dispersion, structural behaviour of materials and interaction of the filler in polymer matrix. Figure 5.10 shows the dynamic temperature sweep analysis conducted to investigate the effect of fillers on storage modulus for neat LDPE, LDPE/MMT and LDPE/OBM slurry nanocomposites.

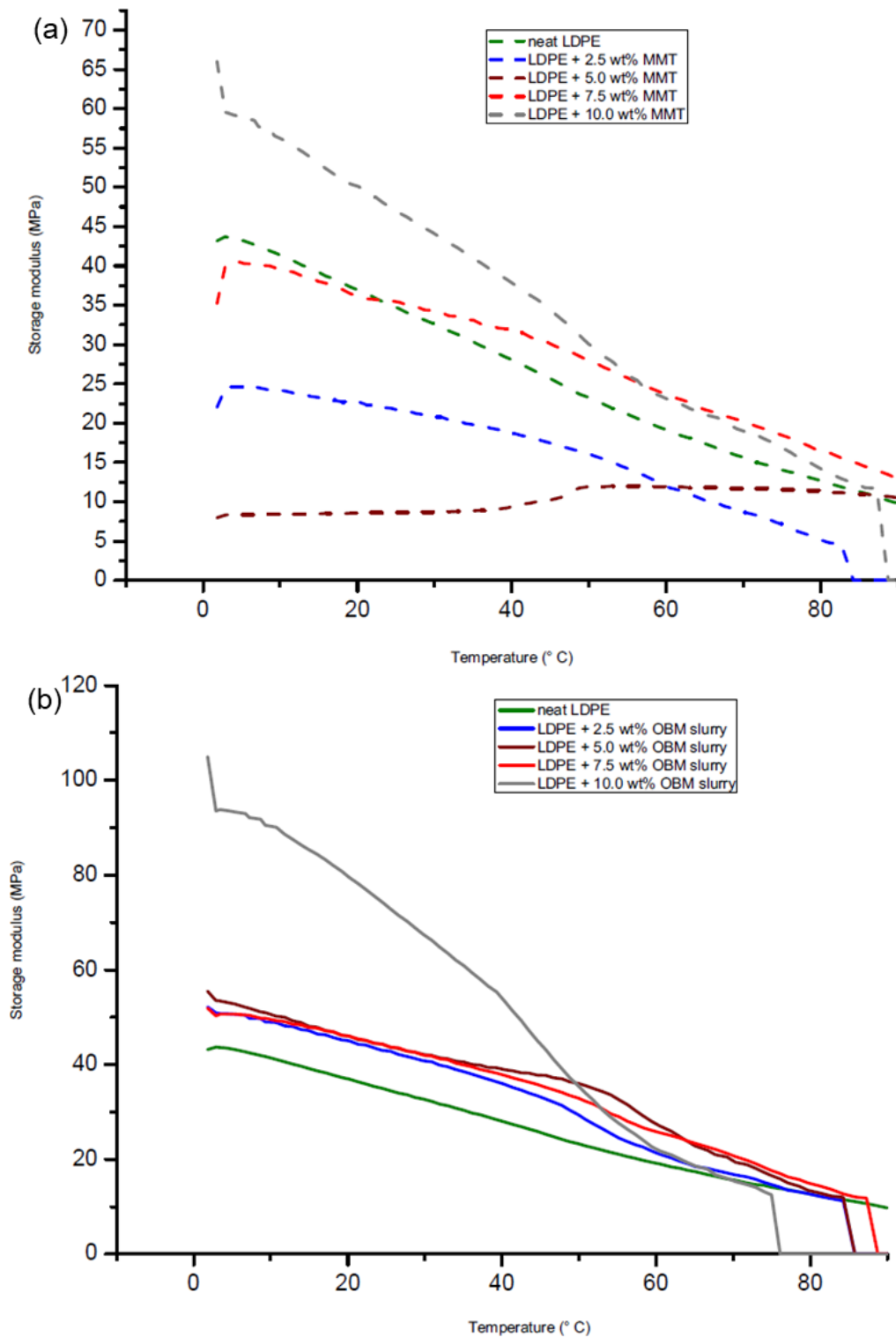
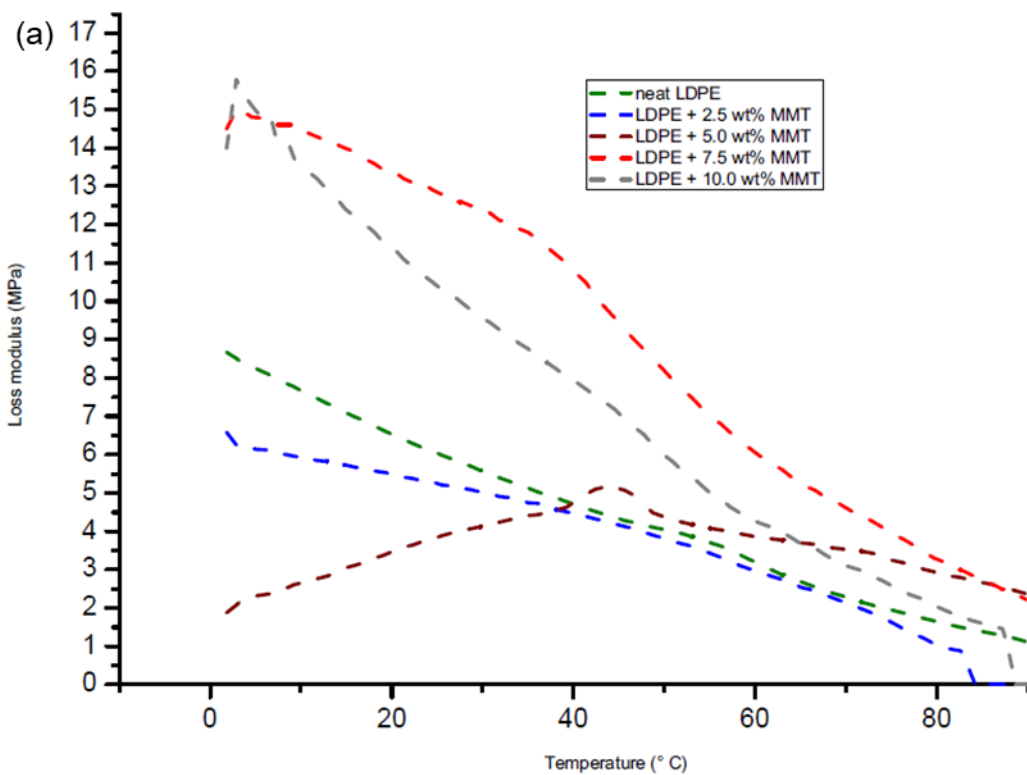


Figure 5.10 Influence of applied shear stress on the storage modulus of (a) neat LDPE and LDPE/MMT and (b) neat LDPE and LDPE/OBM slurry nanocomposites

The storage modulus (E') presented in Figure 5.10 highlights the load bearing capacity of neat LDPE, LDPE/MMT and LDPE/OBM slurry nanocomposites. It is noticeable from Figure

5.10 (a) that the storage modulus of LDPE with 2.5 and 5 wt% MMT nanocomposites is lower than the storage modulus of neat LDPE. However, the storage modulus of LDPE with 7.5 and 10 wt% MMT nanocomposites is higher than the storage modulus of neat LDPE. LDPE with 10 wt% MMT nanocomposite shows the highest storage modulus up to 50° C and between 50 to 90° C, there is a minor storage modulus difference among neat LDPE and LDPE/MMT nanocomposites which is highlighted in Figure 5.10 (a). However, the storage modulus of neat LDPE and LDPE/OBM slurry nanocomposites is presented in Figure 5.10 (b) which shows the storage modulus of LDPE/OBM slurry nanocomposites is higher than the storage modulus of neat LDPE up to the temperature of 50°C. There is a minor storage modulus difference among neat LDPE and LDPE/OBM slurry nanocomposites which is highlighted between 50 to 90° C in Figure 5.10 (a). From this observation, it can be concluded here that the influence of MMT and OBM slurry fillers on storage modulus decreases with the increase of temperature. It is noticeable that 50 to 90° C, the storage modulus of LDPE/MMT and LDPE/OBM slurry nanocomposites is filler independent.

The loss modulus curves of neat LDPE, LDPE/MMT and LDPE/OBM slurry nanocomposites are presented in Figure 5.11 which shows the relaxation peak of neat LDPE shifted from 60° C to lower temperatures due to the addition of fillers in LDPE matrix.



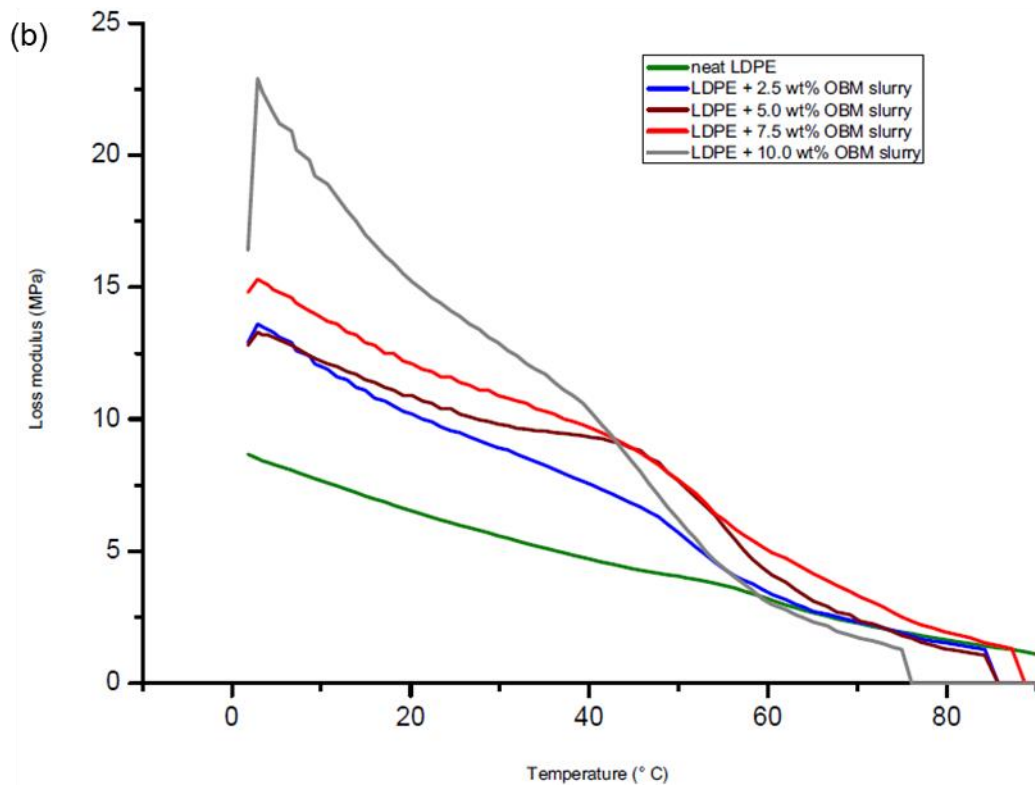


Figure 5.11 Influence of applied shear stress on the loss modulus of (a) neat LDPE and LDPE/MMT and (b) neat LDPE and LDPE/OBM slurry nanocomposites

In Figure 5.11 (a) and Figure 5.11 (b), it is noticeable that there is a sharp decrease of loss modulus between 0 to 50° c for neat LDPE, LDPE/MMT and LDPE/OBM slurry nanocomposites. However, there is a very minor changes in loss modulus is noticeable between 60 to 90° c. The same trend as storage modulus of LDPE/MMT and LDPE/OBM slurry nanocomposites is also evident for loss modulus of LDPE/MMT and LDPE/OBM slurry nanocomposites which can be presented as below.

- Loss modulus of LDPE/MMT nanocomposites: LDPE with 2.5 and 5 wt% MMT < neat LDPE < LDPE with 7.5 and 10 wt%; and
- Loss modulus of LDPE/OBM slurry nanocomposites: neat LDPE < LDPE/OBM slurry nanocomposites.

To identify the damping properties of the materials, the ratio of loss modulus to storage modulus is calculated and presented in Figure. 5.12 (a) and 5.12 (b).

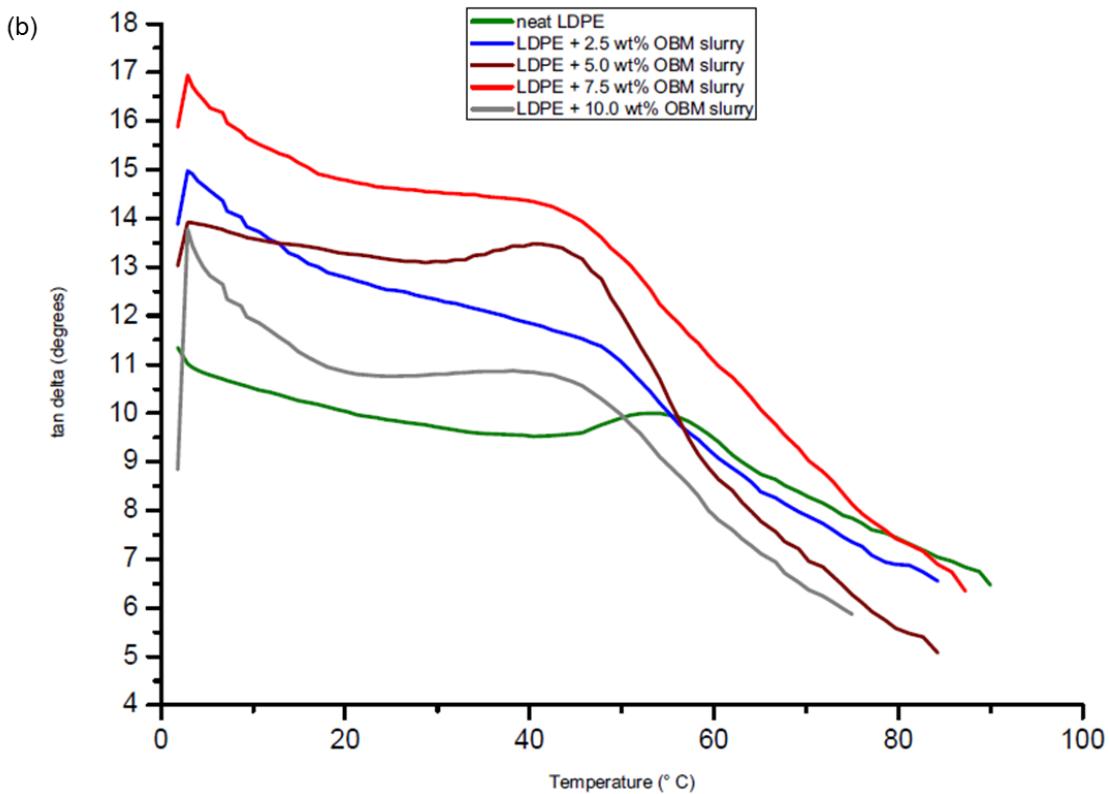
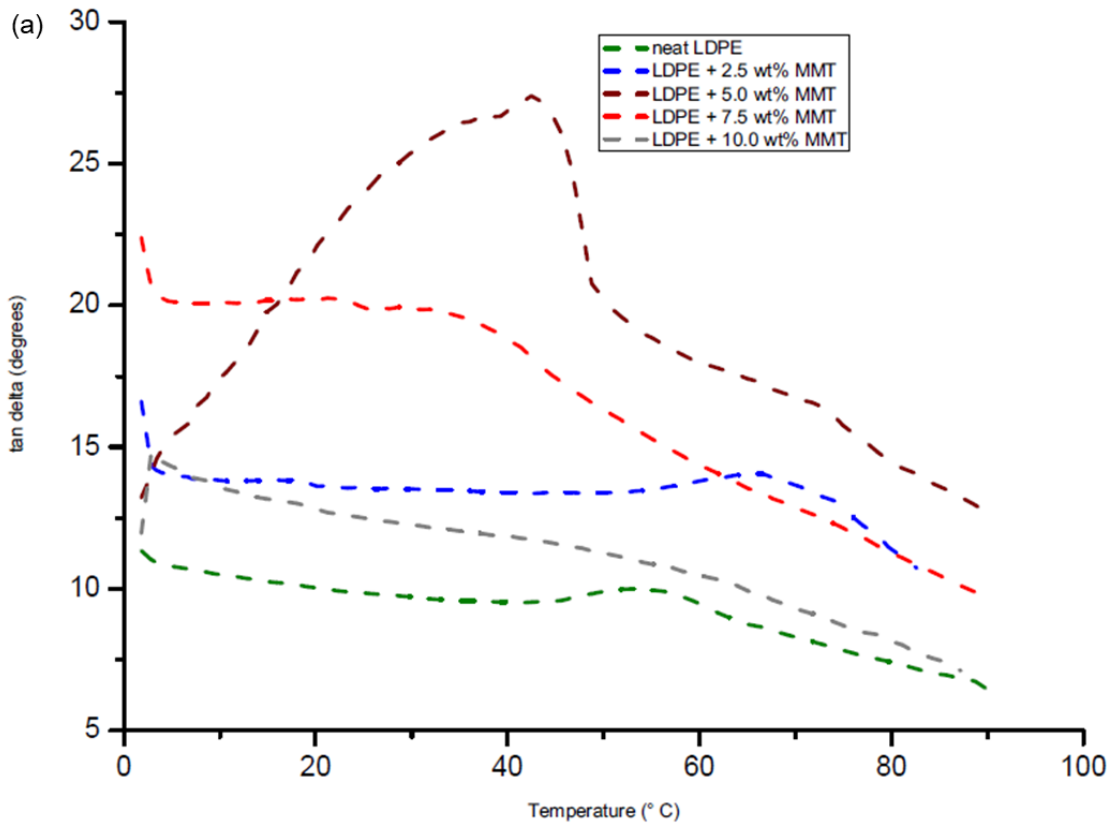


Figure 5. 12 Influence of applied shear stress on damping property of (a) neat LDPE and LDPE/MMT and (b) neat LDPE and LDPE/OBM slurry nanocomposites

The damping peak in both Figure 5.12 (a) and Figure 5.12 (b) showed an increased magnitude of $\tan \delta$ compare to that of neat LDPE. This graphical representation highlighted the balance between the elastic and viscous phases in the polymeric structures. The highest $\tan \delta$ peak of neat LDPE shifted to lower temperatures for both LDPE/MMT and LDPE/OBM slurry nanocomposites.

5.4. Conclusions

The objective of this study was to evaluate if the surfactants present in OBM slurry may improve the interfacial adhesion between OBM slurry and LDPE matrix and thus improve the thermo-mechanical properties of new materials. The tensile, flexural and the rheological properties were investigated. It was observed that addition of this novel filler was ineffective in improving mechanical properties and the mechanical strength of these new materials decreases significantly comparing the results with neat LDPE and LDPE/MMT nanocomposites as a benchmark standard. The morphology was studied in details in another study which is presented in next chapter highlighting the better dispersion capability of this filler after heat treatment compare to those of MMT which also shows similar distribution and dispersion mechanism when the filler was used in raw condition and without any treatment in this study. Furthermore, Observing tensile and flexural test data, it can be inferred that MMT intensifies the anisotropic properties in LDPE/MMT nanocomposites. OBM slurry develops homogeneous dispersion throughout the LDPE matrix and indicates non-structural delamination of clay platelets in LDPE matrix and thus showing isotropic properties in LDPE/OBM slurry nanocomposites. This statement is further validated by investigating shear rheology properties of LDPE/MMT and LDPE/OBM slurry nanocomposites. The storage modulus and loss modulus of LDPE/OBM slurry nanocomposites is higher than that of neat LDPE supports the anticipation of non-structural delamination of OBM slurry clay platelets in LDPE matrix.

Chapter 6: Structural and thermal degradation behaviour of reclaimed clay nano-reinforced low-density polyethylene nanocomposites

6.1. Introduction

Incorporating of fillers in polymer matrix is an interesting area of research in recent years (Moniruzzaman and Winey, 2006 and Potts et al., 2011). This addition of fillers is not limited to saving costs, it improves the mechanical, thermal and flammability properties too (Jordan et al., 2005). The addition of fillers is function specific (Sahoo et al., 2010 and Usuki et al., 2005) such as adding clay in enhancing physical, thermal, and mechanical properties of polymer matrix (Okada and Usuki, 2006). Polymer/clay nanocomposites have drawn an enormous interest recently due to significantly influencing on the physical, thermal, mechanical and flame retardancy properties of nanocomposites (Choudalakis and Gotsis, 2009; Gilman, 1999; Pappalardo, 2016 and Sheng et al., 2004). Findings from the literature highlight that layered silicate fillers provide the most successful results by acting as nano-filler precursors (Peeterbroeck et al., 2004; Sachse et al., 2012 and Fu and Qutubuddin, 2001). However, the literature findings are very limited identifying an information gap to understand the effect of this nanoclay in influencing the physical, thermal, mechanical, and flame retardancy properties of low-density polyethylene (LDPE) polymer in details.

The LDPE is produced on a large industrial scale and one of the most widely consumed polymer materials due to its excellent and desirable properties such as light weight, low cost, low dielectric constant and losses, high chemical resistance and easy manufacturing process (Costa et al., 2007 and Wen et al., 2012). However, the use of LDPE is still limited due to its inherent chemical nature (Zhao et al., 2005), poor thermal stability and flammability (Shah and Paul, 2006 and Zhang and Wilkie, 2003). Improvement of the thermal and flammability properties of synthetic polymeric materials such as LDPE is desirable to replace more traditional inorganic and natural polymeric materials (Zhao et al., 2005 and Kashiwagi et al., 2005). For this improvement, it is common practice to apply flame retardant additives within the polymer matrix. However, some flame retardant additives are considered harmful for the environment and hence have been phased out (Blum and Ames, 1977 and Lu and Hamerton, 2002). Considering the stringent environmental regulations and the need to improve thermal and flammability properties of the polymers, development of an alternative environmentally friendly flame-retardant material is becoming an area of polymer research interest (Sain et al., 2004).

Utilising of industrial by-products as filler in nanocomposite manufacturing is an interest area of research in recent years. Waste fly ash (Khan et al., 2011), waste iron ore tailing (Giri et al., 2014), waste pineapple leaves (Shih et al., 2017), coir (Haque et al., 2012), waste rubber powder (Wang et al., 2016), waste husks ash (Vlaev et al., 2009) etc are predominantly considered as a sustainable source of filler for improving different properties in polymers. In view of the different influential effects of clay minerals on mechanical, thermal and flame retardancy behaviour of nanocomposite materials, the recovery on significant amount of nanoclays in waste drilling fluids warrant investigations. This study inspired by the use of less explored LDPE polymer matrix incorporated with addition of reclaimed clay as nanofiller from oil-based mud waste in oil and gas industry.

In oil and gas industry, drilling through rock generally requires the use of some type of fluid to clear cuttings from the borehole formed by the drill. In some applications, the drilling fluid can be as simple as compressed air. However, when drilling is conducted to tap fossil fuel resources, the drilling fluid used (Caenn and Chillingar, 1996). The drilling fluid (also called drilling mud) is an essential component of the drilling process. In most deep drilling operation, oil-based fluids (OBMFs) are used instead of water-based fluids (WBFs) depending on the drilling conditions for efficient and cost-effective operations (Berthezene et al., 1999). It is quite common practice to use both WBFs and OBMFs in drilling the same well, with WBFs for shallow portion of the well and OBMFs for deep drilling (Zhong et al., 2011). The well drilling process produces waste drilling fluid composed of drill cuttings and spent mud waste. When the drilling process is finished, the drilling fluid waste is composed of drilling fluid, cuttings, water, oil and many additives. The sources of drilling wastes largely depend on the cuttings based on the geological condition of the borehole, the depth of the well, and the fluid used in the drilling operation (Onwukwe and Nwakaudu, 2012).

This study focus on the reclamation and usage of layered silicates from OBM waste, in particular their utilisation in engineering nanocomposite materials, specifically in low-density polyethylene (LDPE) matrix. Detailed investigations were performed to identify the dispersion characteristics of OBMFs in LDPE polymer matrix based on the thermal analysis results, which also lead to highlighting the rigid amorphous fraction (RAF), mobile amorphous fraction (MAF) and percentage of crystallinity along with the mechanical property study.

6.2. Experimental

6.2.1. Materials

The polymer material used in this chapter is described in section 3.2.1.

6.2.2. OBMFs manufacturing process

The development process of OBMFs used in this chapter to manufacture LDPE/OBMFs nanocomposites is mentioned in section 3.2.1.

6.2.3. LDPE/OBMFs nanocomposite manufacturing process

The manufacturing process to produce LDPE/OBMFs nanocomposites in this chapter is described in section 4.2.2 with exception of using OBMFs as filling material in this chapter whereas MMT and OBM slurry are used in section 4.2.2.

6.2. 4. Sample characterisation

To observe the morphology of OBMFs and their dispersion characteristics in LDPE polymer matrices, a cryogenic sampling technique was followed for sample preparation. The fractured samples were gold coated using sputter deposition for 2 minutes prior to the experiment. The fractured sample sections were observed using a Zeiss EVO LS10 Scanning Electron Microscope (SEM) with a magnification of 2.5 KX, 4.5 mm working distance and 25.00 kV accelerating potential. To determine the approximate elemental composition of the samples, energy dispersive x-ray analysis (EDXA) (Oxford Instruments INCA Energy) was carried out by following the same method which is described in section 4.2.4. The morphology of cryo-fractured samples were analysed using SEM.

The ATR-FTIR characterisation method used in this chapter is described in chapter 3.2.2.

The thermal analysis including DSC and TGA method used in this chapter is described in chapter 3.2.4.

The XRD analysis method used in this chapter is described in section 3.2.2.

Dynamic shear measurements are obtained in this chapter by following the method has described in section 5.2.5.

6.2.5. Testing

Tensile test method used in this chapter is described in section 5.2.4.

6.3. Results and discussion

6.3.1. Elemental analysis of nanocomposite materials using ATR-FTIR study and EDXA

The ATR-FTIR spectrum analysis of neat LDPE and its nanocomposite has been carried out and the resulting spectra are presented in Figure 6.1. Review to individual spectra is provided in **Figure B3** at Appendix B.

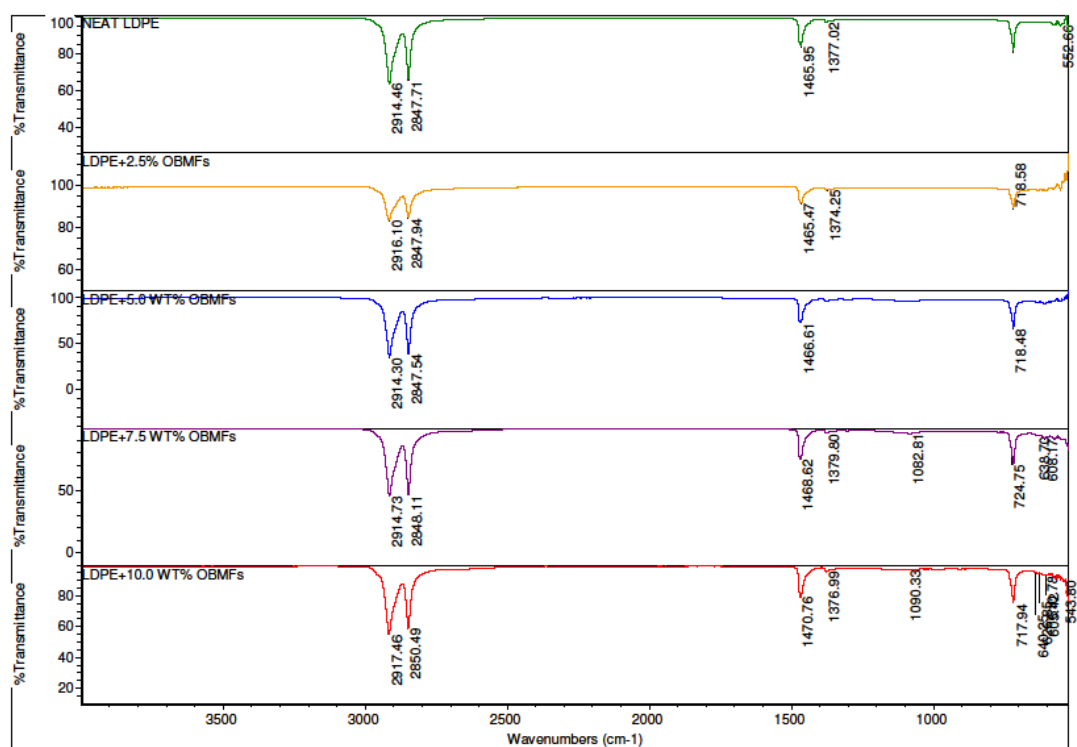


Figure 6.1 Comparison of ATR-FTIR common scale spectra of LDPE and its nanocomposite

A summary of ATR-FTIR peak assignments is presented in Table 6.1 based on information published in the literature (Zhao et al., 2005; Costa et al., 2005; Lu et al., 2006; Morlat-Therias et al., 2008 and Zanetti et al., 2004).

The chemical structure of LDPE/OBMFs nanocomposites has been identified by using ATR-FTIR which shows the IR transmittance peaks at 2914 cm^{-1} and 2850 cm^{-1} corresponding to CH_2 stretching, the peaks at 1465 cm^{-1} and 718 cm^{-1} representing to the bending and rocking of CH_2 , respectively. The peaks at 1377 cm^{-1} highlight the presence of interlayer carbonate

ions. The peak at 1082 cm^{-1} represents the stretching of Si-O, and the peaks at 640 cm^{-1} , 630 cm^{-1} and 608 cm^{-1} correspond to the oxide bonds of metals such as Si, Al, Mg etc. The peak at 580-525 cm^{-1} represents the crystalline forms of rare earth oxides which is observed in LDPE nanocomposite samples with 5.0, 7.5 and 10.0 wt% OBMFs content. It can articulate that the peaks at lower bands between 640-540 cm^{-1} correspond to the chemical structure formed by different minerals present in the OBMFs nanoclay.

Table 6.1 ATR-FTIR peak assignments of LDPE and its nanocomposites

Wave number (cm^{-1})	Assignments
2914	CH_2 stretching
2850	CH_2 stretching
1465	bending of CH_2
1377	inter layer carbonate ions
1082	stretching of Si-O
718	rocking of CH_2
640, 630, 608	oxide bands of metals like Si, Al, Mg, etc.
525-580	$\delta(\text{M-O-M})$ clay

To identify the elemental composition and explain the addition of OBMFs in the LDPE polymer matrix, Energy Dispersive X-ray (EDXA) analysis was carried out as presented in Figure 6.2 (a-e).

Figure 6.2 (a) (b) (c) (d) and (e) show the EDX spectra and also the elemental composition of neat LDPE, LDPE with 2.5 wt% OBMFs, LDPE with 5.0 wt% OBMFs, LDPE with 7.5 wt% OBMFs and LDPE with 10 wt% OBMFs nanocomposite. Elemental analysis of this filler has been reported in Naxos 2018 conference proceedings (Siddique et al., 2018) which showed the presence of O, Na, Al, Si, S, Cl, K, Ca, Fe and Ba. The EDXA study here also confirmed the addition of different elements exist in clay minerals distributed in the LDPE matrix, as highlighted in Figure 6.2. The lower limit of detection of EDXA is 0.01wt%.

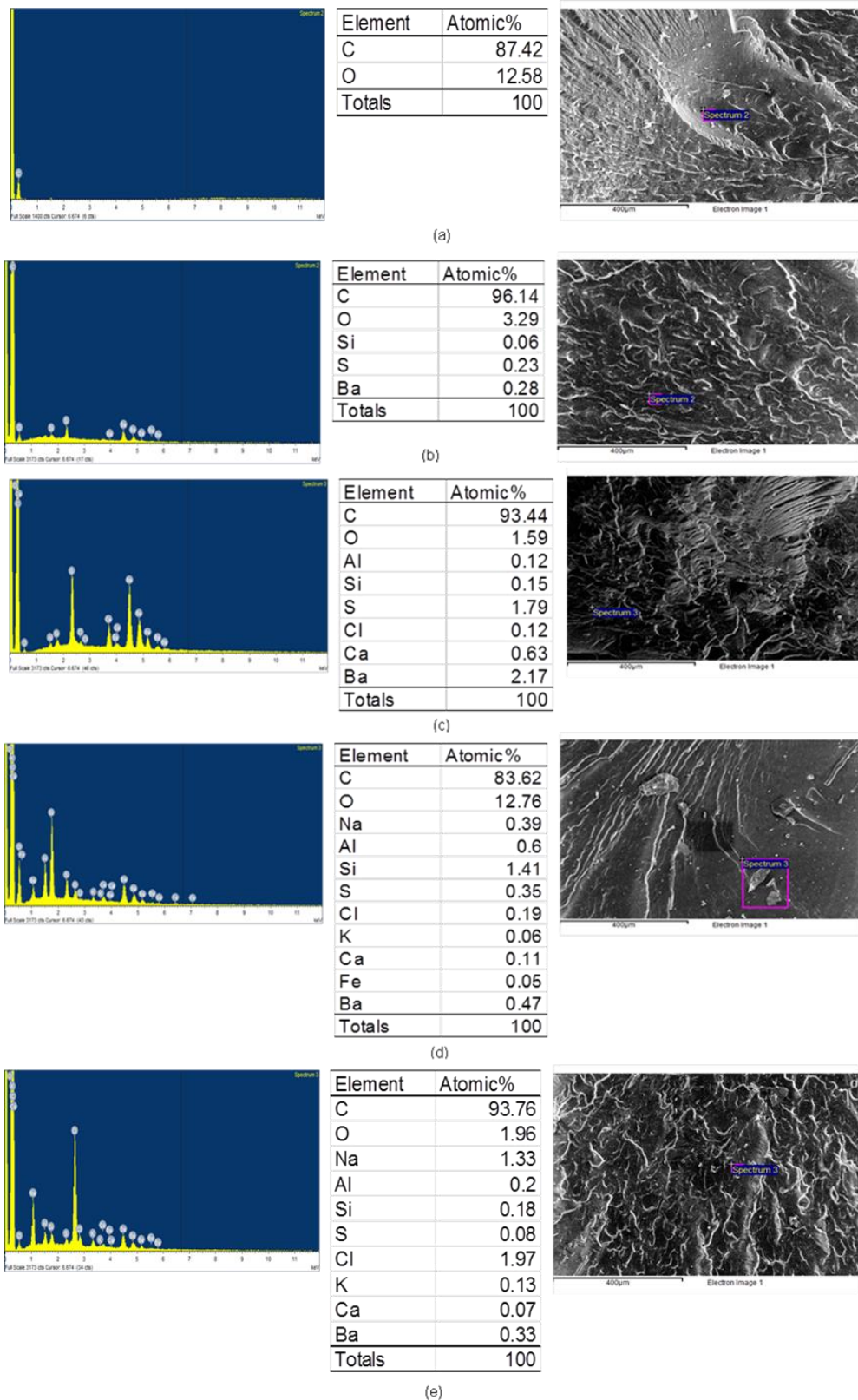
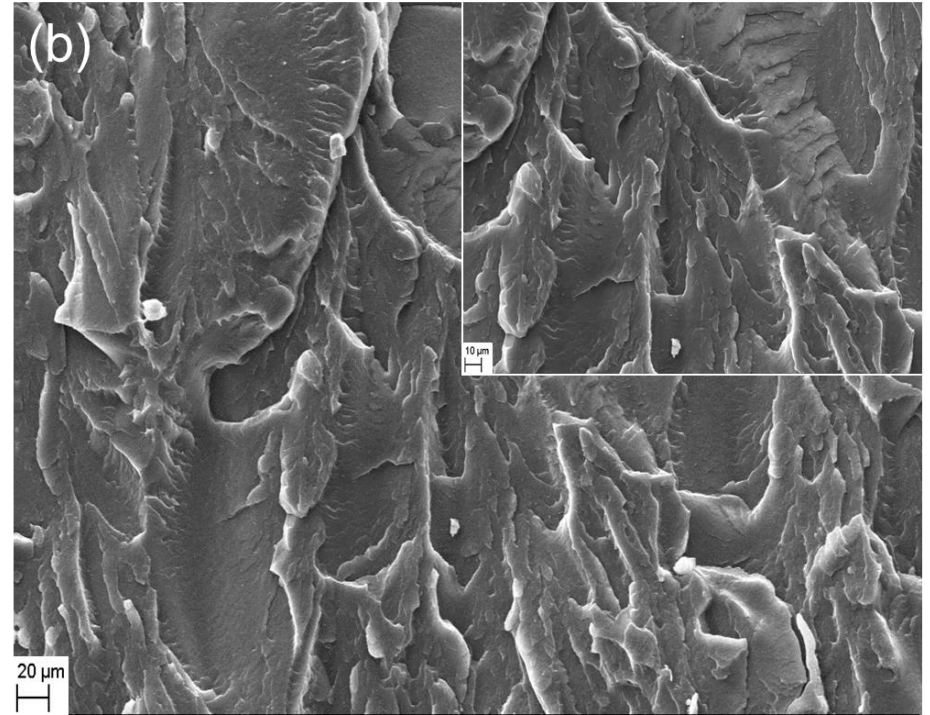
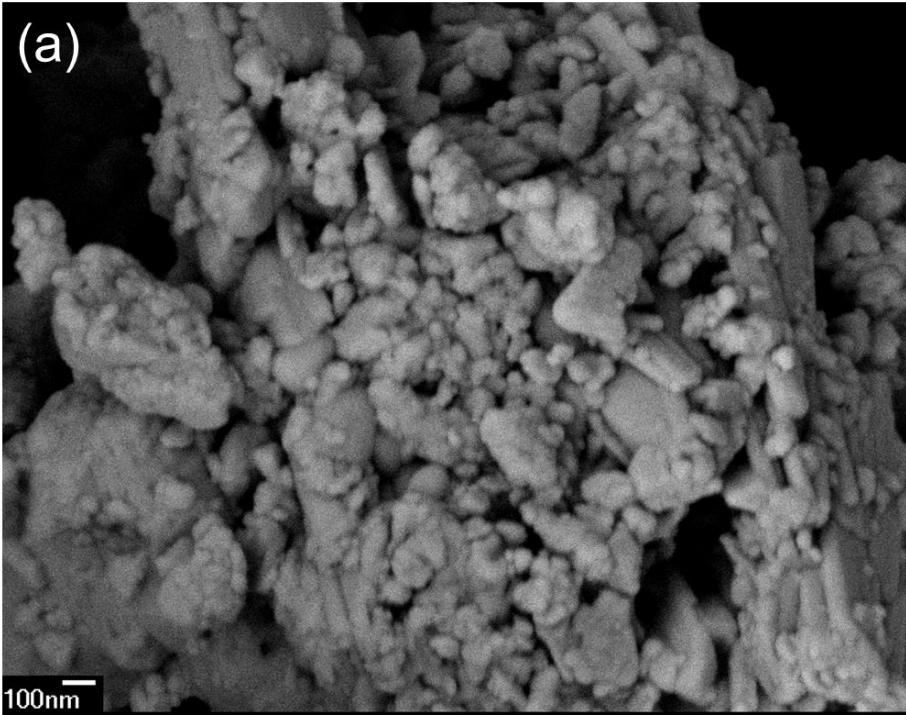
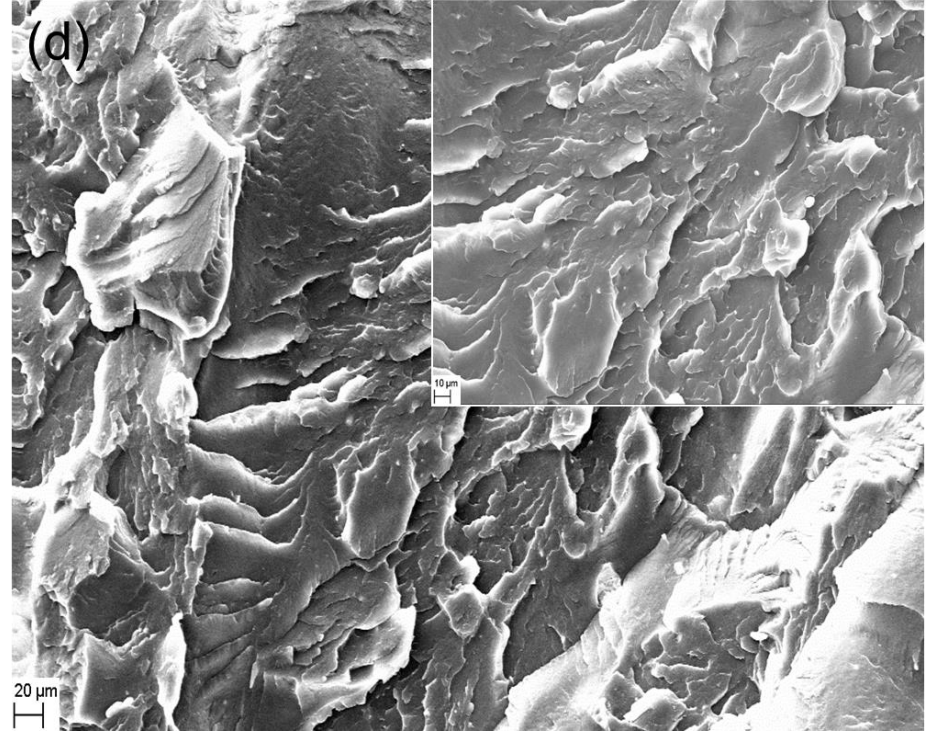
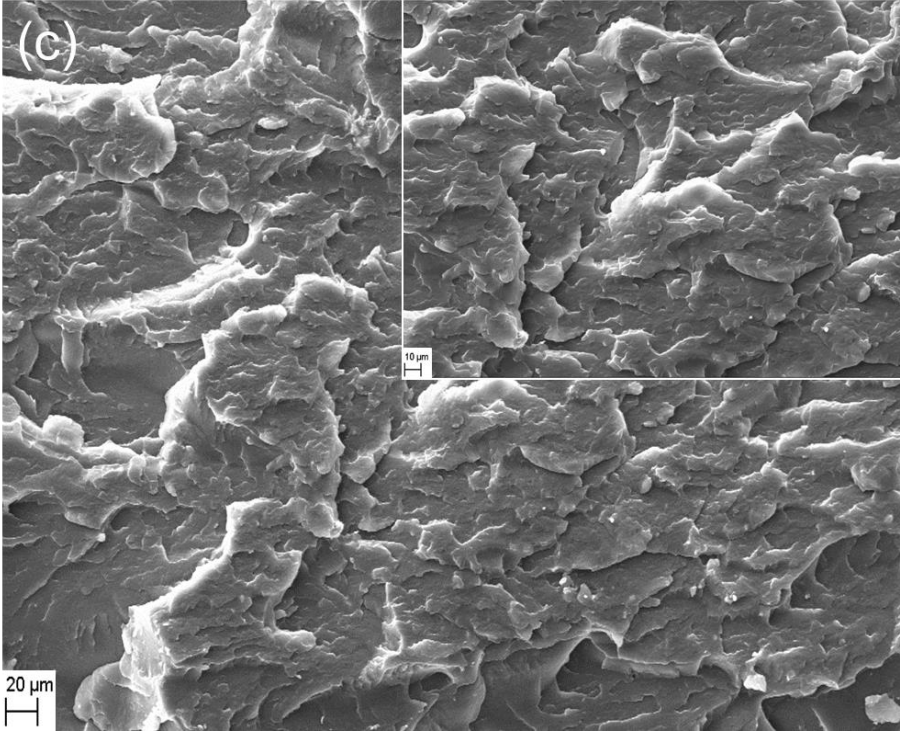


Figure 6.2 EDXA spectra of (a) LDPE; (b) LDPE+2.5 wt% OBMFs; (c) LDPE+5 wt% OBMFs; (d) LDPE+7.5 wt% OBMFs and (e) LDPE+10 wt% OBMFs

6.3.2. Morphology study of OBMFs and LDPE/OBMFs nanocomposite materials

To identify the surface topography of reclaimed clay particles from oil based mud waste and LDPE/OBMFs nanocomposite, morphological studies were carried out by using SEM. The SEM micrographs were used to analyse the changes in morphological structure of OBMFs in LDPE matrix. Figure 6.3 (a) shows the presence of tightly stacked clay platelets with size ranges up to 1000 nm. Figure 6.3 (b) shows the cavity and uneven surfaces due to the cryogenic fracture of the sample. However, Figure 6.3 (c) shows that there is loosely dispersed OBMFs in the LDPE matrix which has higher concentration of OBMFs, noticeable in the LDPE matrix in Figure 6.3 (d). Figure 6.3 (e) shows a mix of agglomeration of OBMFs and local scattered filler in LDPE matrix indicating intercalation of clay platelets. However, Figure 6.3 (f) shows poor dispersion of OBMFs with a remarkable agglomeration of OBMFs in the LDPE matrix.





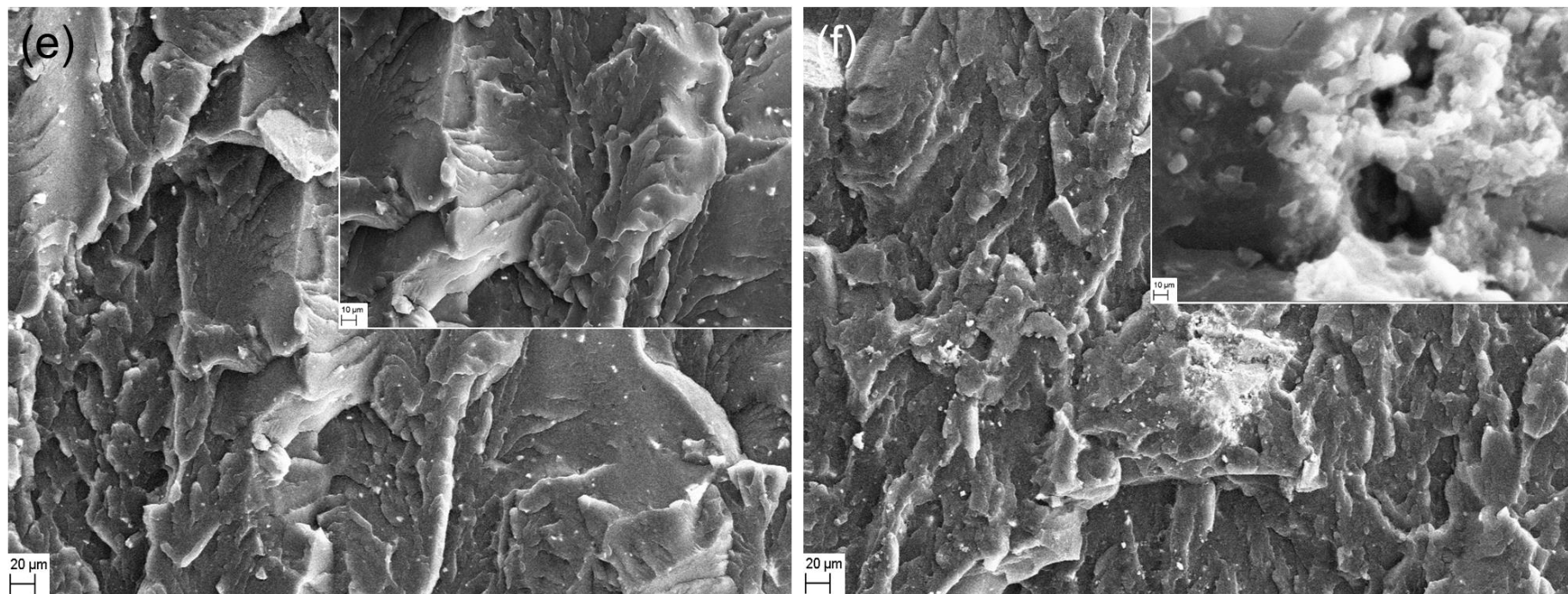


Figure 6.3 SEM images of (a) OBMFs; (b) neat LDPE; (c) LDPE with 2.5 wt% OBMFs; (d) LDPE with 5.0 wt% OBMFs; (e) LDPE with 7.5 wt% OBMFs and (f) LDPE with 10.0 wt% OBMFs

6.3.3. Micro-structure by XRD and TEM

The XRD analyses are illustrated in Figure 6.4 addressing the diffractograms at (a) wide angle X-ray diffraction (WAXD); (b) small angle X-ray diffraction; (c) comparing XRD patterns between MMT (as a reference) and OBMFs and (d) illustrating a few extra peaks for the LDPE polymer matrix potentially caused by adding these phases through OBMFs addition to the polymer matrix.

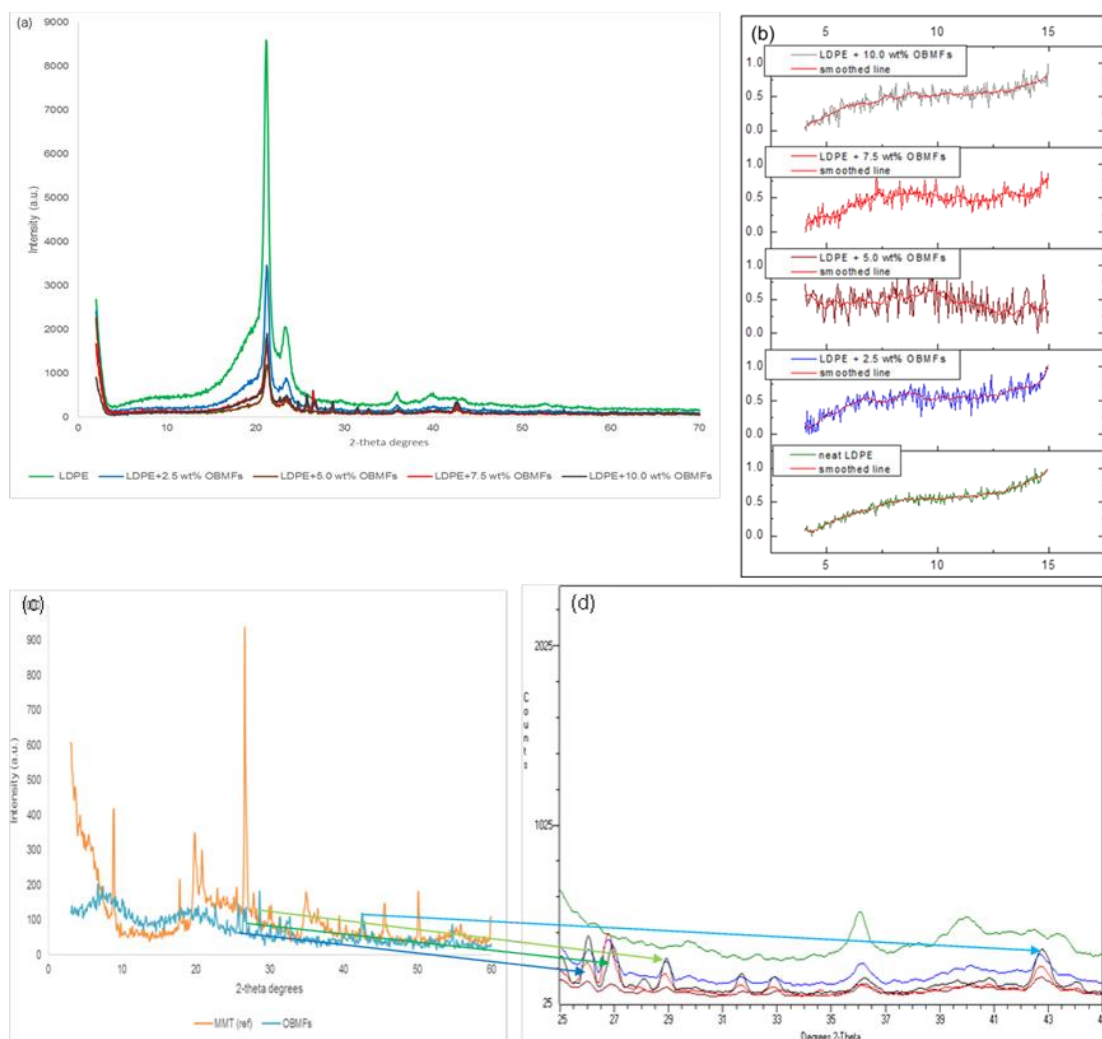


Figure 6.4 Different XRD patterns of LDPE and its nanocomposites at (a) WAXD; (b) SAXD; (c) WAXD patterns of MMT and OBMFs and (d) potential peak initiation in LDPE polymer matrix due to addition with OBMFs

In Figure 6.4, XRD patterns of LDPE and its nanocomposites are reported. A clear shift of the diffraction peaks of the planes (001) of OBMFs towards lower angles for the LDPE/OBMFs nanocomposites is noted. However, it can be seen that the basal spacing of

OBFs increases with different nanocomposites in different ratios. The d_{001} spacings were calculated using Bragg's law $n\lambda = 2d\sin\theta$, where λ is the wavelength of X-ray radiation used in the experiment, d corresponds to the distance between diffraction lattice planes and θ is the half of the diffraction angle. Analysing different peaks from these XRD data, it can be highlighted that the basal spacing increases with the increase of filler contents in nanocomposites. The diffraction peak of OBFs was observed at $2\theta = 11.40^\circ$ which corresponds to a d -spacing of 7.75 Å. The d -spacings of LDPE with 2.5 wt% and 5 wt% OBFs nanocomposites were identified at 9.6° and 5.6° which corresponds to the value of 9.02 Å and 15.77 Å, respectively. Moreover the d -spacings of LDPE with 7.5 wt% and 10 wt% OBFs nanocomposites were determined as 9.06 Å and 16.06 Å.

Analysing the d -spacing data of the corresponding peaks of reclaimed clay and LDPE/OBFs nanocomposites, it can be highlighted here that the trend of d -spacings among OBFs and LDPE/OBFs nanocomposites are not consistent. However, the peak positions of LDPE with 5 wt% and 10 wt% OBFs nanocomposites are noticeable. In both of these materials, the peaks of the planes (001) are shifted towards lower angles, which corresponds to the highest d -spacing value of these materials. This finding also agreed with the findings of the SEM (in Figure 6.3) study. Based on this SEM study, it is important to mention here that LDPE with 10 wt% OBFs nanocomposites indicates both local exfoliation and also shows agglomeration of clay minerals in the morphology study. Considering the data obtained in this XRD analysis, it can be inferred that OBFs is exfoliated in LDPE with 5 wt% and apparently OBFs might locally exfoliated in the LDPE polymer matrix. Transmission electron microscopy analysis is believed to clarify the nanomorphology in more detail in the next section.

TEM analyses were carried out to validate the results obtained from thermal and morphology analyses. It can be highlighted in Figure 6.5 (a) that the clay plates are barely connected with each other, representing the exfoliation nature of the clay platelets which is also noticeable in Figure 6.5 (b). Figure 6.5 (b) clearly shows the tendency of dispersion characteristic from exfoliation towards intercalation. It can be referred as the exfoliation-intercalation interphase.

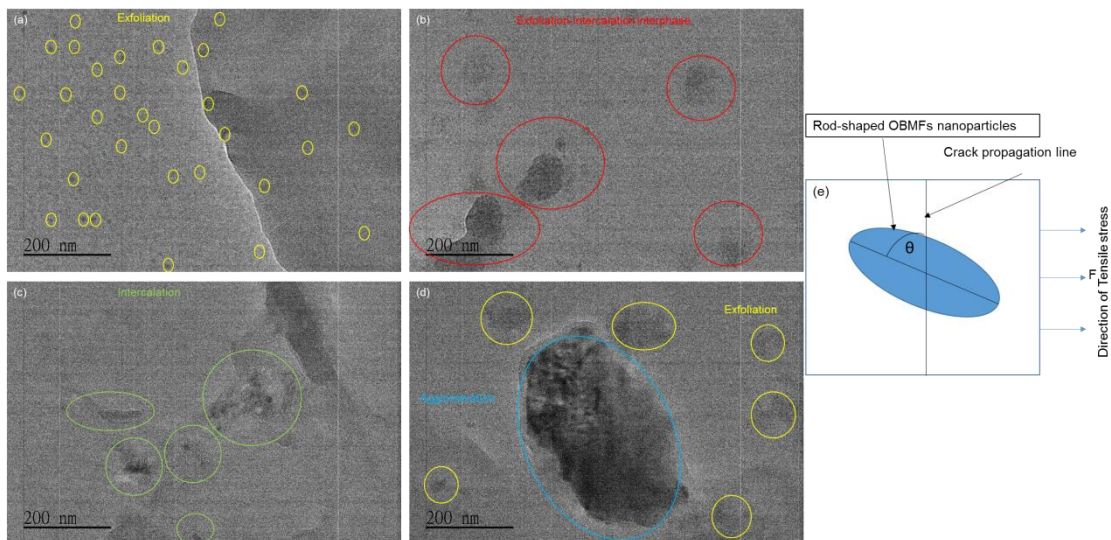
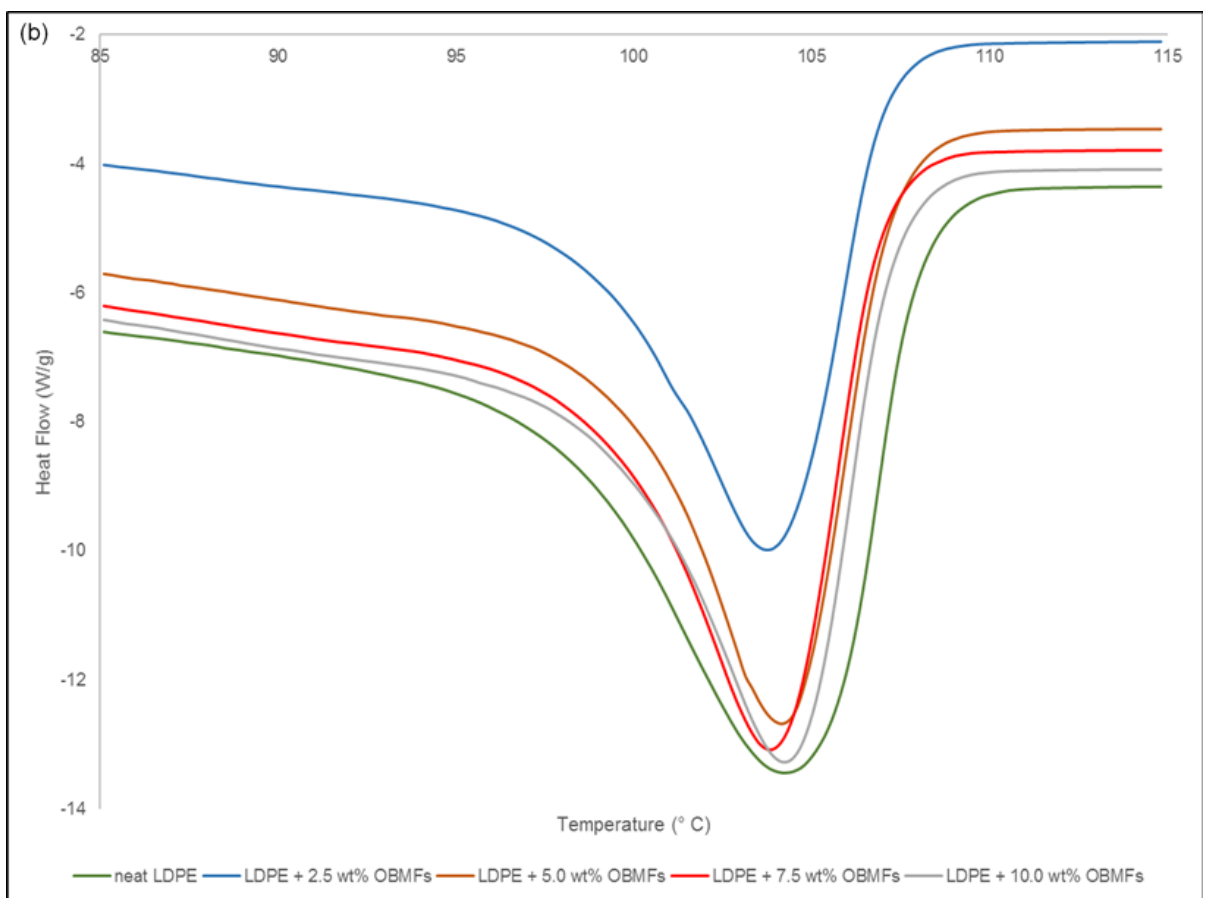
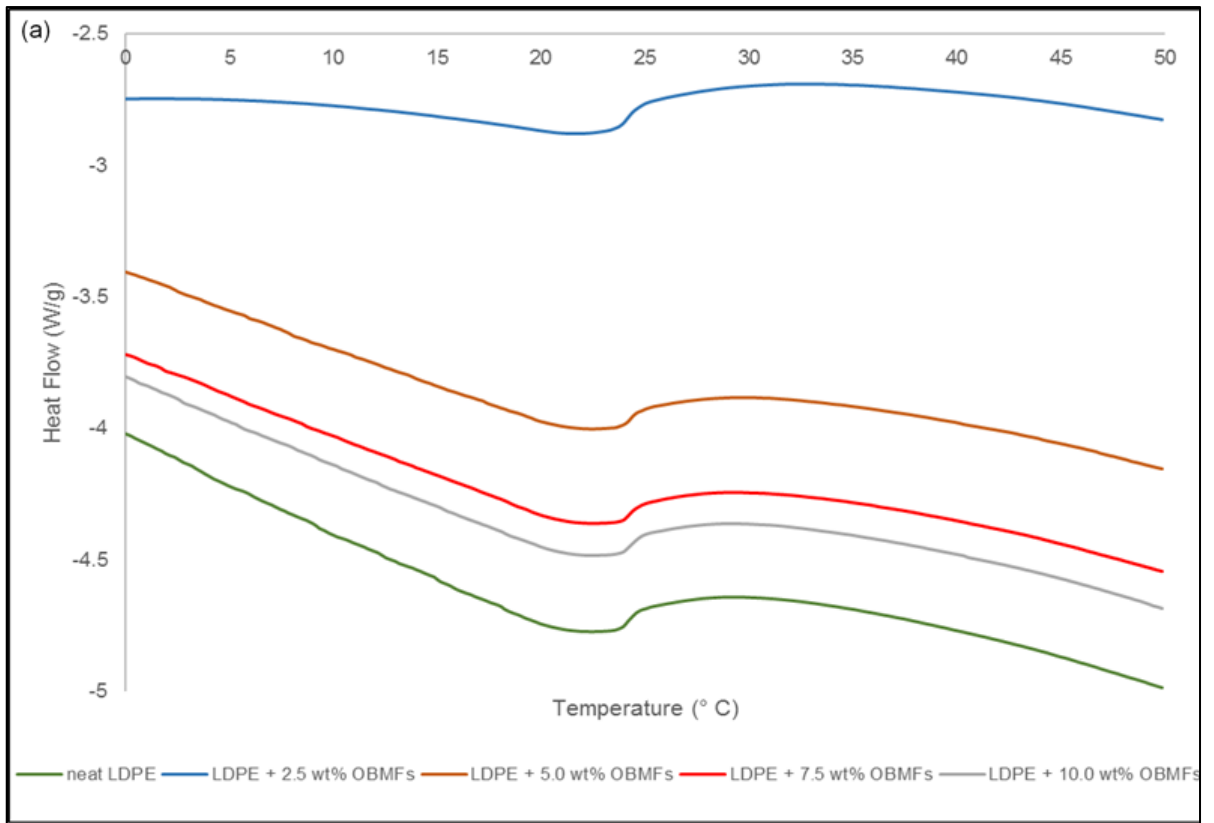


Figure 6.5 TEM micrographs of (a) LDPE with 2.5 wt% OBMFs; (b) LDPE with 5.0 wt% OBMFs; (c) LDPE with 7.5 wt% OBMFs ;(d) LDPE with 10.0 wt% OBMFs nanocomposite and (e) schematic diagram of nanoparticles orientation and tensile stress direction

In Figure 6.5 (c), the loose but structured network of clay platelets is visible which indicates the intercalation nature of these platelets. However, the dark shades and spots in Figure 6.5 (d) highlight the agglomeration of platelets, although a few light spots indicate the local exfoliation of clay platelets.

6.3.4. Thermal properties by DSC and TGA

Non-isothermal DSC studies were conducted to elucidate the influence of novel filler OBMFs on the thermal degradation behaviour of nanocomposite materials. Different phases of degradation stages are shown in Figure 6.6.



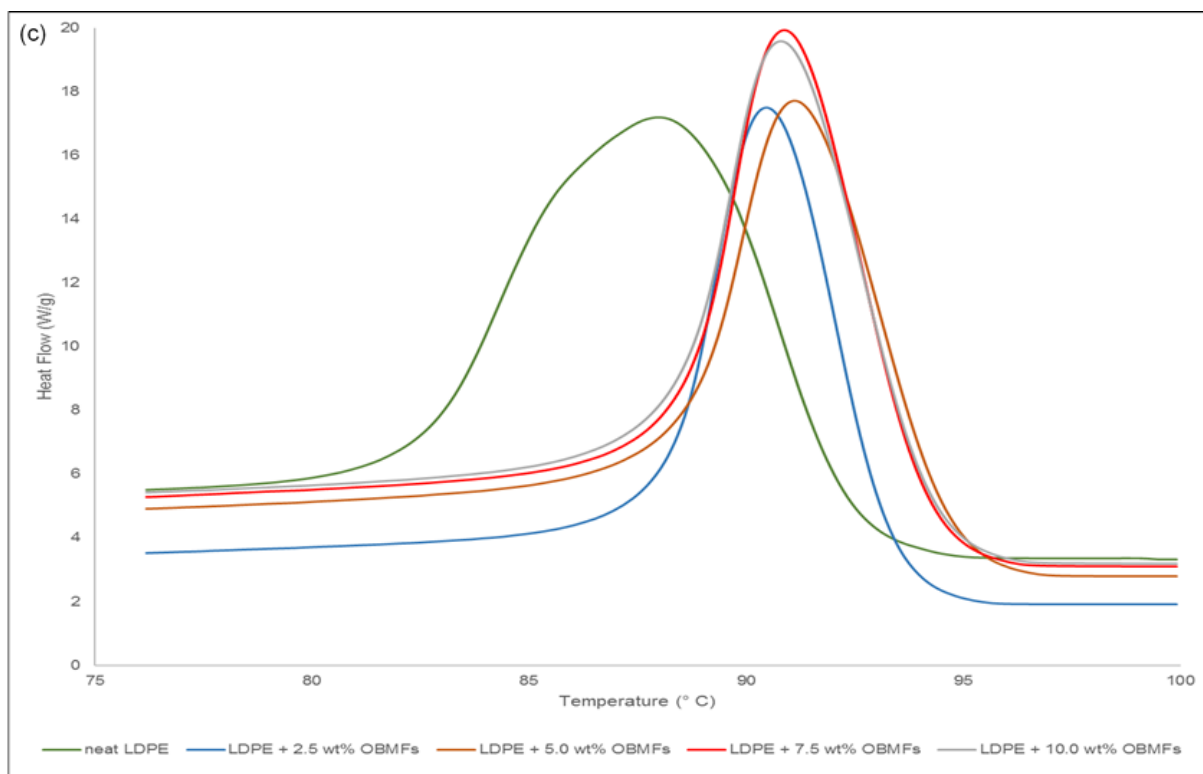


Figure 6.6 DSC thermograms of LDPE and its nanocomposites at (a) T_g; (b) T_m and (c) T_c

Analysing the DSC thermograms in Figure 6.6 (a), it can be highlighted that there is not any significant change in the glass transition temperature of these nanocomposite materials compared to that of neat LDPE polymer. There is a minor change in glass transition temperature (less than 1°C) in LDPE with 2.5 wt% OBMFs nanocomposite. However, the melting point remains almost unchanged, only a fraction of a degree celsius change is noticeable in the Figure 6.6 (b). Figure 6.6 (c) shows a consistent higher recrystallization temperature compares to that of LDPE. These three main heat flow curves in thermograms are discussed in more detail, addressing the potential different thermal properties possessed by these materials.

There is a distinctive peak present in neat LDPE and its nanocomposites in Figure 6.6 (b) which represents the melting behaviour of alpha phase crystals associated with the materials. There is not any associated heat curve shoulder noticeable corresponding to the absence of other crystalline phases or the other phases might be very weak compared to the presence of alpha phase in the materials. Considering the thermograms in melting peaks representing the heat capacity value of LDPE and its nanocomposites, the % of crystallinity can be identified using the following equation:

$$\% \text{ of crystallinity} = [\Delta H_m - \Delta H_c] / \Delta H_m^0 * 100\% \quad (6.1)$$

Where ΔH_m is the heat of melting, ΔH_c the heat of cold crystallisation which is 0 as not present in this experiment ($\Delta H_c=0$ in this case), and ΔH_m^0 is a reference value if the polymer were 100% crystalline. All the units are in J/g and the value of ΔH_m^0 is 293 J/g (Gaska et al., 2017). The % of crystallinity value of LDPE and its nanocomposites are presented in Table 6.2.

Table 6.2 Structural composition and thermal properties details of LDPE and its nanocomposites

Material	% of crystallinity	RAF= (1-MAF-CF)	MAF ($\Delta C_p / \Delta C_{p(am)}$)	Specific heat capacity (C_p) JK ⁻¹ kg ⁻¹
LDPE	16.71	0.13	0.70	4828
LDPE+2.5 wt% OBMFs	13.00	0.29	0.58	3990
LDPE+5.0 wt% OBMFs	12.48	0.28	0.59	3891
LDPE+7.5 wt% OBMFs	12.48	0.23	0.64	4160
LDPE+10.0 wt% OBMFs	11.07	0.31	0.58	3794

It is clearly evident that there is a decreasing trend of % of crystallinity as the percentage of filler content increases. The decreasing trend in the % of crystallinity degree of the nanocomposite materials can be explained by the presence of filler contents in polymer matrix, which can hinder the motion of the polymer chain segments and inhibit crystal growth. The specific heat capacity value of LDPE and its nanocomposites have been identified by analysing the thermograms in Figure 6.6 (c). The specific heat capacity value can be determined by the following equations:

$$C_p = (\delta Q / \delta T) \quad (6.2)$$

$$C_p = (\delta Q / \delta t) \times (\delta t / \delta T) \quad (6.3)$$

Where C_p is the heat capacity in Joules per Kelvin (JK⁻¹), Q is heat energy in Joule and T is the temperature denoted as °C or K. $\delta Q / \delta t$ represents the heat flow and $\delta t / \delta T$ corresponds to

reciprocal heating rate. By using these two equations, the analysed specific heat capacities of neat LDPE and its nanocomposites are identified, as presented in Table 6.2.

The heat capacity data presented in Table 6.2 shows the negative effects of OBMFs in polymer matrix. However, LDPE with 2.5 and 7.5 wt% OBMFs show higher heat capacity property in nanocomposites, LDPE with 10 wt% shows the lowest heat capacity indicating a superior thermal conductivity property of this material among different nanocomposites. The heat capacity value decreases about 21% in LDPE with 10 wt% OBMFs nanocomposite.

In addition to the SEM observation, it is also important to understand that different interphases exist between LDPE and layered silicate nanocomposites. It is believed that there are two interphases present in LDPE polymer matrix and layered silicates in OBMFs. One of these interphases represents the interphases between the crystal fraction and amorphous fraction of the polymer matrix and the other is between filler and polymer matrix (Wurm et al., 2010). To understand the thermal degradation behaviour of any nanocomposite material, it is important to identify the different phases present in the polymer matrix predominantly crystalline and amorphous phases exist in the material. Analysing the heat capacity value, C_p in glass transition temperature, mobile amorphous fraction (MAF) can be identified by the following equation:

$$MAF = \Delta C_p / \Delta C_{pamp} \quad (6.4)$$

Where $\Delta C_p / \Delta C_{pamp}$ are the heat capacity increments at the glass transition temperature of LDPE and its nanocomposites and the pure amorphous LDPE polymer, respectively. Using the MAF value, rigid amorphous fraction (RAF) can also be identified by the following equation:

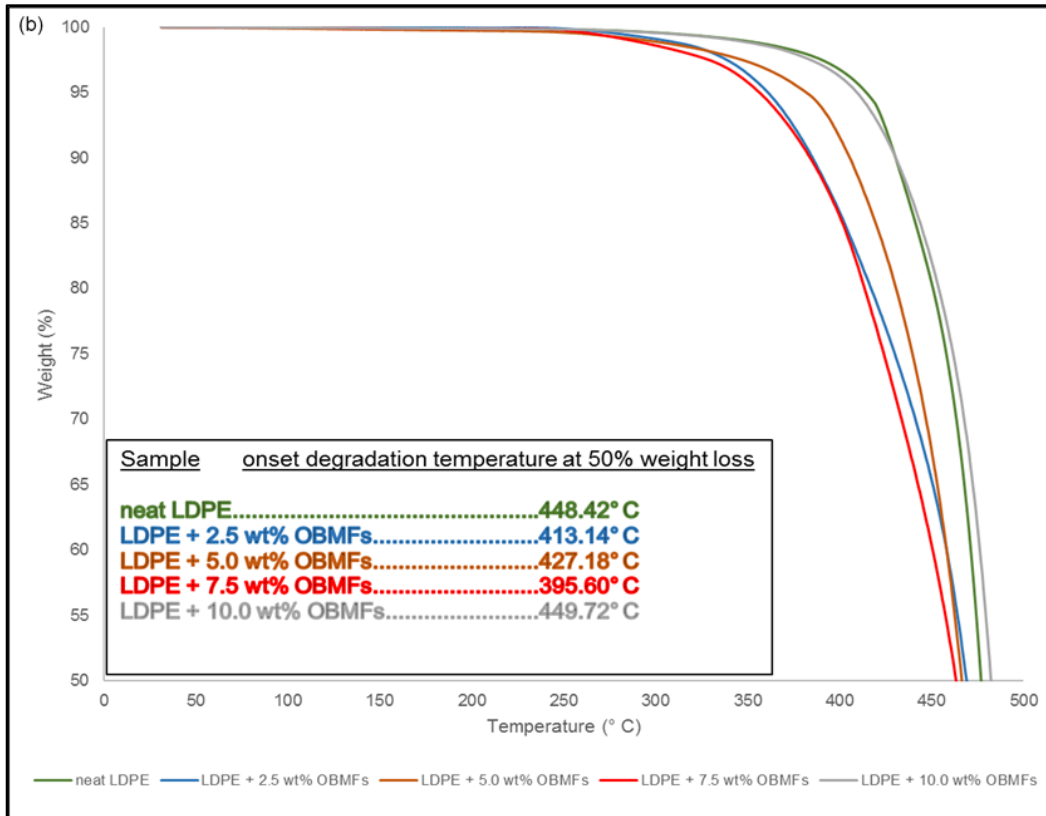
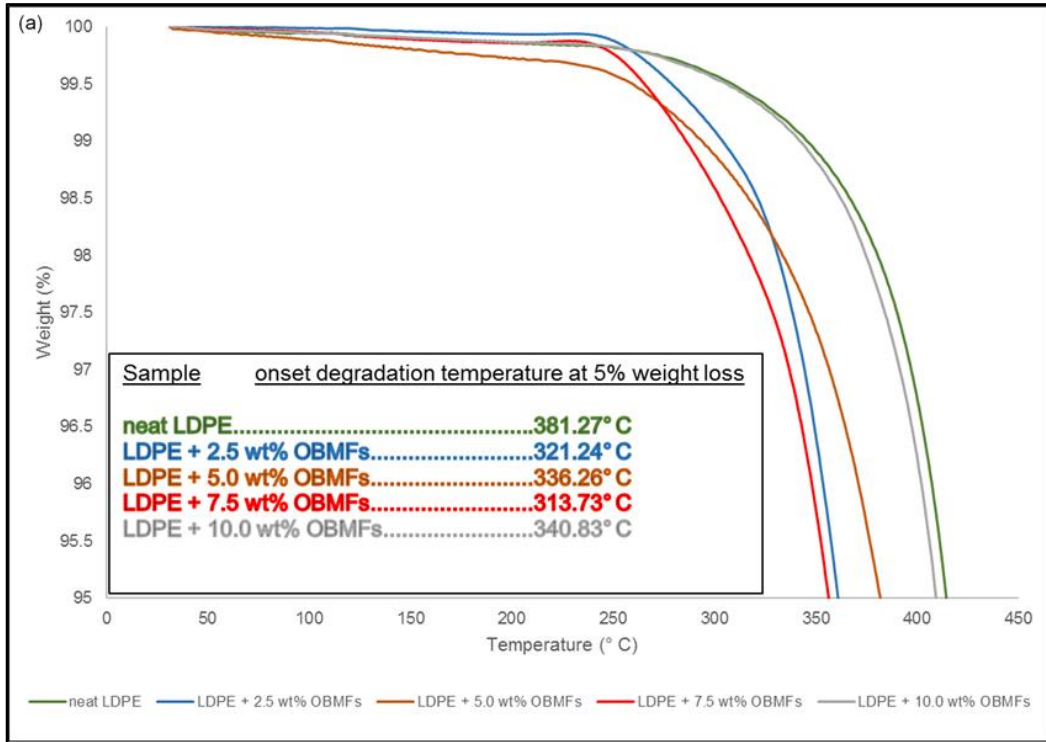
$$RAF = 1 - crystallinity - \Delta C_p / \Delta C_{pamp} \quad (6.5)$$

Using the equations (6.4) and (6.5), the MAF and RAF values are identified and presented in Table 6.2.

It can be highlighted here that although RAF is non-crystalline, it does not participate in the glass transition due to the parts of the molecules are fixed due to the immobilisation of molecules in the polymer chain (Wurm et al., 2010 and Craig et al., 2001). The crystalline fraction in polymer chain, inorganic based filler (OBMFs) (assumed mostly in crystalline phase) and RAF incurs immobilisation in the polymer chain which is evident in the data presented in Table 6.2. It is also manifested based on the data presented in Table 6.2 that the RAF value is increased more than 100% in nanocomposites compared to that of neat

LDPE. The reason can be explained that the incremental filler content acts as a nucleating agent and increases the nucleation ratio.

Thermal degradation of LDPE/OBMFs nanocomposites has been studied under a dry nitrogen environment using a TA instrument TGA Q500.



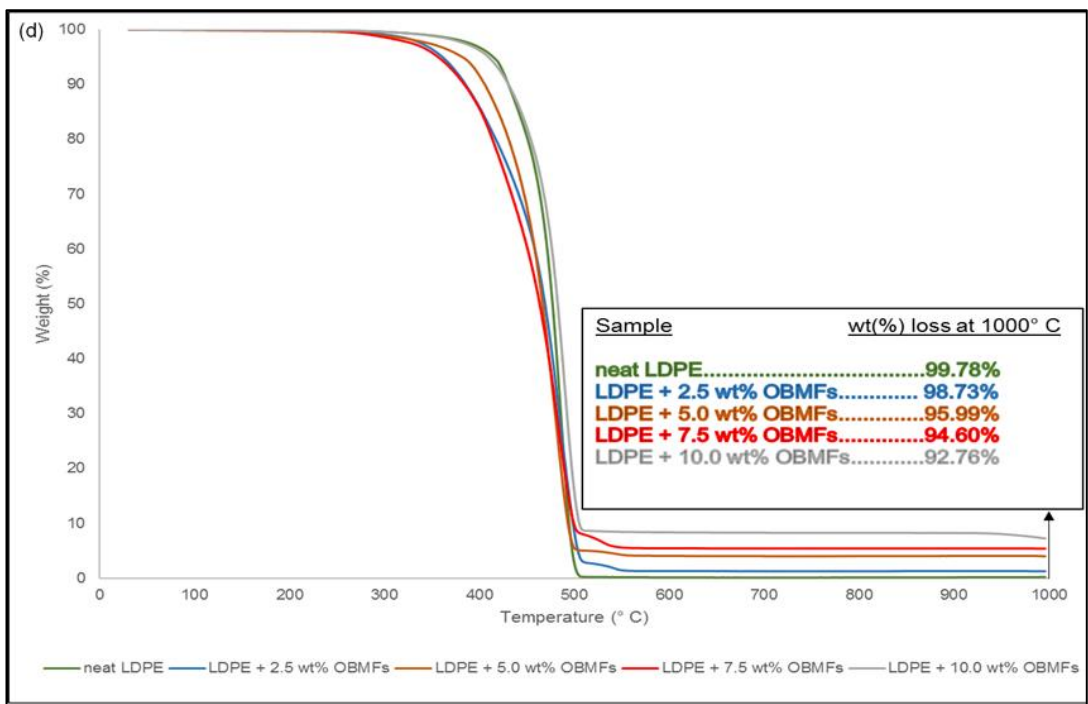
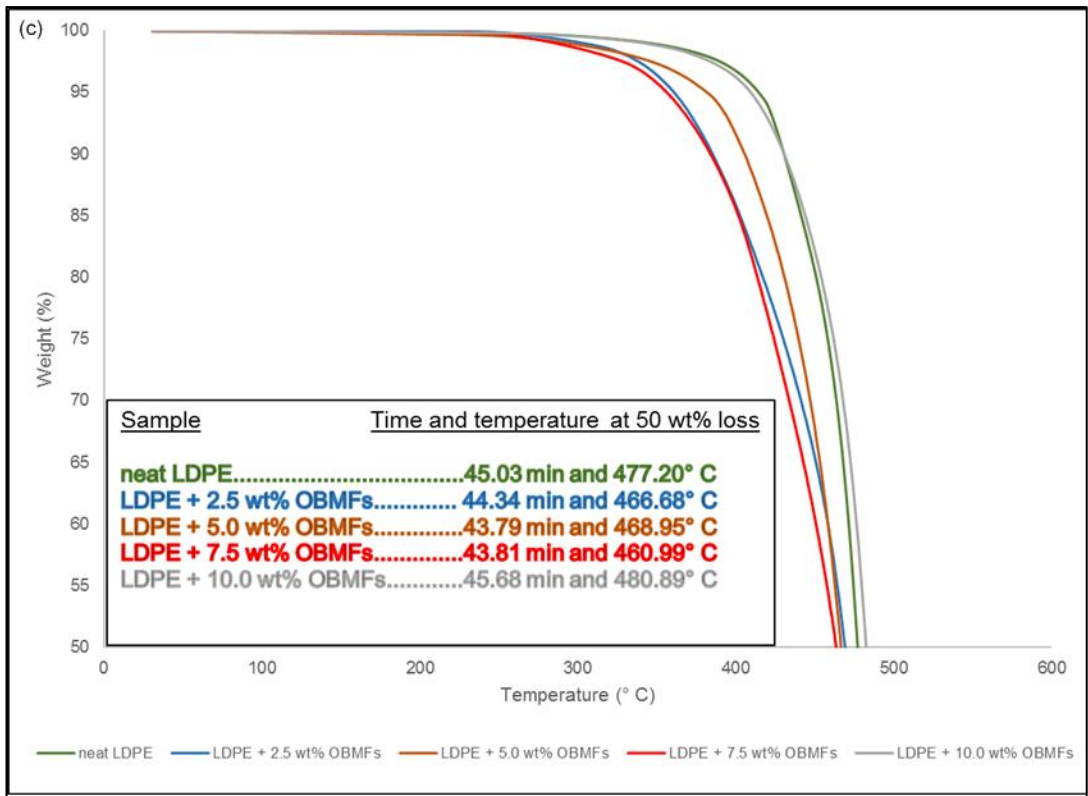


Figure 6.7 TGA thermograms of LDPE and its nanocomposites at: (a) onset degradation at 5% weight loss; (b) onset degradation at 50% weight loss; (C) D-half (50% weight loss) time and (d) residue at 1000°C

The degradation scenario of these materials at different heating stages are analysed and the key findings are presented in Table 6.3.

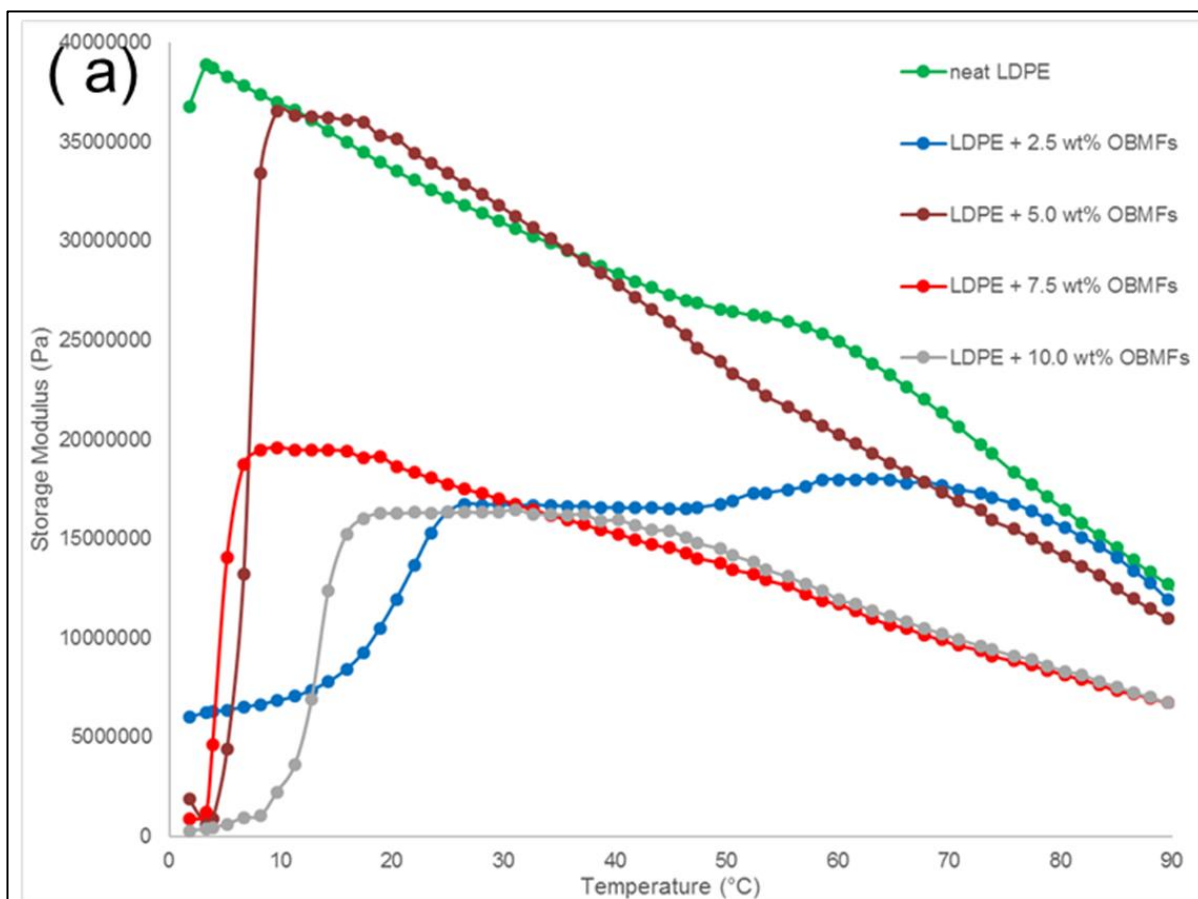
Table 6.3 TGA analysis at different decomposition stages of LDPE and its nanocomposites with different clay contents

Material	T _{D5%} (°C)	T _{D50%} (°C)	D 1/2 Time	Residue (% wt) at 1000°C
LDPE	381.27	448.42	45.03	0.22
LDPE+2.5 wt% OBMFs	321.24	413.14	44.34	1.27
LDPE+5.0 wt% OBMFs	336.26	427.18	43.79	4.01
LDPE+7.5 wt% OBMFs	313.73	395.60	43.81	5.40
LDPE+10.0 wt% OBMFs	340.83	449.72	45.68	7.24

The onset degradation temperature of these materials is identified at weight % losses of 5% and 50%. In both cases, LDPE with 10 wt% OBMFs shows the highest onset degradation temperature among the nanocomposites with different wt% filler contents which represents LDPE with 10 wt% OBMFs nanocomposite possessing the highest thermal stability. However, the thermal stability property is significantly affected in LDPE with 7.5 wt% OBMFs. Considering the lowest temperature at D-half (50% weight loss), the presence of peak assignments representing amorphous phase in FTIR analysis and heat capacity value from DSC analysis, it can be inferred here that LDPE with 7.5 wt% OBMFs possesses a good heat capacity property. It is also noticeable that the addition of OBMFs into LDPE matrix significantly reduces the thermal stability of the material based on T_{D5%} and T_{D50%} data. However, the degradation trend is distinctly noticeable as it does not show any significant changes of weight loss % until 300°C. Degradation mainly occurred between 300-500°C and the poor thermal stability of nanocomposites is clearly visible except for LDPE with 10 wt% OBMFs nanocomposite. In Figure 6.7 (c), LDPE with 10 wt% OBMFs shows the longest time needed to reach the D-half point which also indicates superior thermal stability property among the samples. It is also manifested in this figure that at this D-half point LDPE with 10 wt% OBMFs shows the highest temperature which gives an indication of improving of thermal conductivity property of this material. It is also verified with the lowest heat capacity value obtained from DSC study. It is articulated here that the incremental filler contents may have a strong influence on the thermal stability of LDPE/OBMFs nanocomposites. Filler contents below 10 wt% reduce the thermal stability of the materials whereas LDPE with 10 wt% possesses the best thermal stability and thermal conductivity properties among the nanocomposites with different wt% filler content.

6.3.5. Dynamic mechanical properties

The storage modulus (E') represents the load bearing capacity of a material. The effect of OBMFs in influencing this storage modulus is graphically enumerated in Figure 6.8 (a). It is noticeable from Figure 6.8 (a) that there was a significant decrease in the storage modulus of LDPE/OBMFs nanocomposites compares the storage modulus of neat LDPE matrix. This is perhaps due to the decrease in the stiffness of LDPE matrix with the reinforcing effect of the fillers prone to decrease in stress transfer at the interfacial surface. As noticeable in Figure 6.8 (a), the storage modulus decreased drastically with the increase in temperature and the degree of storage modulus drop was significant in the temperature regions between 20 and 70°C.



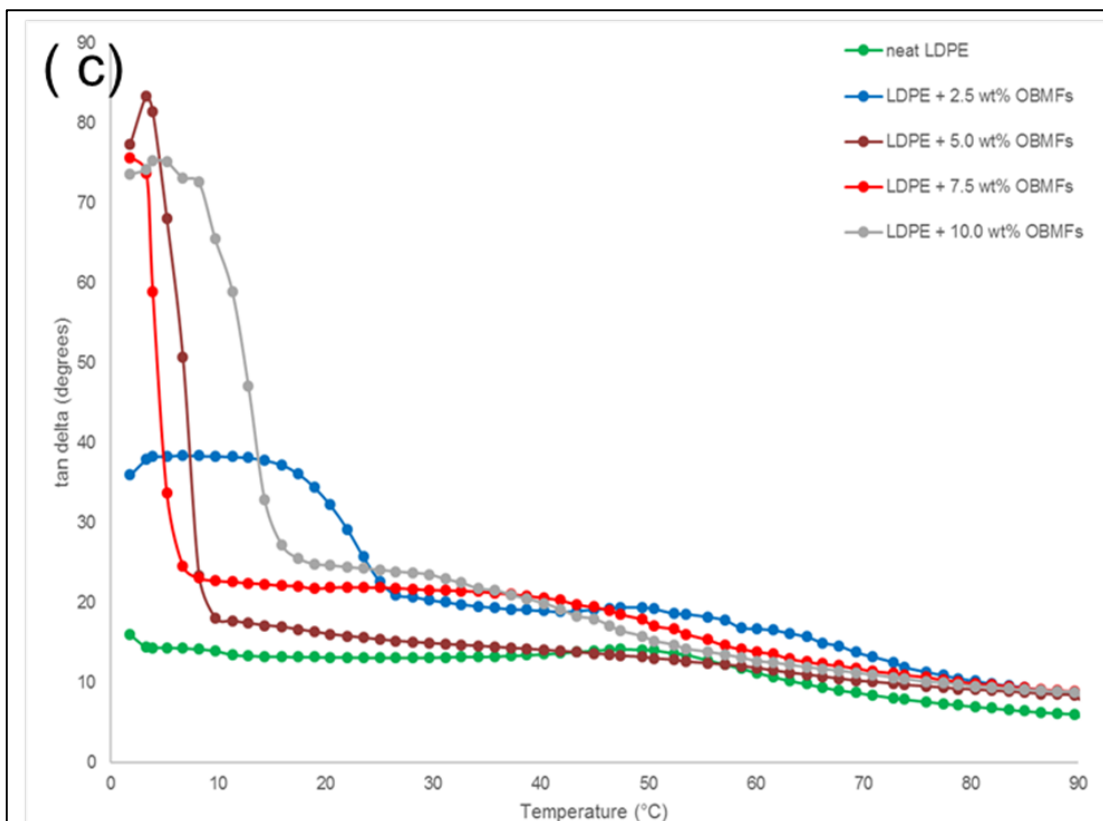
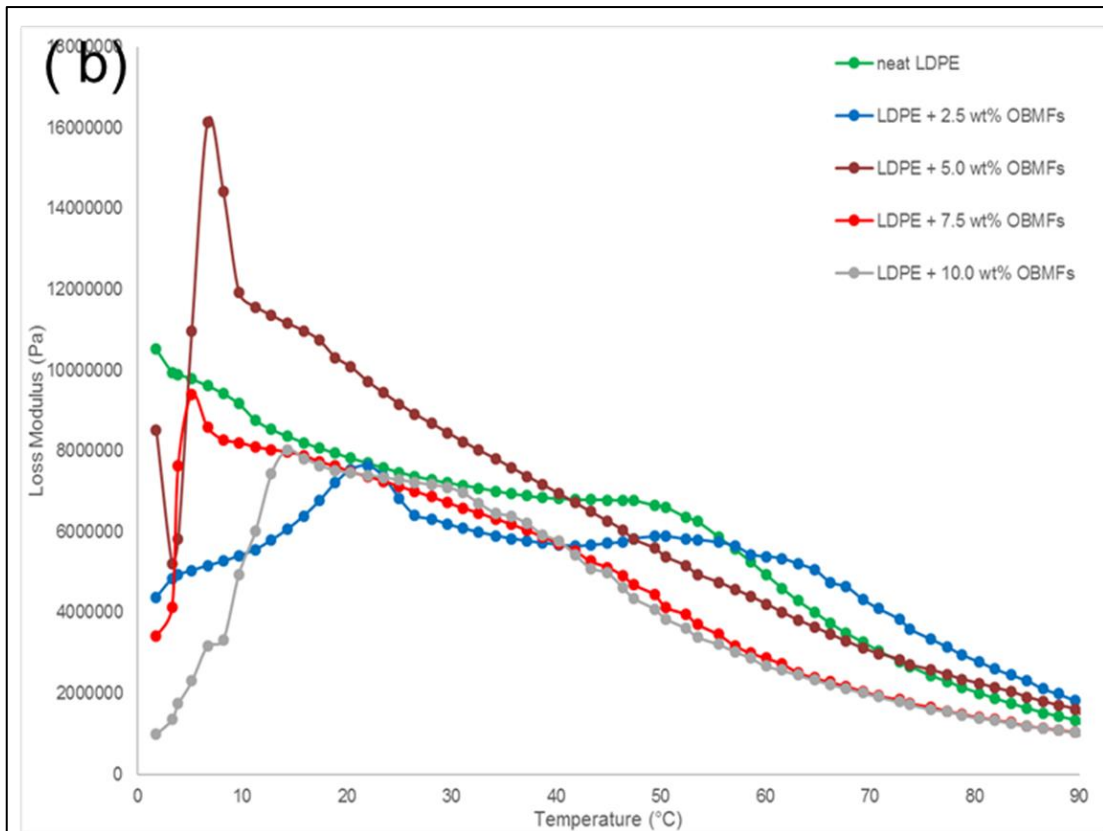


Figure 6.8 Variation of (a) storage modulus, (b) loss modulus and (c) damping intensity ($\tan\delta$) with temperature of LDPE and its nanocomposites

The loss modulus curves of neat LDPE and its nanocomposites are presented in Figure 6.8 (b) which shows a relaxation peak at 50°C in neat LDPE decreased to lower temperatures for nanocomposites such as the peaks were at 25°C, 10°C, 5°C and 15°C for LDPE with 2.5, 5.0, 7.5 and 10 wt% OBMFs respectively. There is a significant change in loss modulus noticeable in the temperature regions between 40 to 55°C which clearly shows the loss modulus is higher for LDPE with 2.5 and 5 wt% OBMFs compare to that of neat LDPE. However, the loss modulus decreased in LDPE with 7.5 and 10 wt% OBMFs in those temperature regions. This trend is also clearly shown between 70 to 90°C temperature regions. This trend completely agreed with the tensile results mentioned in the next section. The equipment which we used for rheology analysis (TA AR1000) is associated with an open hot plate which is not environmentally controlled and we assume the temperature reading in the software may not be the same as the actual temperature in the sample due to the heat absorption by the samples and heat dissipation from the hot plate to open air. It is noticeable that loss modulus reduced drastically from 40°C which we assume is nearly in the same room temperature the tensile tests were performed at 25°C.

The ratio of loss modulus to storage modulus is measured which is graphically presented in Figure 6.8 (c) to identify the damping properties of the materials. The damping peak in the nanocomposites showed an increased magnitude of $\tan \delta$ in comparison to neat LDPE. This graph represents the balance between the elastic phase and viscous phase in the polymeric structure. It is noticeable the maximum peak of neat LDPE at 50°C which is assumed T_g of neat LDPE shifted significantly to lower temperatures for LDPE/OBMFs nanocomposites.

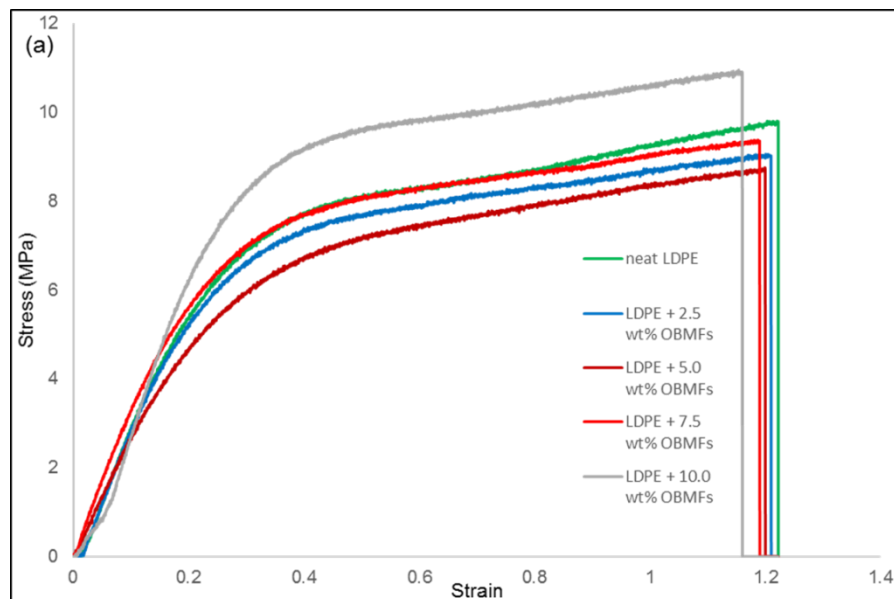
6.3.6. Tensile properties of LDPE/OBMFs nanocomposites

The mechanical properties of LDPE/OBMFs nanocomposites are presented in Table 6.4. It can be seen that the addition of 10 wt% OBMFs can improve tensile strength and elongation at break by 17.5% and 13.7% respectively. However, the tensile strength and elongation at break of other nanocomposites are remained almost same as tensile strength and elongation at break of neat LDPE.

Table 6.4 Mechanical properties of LDPE and its nanocomposites

Sample	Tensile modulus (MPa)	Tensile strength (MPa)	Elongation at break (%)
LDPE	28 ± 1.1	8.0 ± 0.4	66± 4
LDPE+2.5 wt% OBMFs	26 ± 1.6	7.5 ± 0.2	64± 6
LDPE+5.0 wt% OBMFs	27 ± 1.4	7.2 ± 0.1	62± 3
LDPE+7.5 wt% OBMFs	31 ± 1.1	7.9 ± 0.4	61± 5
LDPE+10.0 wt% OBMFs	32 ± 1.2	9.4 ± 0.1	57± 4

There is an increasing trend of improving tensile modulus among nanocomposites, but only LDPE with 7.5 wt% and 10 wt% nanocomposites show higher tensile modulus than that of neat LDPE.

**Figure 6.9** Tensile stress-strain curves of neat LDPE and its nanocomposites

The improvement in mechanical properties of Polyethylene/clay nanocomposites were reported by using compatibilisers by different researchers (Singh et al., 2016; Wang et al., 2001 and Arrakhiz et al., 2013). However, in our recent studies on LDPE/OBMFs nanocomposites, it is clearly noticeable that there is a little but consistent improvement in

tensile property among LDPE/OBMFs nanocomposites. A slight decrease in the tensile strength and modulus can be observed when the OBMFs loading increases from 0 to 5 wt%. The significant enhancement in the tensile strength and modulus were obtained with 7.5 wt% and 10 wt% OBMFs loading. In addition, the decrease trend of elongation at break may be attributed to a reduction in deformability of the rigid interface between nanofillers and matrix (Fu and Lauke, 1996). The OBMFs used in this study is nanoparticle in considering size and shape, but observing the micrographs in Figure 6.5, it can highlighted that without adding any grafting compatibilisers, the OBMFs nanoparticles are uniformly dispersed and no agglomeration is noticeable in LDPE with 2.5 wt% and 5 wt% fillers loading which are difficult to visualise in SEM images in Figure 6.3. However, the orientation of nanoparticles due to the OBMFs compatibility facilitates to act this nanoparticle in a similar manner as fibre which is highlighted in Figure 6.5 (e). After observing carefully the TEM micrographs in Figure 6.5 (a) to (d), schematic diagrams are presented in Figure 6.5 (e) considering the applied force in tensile test and the direction in nanoparticles orientation. It is noticeable that the gradient between nanoparticle orientation and crack propagation plane is decreasing with the increase of filler contents in LDPE matrix which may be attributed to an improvement in materials strength predominantly the fracture strength.

6.4. Conclusions

A series of the LDPE/OBMFs nanocomposites with OBMFs content ranging from 2.5 – 10 wgt% have been prepared by using a melt-blending technique in a twin-screw extruder. The structure of the LDPE/OBMFs nanocomposites was presented using XRD, SEM and TEM. The thermal degradation behaviour of the LDPE/OBMFs nanocomposites was demonstrated by using DSC and TGA. The results of XRD, SEM and TEM indicate that the LDPE/OBMFs nanocomposites are a hybrid material consisting of OBMFs nanoplatelets and LDPE polymer matrix. Moreover, it is highlighted that the OBMFs nanoplatelets exist as aggregates and contribute to different dispersion behaviour with a change of OBMFs content in the LDPE matrix. In this study, OBMFs shows exfoliation characteristics with LDPE with 5 wt% OBMFs nanocomposites whereas it shows structure intercalation in LDPE with 7.5 wt% OBMFs. In addition, OBMFs creates a mix of agglomeration and local exfoliation which was detectable by thermal analysis.

The thermal properties of the LDPE and its nanocomposites were studied by means of DSC and TGA. No changes in melting and recrystallization temperatures due to the addition of OBMFs in the polymer matrix were detected. However, there was a decrease in the percentage of crystallinity noticeable with an increase in filler content. In addition, heat

capacity reduced in nanocomposites compared to the neat LDPE matrix which indicate the inclusion of OBMFs in LDPE improves the thermal conductivity of these nanocomposites in general. LDPE with 10 wt% OBMFs nanocomposites showed the lowest heat capacity (about 21% reduction) addressing the superior thermal conductivity of this material. A significant increase of thermal stability was also achieved with LDPE with 10 wt% OBMFs nanocomposite. Furthermore, the viscoelastic investigation revealed the storage modulus, loss modulus and damping intensity properties of materials which also agreed with the mechanical properties of the material. LDPE with 10 wt% of OBMFs content showed both thermal stability and superior tensile properties compare to those properties of neat LDPE and LDPE with 2.5, 5 and 7.5 wt% OBMFs content nanocomposites.

Chapter 7: The Crystallinity and Thermal Degradation Behaviour of Polyamide 6/Oil Based Mud Fillers (PA6/OBMFs) nanocomposites

7.1. Introduction

The application of layered aluminosilicate as fillers in polyamide nanocomposites has received attention in recent years. PA6-layered-silicates have been studied over years due to its unique properties to reduce flammability, increasing heat resistance, exhibit higher tensile strength, improving tensile modulus, increasing flexural strength and also improving flexural modulus (Fornes and Paul, 2003; Bourbigot et al., 2002; Njuguna et al., 2008; Morgan and Gilman, 2003 and Bourbigot and Duquesne, 2007). The continuous improvement of these achievements has attracted researchers to scale up certain properties such as thermal stability, flame retardancy, ablation and barrier resistance in the composite material to increase the application of this material as advanced structural material in different industries including automotive and space industries (Leszczyńska et al., 2007a; Leszczyńska et al., 2007b; Seymour and Kirshenbaum, 1986 and Qin et al., 2003). The advancement of these properties largely depends upon the nanomorphology of this filler into the polymer chain as this morphology related to the chemical structure of the filler which is source of origin and surface modification dependent (Pavlidou and Papaspyrides, 2008 and Dennis et al., 2001).

Although it is clearly evident that clay/nanoclay improves the mechanical and thermal properties of PA6/clay nanocomposite materials (Zope et al., 2016 and Pereira and Martins, 2014), but there is no information available in literature on the influence of recovered nanoclay from OBM waste on the mechanical and thermal properties of composite materials. Investigations have been carried out in this study to determine the effects of OBMFs on thermal properties in PA6/OBMFs nanocomposites. As part of these investigations, different analysis have been undertaken including scanning electron microscopy (SEM), fourier transform infra-red (FTIR) spectroscopy, energy dispersive x-ray analysis (EDXA), thermo-gravimetric analysis (TGA) and differential scanning calorimetry (DSC) to determine morphological and chemical structure changes, thermal degradation and decomposition behaviour of materials. Additionally the changes in amorphous and crystal fractions have been discussed in this paper.

7.2. Experimental

7.2.1. Materials

Tarnamid[®] T27 (trade name of PA6) polymer was supplied by Grupa Azoty, Poland. It has melting point of 250°C and a V-2 rating in UL94 (vertical burning test) at 1.6 mm thickness. Prior to melt compounding, PA6 was dried at 90°C for 24 hours in a convection oven. Melt mixing of different wt. % concentrations of OBMFs with PA6 was carried out using TwinTech Extrusion LTD 10 mm twin screw extruder at 40 RPM under the following test conditions 1st zone (190°C), 2nd zone (250°C), 3rd zone (240°C), 4th zone (210°C) and die/5th zone (210°C). The granulated material was injection moulded into bar mould (dual cavity) for different analysis using temperature at 270°C with moulding pressure of 10 bar.

7.2.2. OBMFs manufacturing process

The processing method of spent oil based mud used in this chapter is described in section 3.2.1.

7.2.3. PA6/OBMFs nanocomposite manufacturing process

To investigate the influence of reclaimed clay from spent OBM mud in changing different mechanical properties of PA6/OBMFs nanocomposites, PA6 was melt compounded with different wt% of Oil Based Mud fillers (OBMFs) such as 2.5, 5, 7.5 and 10 wt%. Prior to manufacture PA6/OBMFs nanocomposites, PA6 pellets and OBMFs were dried at 90°C for 24 hours in a convection oven. The PA6 pellets and OBMFs were then mixed in Brabender mixer before passed through the co-rotating twin screw extruder at 250°C which was attached to the pelletiser at the end to cut the compounds into small pieces. This manufacturing process is shown step by step in the following figure Figure 7.1.

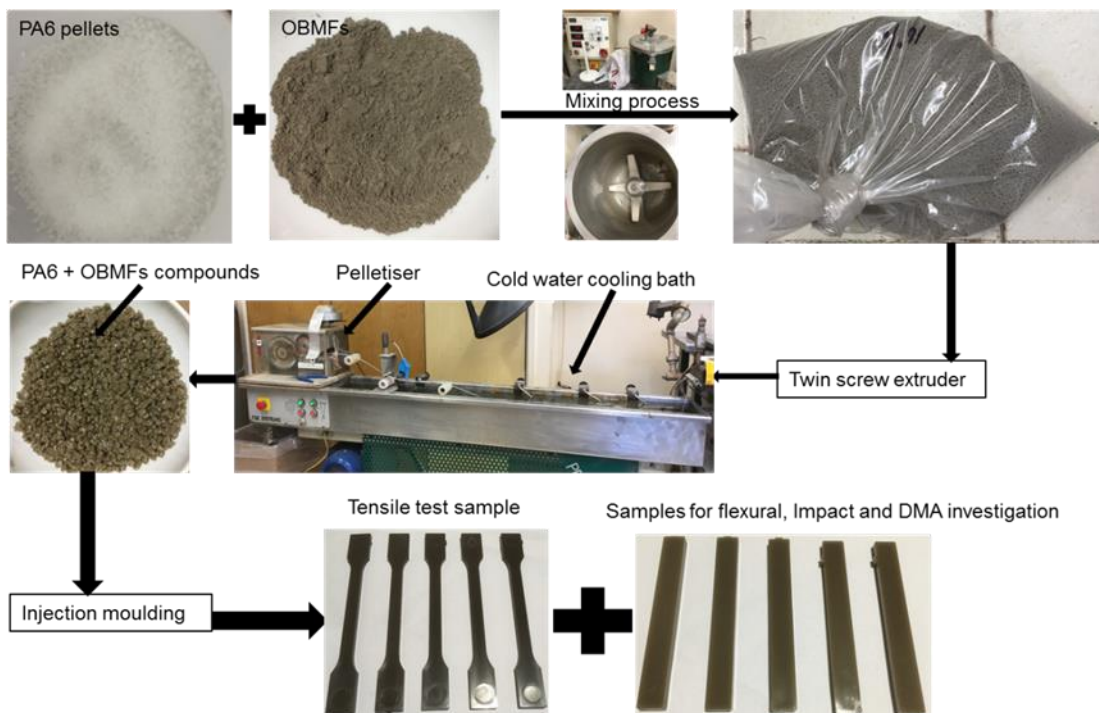


Figure 7.1 Flow diagram of PA6/OBFs nanocomposites sample manufacturing process

The obtained compound pellets were stored in thermally insulated bags for storing the compounds and protecting from absorbing moisture from air. These compounds were used to manufacture tensile, flexural and impact test bars using injection moulding machine. Before using compounds to manufacture different test bars, compounds were dried at 90°C for 12 hours in a convection oven to ensure the effect of moisture in test results are as little as possible. The test bars were stored in two layers of aluminium foil followed by polythene zip bags for moisture absorption protection before performing different tests and analysis.

7.2.4. Characterisation

To observe the morphology of OBFs and its dispersion in polymer matrix, samples were broken into small pieces using liquid N₂. The sections were observed using a Zeiss EVO LS10 Scanning Electron Microscope (SEM) with a magnification of 4000X, 4.5 mm working distance (WD) and accelerating potential of 25.00kV. To minimise the sample being altered all the samples are gold coated using sputter deposition for 2 minutes prior to the experiment. To determine the approximate elemental composition of the samples, energy dispersive x-ray analysis (EDXA) (Oxford Instruments INCA Energy) was carried out by following the same method which is described in section 4.2.4. The cryo-fractured surface morphologies and the associated failure mechanisms were analysed using SEM.

The ATR-FTIR characterisation method used in this chapter is described in chapter 3.2.2. The thermal analysis including DSC and TGA method used in this chapter is described in chapter 3.2.4.

The XRD analysis method used in this chapter is described in section 3.2.2.

TEM images of PA6/OBMFs nanocomposites were obtained at 80 kV, using the Titan Themis 200 scanning transmission electron microscope (S/TEM). In order to prepare TEM samples, small sections of the injection moulded samples were embedded in epoxy resin and cured in histology cassettes overnight at room temperature following the same sampling technique reported by Williamson et al., (2007) except epoxy resin was used instead of paraffin wax which is normally used for soft tissue analysis. Finally, thin sections were cut using Leica microtome and deposited on copper grids.

7.3. Results and discussion

7.3.1. ATR-FTIR analysis of materials

The resulting spectra from the ATR-FTIR analysis of the PA6 and PA6/OBMFs nanocomposites is presented in Figure 7.2.

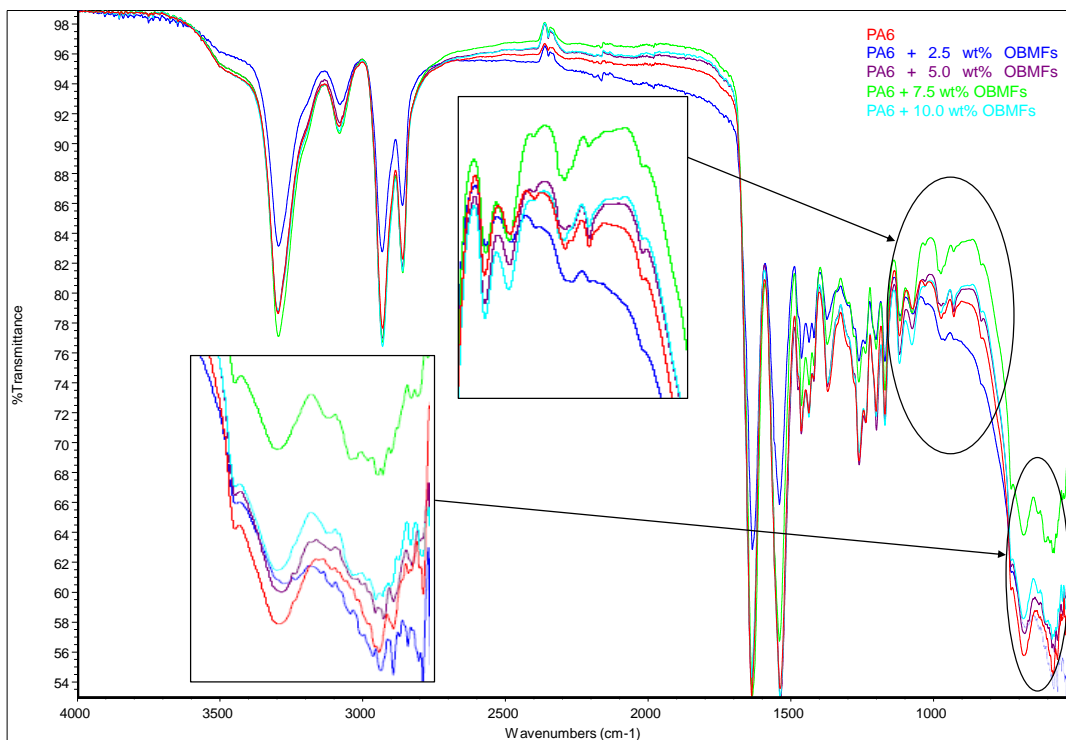


Figure 7.2 Comparison of FTIR full scale spectra of PA6 and its nanocomposite

Review to individual spectra are provided in Appendix C (**Figure C.1-C.5**) and a summary of ATR-FTIR peak assignments presented in Table 7.1 based on literature (Chen et al., 2004; Pramoda et al, 2003; Socrates, 2004 and Vasanthan and Salem, 2001).

Table 7.1 ATR FT-IR peak assignments (Chen et al., 2004; Pramoda et al, 2003; Socrates, 2004 and Vasanthan and Salem, 2001)

Wave number (cm ⁻¹)	Assignments
3295	Hydrogen-bonded N-H stretching
3079	Fermi-resonance of N-H stretching
2930	V _{as} (CH ₂)
2859	V _s (CH ₂)
1633	Amide I
1539	Amide II
1462	CH ₂ deformation
1435	CH ₂ deformation
1370	Amide III & CH ₂ wag
1259	Amide III & CH ₂ wag
1200	Amide III & CH ₂ wag
1169	CO-NH, skeletal motion (Am)
1118	C-C stretching (Am)
1074	C-C stretch (Am)
973	CO-NH in plane vibration
680	Amide V
525-580	Primary aliphatic nitriles (C≡N)

The presence of band peak at 3294-3296 cm⁻¹ for all samples, it is evident that nearly 100% hydrogen bonding in linear aliphatic homopolyamides at room temperature. Since the transmittance coefficients of the band at 3295 cm⁻¹ for the five specimens are different and then the strength of hydrogen bonds among these five samples is not comparable. However, the wavenumbers of these five samples are similar representing the OBMFs had little effect on the average strength of hydrogen bonding.

It is interesting that these FTIR spectra are applicable effectively to qualitatively analyse the crystallinity phase changes (e.g. amorphous phase to crystal phase or γ form to α form). To investigate the amorphous and both α and γ crystalline phases in this study, certain band assignments positions are important. The band at 1118 cm⁻¹ is attributed as the amorphous phase whereas the band at 973 cm⁻¹ is attributed as the γ phase crystal form. In addition the

band at 930 cm^{-1} and 1200 cm^{-1} are attributed as α phase crystal form (Chen et al., 2004 and Vasanthan and Salem, 2001).

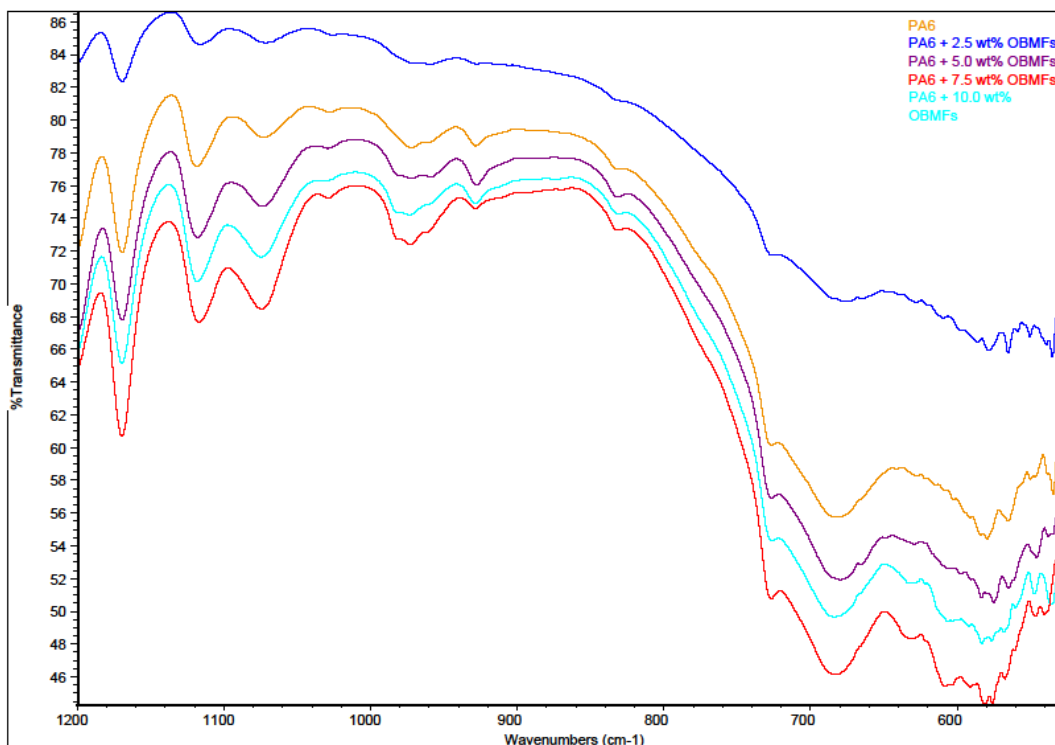


Figure 7.3 Comparison of FTIR spectra between 1200-525 of PA6 and its nanocomposite

Figure 7.3 shows a magnified comparison of ATR-FTIR spectra for the studied materials between $1200\text{--}525\text{ cm}^{-1}$. In this study, there is a band at 1200 cm^{-1} for neat PA6 and its nanocomposite, showing the strong α form although the band at 930 cm^{-1} is very weak for all the samples. However, the γ crystalline phase is noticeable at band 973 cm^{-1} in neat PA6 with 7.5 wt.% OBMFs and PA6 with 10 wt.% OBMFs nanocomposites whereas this phase is very weak for other nanocomposites. It is attributed here that this influencing γ crystalline phase contributes the incremental % of crystallinity for neat PA6 with 7.5 wt. % OBMFs and PA6 with 10 wt. % OBMFs nanocomposites than the % of crystallinity of PA6 with 2.5 wt. % and 5 wt. % OBMFs nanocomposites. This is agreed with the % of crystallinity results presented in Table 7.3.

Investigating the spectrum for individual material in Appendix C, it can be highlighted that the bands at 1169 cm^{-1} , 1118 cm^{-1} and 1074 cm^{-1} represents the amorphous phase. The intensity of bands at 1169 cm^{-1} and 1118 cm^{-1} is similar for neat PA6 and PA6 with 2.5 wt.% OBMFs materials whereas the intensity of these bands are stronger for PA6 with 5 wt.% OBMFs and PA6 with 7.5 wt.% OBMFs materials. However, PA6 with 10 wt. % OBMFs shows a weaker intensity in this amorphous bands compare to PA6 with 5 wt. % OBMFs and

PA6 with 7.5 wt. % OBMFs materials. It is important to mention here that there is another additional band at 1074 cm^{-1} in PA6 with 7.5 wt. % OBMFs spectra which is characterised as amorphous phase. Only PA6 with 7.5 wt. % OBMFs material shows strongest intensity and subtle peaks at these three 1169 cm^{-1} , 1118 cm^{-1} and 1074 cm^{-1} amorphous bands which is also agreed with the superior heat capacity value for PA6 nanocomposite materials from DSC results presented in Table 7.4. Identifying the intensity and frequency nature of these materials, it can be attributed that the band at 1169 cm^{-1} represents the Mobile Amorphous Fraction (MAF) and the bands at 1118 cm^{-1} and 1074 cm^{-1} represents the Rigid Amorphous Fraction (RAF).

7.3.2. Morphology of OBMFs and polyamide/OBMFs nanocomposite materials

Morphological studies are carried out to understand the surface topography and composition of the specimen. A visual inspection of the thermally treated OBM sample (**Figure D.1** at Appendix D) and subsequent SEM image (**Figure D.2** at Appendix D) suggests perforation at the surface of the OBM sample which is attributed to the formation of bubbles as a consequence of the vaporisation of volatile organic compounds during the heating stage.

In **Figure D.2** at Appendix D, the micrograph of treated/untreated OBMFs clearly shows the presence of tightly stacked spherical particles with size ranges up to 1000nm.

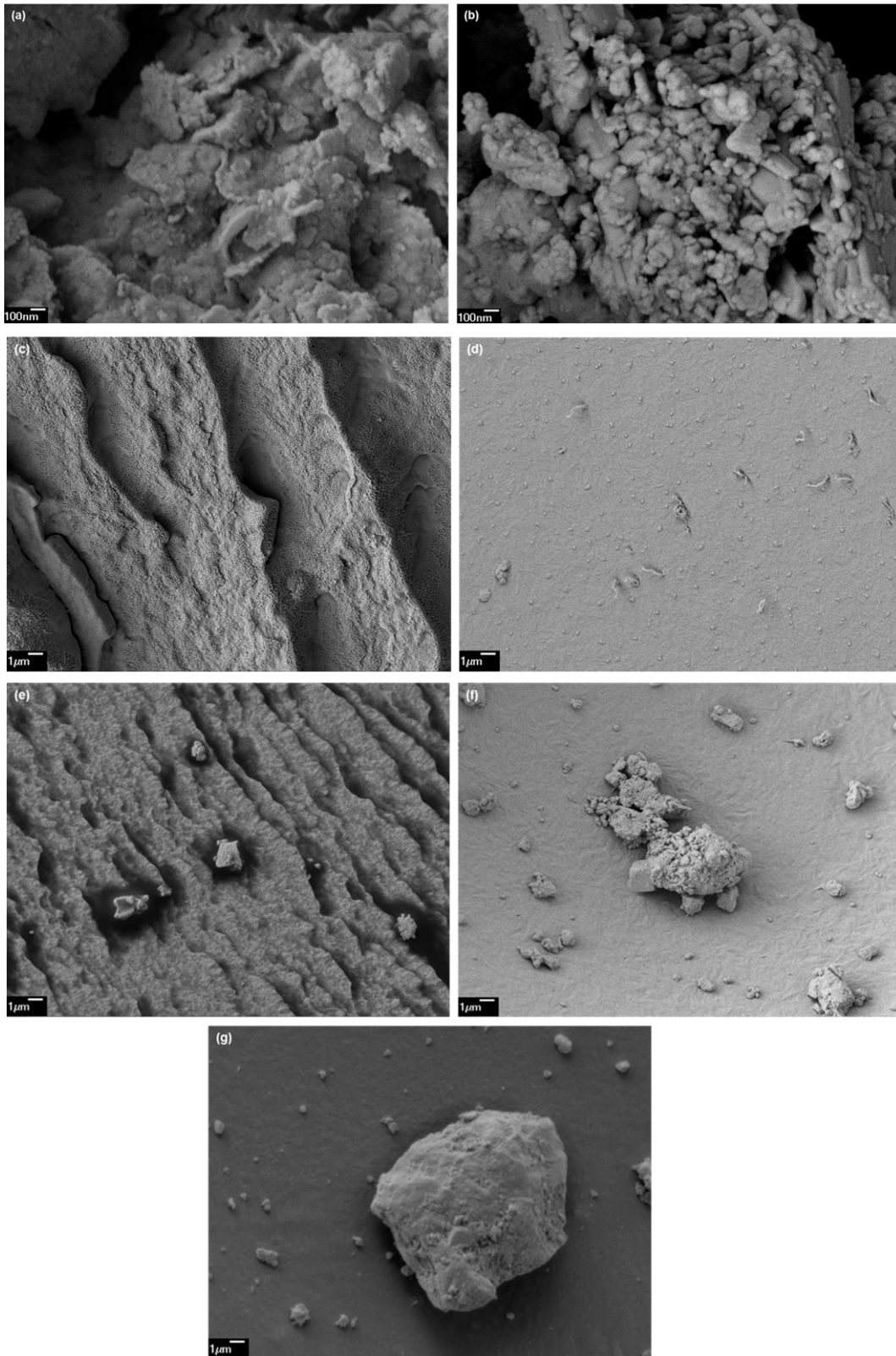
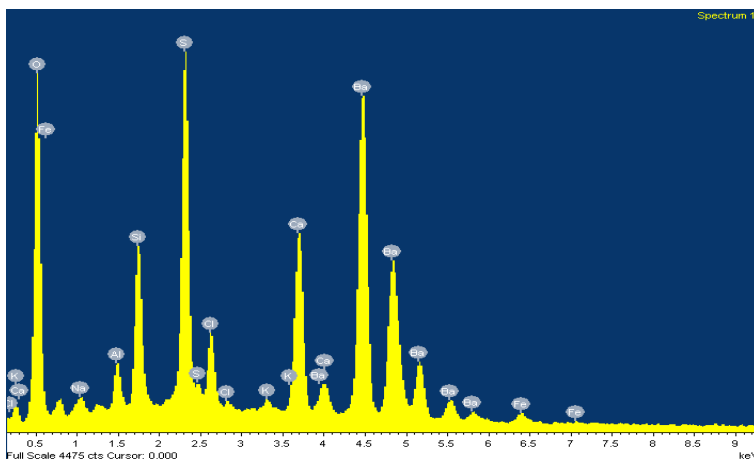


Figure 7.4 SEM images of (a) montmorillonite; (b) OBMFs; (c) PA6; (d) PA6 with 2.5 wt% OBMFs; (e) PA6 with 5.0 wt% OBMFs; (f) PA6 with 7.5 wt% OBMFs; and (g) PA6 with 10.0 wt% OBMFs

The SEM micrographs were used to investigate the effect of OBMFs on the morphology of PA6 and its nanocomposite. Figure 7.4 (a) shows morphology of montmorillonite as a reference clay mineral to compare to the morphology of OBMFs which is presented in Figure 7.4 (b). Both Figure 7.4 (a) and Figure 7.4 (b) illustrate the shape and size of the clay platelets which is in nanoscale. Fig. 3(c) shows some cavitation and uneven surfaces for the fractured PA6 structures. The SEM micrograph of the composite made with 2.5 wt. % filler (OBMFs) shows dispersed (unsaturated) OBMFs into PA6 matrix and also these particles are scattered over the PA6 matrix which is also noticeable in Figure 7.4 (d). The well dispersed OBMFs in PA6 matrix is clearly visible in Figure 7.4 (e). It can be articulated from the investigation of the geometrical structure of the particles that mostly exfoliation occurs in this nanocomposite. Figure 7.4 (f) shows a clustering of small particles which is suggested to be the intercalation between PA6 and layered silicates and also an agglomeration of particles. An uneven and poor dispersion of OBMFs into the PA6 polymer matrix with a noticeable (Figure 7.4 (g)) agglomeration of particles is observed.

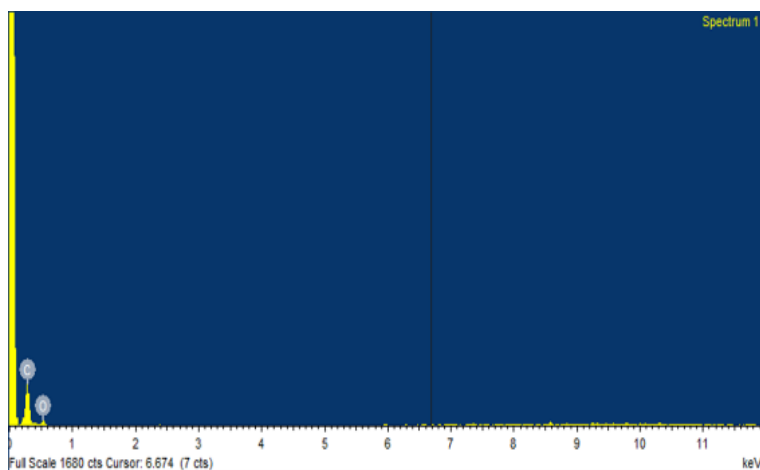
7.3.3. Elemental Composition

To determine the elemental composition and elucidate the effect of filler interactions with the PA6 matrix at varying filler compositions, Energy Dispersive X-ray (EDX) analysis was carried out as shown in Figure 7.5 (a-e).



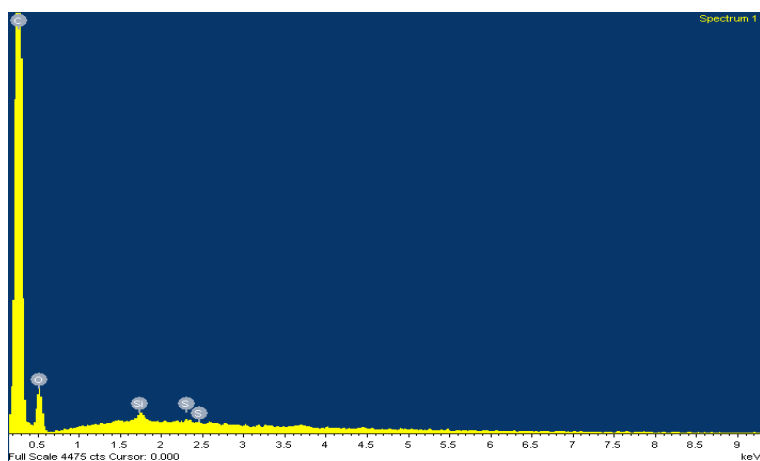
Element	Atomic%
O	61.85
Na	0.87
Al	1.77
Si	5.43
S	10.55
Cl	2.38
K	0.27
Ca	5.36
Fe	0.52
Ba	11
Totals	100

(a)



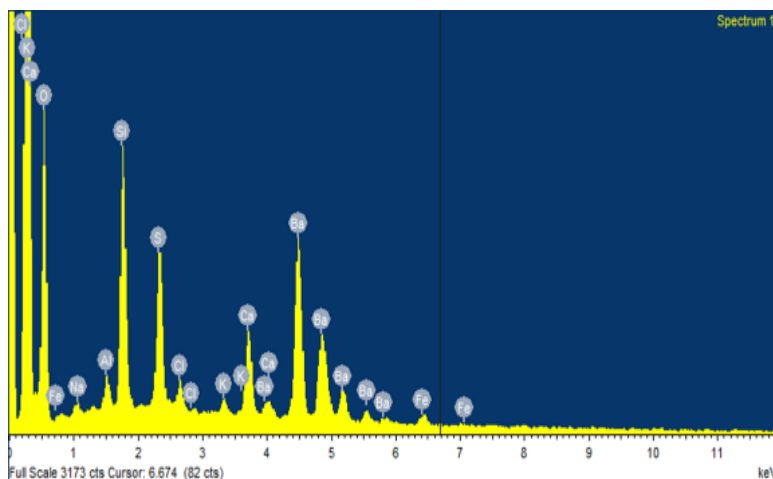
Element	Atomic%
C	77.42
O	22.58
Totals	100

(b)



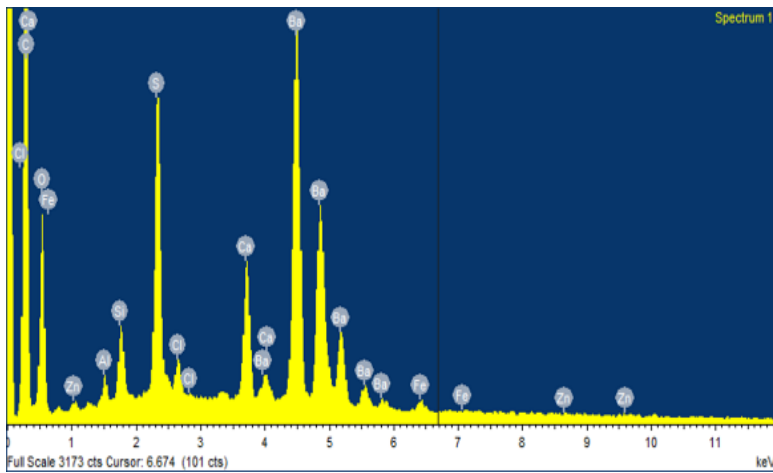
Element	Atomic%
C	85.06
O	14.8
Si	0.12
S	0.02
Totals	100

(c)



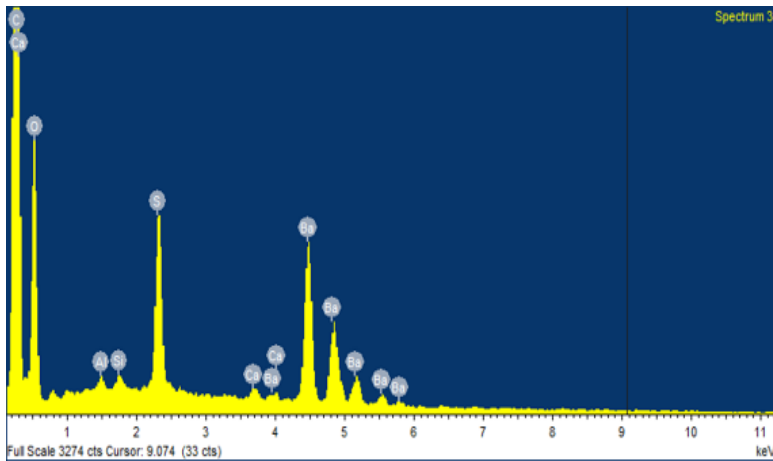
Element	Atomic%
O	66.06
Na	0.93
Al	1.53
Si	11.19
S	6.42
Cl	1.2
K	0.53
Ca	3.34
Fe	0.84
Ba	7.97
Totals	100

(d)



Element	Atomic%
C	68.02
O	19.76
Al	0.34
Si	0.84
S	3.35
Cl	0.46
Ca	1.58
Fe	0.24
Zn	0.02
Ba	5.38
Totals	100

(e)



Element	Atomic%
C	76.32
O	21.09
Al	0.08
Si	0.07
S	1.06
Ca	0.07
Ba	1.3
Totals	100

(f)

Figure 7.5 EDX spectra of (a) OBMFs; (b) PA6; (c) PA6+2.5 wt% OBMFs; (d) PA6+5.0 wt% OBMFs; (e) PA6+7.5 wt% OBMFs and (f) PA6+10.0 wt% OBMFs

In Figure 7.5 (a) (b) (c) (d) (e) and (f) shows the EDX spectra and also the elemental profile (atomic wt %) of OBMFs, neat PA6, PA6 with 2.5 wt. % OBMFs, PA6 with 5 wt. % OBMFs, PA6 with 7.5 wt. % OBMFs and PA6 with 10 wt. % OBMFs nanocomposites respectively.

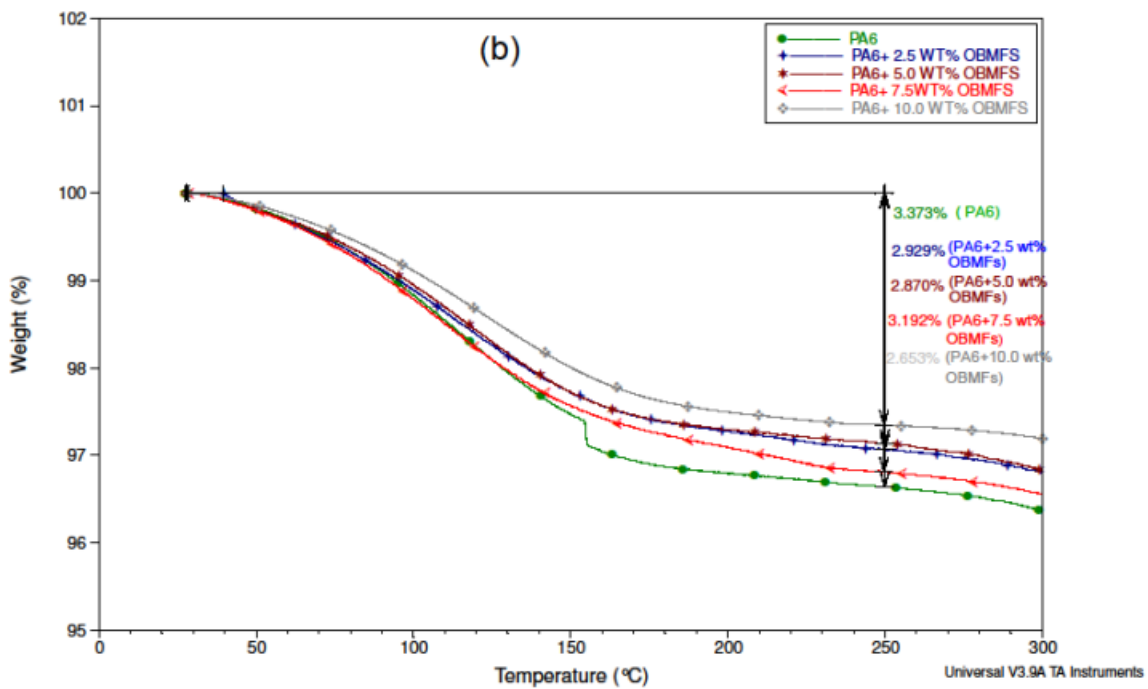
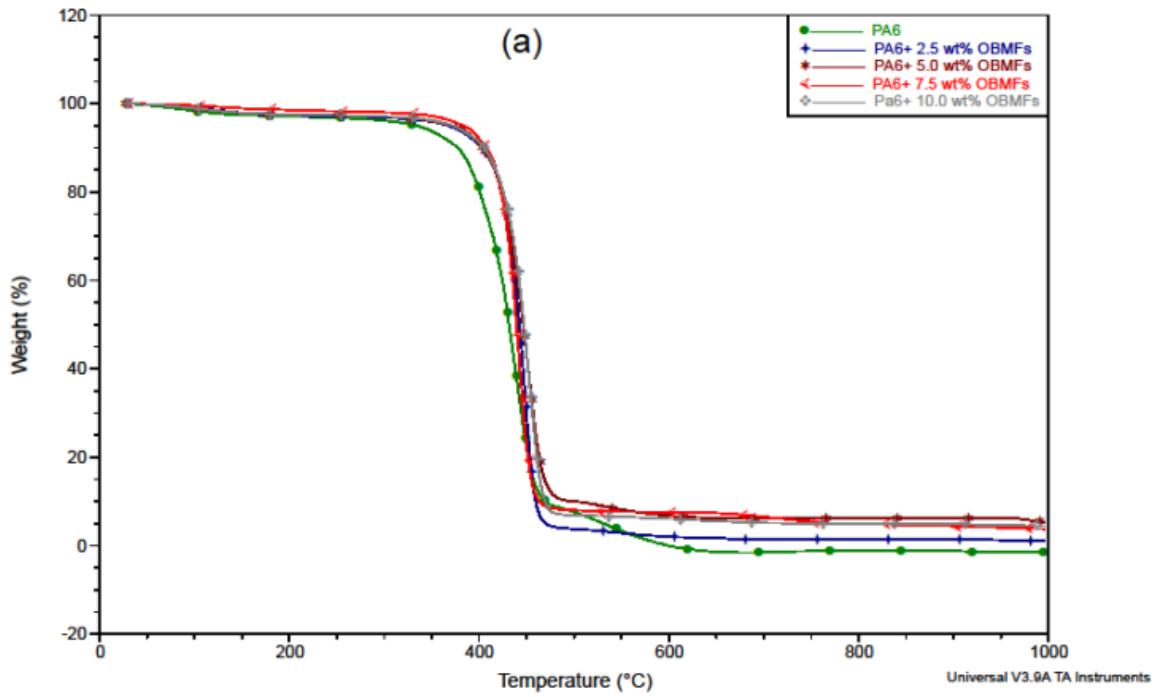
As the filler content in the nanocomposites increases, there is an apparent increase in intensity and presence of other elements such as barium (Ba), silicon (Si), sulphur (S), iron (Fe), sodium (Na) and aluminium (Al). The presence of zinc (Zn) is noticeable only in PA6 with 7.5 wt. % nanocomposite sample. The intensity of C and oxygen (O) increase significantly with the addition of filler in nanocomposite as shown in Figure 7.5. It can infer here that the incremental intensity of C and O and also the presence of other elements are originated from the OBMFs which have been used in manufacturing this nanocomposite.

Analysis of the EDX spectra for PA6 and its nanocomposites as shown in Figure 7.5 indicates a high wt. % of barium (Ba) is present in the sample. This is probably a reflection of the large quantities of barium sulphate (BaSO_4) as weighting agent used in the formulation of the drilling fluid. The presence of silicon (Si) and oxygen (O) peaks is expected due to the silicate matrix known to be present in bentonite clays. The incremental intensity of Carbon (C) peaks implies limestone (CaCO_3) may have been used as an additive in the drilling fluid to control circulation loss amongst other functions whereas the sulphur (S) and iron (Fe) peaks could be from iron sulfide (FeS_2) resulting from the use of iron oxide (Fe_3O_4) usually used as an additive for scavenging hydrogen sulfide (H_2S). Also, peaks of chlorine from the analysis are an indication that chloride salts (NaCl or KCl) may have been used as an electrolyte. Finally, the calcium (Ca), potassium (K), aluminium (Al) and sodium (Na) peaks may be characteristic of the ion exchange surface of the clay or the minerals associated with the clay reclaimed from drilling fluid waste.

7.3.4. Thermogravimetric analysis (TGA)

The thermal degradation of PA6/OBMFs nanocomposite has been analysed in N_2 environment using TA instrument TGA Q500. Weight loss curves of the samples in different stages are given in Figure 7.6.

In addition Table 7.2 shows the degradation at different stages such as at 250 °C, temperature and time at D1/2 (50% weight loss) and the residue at 600 °C. Although the analysis temperature has been selected from room temperature (20 °C) to 1000 °C at 10 °C/minute rate, there were not any significant changes in decomposition curve noticeable in the Figure 7.6 after 600 °C.



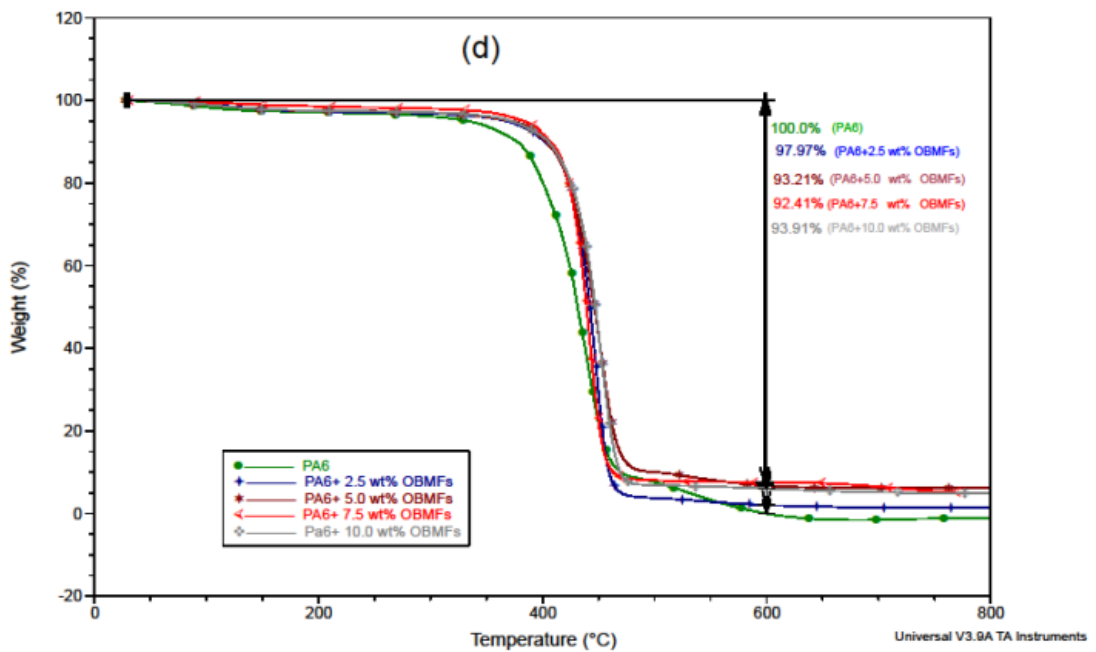
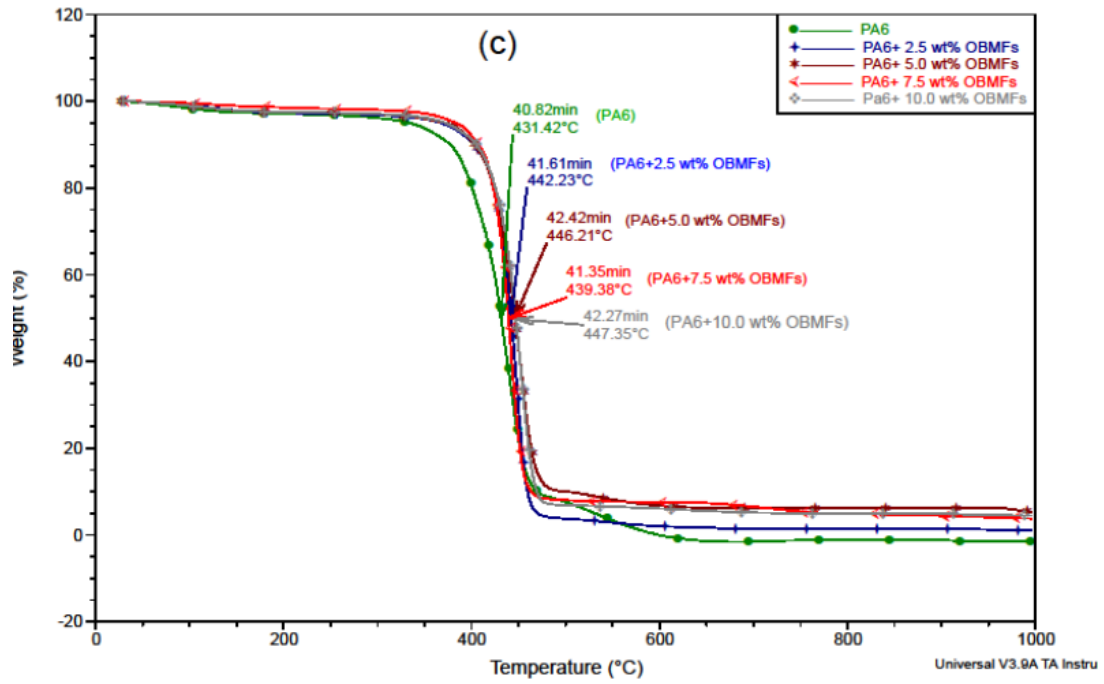


Figure 7.6 TGA of PA6 and PA6/OBMFs nanocomposites at: (a) complete thermograms of all samples; (b) 250°C; (c) D ½; (d) 600 °C

However, the neat PA6 shows the lowest thermal stability among the samples. The degradation trends for all the samples were similar until the temperature reached to 300 °C. Between 350 °C to 450 °C temperature, PA6 decomposed distinctly faster than any other samples. This is the temperature range when maximum weight has been lost in PA6 and its nanocomposite samples. However, the onset decomposition of PA6 starts at 300° C whereas the onset decomposition of other samples starts at 420°C. This indicated that PA6/OBMFs nanocomposites had greater thermal stability than neat PA6.

Table 7.2 TGA analysis at different decomposition stages of PA6 and its nanocomposites with different clay loadings

Material	% wt loss at 250 °C	T _{D10%} (° C)	T _{D50%} (° C)	D 1/2 Time	Residue (% wt) at 600 °C
PA6	3.37	399.24	431.42	40.82	0.00
PA6+2.5 wt% OBMFs	2.93	407.77	442.23	41.61	2.03
PA6+5.0 wt% OBMFs	2.87	416.87	446.21	42.42	6.79
PA6+7.5 wt% OBMFs	3.19	412.32	439.38	41.35	7.59
PA6+10.0 wt% OBMFs	2.65	416.87	447.35	42.27	6.09

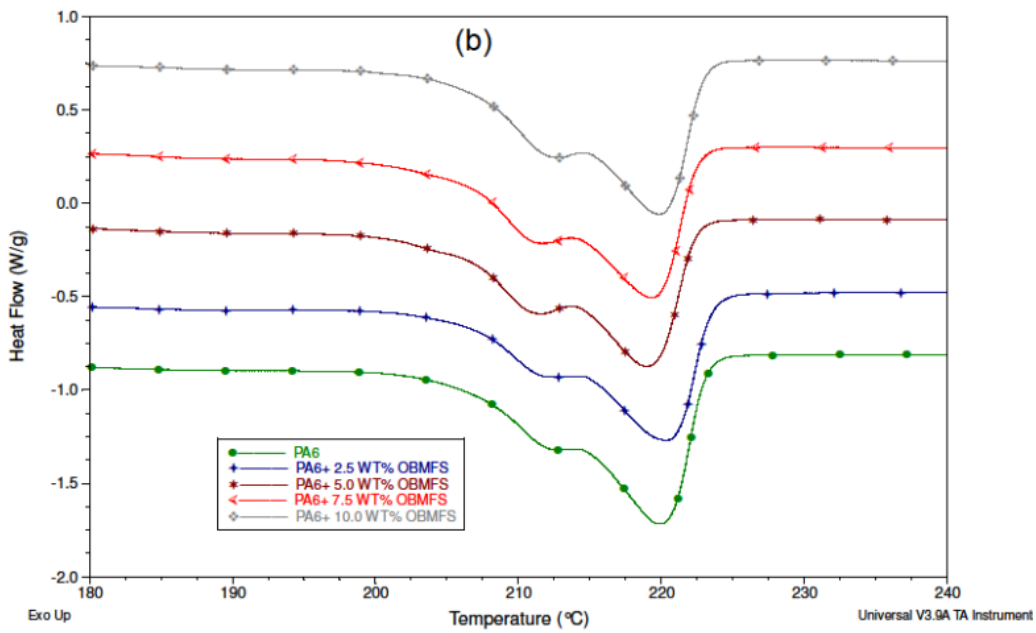
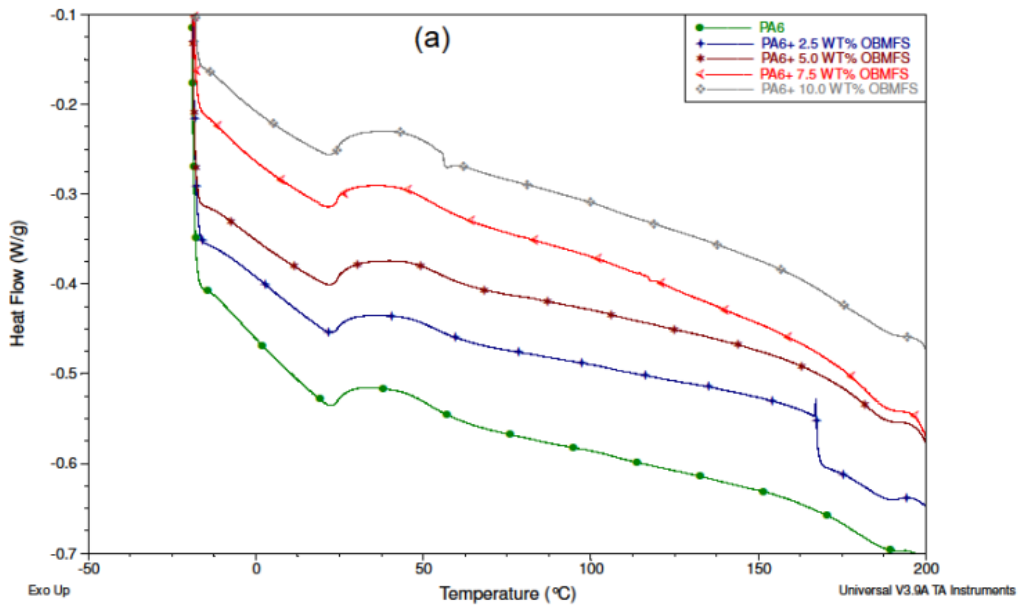
Investigating D1/2 for PA6 and its nanocomposite, it is clearly noticeable that PA6 with 5 wt. % OBMFs nanocomposite took the longest time (42.42 min) to reach D1/2 that is related to the flame retardancy property of polymeric material and it is believed this result is a consequence of combined effects of clay dispersion and confinement of polyamide chains in the interlayers of clay platelets. This is in a good agreement with the morphological observations in Figure 7.4 (c) which indicated exfoliated structure for PA6 with 5 wt. % OBMFs nanocomposite. However, PA6 with 10 wt. % OBMFs showed the highest temperature (447.35 °C) at D1/2 which indicated the best thermal stability among the samples. In addition, the onset degradation temperature in both 10% and 50% weight loss cases showed the thermal stability trend as: PA6 + 10 wt% OBMFs > PA6+5 wt% OBMFs > PA6+2.5 wt% OBMFs/PA6+ 7.5 wt% OBMFs >PA6. These findings also agree with the results obtained from heat capacity in Table 7.4 which suggested PA6 with 7.5 wt% showed the maximum heat capacity property. It is assumed the excess energy is stored by nanocomposite during the solid-liquid phase change process.

It is manifested here that the incremental filler contents which are mostly clay minerals may influence the thermal stability in PA6 with 10 wt. % OBMFs nanocomposite. In addition to this, the heat capacity results presented in Table 7.4 showed significant number in heat capacity reduction (about 47% decrease) which also indicated the increase in thermal conductivity of the material and also indicated the potential incremental heat release property of the material under combustion condition. These findings are also agreed with the morphological observations in Figure 7.4 (e) which showed 10 wt. % of OBMFs incurred the agglomeration in PA6 with 10 wt. % OBMFs nanocomposite.

It is interesting to mention here that the time needed for PA6 with 7.5 wt. % OBMFs to reach D1/2 is less than the time needed for PA6 with 2.5 wt. % OBMFs (unsaturated exfoliation). On the other hand PA6 with 7.5 wt. % nanocomposite took more time to reach D1/2 than the time is taken by neat PA6. Additionally the temperature at D1/2 for PA6 with 7.5 wt. % OBMFs is the lowest among the PA6/OBMFs nanocomposites indicating the best heat capacity material among these PA6/OBMFs nanocomposite material. The ordered intercalated structure within the PA6 with 7.5 wt. % OBMF may have influenced its heat capacity in this manner which is also noticeable in the morphological observations in Figure 7.4 (d). There is an incremental trend of residue left at 600 °C except PA6 with 10 wt. % OBMFs nanocomposite presented in Table 7.2. It can be explained by the findings in this analysis for PA6 with 10 wt. % OBMFs nanocomposite which showed the incremental thermal conductivity may generate excessive heat in the interlayer between clay platelets which may affect the decomposition of fractions of total filler contents.

7.3.5. Differential Scanning Calorimetry (DSC)

In order to obtain information about the polymorphic behaviour in PA6/OBMFs and to evaluate the influence of fillers on thermal degradation behaviour of nanocomposite materials, nonisothermal measurements were conducted using a differential scanning calorimeter (DSC) and the results are shown in Figure 7.7.



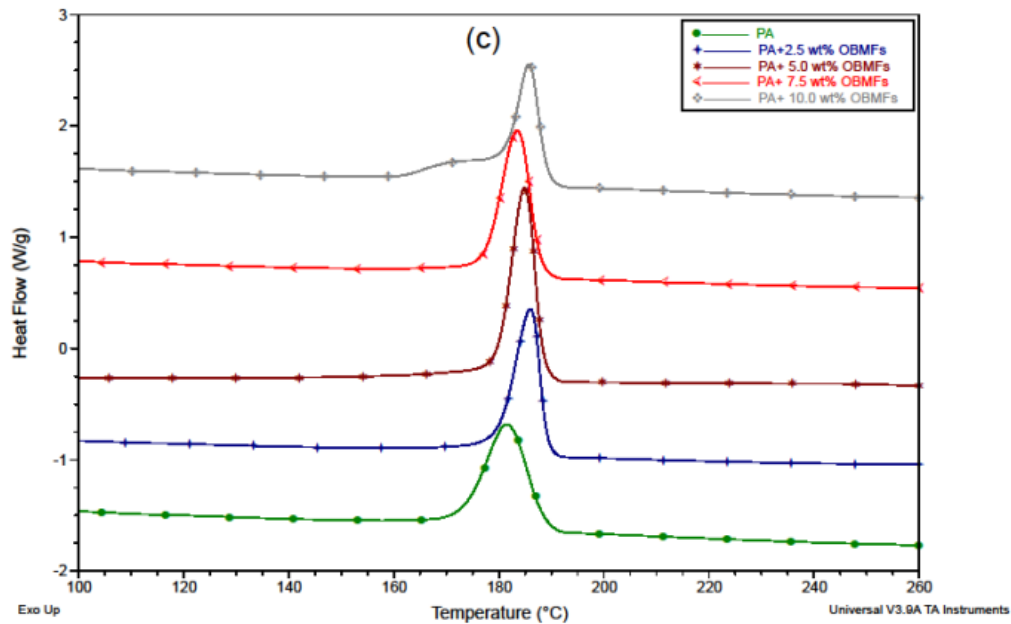


Figure 7.7 DSC thermograms of PA6 and its nanocomposites at (a) T_g; (b) T_m and (c) T_c

Comparing different thermograms in Figure 7.7 (b) no major changes in melting temperature is observed and there are two peaks present in thermograms at melting temperature of PA6 and PA6/OBMFs nanocomposites. there is a peak at 212.5 °C which is representative of the gamma crystal phase whilst a stronger melting peak at ~220 °C typically associated with the alpha phase is observed in the neat PA6 and PA6/OBMF nanocomposites.

Heat capacity is believed to be one of the main factors influencing the thermal degradation nature and behaviour of polymer nanocomposites (Pramoda et al, 2003). This heat capacity has become an important part of nanocomposite material characterisation. Based on the three distinct peaks obtained in thermograms in Figure 7.7, the important features explored for PA6 and its nanocomposites (T_g, T_m and T_c) are discussed in this section.

The heat capacity peak at melting temperature phase was used to identify the % of crystallinity of the material. The % of crystallinity of PA6 and its nanocomposites is calculated using the following equation:

$$\% \text{ crystallinity} = [\Delta H_m - \Delta H_c] / \Delta H_m^0 * 100\% \quad (7.1)$$

Where ΔH_m is the heat of melting, ΔH_c the heat-of cold crystallisation which is not present in this experiment ($\Delta H_c=0$ in this case), and ΔH_m^0 is a reference value if the polymer were 100% crystalline. All the units are in J/g and the value of ΔH_m^0 is 230.1 J/g (Sichina, 2000).

It is clearly evident from the investigation that there is not any significant effect of OBMFs on the melting temperature and % of crystallinity in PA6/OBMFs nanocomposite. It can be inferred here that there is an increasing trend of % of crystallinity in PA6 nanocomposites with the increase of filler content in the materials except in 10 wt. % which showed a drop in % of crystallinity presented in Table 7.3.

Table 7.3 % of crystallinity of PA6 and its nanocomposite using DSC

Material	ΔH_m (J/g)	ΔH_c (J/g)	$\Delta H_m - \Delta H_c$ (J/g)	$((\Delta H_m - \Delta H_c) / \Delta H_m^\circ) * 100\%$
PA6	52.83	0	52.83	22.96
PA6+2.5 wt% OBMFs	48.05	0	48.05	20.88
PA6+5.0 wt% OBMFs	49.32	0	49.32	21.43
PA6+7.5 wt% OBMFs	51.56	0	51.56	22.41
PA6+10.0 wt% OBMFs	50.73	0	50.73	22.05

The heat capacity of PA6 and its nanocomposites have been identified using the integrated two points at crystallisation peak baseline presented in Figure 7.7 (c). The heat capacity of material can be represented by the following equation:

$$C_p = (\delta Q / \delta T) \quad (7.2)$$

Where C_p is the heat capacity and expressed in JK^{-1} , Q is the heat energy in Joule and T is the temperature expressed as $^\circ\text{C}$ or K . To determine the heat capacity from a heat flow (W/g) thermogram against temperature, the Eq. (7.2) may be represented as the following:

$$C_p = (\delta Q / \delta T) \times (\delta t / \delta T) \quad (7.3)$$

In Eq. (7.3) $\delta Q / \delta t$ is the heat flow and $\delta t / \delta T$ is the reciprocal heating rate (Coleman and Craig, 1996). By using Eq. (7.3), the specific heat capacity of PA6 and PA6/OBMFs nanocomposite samples are presented in Table 7.4.

Table 7.4 Heat capacity of PA6 and its nanocomposite

Material	Mass of samples (<i>m</i>) mg	Heat capacity (J/g)	Specific heat capacity (<i>C_p</i>) Jk ⁻¹ kg ⁻¹
PA6	6.20	60.57	2523
PA6+2.5 wt% OBFs	6.30	55.87	2327
PA6+5.0 wt% OBFs	6.30	57.66	2402
PA6+7.5 wt% OBFs	7.80	60.55	2522
PA6+10.0 wt% OBFs	6.30	64.69	1321

The heat capacity of PA6/OBFs nanocomposites also shows the similar trend as % of crystallinity. It can be articulated by investigating the results in Table 7.4 that these nanocomposite materials may absorb the optimum heat energy when the polymer intercalated with the OBFs platelets. Based on the findings of this study, it may be inferred that if the OBMF content exceeds 7.5 wt. % in the PA6 content limit in PA6/OBFs nanocomposites, the material may deteriorate the heat capacity property significantly as noticeable in the results in Table 7.4. By increasing filler content from 7.5 wt. % to 10 wt. %, the heat capacity of the material decreases about 47%. Investigating these results, 7.5 wt. % OBMF may be the optimal content to ensure maximum heat capacity.

Investigating the aforementioned two important properties (% of crystallinity and heat capacity) of polyamide semi crystalline polymer nanocomposite, it is also interesting to see how the polyamide chain reacts with the crystalline nanofiller. It is believed that there are two interphases present in polyamide/layered silicate nanocomposites. One is between the crystal fraction and amorphous fraction in polyamide chain and the other one is between inorganic filler and polymer matrix (Wurm et al., 2010). The heat capacity, *C_p* at the glass transition phase is identified and using this heat capacity, the RAF is calculated using the following equations.

$$RAF = 100 - crystallinity - \Delta C_p / \Delta C_{p \text{ pure}} \quad (7.4)$$

Where ΔC_p and $\Delta C_{p \text{ pure}}$ are the heat capacity increments at the glass transition temperature of semi crystalline polymers such as PA6 and PA6/OBFs nanocomposites in this analysis and the pure amorphous polymer respectively. Schick (2017) also mentioned in DSC

application note that the RAF can also be calculated from heat capacity according to eq. 7.4 replacing the crystallinity by the nanoparticle fraction.

$$RAF = 100 - \text{filler content} - \Delta C_p / \Delta C_{p \text{ pure}} \quad (7.5)$$

Based on the eq. 7.5, the crystal fraction of neat PA6 in this analysis is avoided and hence the CF' value in Table 7. 5 for neat PA6 is 0, to describe the net incremental fraction of crystallinity in nanocomposite due to adding the inorganic filler (assumed 100% crystal phase in filler structure) and also to identify the net changes in interface between amorphous fraction of polyamide chain and nanofiller crystals. It can be concluded that the rigid amorphous fraction which is noncrystalline but does not participate in the glass transition due to parts of the molecules which are fixed because of immobilisation of molecules in polymer chain (Wurm et al., 2010 and Schick et al., 2001).

Table 7. 5 TIF determination using DSC

Material	MAF	CF	CF'	RAF= 100- MAF-CF	RAF'= 100- MAF-CF'	TIF
PA6	27.26	22.96	0.00	49.78	72.74	72.74
PA6+2.5 wt%						
OBFs	27.46	20.88	2.50	51.66	70.04	72.54
PA6+5.0 wt%						
OBFs	58.91	21.43	5.00	19.66	36.09	41.09
PA6+7.5 wt%						
OBFs	46.01	22.41	7.50	31.58	46.49	53.99
PA6+10.0 wt%						
OBFs	55.04	22.05	10.00	22.91	34.96	44.96

Investigating the measured curves at T_g as illustrated in Figure 7.7 (a) there is not any significant changes in glass transition temperature for neat PA6 and PA6/OBFs nanocomposites. To determine the RAF and MAF value of PA6 and its nanocomposite, the heat capacity peak at T_g was considered. The reference value for $\Delta C_{p \text{ pure}}$ for PA6 and its nanocomposites was 0.15 J/(gK) in this study (Wurm et al., 2010).

Considering both eq. 7.4 and eq. 7.5 there is a good agreement found in this analysis termed as total immobilised fraction (TIF) which is the sum of either RAF and CF or RAF' and CF', highlighted in Table 7. 5.

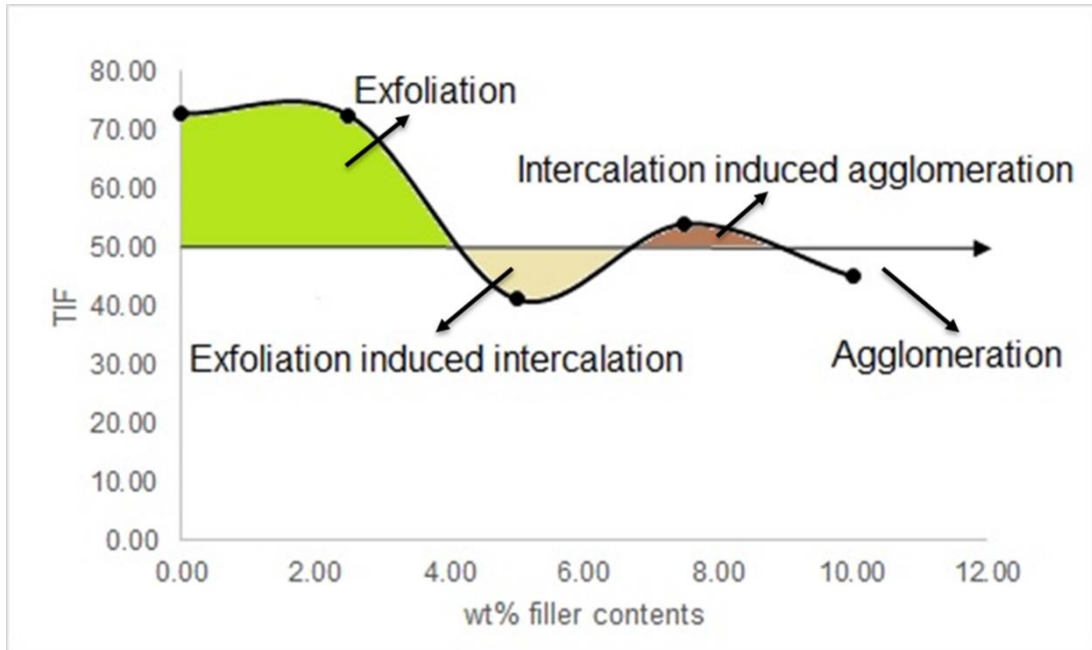


Figure 7.8 Relation between TIF and dispersion behaviour of OBMFs in PA6 matrix

From the findings in Table 7.5 and the Figure 7.8, one can infer that when the ratio between TIF and MAF is 1 (50% TIF line in Figure 7.8) in PA6/OBMFs nanocomposites, there are three significant points found in its sigmoidal curve. These three points represent exfoliation (first point), intercalation (second point) and agglomeration (third point).

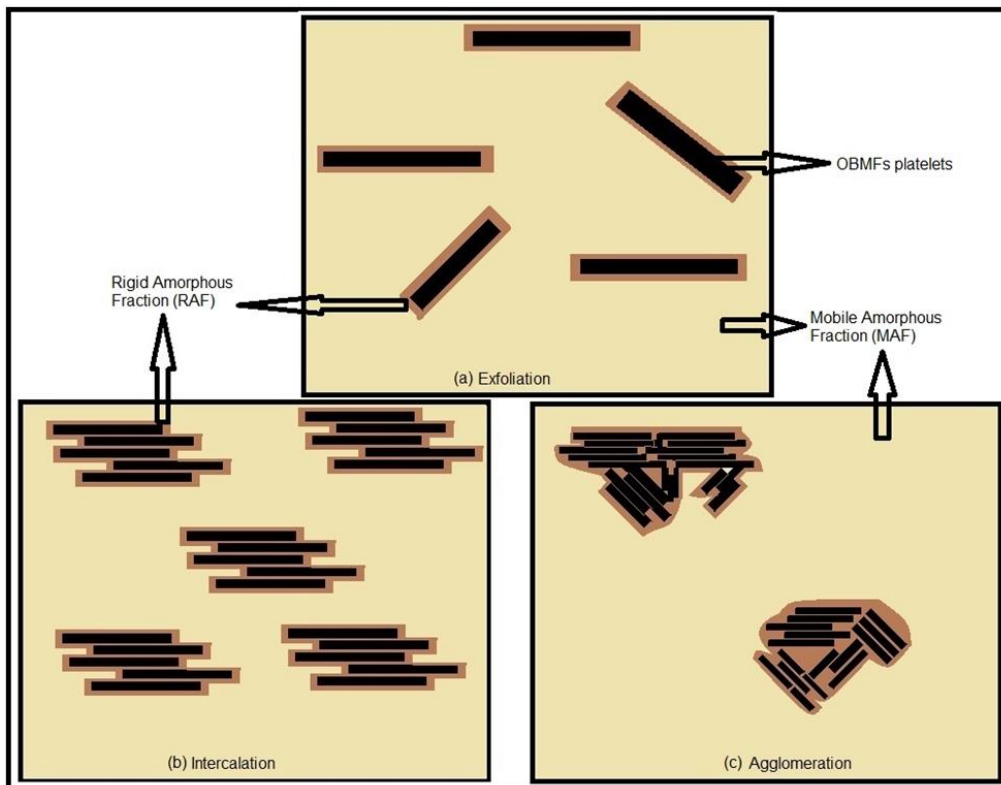


Figure 7.9 Schematic diagram of OBMFs platelets associated with MAF and RIF of PA6 matrix

It is also articulated here that from the Figure 7.8 one can conclude that upto 4.2 wt% OBMFs content generate exfoliation, 4.2 to 6.8 wt% OBMFs content influence exfoliation induced intercalation, 6.8 to 9 wt% OBMFs incur intercalation induced agglomeration and above 9 wt% OBMFs cause agglomeration in the nanocomposite structure. This MAF, RAF and OBMFs platelets and their schematic structures are shown in Figure 7.9.

7.3.6. X-ray Diffraction (XRD) analysis

Figure 7.10 (a) displays the wide-angle XRD patterns of OBMFs nanoclays and PA6/OBMFs nanocomposites associated with different weight percentage of OBMFs in stacked form whereas in Figure 7.10 (b) displays the overlaid XRD patterns of nanocomposite materials in common scale. Low-angle peaks in WAXD assists in quantifying the changes in layer spacing. Considering low-angle in WAXD pattern in Figure 7.10 (a) the graph clearly shows that the original peak of OBMFs (marked by red circle in Figure 7.10) is completely absent in the diffraction patterns of PA6 with 2.5 wt%, 5 wt% and 10 wt% OBMFs nanocomposites (marked by green circle in Figure 7.10) demonstrating that the clay is dispersed on a nanometric scale in these systems (Scarfato et al., 2016). XRD patterns of polymeric layered silicates are well established in the literature. Comparing qualitatively the XRD patterns of the materials in this study and literature findings, it can be concluded that OBMFs is exfoliated in PA6 with 2.5 wt%, 5 wt% and 10 wt% nanocomposites and it is intercalated in PA6 with 7.5 wt% OBMFs nanocomposite (marked by blue circle in Figure 7.10) (Vaia and Giannelis, 1997; Liu et al., 2003 and Ray and Okamoto, 2003). However, by monitoring the position, shape, and intensity of the basal reflections from phase initiation in PA6 with 10 wt% OBMFs (marked by golden circle in Figure 7.10) it can be assumed that the incremental loading of fillers (here more than 7.5 wt% OBMFs) generates agglomeration in PA6/OBMFs nanocomposites.

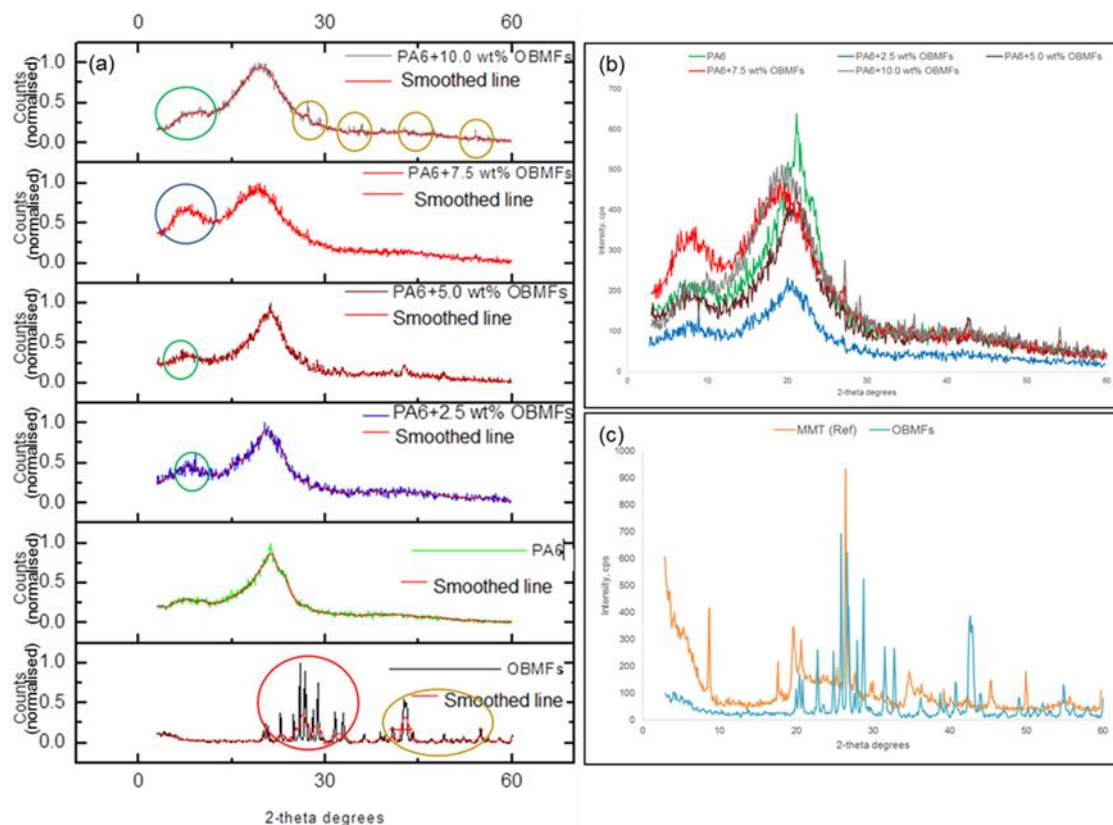


Figure 7.10 WAXD patterns of (a) OBMFs and PA6/OBMFs nanocomposite in stack form; (b) nanocomposite in common scale; and (c) OBMFs and MMT

Figure 7.10 (c) shows the peaks of OBMFs nanoclays compared with those of the different minerals present in the montmorillonite sample (reference material).

In this study full dispersion is not achieved which is attributed due to the insufficient shear stress and the short residence time in extrusion process. This poor dispersion is noticeable in SEM images in Figure 7.4. From the findings from literature it is articulated that PA6 exhibited two dominant monoclinic crystalline forms α and γ (Chiu et al., 2005). Although it is highlighted in the literature that the XRD peaks of α form at room temperature are located around $2\theta = 21$ and 24° , and also indexed as (200) and (002) / (202) diffractions, in this study a strong peak attributed of α form is found at 21° (Chiu et al., 2005 and Cho and Paul, 2001). However, at 23° a weak peak is noticeable in composite materials. There are a few small but sharp peaks are noticeable in PA6 with 5 wt% OBMFs, PA6 with 7.5 wt% OBMFs and PA6 with 10 wt% OBMFs nanocomposites which is evident of the influence of barite phases present in OBMFs and the presence of this barite phases in PA6 with 5 wt% OBMFs nanocomposite is presented in Figure 7.3 as an example. The strong peaks of barite is clearly noticeable at $2\theta = 27.2^\circ, 29.1^\circ, 35.9^\circ, 42.7^\circ, 47.3^\circ$ and 54.1° locations which is believed to influence PA6 with 10 wt% OBMFs nanocomposite behaving as a thermal conductive material. It is noticeable in Figure 7.11 (a) and (b), numerous peaks were

appeared and smoothing the XRD patterns was avoided due to the aim of this study was to identify the specific peaks incurred by the specific phases of minerals present in the material. Matching the peaks with their degree of intensity of different nanocomposite materials with the help of Rietveld refinement leading to a clear representation of new peaks addition in nanocomposite material due to addition of OBMFs which is composed of different clay minerals.

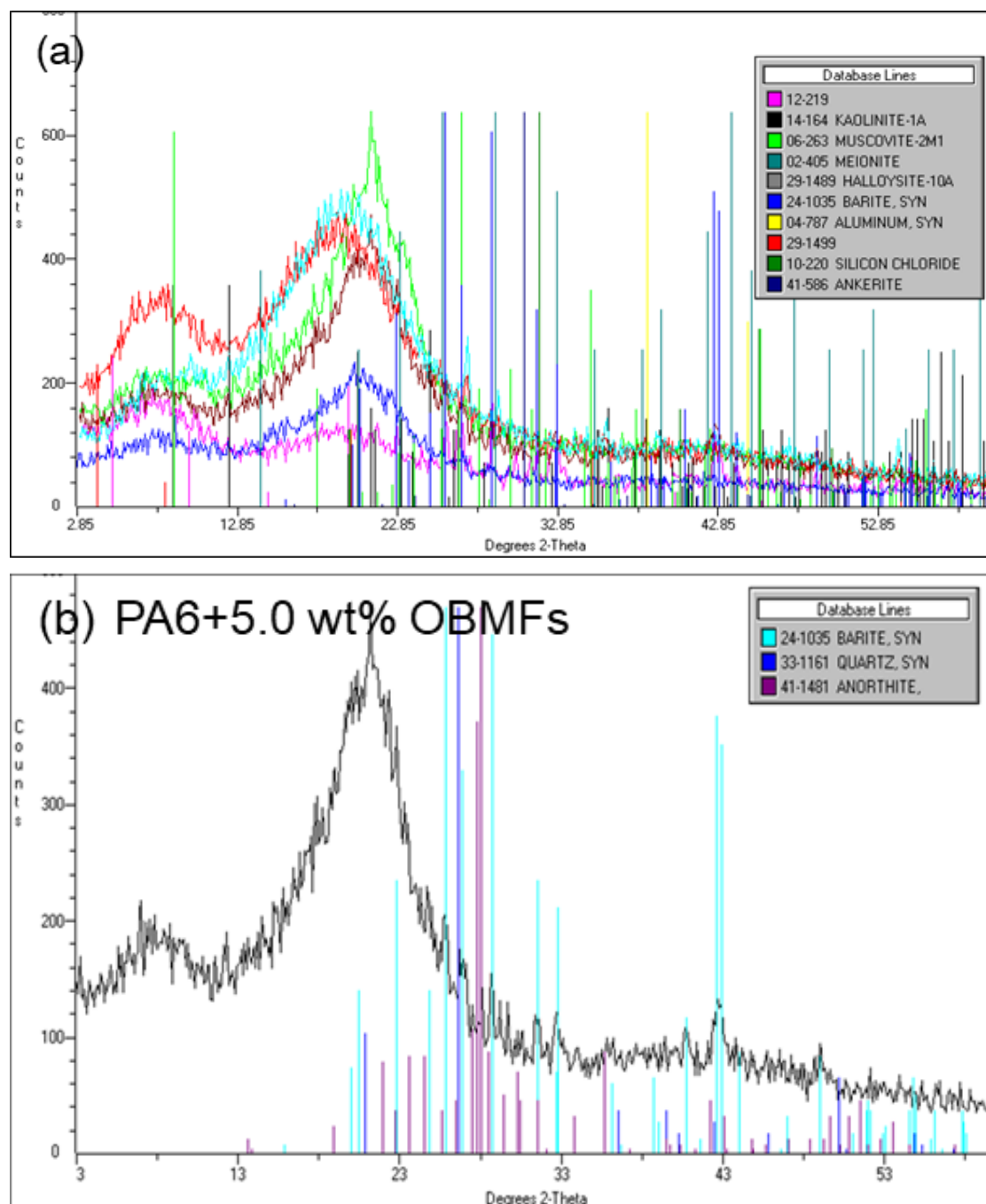


Figure 7.11 WAXD patterns of (a) mineral composition of different nanocomposite; (b) new peaks identification in nanocomposites

Figure 7.11 (a) shows the different mineral phases present in nanocomposite materials, in particular the different clay minerals present in nanocomposites. By using Rietveld refinement software, the peaks corresponding to the sets in JCPDS cards 12-219 and 29-1499 were identified as montmorillonite, as presented in Figure 7.11 (a). Since OBMFs is a complex mixture of different minerals and compounds, it is difficult to present a complete compositional database profile, but from this study it is highlighted that muscovite, barite and montmorillonite are the main dominant clay mineral phases present in PA6/OBMFs nanocomposites.

The d_{001} spacing was calculated from peak positions using Bragg's law $n\lambda = 2d \sin \theta$ where λ is the wavelength of X-ray radiation used in the experiment, d represents the distance between diffraction lattice planes and θ is the half diffraction angle. In the case of OBMFs (Figure 7.12 a), a diffraction peak at $2\theta = 7.500^\circ$ was observed which corresponds to a d -spacing of 9.1 Å. This is very close to the XRD pattern of neat PA6 (Figure 7.12 a) at $2\theta = 8.000^\circ$ with a d -spacing of 11.042 Å. The d -spacing of PA6 with 2.5 wt% and 5 wt% OBMFs nanocomposites were identified 14.477 Å and 15.768 Å corresponding the reflection peaks at $2\theta = 6.100^\circ$ and $2\theta = 5.600^\circ$ respectively. The d -spacing of PA6 with 7.5 wt% and 10 wt% OBMFs nanocomposites were determined at $2\theta = 6.700^\circ$ and $2\theta = 6.400^\circ$, respectively, which represent the values of 13.182 Å and 13.799 Å. The trend of d -spacing increment is not consistent. The incremental trend of d -spacing in PA6/OBMFs is noticeable with PA6 with 2.5 wt% and 5 wt%. Surprisingly d -spacing reduces in PA6 with 7.5 wt% OBMFs and then a little increase of d -spacing is observed in PA6 with 10 wt% nanocomposites. It can be inferred here that exfoliation of clay minerals may increase the basal spacing in PA6 with 2.5 and 5 wt% OBMFs nanocomposites, whereas intercalation of clay platelets may influence the basal spacing in PA6 with 7.5 wt% OBMFs nanocomposite. The basal spacing in PA6 with 10 wt% OBMFs is not understood clearly. On investigating the SEM images in Figure 7.4, it might be anticipated that PA6 with 10 wt% OBMFs nanocomposites may possess agglomeration of platelets and also some platelets may have exfoliated locally.

Furthermore, Kim et al. (2002) described two parameters which can dictate the degree of exfoliation – Bragg's $d_{(001)}$ and apparent crystallite size of silicate (D_c). In addition of the interlayer spacing which is presented in previous paragraph, full width at half maximum (FWHM) of the (001) reflections is also useful to identify the degree of filler dispersion in this study. The FWHM of OBMFs, PA6 with 2.5 wt% OBMFs, PA6 with 5 wt% OBMFs, PA6 with 7.5 wt% OBMFs and PA6 with 10 wt% OBMFs are 0.600, 0.700, 0.400, 1.000 and 0.600 respectively. The broader the width of the diffraction peak, the smaller the thickness of silicate layers and the relation of the thickness of silicate layers with the degree of exfoliation is highlighted in the literature (Kim et al., 2002 and Strawhecker and Manias, 2000).

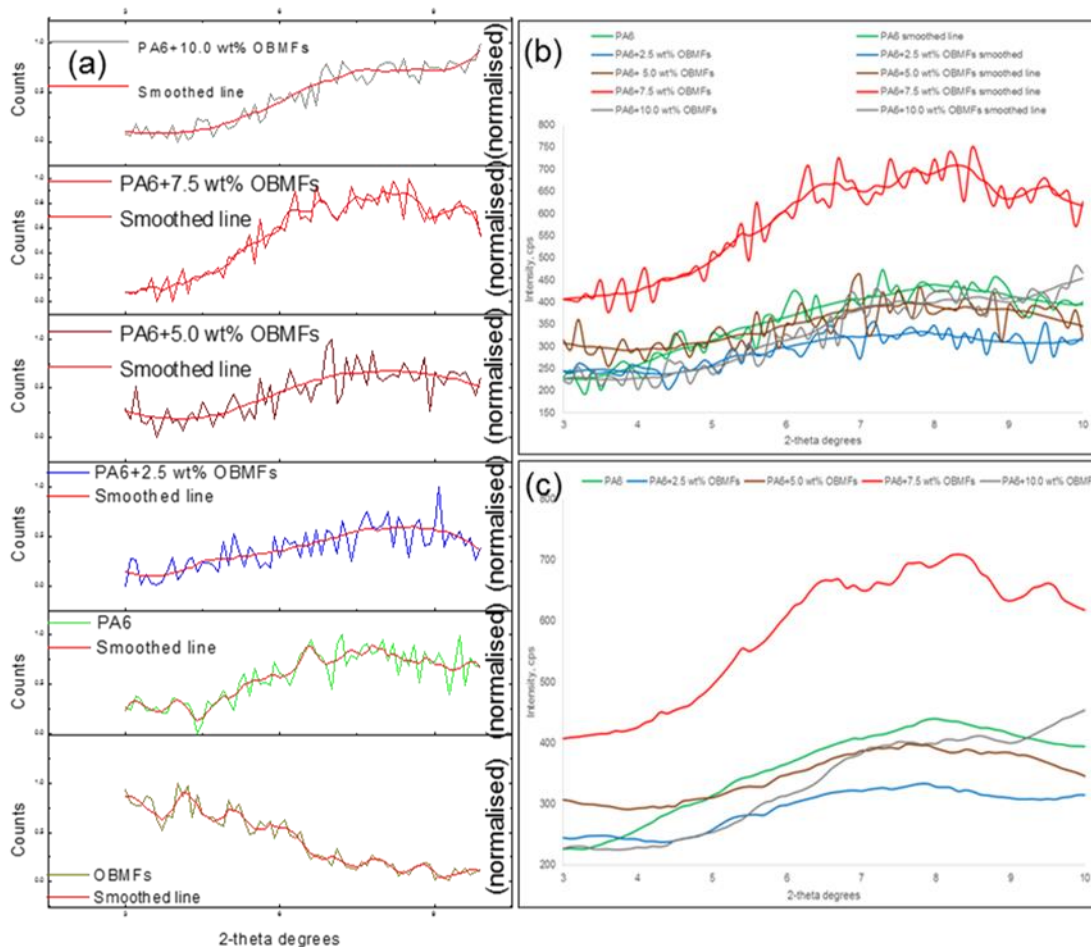


Figure 7.12 SAXD patterns of (a) OBMFs and PA6/OBMFs nanocomposite in stack form; (b) nanocomposite in common scale; and (c) smoothed nanocomposite profile

It can be assumed considering the FWHM data that OBMFs exfoliated in PA6 with 5 wt% OBMFs and this layered silicates intercalated in PA6 with 7.5 wt% OBMFs. It was expected that the FWHM of PA6 with 2.5 wt% would be the lowest number, but this inconsistent result is not clearly understood.

X-ray diffraction patterns of the nanocomposites prepared with different weight percentage of OBMFs contents such as 2.5 wt%, 5 wt%, 7.5 wt% and 10 wt% are illustrated in Figure 7.12 b (original data with smoothed line) and Figure 7.12 c (smoothed line only). Observing Figure 7.12 a, c, the basal space in PA6 with 2.5 wt% and 5. wt% OBMFs nanocomposites is wider than the basal space in neat PA6, resulting that the XRD pattern is wider than that of PA6. The presence of very weak XRD peak/crest in PA6 with 2.5 wt% and 5 wt% OBMFs nanocomposites probably suggests the formation of an exfoliated nanostructure. However, PA6 with 7.5 wt% OBMFs nanocomposite shows a distinct sharp peak, which may indicate the formation of an intercalated nanostructure. The XRD pattern in PA6 with 10 wt% OBMFs shows both intercalation and exfoliation characteristics. The XRD patterns in PA6 with

10 wt% OBMFs nanocomposite show exfoliated characteristic up to $2\theta = 5.4^\circ$ location, whereas the XRD pattern shows not the same as exfoliated structure or intercalated structure. The intensity of the diffraction in nanocomposites except PA6 with 7.5 wt% OBMFs nanocomposites also suggests the disordered feature of clay platelets in the nanocomposite. However, the sharp XRD pattern in PA6 with 7.5 wt% OBMFs nanocomposite indicates the intercalation characteristic of platelets in the PA6 matrix.

7.3.7. TEM analysis

TEM images of OBMFs filled PA6 polymer nanocomposites are shown in Figure 7.13. A generally good state of dispersion was observed in PA6 polymer matrix. There were small clusters of OBMFs platelets observed in PA6 matrix in lowest concentration of fillers content such as 2.5 wt% of OBMFs in PA6 matrix in this study. However, these clusters tended to create agglomeration in higher weight percentage of OBMFs in PA6 matrix which is shown in Figure 7.13 (c) and (d).

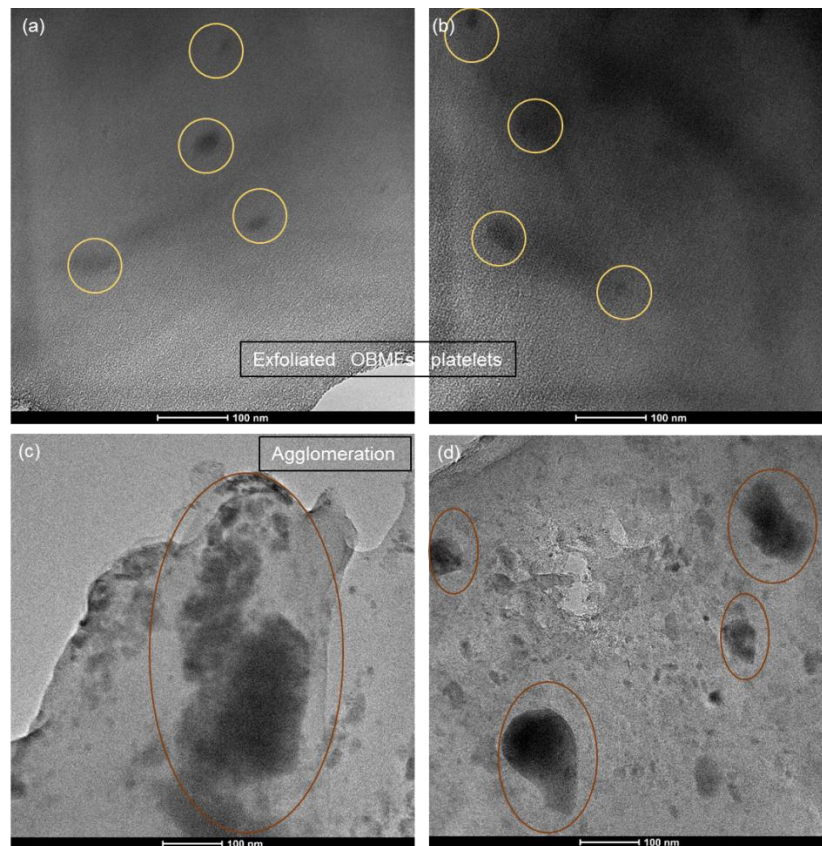


Figure 7.13 TEM images of PA6 with 2.5 wt% OBMFs nanocomposites (a) and (b) and PA6 with 10.0 wt% OBMFs nanocomposites (c) and (d)

The size of the agglomerates was in the range of 100 to 150 nm, whereas the size of the small clusters was in the range of 10 to 30 nm. From the micrographs in Figure 7.13 (a) (b), it could be observed that OBMFs was exfoliated randomly. However, there were agglomerates noticeable in Figure 7.13 (c) (d), which can be inferred that an incremental addition of OBMFs in PA6 matrix may hinder the platelets to be separated from each other. In addition, the higher content of OBMFs is prone to cause agglomeration in PA6 matrix and a number of local exfoliation is also visible which is observed in Figure 7.13 (c) (d).

7.4. Conclusion

In this work, we have investigated the thermal degradation behaviour of PA6 nanocomposite containing oil based drilling fluid waste as nanofiller. PA6/OBMFs nanocomposite exhibit different characteristics under different conditions mainly due to variation in nanomorphology (exfoliation, intercalation and presence of tactoids or agglomeration). From the findings in TGA investigation, OBMFs platelets exfoliated in PA6 matrix in PA6 with 5 wt% OBMFs nanocomposite showed maximum heat resistant property (maximum D1/2 time), OBMFs platelets intercalated in PA6 matrix in PA6 with 7.5 wt% OBMFs nanocomposite showed optimum heat absorbance capacity whilst PA6 with 10 wt% OBMFs nanocomposite showed maximum thermal stability. Furthermore, the heat capacity data at T_g using DSC provided very useful RAF and MAF information which depicts a sigmoidal curve showing exfoliation point, exfoliation induced intercalation point, intercalation induced agglomeration point and finally the agglomeration point. This new technique to identify the nanomorphology is step forward in the mechanical and thermal characterisation of PA6/OBMFs nanocomposites.

Chapter 8: Mechanical properties of PA6/ Oil Based Mud Fillers nanocomposites

8.1. Introduction

Polymer/montmorillonite (MMT) nanocomposites become an interesting area of research since Toyota group first successfully developed PA6/MMT nanocomposites in 1987 (Choi et al., 2001; Huskić and Žigon, 2007 and Ma et al., 2003). Since 1987 numerous reports have been published and claiming the improvements of different properties of material including increased stiffness and strength (Shah et al., 2016 and Zare et al., 2019), improved thermal stability (Leszczyńska et al., 2007, Davis et al., 2004, Lakshmi et al., 2008), reduced flammability (Qin et al., 2004 and Li et al., 2009), improved chemical and solvent resistance (Wang et al., 2012 and Huang et al., 2001), enhanced energy absorption (Sun et al., 2009, Silva et al., 2013) and augmented gas barrier properties (Priolo et al., 2011, Kalendová et al., 2013) by reinforcing only a few percent of MMT platelets in polymer matrix. MMT platelets are generally tightly stacked together due to the strong electrostatic forces between them and inhibit them to easily exfoliate in most polymers due to the incompatible nature of chemical features between MMT and polymer matrix surfaces (Zheng et al., 2004; Xie et al., 2001 and Liu, 2007).

In our previous work (shohel et al., 2017, 2018, 2019a and 2019b), detailed investigations were completed based on the morphological, structural and thermal degradation study of heat treated reclaimed nanoclay reinforced PA6/OBMFs nanocomposites. The present work is an extension of previous study showing the influence of this novel filler in different mechanical properties of PA6/OBMFs nanocomposites.

8.2. Experiments

8.2.1. Materials

The PA6 (AlphalonTM 27C) manufactured by Grupa Azoty was donated by Grupa Azoty. It has a melting point of 220°C, relative viscosity of 2.7 ± 0.10 , density 1.13 g/cm^3 , cylindrical chip shape and chip size is 2.5 mm. the spent OBM slurry was supplied in kind by a local oil and gas service company in Aberdeen, United Kingdom.

8.2.2. OBMFs manufacturing process

The processing method of spent oil-based mud used in this chapter is described in section 3.2.1.

8.2.3. PA6/OBMFs nanocomposite manufacturing process

The method to manufacture PA6/OBMFs nanocomposites in this chapter is described in section 7.2.3.

8.2.4. Testing and characterisation

The sample processing and SEM equipment settings were mentioned in previous chapter in section 7.2.4.

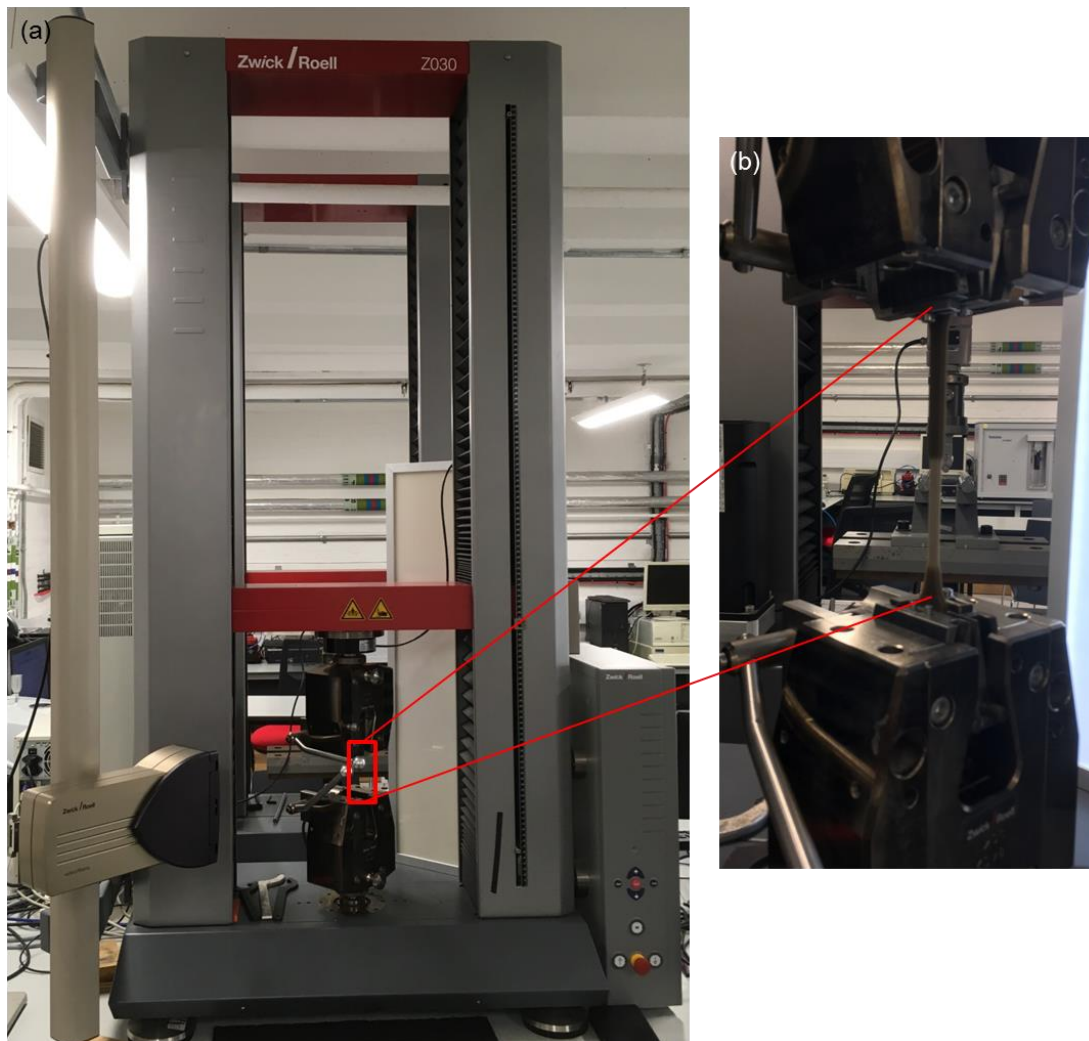


Figure 8.1 Tensile test of PA6/OBMFs nanocomposites: (a) test rig set up and (b) plastic deformation of sample is on progress

Tensile tests were performed according to the EN ISO 527 standard on a Zwick (Ulm, Germany) Z030 universal testing machine. The gauge length was 80 mm and the test speed was 2 mm/min. The test process including elongation was monitored by video extensometer. Figure 8.1 (a) shows the test rig for tensile test. A close visualisation of plastic deformation of sample is presented in Figure 8.1 (b).

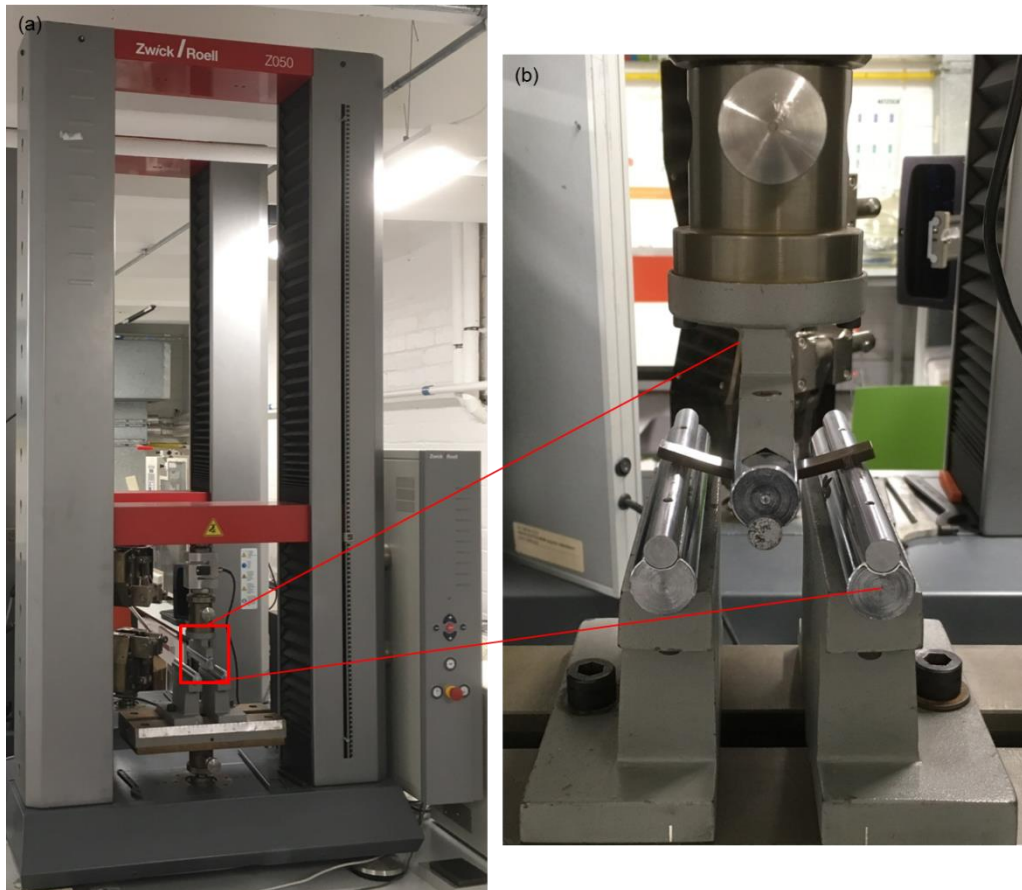


Figure 8.2 Flexural test of PA6/OBMFs nanocomposites: (a) test rig set up and (b) deformation of sample is on progress

The latest technology developed by Zwick, the laserXtens is the technique which is able to determine the extension without marking on the sample surface or other contact extensometer. In this technique, the surface structure of sample is considered as a fingerprint to generate a virtual measurement mark. However, calibration was carried out to confirm the accuracy of the measurement before the test performed. When the gauge length and other dimension including width and thickness of samples updated in the data acquisition software as part of the method development, the laser targets the specific point on the sample surface. When the sample surface is being changed and thus the speckle pattern, the laser detector continuously follows the extension occurred and is continuously evaluated during the specimen deformation. The more detailed information is available in the literature

published by Dripke (2008). The data acquisition software TestXpert III reported the results while the test was performed including the raw data in excel spreadsheet form. The calculation based on these raw data confirmed the accuracy of the test performed.

Different mechanical properties were determined based on the acquired load-extension data. The equations followed to convert applied load to stress and the extensions to strain as follows:

$$\text{Stress} = \frac{\text{Force}}{\text{original cross-section area}} \text{ unit (N/mm}^2\text{)} \quad (8.1)$$

$$\text{Strain} = \frac{\text{Change in length}}{\text{gauge length}} \text{ (non-dimensional)} \quad (8.2)$$

The stiffness of these samples was identified by measuring Yong's modulus (E) which determined the stress required to cause a unit strain in the sample. Using the load-extension data, different tensile properties were determined and presented the data in Figure 8.6 and 8.7.

The three point bending tests were performed according to the EN ISO 178 standard on a Zwick (Ulm, Germany) Z050 universal testing machine. The span length for the tests was 64 mm and the test speed of 2 mm/min. Figure 8.2 (a) shows the test rig for flexural test. A close visualisation of sample deformation is presented in Figure 8.2 (b).

The Charpy impact tests were performed according to the EN ISO 179 standard with a on a Zwick (Ulm, Germany) Impactor instrument using both notched and un-notched specimens. Figure 8.3 shows equipment setting to prepare v-notch samples for impact test. Figure 8.3 (a) shows a set of 5 samples were in progress for V-notch test. The notch was 'A' type with a radius of 0.25 mm notch tip, 45° angle and 2 mm depth.

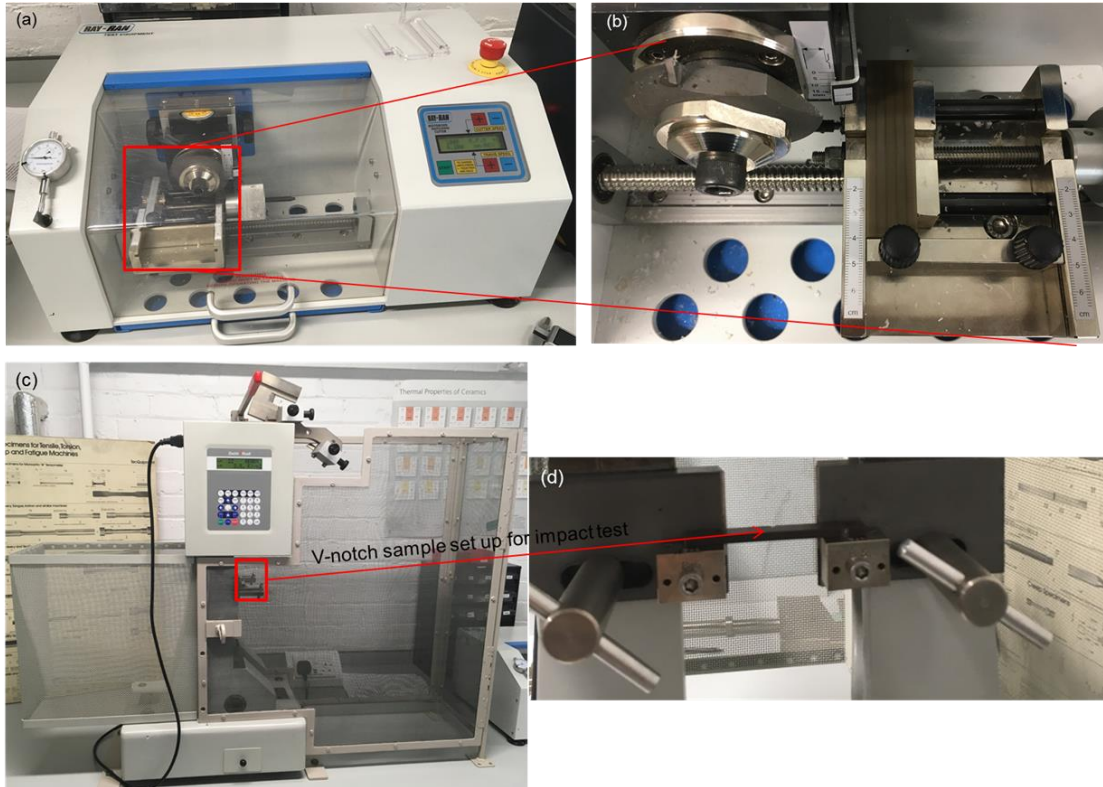


Figure 8.3 Impact test of PA6/OBMFs nanocomposites: (a) V-notch sample cutter; (b) a set of 5 samples are on progress for v-notch sample; (c) impact test rig and (d) V-notch sample sitting on sample holder for test

The cross section of the notched specimens was $4 \times 8.1 \pm 0.5\%$ variance and the cross section of un-notched specimens was $4.01 \times 9.9 \pm 0.4\%$ variance among different samples. Figure 8.3 (c) shows the impact test rig and Figure 8.3 (d) shows a V-notch sample was sitting on the sample holder during the test.

The energy absorbed by the sample was recorded during test and impact strengths α_{cU} and α_{cN} were calculated with the following equation (Deák et al., 2010):

$$\alpha_{cU} \text{ or } \alpha_{cN} = \frac{E_c}{h \cdot w} \cdot 10^3 \quad (8.3)$$

Where E_c is the energy absorbed by the tested sample, h is the thickness and w are the width of the samples. For notched test, w is the residual width of the samples.

Dynamic mechanical analysis (DMA) was performed using Perkin Elmer DMA 8000. The sample dimension was $11.5 \text{ mm} \times 10 \text{ mm} \times 4 \text{ mm}$ and the testing temperature ranged from 25°C to 70°C at the temperature ramp of $2^\circ\text{C}/\text{min}$. The samples were tested under single cantilever-rectangle mode.

8.3. Results and discussion

8.3.1. Morphology of PA6/OBMFs nanocomposites

The difference in OBMFs dispersion in PA6 matrix and micromechanical deformation behaviour among different nanocomposites is obvious from SEM observations of fractured surfaces is shown in previous chapter in Figure 7.4. A lesser extent of plastic deformation is noticeable in nanocomposites with 7.5 and 10 wt% OBMFs contents in comparison with neat PA6 matrix and nanocomposites with 2.5 and 5 wt% OBMFs loadings. For the PA6/OBMFs nanocomposites specimens studied at room temperature, significant particles dictating dispersion characteristics showed in Figure 7.4.

The morphology of OBMFs is presented in Figure 7.4 (a) which illustrates the shape and size of clay platelets present in OBMFs. The fracture surface in PA6 matrix demonstrates elastic deformation in Figure 7.4 (b) and is different from brittle fracture. However, the matrix was plastically deformed due to addition of OBMFs in matrix and the degree of plastic deformation increased with the incremental addition of OBMFs in PA6 matrix. The elastic deformation is visible in Figure 7.4 (c) and Figure 7.4 (d) where clay platelets were closely embedded in matrix. The matrix/OBMFs adhesion was much stronger in Figure 7.4 (e) and Figure 7.4 (f) such that the clay particles had to break instead of just pulling out of the matrix. This explains the higher tensile strength and Young's modulus of OBMFs reinforced polyamide while observing the tensile test.

8.3.2. Tensile properties of PA6/OBMFs nanocomposites

In this study, tensile properties of polyamide-6/OBMFs nanocomposites were investigated. a set of five samples for each material were tested which are shown in Figure 8.4 (a-e). The average data is taken into account to identify different mechanical properties of each material.

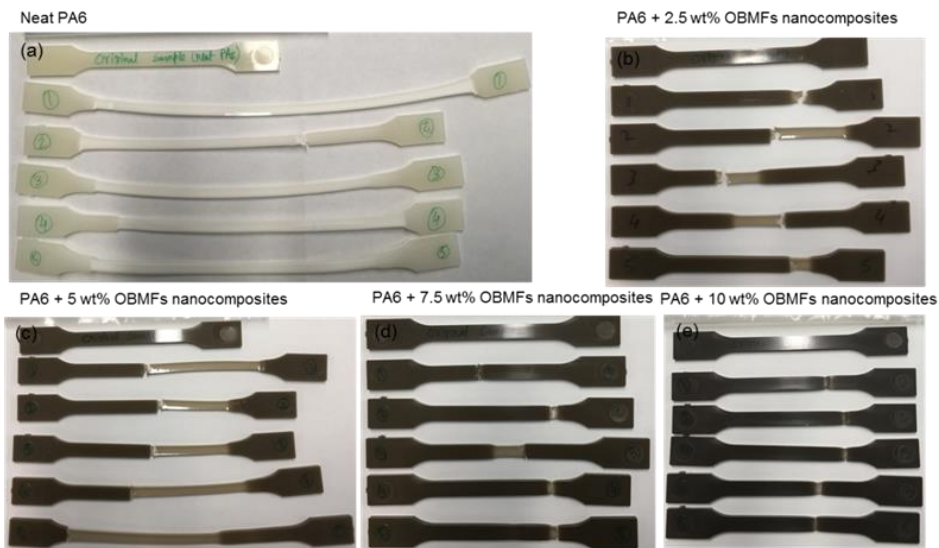


Figure 8.4 Tensile test samples before and after the test

Figure 8.4 (a-e) presents the plastic deformation of materials by observing the colour changes in sample while the sample was under stress during tensile test. Figure 8.5 illustrates the tensile stress vs tensile strain curves for PA6/OBMFs nanocomposites.

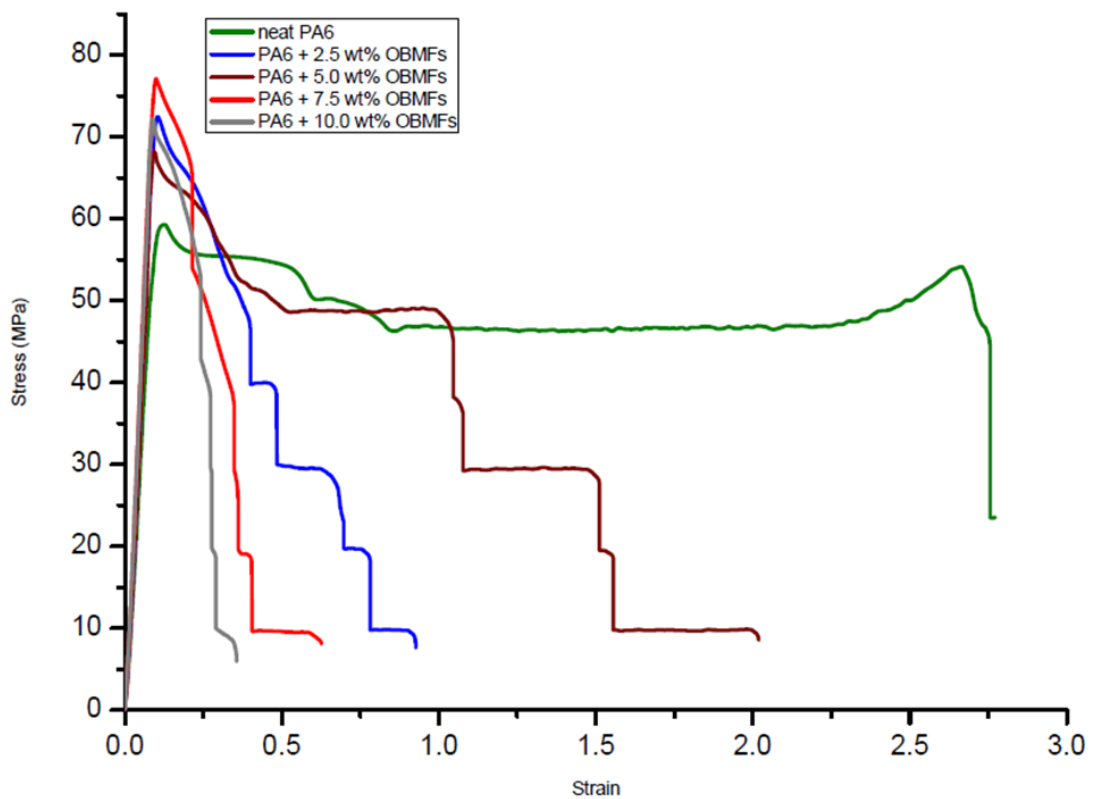


Figure 8.5 Stress-strain curves of neat PA6 and PA6/OBMFs nanocomposites

The materials showed an incremental brittle behaviour without yield point which are observed in Figure 8.4 (a-e) and stress-strain curves in Figure 8.5. It can be observed that the Young's Modulus was improved with the OBMFs loading from 0 to 10 wt% in Figure 8.6. On the other hand, the deformation failure at lower stress and strain values are increases as the filler concentration decreases from 10 to 0 wt% (neat PA6) which is highlighted in Figure 8.5.

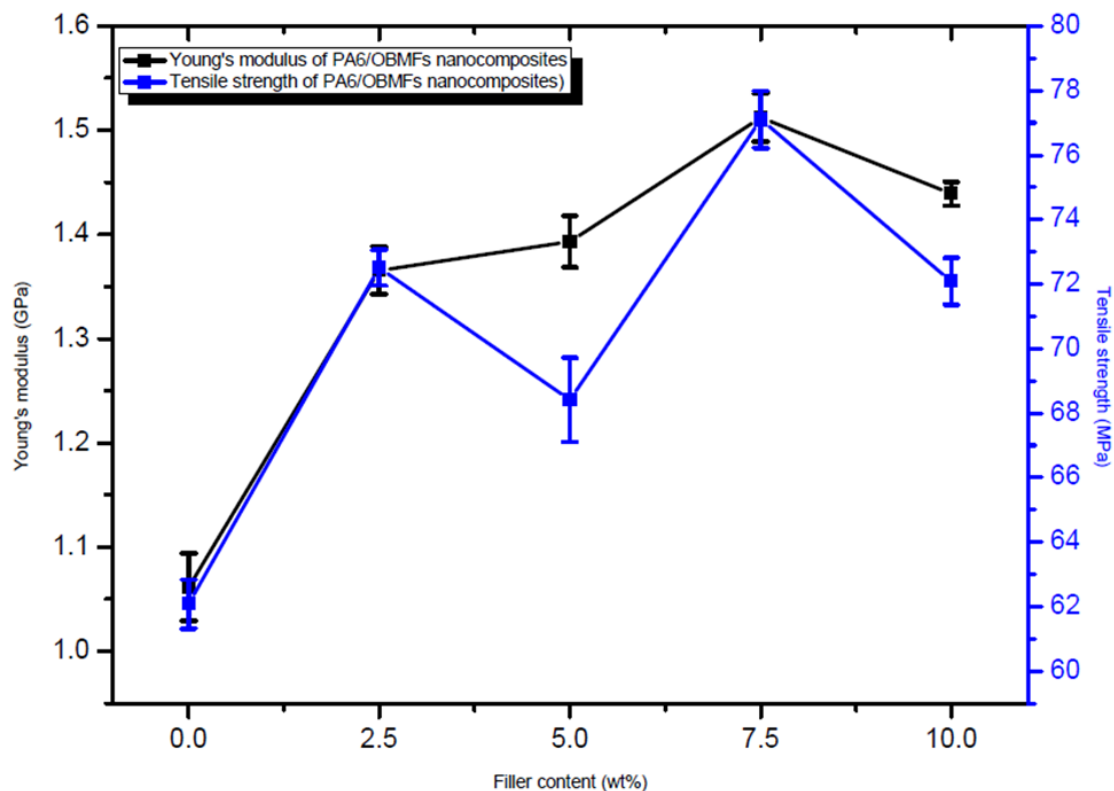


Figure 8.6 Young's modulus and tensile strength of neat PA6 and PA6/OBMFs nanocomposites with filler loading of 2.5, 5, 7.5 and 10 wt%

This deformation characteristic indicates the improvement in brittleness in nanocomposites due to the OBMFs reinforcement in PA6 matrix. These results can be explained by the relation highlighted in our previous report (shohel et al., 2019a and shohel et al., 2019b) where the effect of OBMFs loadings on structural and dispersion characteristic has been presented. It was found in that previous study that 2.5 and 5 wt% of OBMFs loadings in PA6 matrix showed exfoliation of OBMFs in PA6 matrix whereas 7.5 wt% of OBMFs in PA6 matrix showed intercalation of OBMFs platelets and 10 wt% OBMFs loading in PA6 matrix resulting agglomeration of OBMFs in PA6 matrix. The Young's modulus and tensile strength results highlighted in Figure 8.6 indicates that the larger the diameter of OBMFs, the stress concentration factor is lower, but the maximum stress acts when the cross sectional area of filler increases. Based on this argument, the superior Young's Modulus and tensile strength

can be explained when OBMFs were intercalated and agglomerated in PA6 with 7.5 and 10 wt% OBMFs nanocomposites respectively. The Yong's moduli were increased by 42% and 35% in PA6 with 7.5 and 10 wt% OBMFs nanocomposites respectively. In addition to Young's moduli, the tensile strength was increased by 24% and 16% in PA6 with 7.5 and 10 wt% OBMFs nanocomposites respectively.

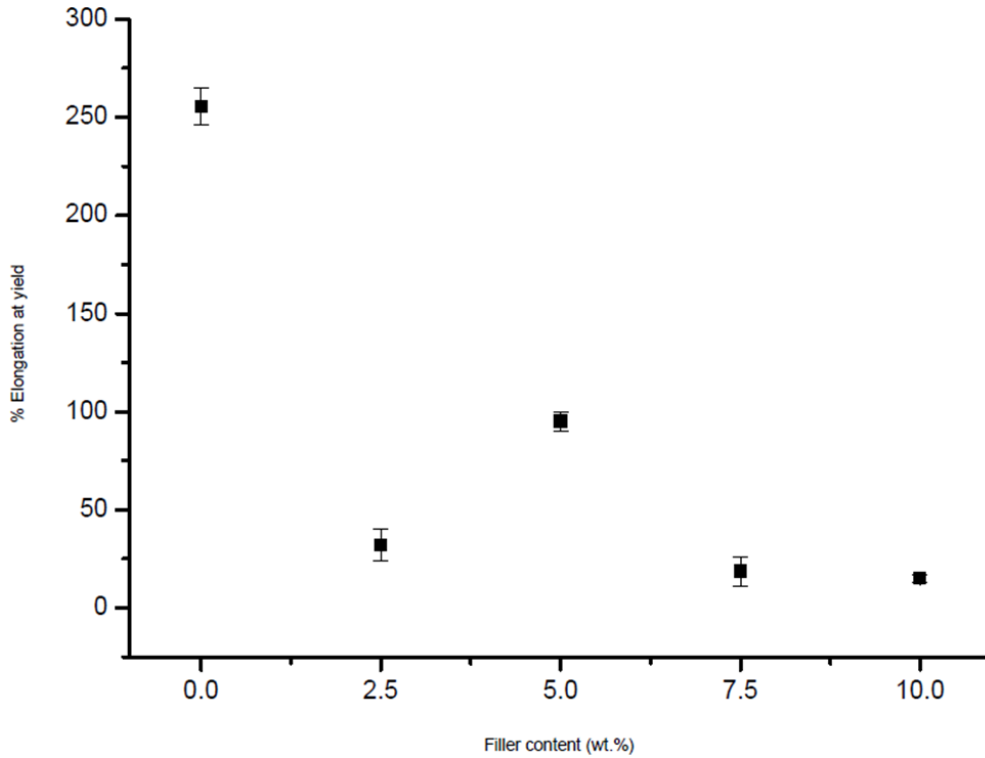


Figure 8.7 Comparison of percentage elongation at yield of neat PA6 and OBMFs reinforced PA6 nanocomposites

The percentage of elongation was decreased by 236% and 240% in PA6 with 7.5 and 10 wt% OBMFs nanocomposites respectively. The relation between stress concentration and dispersion behaviour of OBMFs in PA6 matrix also helps to understand the reduction of percentage elongation among neat PA6 and PA6/OBMFs nanocomposites which is presented in Figure 8.7.

The fractured surfaces of the tensile samples tested at 23°C correspond to an increasing trend of brittle fracture of samples as the filler concentration increases which is presented in Figure 8.4 (a-e). Figure 8.4 (a-e) illustrates the decreasing tendency of plastic deformation in samples transforming ductile fracture of samples to brittle failure of samples due to increasing the filler concentration from 0 to 10 wt% of OBMFs in PA6 matrix. Observing the effect of the nano-fillers content on mechanical properties and failure behaviour showed that

the increase of OBMFs in PA6 matrix influenced the brittleness of the material. It can also be highlighted observing the morphology and tensile test results that the distances among the OBMFs in PA6 matrix increase with the OBMFs loading from 0 to 10 wt% in PA6 matrix which hinders chain scissioning reflecting the mechanical properties and fracture behaviour of materials.

8.3.3. Flexural properties of PA6/OBMFs nanocomposites

In this study, flexural properties of polyamide-6/OBMFs nanocomposites were investigated. A set of five samples for each material were tested which are shown in Figure 8.8 (a-e). The average data is taken into account to identify different mechanical properties of each material.

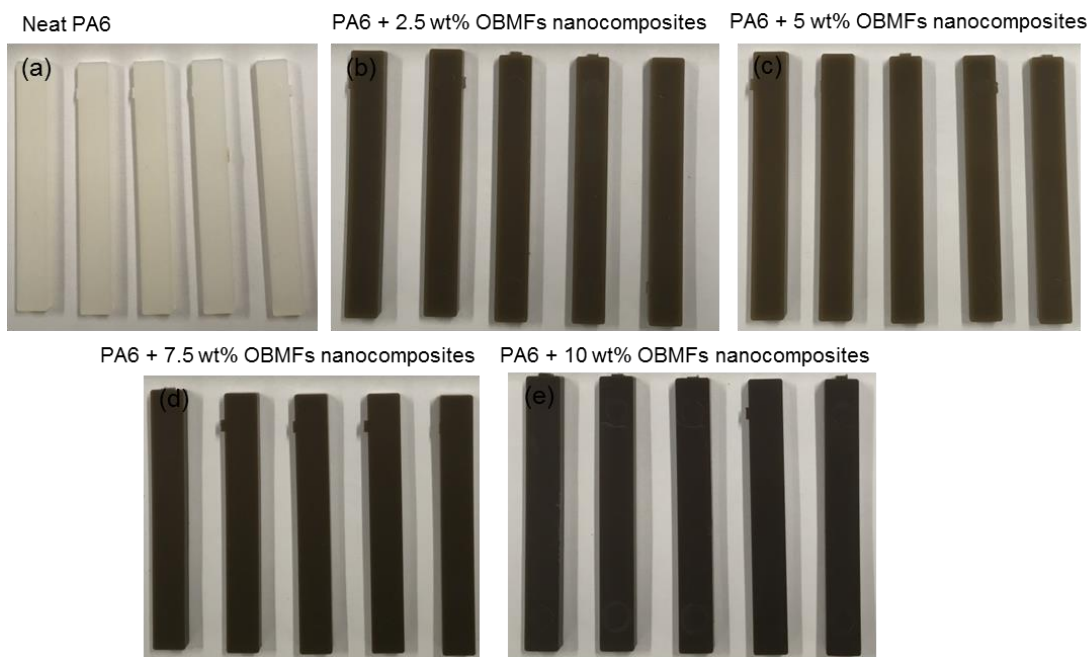


Figure 8.8 Presentation of flexural test sample after the test

To identify different flexural properties of neat PA6 and PA6/OBMFs nanocomposites, flexural stress-strain curves were presented in Figure 8.9.

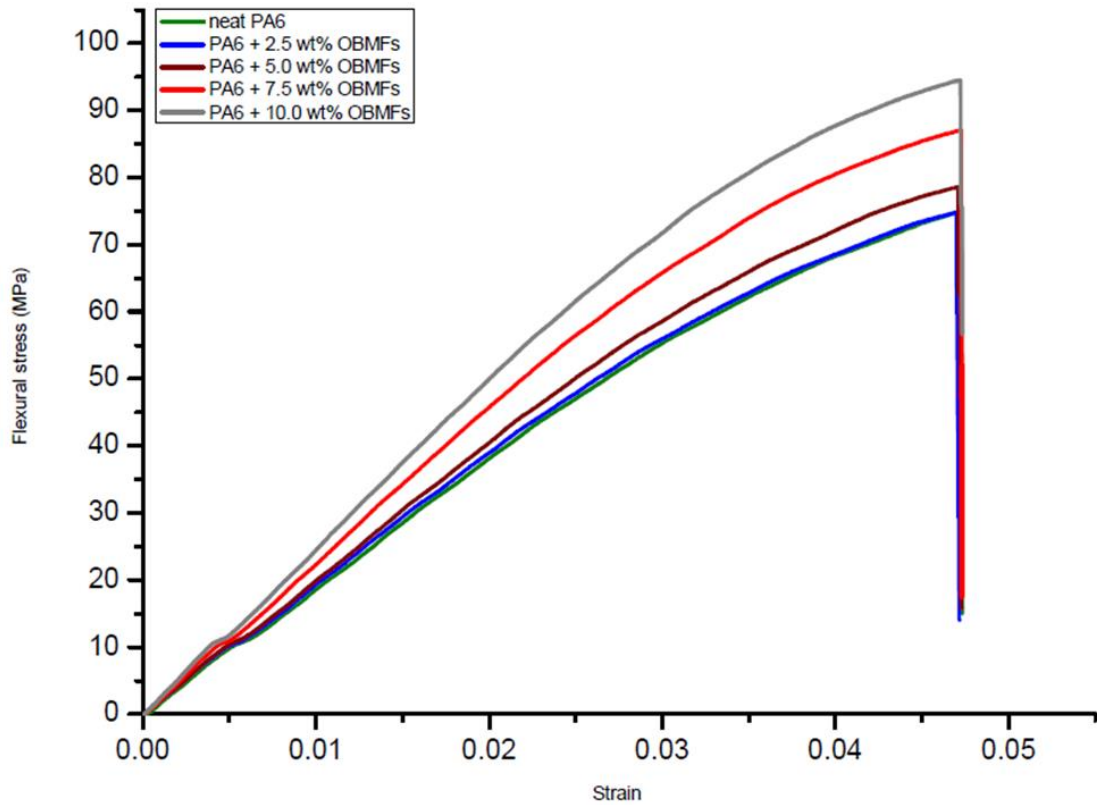


Figure 8.9 Flexural stress-strain curve from 3-point bend test of neat PA6 and PA6/OBMFs nanocomposites with varying OBMFs concentrations

Figure 8.9 showed that PA6/OBMFs nanocomposites have a higher stress points in respect to the corresponding strain points. It is also noticeable that the gradient of stress-strain curve increases with the increase of OBMFs loadings from 0 to 10 wt%. In Figure 8.10 shows the flexural strength and flexural modulus of neat PA6 and PA6/OBMFs nanocomposites as a function of OBMFs loadings. The flexural strength and flexural modulus of PA6/OBMFs nanocomposites increase with the incremental OBMFs loadings from 0 to 10 wt% which is presented in Figure 8.10.

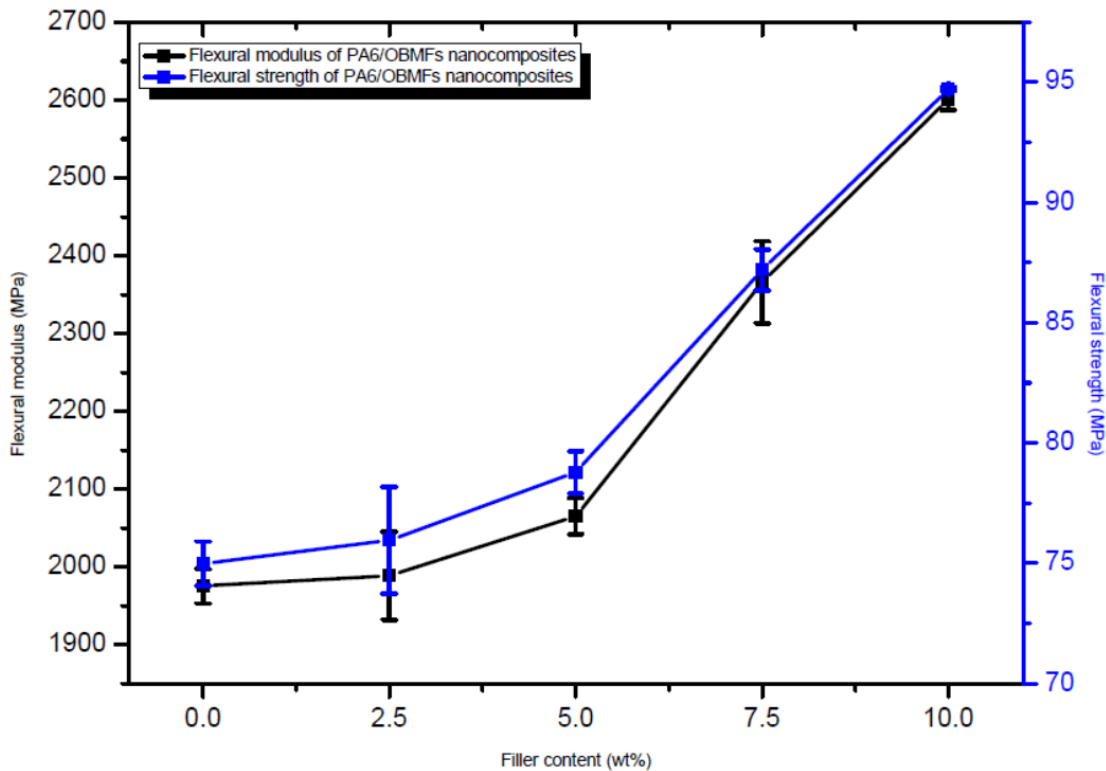


Figure 8.10 Comparison of modulus of elasticity in bending and flexural strength of neat PA6 and OBMFs reinforced PA6/OBMFs nanocomposites with varying OBMFs concentrations

A sharp increasing trend in flexural strength and flexural modulus is presented in Figure 8.10. The significant improvement in both flexural strength and flexural modulus is noticeable in PA6 with 7.5 and 10 wt% OBMFs nanocomposites. The flexural strength increases by 26% with the addition of OBMFs from 0 to 10 wt% in PA6. However, PA6 with 10 wt% OBMFs shows a more than 30% higher flexural modulus than the one with a neat PA6 matrix.

8.3.4. Impact fracture toughness properties of PA6/OBMFs nanocomposites

The Charpy impact test is a versatile method for evaluating the fracture behaviour of polymeric materials at high strain rates due to the simplicity and convenience of the test. The test equipment setting and the sample preparation process in this study is described in previous section.

The influence of OBMFs on the toughness of PA6/OBMFs nanocomposites were evaluated comparing to the toughness of neat PA6 matrix. The toughness of both notched and un-notched neat PA6 and PA6/OBMFs nanocomposites samples is plotted against OBMFs contents in Figure 8.11.

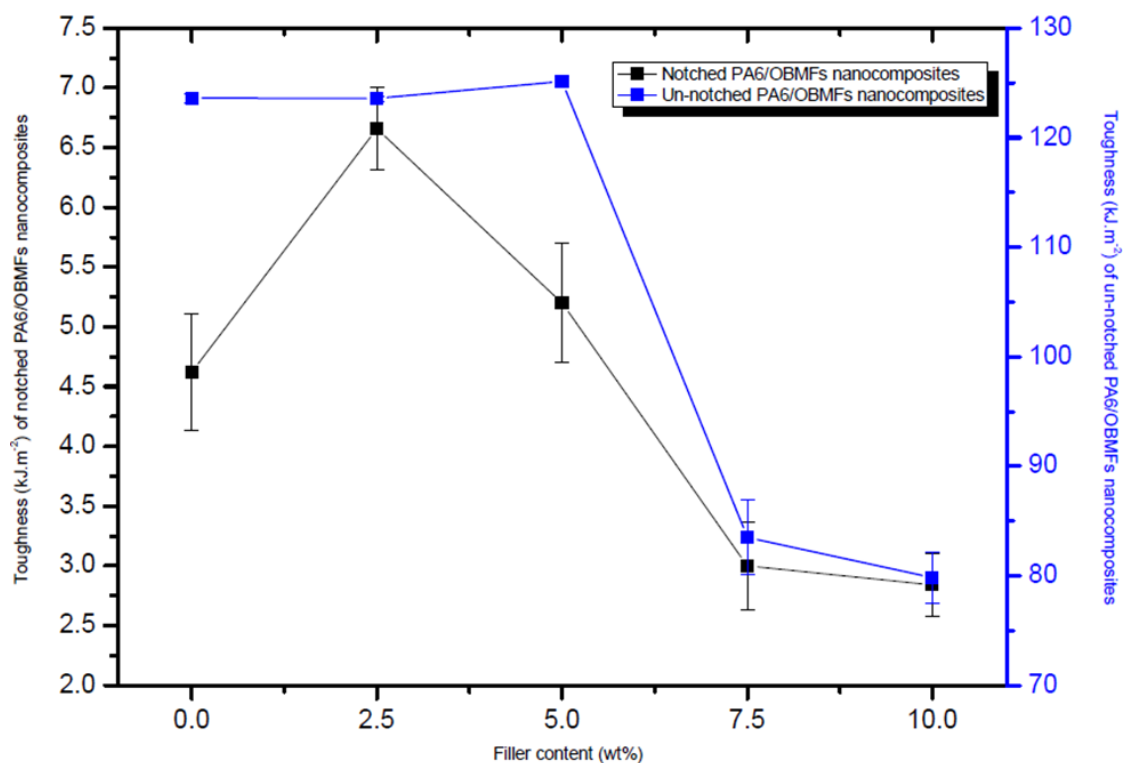


Figure 8.11 Impact strength of both notched and un-notched neat PA6 and OBMFs reinforced PA6/OBMFs nanocomposites with varying OBMFs concentrations

The toughness is distinctly enhanced at lower OBMFs contents up to 5 wt% for notched samples whereas there is not any significant change noticeable for un-notched samples. However, the toughness is drastically reduces for both notched and un-notched PA6/OBMFs nanocomposites samples with OBMFs loadings from 5 to 7.5 wt%. For both notched and un-notched samples, there is not any remarkable effect is noticed in samples with 7.5 and 10 wt% OBMFs content. Stress whitening can be readily noticeable in the impact specimens of various wt% of OBMFs reinforced PA6 nanocomposite samples which is presented in Figure 8.12.

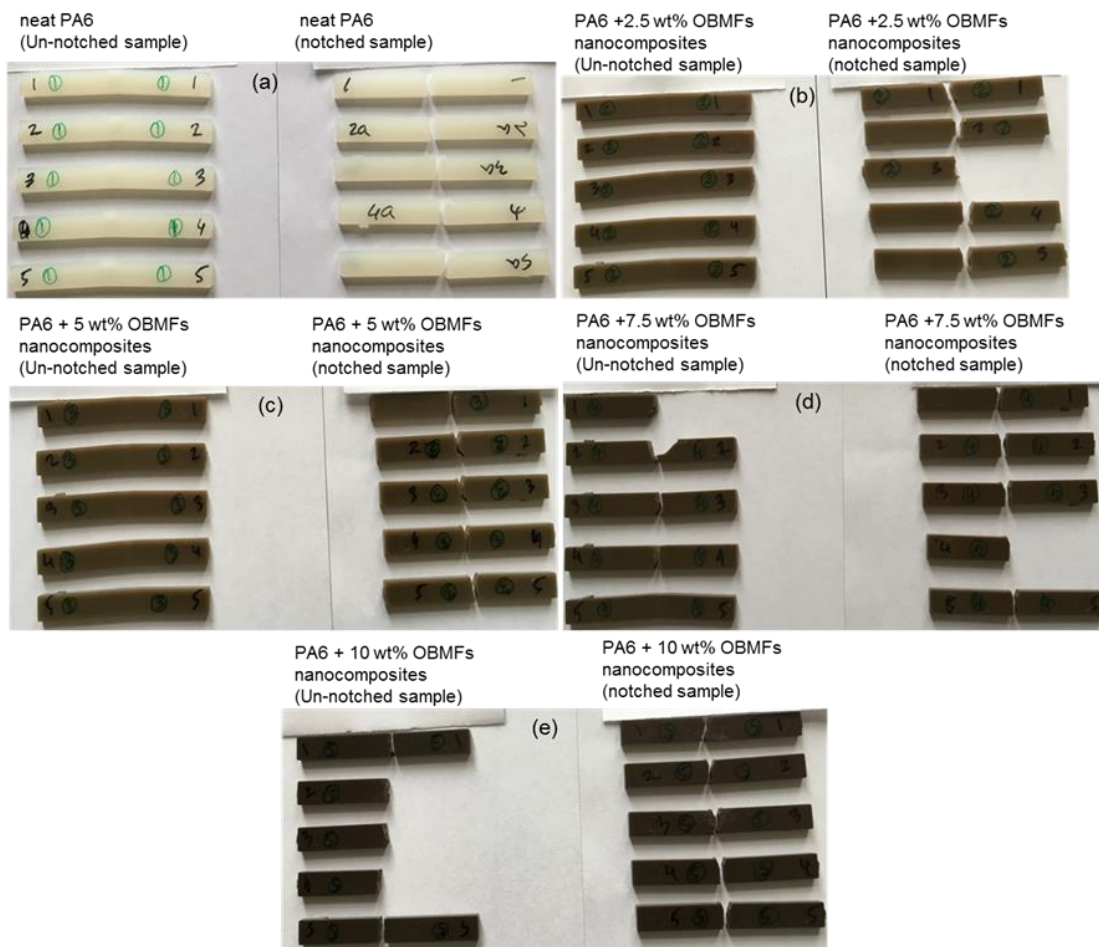


Figure 8.12 Comparison and fracture analysis of Impact test samples

For notched samples, the stress whitening can be clearly noticeable through the fracture surfaces of samples which is not apparent to the top surfaces of samples which implies the total fracture energy is completely dissipated in the inner region near the fracture surface, and no sign of energy dissipated in the outer plastic zone. The dispersion characteristics of OBMFs platelets influence the yielding or deforming behaviour of PA6/OBMFs nanocomposites. Findings from the previous study (shohel et al., 2019a), it is anticipated that the exfoliation of OBMFs platelets in PA6 with 2.5 and 5 wt% OBMFs increases the toughness of materials whereas the toughness of PA6 with 7.5 and 10 wt% OBMFs nanocomposites are severely reduced due to the intercalation and agglomeration of OBMFs platelets in PA6 matrix. However, among different wt% contents of OBMFs in PA6 matrix, the impact strength of exfoliated OBMFs reinforced PA6 (PA6 with 2.5 and 5 wt% OBMFs nanocomposites) were higher than that of intercalated and agglomerated (PA6 with 7.5 and 10 wt% OBMFs nanocomposites respectively) OBMFs in PA6 matrix.

8.3.5. Dynamic mechanical analysis of PA6/OBMFs nanocomposites

Figure 8.13 shows the storage modulus as a function of temperature for the PA6/OBMFs nanocomposites. It is clearly evident that OBMFs increased the storage modulus of PA6 within the temperature range tested. This result agrees with the tensile and flexural tests, where at ambient temperature it is also increased gradually with the incremental loading of OBMFs in PA6 matrix. The improvement in modulus of PA6/OBMFs nanocomposites is caused by the stiffness of the OBMFs layers and the constraining effect of OBMFs platelets on molecular motion of PA6 chains.

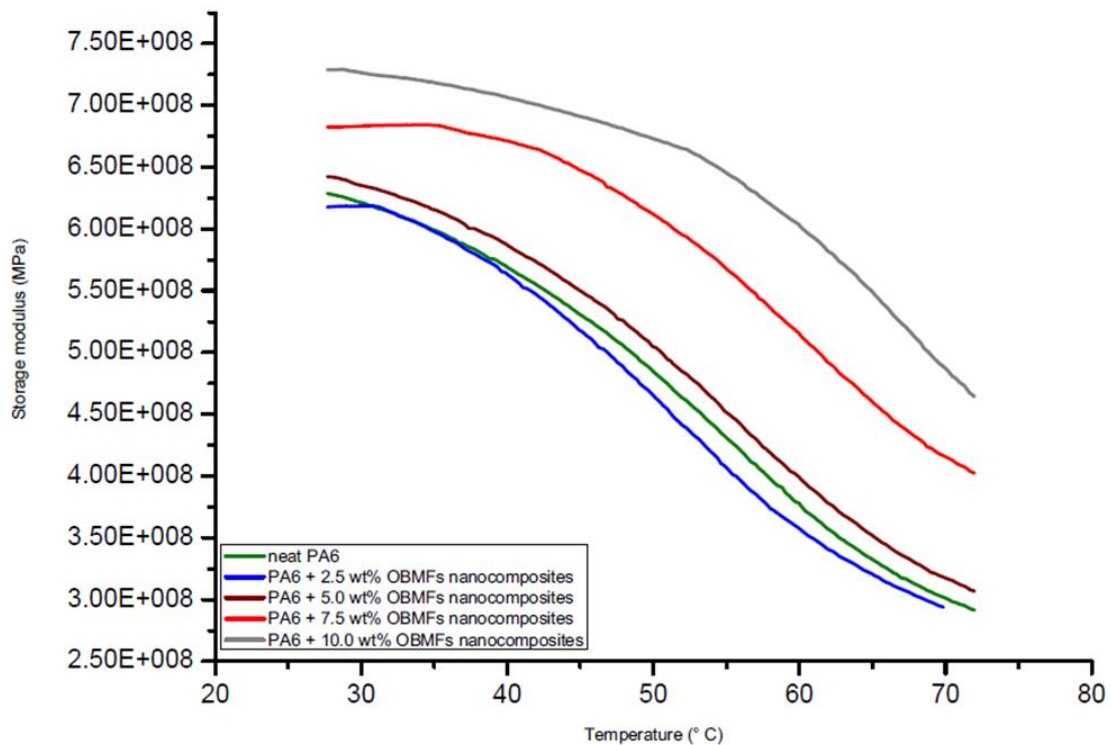


Figure 8.13 Dependence of storage modulus on temperature for neat PA6 and OBMFs reinforced PA6/OBMFs nanocomposites with varying OBMFs concentrations

However, observing Figure 8.13 it can be highlighted here that the storage modulus of the nanocomposite containing 10 wt% OBMFs was 16% higher than the storage modulus of neat PA6 at 30°C, whereas at 60°C (glass transition temperature, T_g of neat PA6) the storage modulus of PA6 with 10 wt% OBMFs was 56% higher than that of neat PA6. It is also clearly noticeable that the storage modulus of PA6 with 2.5 and 5 wt% OBMFs nanocomposites were very close to that of neat PA6 which governs the exfoliation of OBMFs in PA6 matrix does not have any significant effect on storage modulus of nanocomposite materials whereas the intercalation (PA6 with 7.5 wt% OBMFs) and agglomeration (PA6 with 10 wt% OBMFs) of OBMFs in PA6 matrix significantly increase the storage modulus property of materials.

The loss modulus curves of neat PA6 and its nanocomposites are presented in Figure 8.14.

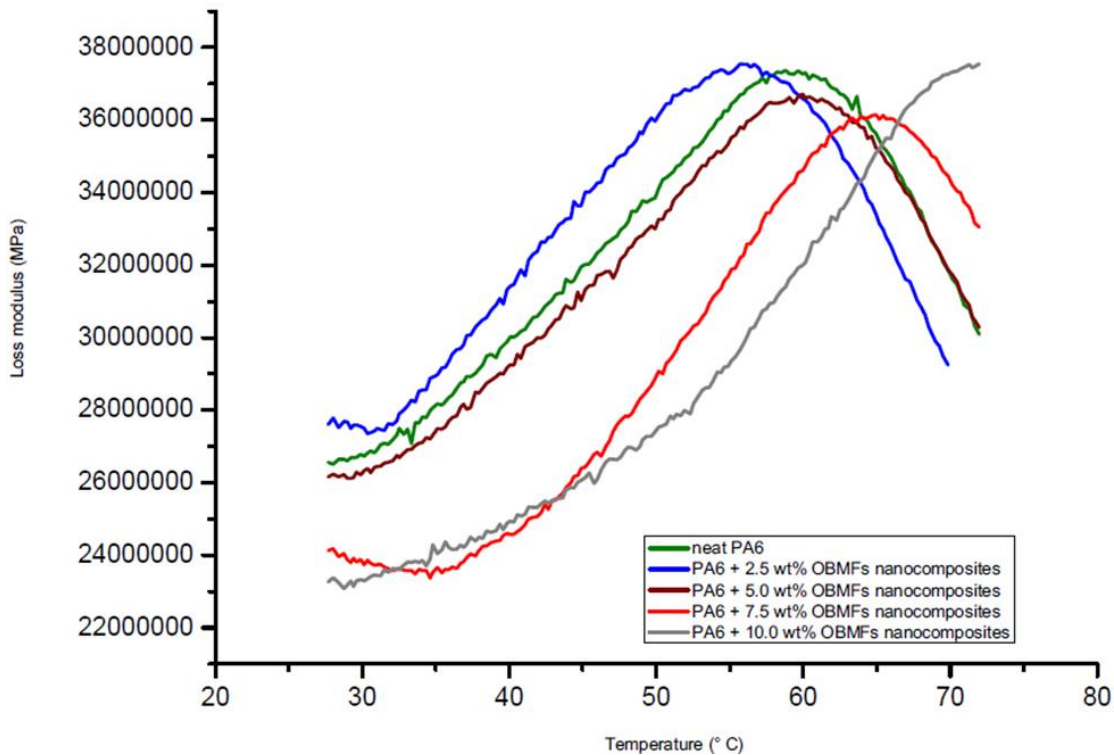


Figure 8.14 Dependence of loss modulus on temperature for neat PA6 and OBMFs reinforced PA6/OBMFs nanocomposites with varying OBMFs concentrations

Observing the loss modulus curves of neat PA6 and its nanocomposites in Figure 8.14, it can be articulated that there was not any significant change in loss modulus for PA6 with 2.5 and 5 wt% OBMFs nanocomposites compare to that of neat PA6. However, there were significant drop in loss moduli of PA6 with 7.5 and 10 wt% OBMFs noticed in Figure 8.14 which indicates that PA6 with 7.5 and 10 wt% OBMFs showed higher viscosity compare to that of neat PA6 in the same temperature profile. The relaxation peak of neat PA6 at 60°C shifted to higher temperature for PA6 with 7.5 (65°C) and 10 (above 70°C) wt% OBMFs nanocomposites.

Tan delta is the ratio of loss modulus to storage modulus which represents the damping properties of material. It is a way of measuring the energy dissipation of a material which identifies the energy absorbing characteristics of material.

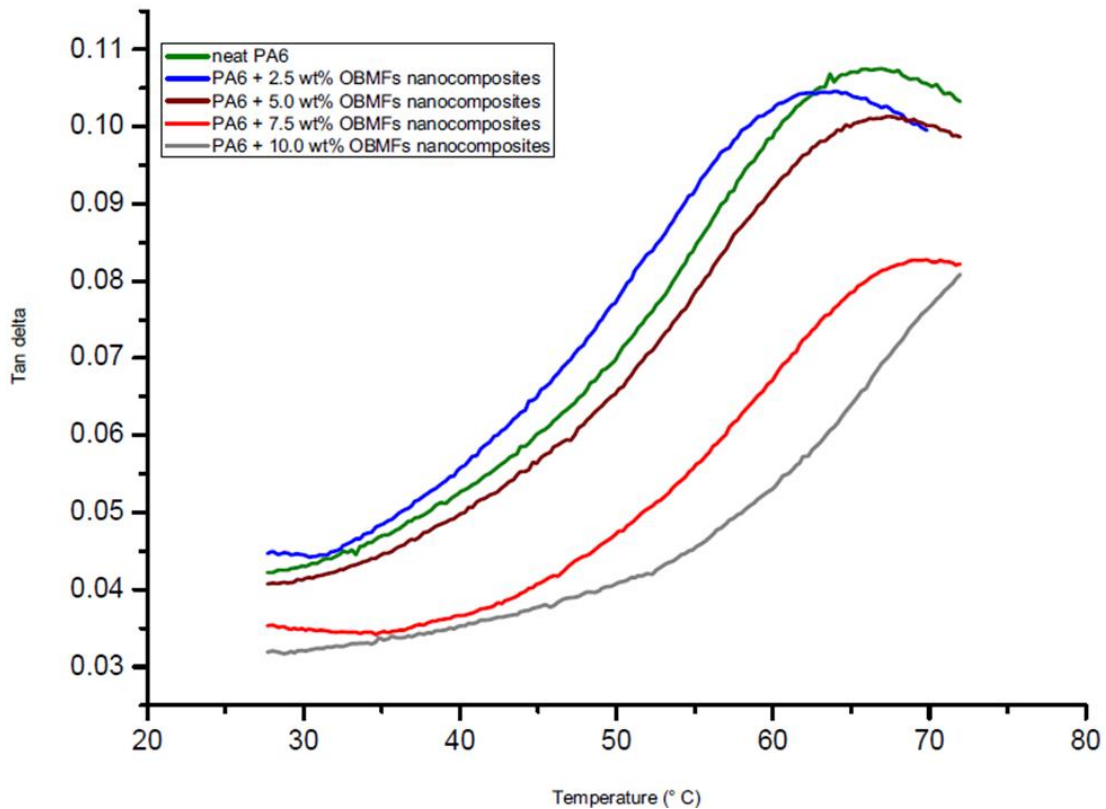


Figure 8.15 Dependence of loss factor (tan delta) on temperature for neat PA6 and OBMFs reinforced PA6/OBMFs nanocomposites with varying OBMFs concentrations

Figure 8.15 shows the magnitude of dynamic loss increased with the incremental loading of OBMFs in PA6 matrix. When the OBMFs platelets exfoliate in PA6 polymer chain, it is believed that the smaller crystallites produce more interfacial area. The increase in interfacial area influences to increase the restraint of tie chains between crystallites which results the reduction in the alpha loss tangent peak and thus increase in T_g which also agrees with findings reported by Gendre et al., (2015) and Yu et al., (2004). The tan delta curves between 60 to 70°C indicates the rubbery state of neat PA6 at this temperature range whereas the tan delta peak shifts to higher temperature for PA6 with 10 wt% OBMFs nanocomposite represents the enhancement of relaxation peak due to the agglomeration of OBMFs in PA6 matrix.

8.4. Conclusions

The effect of OBMFs addition in PA6 matrix in different weight percentage was studied by manufacturing several PA6/OBMFs nanocomposites using melt compounding process. Addition of OBMFs clearly increased Young's modulus and tensile strength with compromising reductions in ductility and fracture toughness of PA6. Tensile testing shows

that the tensile modulus and strength of PA6/OBMFs nanocomposites increase with the incremental loading of OBMFs in PA6 matrix. The observed high elastic modulus, tensile strength, flexural modulus and flexural strength were attributed to reclaimed OBMFs nanoclay aggregation which was confirmed microscopically. A potential correlation between the filler surface area governed by the dispersion and distribution features of OBMFs in PA6 matrix was observed and discussed. The storage modulus and loss modulus curves of DMA highlight information regarding the quality of interface exist between OBMFs and PA6 polymer chains. The peak height of $\tan\delta$ reflects the close relationship with the mobility of PA6 molecular chain segments and OBMFs nanoclay platelets. These properties make OBMFs reinforced PA6 matrix as a suitable candidate in polymeric engineering nanocomposite materials which can be used in industry in all fields where environmentally toxic, expensive, non-recyclable or limited recyclable nanocomposites have gained attention.

Chapter 9: Conclusion and future work

9.1. Summary

Nanotechnology is a niche area of research in both academic and industrial domain. Recently polymer-clay nanocomposites have attracted a great interest due to its potential application in improving different properties including thermal, mechanical, barrier, flame retardant and chemical and solvent resistant materials. Although the future of polymer-clay nanocomposites is promising due to its superior properties compare to that of conventional composites, the application of this nanocomposite is still limited. The major barriers to achieve this goal can be categorised in three factors such as uneven distribution and dispersion of clay platelets in polymer matrices, poor understanding of clay surface chemistry which causes poor interfacial adhesion and poor control on clay platelets orientation. These factors become more complex if the source of this clay mineral is from a waste source.

In this thesis, objectives were designed in such a way to tackle these factors mentioned above. In depth literature review and detailed characterisation of OBM slurry and powder is completed to highlight the possibility of harnessing environmentally hazardous OBM waste as filler in polymer nanocomposites which is highlighted in chapter 2 and 3. Findings from chapter 3 and 4 create a solid foundation to develop novel reclaimed nanoclay to utilise in polymer matrix. Chapter 4 highlighted the superior thermal stability of OBM slurry compare to that of MMT while reinforced these two fillers in LDPE polymer. However, LDPE with higher OBM slurry content (7.5 and 10 wt% in this case) indicated to act as a thermal conductive material based on thermal analysis data.

However, it was observed in chapter 5 that addition of this novel filler was ineffective in improving mechanical properties and the mechanical strength of these new materials decreases significantly comparing the results with neat LDPE and LDPE/MMT nanocomposites as a benchmark standard. The possible reasons of damaging mechanical properties were studied thoroughly and decision was made to follow the thermal treatment to produce OBM powder which is also mimicking the treatment process of OBM waste in the industry. Further thermo-mechanical investigations were carried out by manufacturing thermally treated OBMFs reinforced LDPE polymer which is discussed in chapter 6. LDPE with 10 wt% OBMFs showed superior thermal stability property, higher thermal conductivity and highest mechanical strength.

Observing the outcomes from chapter 3, 4, 5 and 6, the question aroused does this filler act in the same way when reinforce in polar polymer? PA6 was selected as a polymer to find the

answers for this question. Detail morphological, structural and thermal analyses were performed which is highlighted in chapter 7. PA6 with 10 wt% OBMFs nanocomposites showed the maximum thermal stability and indicated to act as a thermal conductive material too. Chapter 8 highlighted the mechanical properties of PA6/OBMFs nanocomposites. Addition of higher loading (7.5 and 10 wt%) of OBMFs in PA6 increased the tensile and flexural properties with compromising ductility which is presented in chapter 8.

It can be claimed now based on the performance of this OBM waste in this study that there is an enormous possibility to explore a new window of extracting or utilizing renewable resources which are now abandoned in landfill site. To protect the exploitation of this source of resources, a combined action to utilize the natural resources is needed particularly contributions from different levels of disciplines from engineering to biotechnology, environmental sciences, health and safety executives, occupational health security, governmental agencies and mainly oil and gas industries. The combined initiative may lead to apply innovative technologies and approaches that may bring the sustainable OBM waste management practices in oil and gas industries.

9.2. Recommendations for future work

Based on the findings and understandings of this novel filler throughout this research, the following recommendations were made:

- The composition of oil based mud waste is versatile. There is no standardisation or customised process developed yet which can convert this waste into useful reproducible products. Although the potential application of this waste as filler in new nanocomposite material manufacturing is promising based on the observation of different thermo-mechanical properties in this study, but the limitation is to reproducibility and quality of this filler produced. Hence, observing the drawbacks, it would be a really ground-breaking step to design a process which can control the composition and quality of this filler. Some ingredients which are common in drilling fluid processing all over the world such as bentonite and barium sulphate which ends up as waste after the drilling operation. These useful and limited source compounds regardless the wellfield being drilled or the geological boundaries-could be an opportunity to extract or recover and developing a standard process which ensures the reproducible and well quality controlled secondary raw materials.
- Since this novel filler showed superior thermal stability property, an investigation is logical to explore in details the thermal conductivity and flammability studies which

may open up a candidate material to use as an under-bonnet component in automotive industry. It would be interesting to identify the emission level and level of toxicity if this material is used in high temperature environment such as engine area in a car.

- Clay is hydrophilic by its nature, but OBM clay remains suspended condition in liquid due to strong surfactants are used in drilling mud formulation. Generally, thermal treatment agglomerates the clay platelets. It would be quite interesting to use this dispersed clay as in its natural phase (multiphase) to separate this from continuous phase (liquid phase) and then transfer/preserve in nanoscale clay platelets. However, it would be interesting to identify the mechanism of dispersed clay platelets exist in suspended condition in OBM waste which may applicable to disperse clay in powder form to mix homogeneously and disperse evenly in polymer matrix.
- Findings from this study showed even distribution and dispersion of clay platelets throughout the polymer samples which dictates sort of barrier/shielding between polymer chains. The formation of these shielding layer may facilitate to lower the water/gas permeation property in polymeric materials which may be an interesting area to explore in the future.
- Test and analysis results from LDPE/OBM slurry and LDPE/OBMFs nanocomposites, it was highlighted that the residue left over after TGA study increases with the incremental loading of OBM slurry and powder. It would worth to investigate how this novel filler affect the biodegradability of polymer nanocomposite material which is a necessary area of research considering different aspects of pollutions routes associated with this polymer material.
- Chapter 7 highlighted and proposed a hypothesis on relationship between % of crystallinity and degree of dispersion of filler in polymer nanocomposites. Further work is needed by investigating using different fillers in different polymer matrix to establish this theory which might be a new technique to predetermine the amount of fillers needed to any specific target dispersion required for any specific application. For example, high density of fillers are expected to increase the electroconductivity property in polymer nanocomposite material.
- Elemental analysis revealed some precious metals including rare earth metals are exist in this waste. It might be interesting to design a separation process which will recover the natural resources- an economic gain for the industry and safer environment for all. It would be worth investigating to separate certain clay minerals from this waste too and explore the effect of these clay minerals both in individually or synergistically in improving engineering polymer materials.

References:

- ADAMO, P., VIOLANTE, P. and WILSON, M.**, 2001. Tubular and spheroidal halloysite in pyroclastic deposits in the area of the Roccamonfina volcano (Southern Italy). *Geoderma*, 99(3-4), pp. 295-316
- ADDY, J., HARTLEY, J. and TIBBETTS, P.**, 1984. Ecological effects of low toxicity oil-based mud drilling in the Beatrice oilfield. *Marine pollution bulletin*, 15(12), pp. 429-436
- ADEGBOTOLU, U.V., NJUGUNA, J., POLLARD, P. and YATES, K.**, 2014. Waste to Want: Polymer nanocomposites using nanoclays extracted from Oil based drilling mud waste. IOP Conference Series: Materials Science and Engineering. IOP Publishing. pp. 012023
- ADEGBOTOLU, U.V.**, 2016. *Demulsification and recycling of spent oil based drilling fluid as nanofiller for polyamide 6 nanocomposites* (Doctoral dissertation, Robert Gordon University).
- ADVANI SURESH, G. and MURAT, S.E.**, 2003. Process modeling in composites manufacturing. Marcel D.: New York,
- AL-ANSARY, M.S. and AL-TABBAA, A.**, 2007. Stabilisation/solidification of synthetic petroleum drill cuttings. *Journal of hazardous materials*, 141(2), pp. 410-421
- ALEXANDRE, M. and DUBOIS, P.**, 2000. Polymer-layered silicate nanocomposites: preparation, properties and uses of a new class of materials. *Materials Science and Engineering: R: Reports*, 28(1-2), pp. 1-63
- ANDRADE, P.F., AZEVEDO, T.F., GIMENEZ, I.F., SOUZA FILHO, A.G. AND BARRETO, L.S.**, 2009. Conductive carbon–clay nanocomposites from petroleum oily sludge. *Journal of hazardous materials*, 167(1-3), pp. 879-884
- AQUATEAM, C., STANG, P. and HENNINGE, L.B.**, 2014. Characterising Thermal Treated OBM Drill Cuttings.
- ARANDA, P. and RUIZ-HITZKY, E.**, 1992. Poly (ethylene oxide)-silicate intercalation materials. *Chemistry of Materials*, 4(6), pp. 1395-1403
- ARCE-ORTEGA, J., ROJAS-AVELIZAPA, N.G. and RODRÍGUEZ-VÁZQUEZ, R.**, 2004. Identification of recalcitrant hydrocarbons present in a drilling waste-polluted soil. *Journal of Environmental Science and Health, Part A*, 39(6), pp. 1535-1545
- ARRAKHIZ, F.Z., EL ACHABY, M., MALHA, M., BENSALAH, M.O., FASSI-FEHRI, O., BOUHIFID, R., BENMOUSSA, K. AND QAISS, A.**, 2013. Mechanical and thermal properties of natural fibers reinforced polymer composites: Doum/low density polyethylene. *Materials & Design*, 43, pp. 200-205
- ATTARAN, S.A., HASSAN, A. and WAHIT, M.U.**, 2015. Effects of ENR and OMMT on barrier and tensile properties of LDPE nanocomposite film. *Iranian Polymer Journal*, 24(5), pp. 367-378

- AZAR, J.J. and SAMUEL, G.R.**, 2007. Drilling engineering. PennWell books.
- BAKKE, T., KLUNGSØYR, J. and SANNI, S.**, 2013. Environmental impacts of produced water and drilling waste discharges from the Norwegian offshore petroleum industry. *Marine environmental research*, 92, pp. 154-169
- BALL, A.S., STEWART, R.J. and SCHLIEPHAKE, K.**, 2012. A review of the current options for the treatment and safe disposal of drill cuttings. *Waste Management & Research*, 30(5), pp. 457-473
- BAO, C., SONG, L., WILKIE, C.A., YUAN, B., GUO, Y., HU, Y. AND GONG, X.**, 2012. Graphite oxide, graphene, and metal-loaded graphene for fire safety applications of polystyrene. *Journal of Materials Chemistry*, 22(32), pp. 16399-16406
- BASHAT, H.**, 2002. Managing waste in exploration and production activities of the petroleum industry. *Environmental Advisor, SENV*, 1, pp. 1-37
- BERGAYA, F. and LAGALY, G.**, 2006. General introduction: clays, clay minerals, and clay science. *Developments in clay science*, 1, pp. 1-18
- BERTHEZENE, N., DE HEMPTINNE, J.C., AUDIBERT, A. AND ARGILLIER, J.F.**, 1999. Methane solubility in synthetic oil-based drilling muds. *Journal of Petroleum Science and Engineering*, 23(2), pp. 71-81
- BESQ, A., MALFOY, C., PANTET, A., MONNET, P. AND RIGHI, D.**, 2003. Physicochemical characterisation and flow properties of some bentonite muds. *Applied Clay Science*, 23(5-6), pp. 275-286
- BHATTACHARYA, M.**, 2016. Polymer nanocomposites—a comparison between carbon nanotubes, graphene, and clay as nanofillers. *Materials*, 9(4), pp. 262
- BIGNERT, A., COSSA, D., EMMERSON, R., FRYER, R., FÜLL, C., FUMEGA, J., LAANE, R., CALLS, H.M., MCHUGH, B., MILLER, B. AND MILLWARD, G.**, 2004. OSPAR/ICES workshop on the evaluation and update of background reference concentrations (B/RCS) and ecotoxicological assessment criteria (EACs) and how these assessment tools should be used in assessing contaminants in water, sediment, and biota: Workshop The Hague, 9-13 February 2004. Final Report.
- BILOTTI, E., FISCHER, H. and PEIJS, T.**, 2008. Polymer nanocomposites based on needle-like sepiolite clays: Effect of functionalized polymers on the dispersion of nanofiller, crystallinity, and mechanical properties. *Journal of Applied Polymer Science*, 107(2), pp. 1116-1123
- BIN MERDHAH, A.**, 2010. Inhibition of calcium sulfate and strontium sulfate scale in waterflood. *SPE Production & Operations*, 25(04), pp. 545-552
- BINNEMANS, K., JONES, P.T., BLANPAIN, B., VAN GERVEN, T. AND PONTIKES, Y.**, 2015. Towards zero-waste valorisation of rare-earth-containing industrial process residues: a critical review. *Journal of Cleaner Production*, 99, pp. 17-38

BLUM, A. and AMES, B.N., 1977. Flame-retardant additives as possible cancer hazards. *Science* (New York, N.Y.), 195(4273), pp. 17-23

BORSE, N.K. and KAMAL, M.R., 2006. Melt processing effects on the structure and mechanical properties of PA-6/clay nanocomposites. *Polymer Engineering & Science*, 46(8), pp. 1094-1103

BOURBIGOT, S., DEVAUX, E. and FLAMBARD, X., 2002. Flammability of polyamide-6/clay hybrid nanocomposite textiles. *Polymer Degradation and Stability*, 75(2), pp. 397-402

BOURBIGOT, S. and DUQUESNE, S., 2007. Fire retardant polymers: recent developments and opportunities. *Journal of Materials Chemistry*, 17(22), pp. 2283-2300

BOURBIGOT, S., DUQUESNE, S. and JAMA, C., 2006. Polymer nanocomposites: how to reach low flammability? *Macromolecular Symposia*. Wiley Online Library. pp. 180-190

BREUER, E., STEVENSON, A.G., HOWE, J.A., CARROLL, J. AND SHIMMIELD, G.B., 2004. Drill cutting accumulations in the Northern and Central North Sea: a review of environmental interactions and chemical fate. *Marine pollution bulletin*, 48(1-2), pp. 12-25

BREUER, E., SHIMMIELD, G. and PEPPE, O., 2008. Assessment of metal concentrations found within a North Sea drill cuttings pile. *Marine pollution bulletin*, 56(7), pp. 1310-1322

CAENN, R. and CHILLINGAR, G.V., 1996. Drilling fluids: State of the art. *Journal of petroleum science and engineering*, 14(3-4), pp. 221-230

CAENN, R., DARLEY, H.C. and GRAY, G.R., 2011. Composition and properties of drilling and completion fluids. Gulf professional publishing.

CARRADO, K.A., THIYAGARAJAN, P. and ELDER, D.L., 1996. Polyvinyl alcohol-clay complexes formed by direct synthesis. *Clays and Clay Minerals*, 44(4), pp. 506-514

CARRETERO, M.I. and POZO, M., 2009. Clay and non-clay minerals in the pharmaceutical industry: Part I. Excipients and medical applications. *Applied Clay Science*, 46(1), pp. 73-80

CHEN, B. and EVANS, J.R., 2009. Impact strength of polymer-clay nanocomposites. *Soft matter*, 5(19), pp. 3572-3584

CHEN, G., SHEN, D., FENG, M. AND YANG, M., 2004. An Attenuated Total Reflection FT-IR Spectroscopic Study of Polyamide 6/Clay Nanocomposite Fibers. *Macromolecular rapid communications*, 25(11), pp. 1121-1124

CHEN, T., LIN, S. and LIN, Z., 2007. An innovative utilization of drilling wastes as building materials. E&P Environmental and Safety Conference. Society of Petroleum Engineers.

CHIU, F.C., LAI, S.M., CHEN, Y.L. AND LEE, T.H., 2005. Investigation on the polyamide 6/organoclay nanocomposites with or without a maleated polyolefin elastomer as a toughener. *Polymer*, 46(25), pp. 11600-11609

CHO, J. and PAUL, D.R., 2001. Nylon 6 nanocomposites by melt compounding. *Polymer*, 42(3), pp. 1083-1094

- CHOI, Y.S., CHOI, M.H., WANG, K.H., KIM, S.O., KIM, Y.K. AND CHUNG, I.J.**, 2001. Synthesis of exfoliated PMMA/Na-MMT nanocomposites via soap-free emulsion polymerization. *Macromolecules*, 34(26), pp. 8978-8985
- CHOUDALAKIS, G. and GOTSIS, A.**, 2009. Permeability of polymer/clay nanocomposites: a review. *European polymer journal*, 45(4), pp. 967-984
- CHRISTIDIS, G.E.**, 2011. *Advances in the characterization of industrial minerals*. The Mineralogical Society of Great Britain and Ireland.
- CLARK, B.M.**, 2002. DIRTY DRILLING.
- CLEGG, F. and BREEN, C.**, 2014. Synergistic and Competitive Aspects of the Adsorption of Poly (ethylene glycol) and Poly (vinyl alcohol) onto Na-Bentonite. *The Journal of Physical Chemistry B*, 118(46), pp. 13268-13278
- COLBORN, T., KWIATKOWSKI, C., SCHULTZ, K. AND BACHRAN, M.**, 2011. Natural gas operations from a public health perspective. *Human and ecological risk assessment: An International Journal*, 17(5), pp. 1039-1056
- COLEMAN, N.J. and CRAIG, D.Q.**, 1996. Modulated temperature differential scanning calorimetry: a novel approach to pharmaceutical thermal analysis. *International journal of pharmaceutics*, 135(1-2), pp. 13-29
- COLLIVER AND CARTER**, 2000. Colliver and carter drill cuttings; Available at: <http://www.kgs.ku.edu/CO2/CO2Core/TBCarter3-2854-57.html>
- COSTA, F.R., ABDEL-GOAD, M., WAGENKNECHT, U. AND HEINRICH, G.**, 2005. Nanocomposites based on polyethylene and Mg–Al layered double hydroxide. I. Synthesis and characterization. *Polymer*, 46(12), pp. 4447-4453
- COSTA, F.R., WAGENKNECHT, U. and HEINRICH, G.**, 2007. LDPE/Mg–Al layered double hydroxide nanocomposite: thermal and flammability properties. *Polymer Degradation and Stability*, 92(10), pp. 1813-1823
- CRAIG, D.Q., KETT, V.L., MURPHY, J.R. AND PRICE, D.M.**, 2001. The measurement of small quantities of amorphous material--should we be considering the rigid amorphous fraction? *Pharmaceutical research*, 18(8), pp. 1081-1082
- CRANFORD, P. and GORDON, D.**, 1991. Chronic sublethal impact of mineral oil-based drilling mud cuttings on adult sea scallops. *Marine pollution bulletin*, 22(7), pp. 339-344
- CUI, Y., KUMAR, S., KONA, B.R. AND VAN HOUCKE, D.**, 2015. Gas barrier properties of polymer/clay nanocomposites. *Rsc Advances*, 5(78), pp. 63669-63690
- DADFAR, S.A., ALEMZADEH, I., DADFAR, S.R. AND VOSOUGHI, M.**, 2011. Studies on the oxygen barrier and mechanical properties of low-density polyethylene/organoclay nanocomposite films in the presence of ethylene vinyl acetate copolymer as a new type of compatibilizer. *Materials & Design*, 32(4), pp. 1806-1813

DAVIS, R.D., GILMAN, J.W., SUTTO, T.E., CALLAHAN, J.H., TRULOVE, P.C. AND HUGH, C., 2004. Improved thermal stability of organically modified layered silicates. *Clays and Clay Minerals*, 52(2), pp. 171-179

DEÁK, T., CZIGÁNY, T., TAMÁS, P. AND NÉMETH, C., 2010. Enhancement of interfacial properties of basalt fiber reinforced nylon 6 matrix composites with silane coupling agents. *Express Polymer Letters*, 4(10),

DENNEY, D., 2008. Hydraulic Fracturing: Compensation of Surge and Swab Pressures in Floating Drilling Operations. *Journal of Petroleum Technology*, 60(03), pp. 57-60

DENNIS, H., HUNTER, D.L., CHANG, D., KIM, S., WHITE, J.L., CHO, J.W. AND PAUL, D.R., 2001. Effect of melt processing conditions on the extent of exfoliation in organoclay-based nanocomposites. *Polymer*, 42(23), pp. 9513-9522

DIRECTIVE HAT. Council Directive 76/464/EEC of 4 May 1976 on pollution caused by certain dangerous substances discharged into the aquatic environment of the Community. *Official Journal L* 1976;**129(18/05)**:0023-0029.

DJOMGOUE, P. and NJOPWOUO, D., 2013. FT-IR spectroscopy applied for surface clays characterization. *Journal of Surface Engineered Materials and Advanced Technology*, 3(04), pp. 275

DJOWE, A.T., LAMINSI, S., NJOPWOUO, D., ACAYANKA, E. AND GAIGNEAUX, E.M., 2013. Surface modification of smectite clay induced by non-thermal gliding arc plasma at atmospheric pressure. *Plasma Chemistry and Plasma Processing*, 33(4), pp. 707-723

DONG, Y., MARSHALL, J., HAROOSH, H.J., MOHAMMADZADEHMOGHADAM, S., LIU, D., QI, X. AND LAU, K.T., 2015. Polylactic acid (PLA)/halloysite nanotube (HNT) composite mats: Influence of HNT content and modification. *Composites Part A: Applied Science and Manufacturing*, 76, pp. 28-36

DRIPKE, M., 2008. Choosing the right extensometer for every materials testing application. *Quality Magazine*.

DURMUŞ, A., WOO, M., KAŞGÖZ, A., MACOSKO, C.W. AND TSAPATSI, M., 2007. Intercalated linear low density polyethylene (LLDPE)/clay nanocomposites prepared with oxidized polyethylene as a new type compatibilizer: structural, mechanical and barrier properties. *European Polymer Journal*, 43(9), pp. 3737-3749

ELEKTOROWICZ, M. and HABIBI, S., 2005. Sustainable waste management: recovery of fuels from petroleum sludge. *Canadian Journal of Civil Engineering*, 32(1), pp. 164-169

EL-MAHLLAWY, M.S. and OSMAN, T.A., 2010. Influence of oil well drilling waste on the engineering characteristics of clay bricks. *Journal of American Science*, 6(7), pp. 48-54

EUROPEAN COMMISSION, 2014; COMMISSION DECISION of 18 December 2014 amending Decision 2000/532/EC on the list of waste pursuant to Directive 2008/98/EC of the European Parliament and of the Council. EUROPEAN COMMISSION; 2014.

EUROPEAN UNION, 2008. Directive 2008/98/EC of the European Parliament and of the Council of 19 November 2008 on waste and repealing certain Directives. Official Journal of the European Union L, 312(3),

FALCÓN, J.M., SAWCZEN, T. and AOKI, I.V., 2015. Dodecylamine-loaded halloysite nanocontainers for active anticorrosion coatings. *Frontiers in Materials*, 2, pp. 69

FERNÁNDEZ-SAAVEDRA, R., ARANDA, P., CARRADO, K.A., SANDÍ, G., SEIFERT, S. AND RUIZ-HITZKY, E., 2009. Template synthesis of nanostructured carbonaceous materials for application in electrochemical devices. *Current Nanoscience*, 5(4), pp. 506-513

FIJAŁ, J., GONET, A. and JAMROZIK, A., 2015. Characterization, properties and microstructure of spent drilling mud from the point of view of environmental protection. *AGH Drilling, Oil, Gas*, 32

FINK, J., 2015. Water-based chemicals and technology for drilling, completion, and workover fluids. Gulf Professional Publishing.

FISCHER, H., 2003. Polymer nanocomposites: from fundamental research to specific applications. *Materials Science and Engineering: C*, 23(6-8), pp. 763-772

FOLLAIN, N., ALEXANDRE, B., CHAPPEY, C., COLASSE, L., MÉDÉRIC, P. AND MARAIS, S., 2016. Barrier properties of polyamide 12/montmorillonite nanocomposites: Effect of clay structure and mixing conditions. *Composites Science and Technology*, 136, pp. 18-28

FORCE, D.F.T., 2009. Drilling fluids and health risk management. A guide for drilling personnel, managers and health professionals in the oil and gas industry,

FORNES, T. and PAUL, D.R., 2003. Crystallization behavior of nylon 6 nanocomposites. *Polymer*, 44(14), pp. 3945-3961

FRANCIS, C., 1973. Adsorption of polyvinylpyrrolidone on reference clay minerals. *Soil Science*, 115(1), pp. 40-54

FU, S. and LAUKE, B., 1996. Effects of fiber length and fiber orientation distributions on the tensile strength of short-fiber-reinforced polymers. *Composites Science and Technology*, 56(10), pp. 1179-1190

FU, X. and QUTUBUDDIN, S., 2001. Polymer–clay nanocomposites: exfoliation of organophilic montmorillonite nanolayers in polystyrene. *Polymer*, 42(2), pp. 807-813

GAETZ, C.T., MONTGOMERY, R. AND DUKE, T.W., 1986. Toxicity of used drilling fluids to mysids (*Mysidopsis bahia*). *Environmental Toxicology and Chemistry: An International Journal*, 5(9), pp.813-821.

GAO, F., 2004. Clay/polymer composites: the story. *Materials today*, 7(11), pp. 50-55

GASKA, K., XU, X., GUBANSKI, S. AND KÁDÁR, R., 2017. Electrical, mechanical, and thermal properties of LDPE graphene nanoplatelets composites produced by means of melt extrusion process. *Polymers*, 9(1), pp. 11

GBADEBO, A., TAIWO, A. and EGHELE, U., 2010. Environmental impacts of drilling mud and cutting wastes from the Igbokoda onshore oil wells, Southwestern Nigeria. *Indian Journal of Science and Technology*, 3(5), pp. 504-510

GEETHAMMA, V. and LUYT, A.S., 2008. Oxidized wax as compatibilizer in linear low-density polyethylene-clay nanocomposites: x-ray diffraction and dynamic mechanical analysis. *Journal of nanoscience and nanotechnology*, 8(4), pp. 1886-1894

GENDRE, L., NJUGUNA, J., ABHYANKAR, H. AND ERMINI, V., 2015. Mechanical and impact performance of three-phase polyamide 6 nanocomposites. *Materials & Design*, 66, pp. 486-491

GHOLAMI, R., ELOCHUKWU, H., FAKHARI, N. AND SARMADIVALEH, M., 2018. A review on borehole instability in active shale formations: Interactions, mechanisms and inhibitors. *Earth-Science Reviews*, 177, pp. 2-13

GIANNAKAS, A., XIDAS, P., TRIANTAFYLLIDIS, K.S., KATSOULDIS, A. AND LADAVOS, A., 2009. Preparation and characterization of polymer/organosilicate nanocomposites based on unmodified LDPE. *Journal of Applied Polymer Science*, 114(1), pp. 83-89

GILMAN, J.W., 1999. Flammability and thermal stability studies of polymer layered-silicate (clay) nanocomposites. *Applied Clay Science*, 15(1-2), pp. 31-49

GILMAN, J.W., KASHIWAGI, T. and LICHTENHAN, J.D., 1997. Nanocomposites: a revolutionary new flame-retardant approach. *INTERNATIONAL SAMPE SYMPOSIUM AND EXHIBITION. SAMPE SOCIETY FOR THE ADVANCEMENT OF MATERIAL.* pp. 1078-1089

GIRI, S.K., PRADHAN, G.C. and DAS, N., 2014. Thermal, electrical and tensile properties of synthesized magnetite/polyurethane nanocomposites using magnetite nanoparticles derived from waste iron ore tailing. *Journal of Polymer Research*, 21(5), pp. 446

GOU, J., ZHUGE, J. and LIANG, F., 2012. Processing of polymer nanocomposites. *Manufacturing Techniques for Polymer Matrix Composites (PMCs).* Elsevier. pp. 95-119

GRANT, A. and BRIGGS, A.D., 2002. Toxicity of sediments from around a North Sea oil platform: are metals or hydrocarbons responsible for ecological impacts? *Marine environmental research*, 53(1), pp. 95-116

GREENLAND, D., 1963. Adsorption of polyvinyl alcohols by montmorillonite. *Journal of colloid science*, 18(7), pp. 647-664

Grigoriadi, K., Giannakas, A., Ladavos, A. and Barkoula, N.M., 2013. Thermomechanical behavior of polymer/layered silicate clay nanocomposites based on unmodified low density polyethylene. *Polymer Engineering & Science*, 53(2), pp. 301-308

GRIM, R.E. and ROWLAND, R.A., 1942. Differential thermal analysis of clay minerals and other hydrous materials. Part 1. *American Mineralogist: Journal of Earth and Planetary Materials*, 27(11), pp. 746-761

- GUANCHENG, J., YOURONG, Q., YUXIU, A., XIANBIN, H. AND YANJUN, R.,** 2016. Polyethyleneimine as shale inhibitor in drilling fluid. *Applied Clay Science*, 127, pp. 70-77
- GUGGENHEIM, S. and MARTIN, R.,** 1995. Definition of clay and clay mineral: joint report of the AIPEA nomenclature and CMS nomenclature committees. *Clays and Clay Minerals*, 43(2), pp. 255-256
- GUO, F., ARYANA, S., HAN, Y. AND JIAO, Y.,** 2018. A review of the synthesis and applications of polymer–nanoclay composites. *Applied Sciences*, 8(9), pp. 1696
- GUO, Q., GHADIRI, R., WEIGEL, T., AUMANN, A., GUREVICH, E.L., ESEN, C., MEDENBACH, O., CHENG, W., CHICHKOV, B. AND OSTENDORF, A.,** 2014. Comparison of in situ and ex situ methods for synthesis of two-photon polymerization polymer nanocomposites. *Polymers*, 6(7), pp. 2037-2050
- HALIT, M.K.M.,** 2018. Processing, Structure and Properties of Polyamide 6/Graphene Nanoplatelets Nanocomposites,
- HAQUE, M.M., ISLAM, M.S. and ISLAM, M.N.,** 2012. Preparation and characterization of polypropylene composites reinforced with chemically treated coir. *Journal of Polymer Research*, 19(5), pp. 9847
- HEMATI, F. and GARMABI, H.,** 2011. Compatibilised LDPE/LLDPE/nanoclay nanocomposites: I. Structural, mechanical, and thermal properties. *The Canadian Journal of Chemical Engineering*, 89(1), pp. 187-196
- HERRERO, M., NÚÑEZ, K., GALLEGRO, R., MERINO, J.C. AND PASTOR, J.M.,** 2016. Control of molecular weight and polydispersity in polyethylene/needle-like shaped clay nanocomposites obtained by in situ polymerization with metallocene catalysts. *European Polymer Journal*, 75, pp. 125-141
- HICKENBOTTOM, K.L., HANCOCK, N.T., HUTCHINGS, N.R., APPLETON, E.W., BEAUDRY, E.G., XU, P. AND CATH, T.Y.,** 2013. Forward osmosis treatment of drilling mud and fracturing wastewater from oil and gas operations. *Desalination*, 312, pp. 60-66
- HIGGINBOTHAM, A.L., LOMEDA, J.R., MORGAN, A.B. AND TOUR, J.M.,** 2009. Graphite oxide flame-retardant polymer nanocomposites. *ACS applied materials & interfaces*, 1(10), pp. 2256-2261
- HILL, H.E.,** 2007. *Method and apparatus for converting spent water-based drilling muds into fertile indigenous top soil*. U.S. Patent 7,272,912.
- HILLIER, S.,** 2000. Accurate quantitative analysis of clay and other minerals in sandstones by XRD: comparison of a Rietveld and a reference intensity ratio (RIR) method and the importance of sample preparation. *Clay Minerals*, 35(1), pp. 291-302
- HOLDWAY, D.A.,** 2002. The acute and chronic effects of wastes associated with offshore oil and gas production on temperate and tropical marine ecological processes. *Marine pollution bulletin*, 44(3), pp. 185-203

HOLLAWAY, L.C. and TENG, J., 2008. Strengthening and rehabilitation of civil infrastructures using fibre-reinforced polymer (FRP) composites. Elsevier.

HORROCKS, A.R., PRICE, D. and PRICE, D., 2001. Fire retardant materials. woodhead Publishing.

HOSSEN, M.F., HAMDAN, S., RAHMAN, M.R., RAHMAN, M.M., LIEW, F.K. AND LAI, J.C., 2015. Effect of fiber treatment and nanoclay on the tensile properties of jute fiber reinforced polyethylene/clay nanocomposites. *Fibers and Polymers*, 16(2), pp. 479-485

HSE, U., 2000. Drilling fluids composition and use within the UK offshore drilling industry - oto99089.pdf; Health and Safety Executive, UK. Available at: <http://www.hse.gov.uk/research/otopdf/1999/oto99089.pdf>

HU, J., GAN, M., MA, L., LI, Z., YAN, J. AND ZHANG, J., 2014. Synthesis and anticorrosive properties of polymer–clay nanocomposites via chemical grafting of polyaniline onto Zn-Al layered double hydroxides. *Surface and Coatings Technology*, 240, pp. 55-62

HUANG, J.C., ZHU, Z.K., YIN, J., QIAN, X.F. AND SUN, Y.Y., 2001. Poly (etherimide)/montmorillonite nanocomposites prepared by melt intercalation: morphology, solvent resistance properties and thermal properties. *Polymer*, 42(3), pp. 873-877

HUDGINS JR, C.M., 1994. Chemical use in North Sea oil and gas E&P. *Journal of Petroleum Technology*, 46(01), pp. 67-74

HUSKIĆ, M. and ŽIGON, M., 2007. PMMA/MMT nanocomposites prepared by one-step in situ intercalative solution polymerization. *European Polymer Journal*, 43(12), pp. 4891-4897

HUSSAIN, F., HOJJATI, M., OKAMOTO, M. AND GORGA, R.E., 2006. Polymer-matrix nanocomposites, processing, manufacturing, and application: an overview. *Journal of Composite Materials*, 40(17), pp. 1511-1575

IBARRA-ALONSO, M.C., SÁNCHEZ-VALDES, S., RAMÍREZ-VARGAS, E., FERNANDEZ-TAVIZÓN, S., ROMERO-GARCIA, J., LEDEZMA-PEREZ, A.S., RAMOS DE VALLE, L.F., RODRIGUEZ-FERNANDEZ, O.S., ESPINOZA-MARTINEZ, A.B., MARTINEZ-COLUNGA, J.G. AND CABRERA-ÁLVAREZ, E.N., 2015. Preparation and characterization of Polyethylene/Clay/Silver nanocomposites using functionalized polyethylenes as an adhesion promoter. *Journal of Adhesion Science and Technology*, 29(18), pp. 1911-1923

IQBAL, M.Z., ABDALA, A.A., MITTAL, V., SEIFERT, S., HERRING, A.M. AND LIBERATORE, M.W., 2016. Processable conductive graphene/polyethylene nanocomposites: Effects of graphene dispersion and polyethylene blending with oxidized polyethylene on rheology and microstructure. *Polymer*, 98, pp.143-155.

ISMAIL, A.R., AFTAB, A., IBUPOTO, Z.H. AND ZOLKIFILE, N., 2016. The novel approach for the enhancement of rheological properties of water-based drilling fluids by using multi-walled carbon nanotube, nanosilica and glass beads. *Journal of Petroleum Science and Engineering*, 139, pp.264-275.

- ISMAIL, A.R., ALIAS, A.H., SULAIMAN, W.R.W., JAAFAR, M.Z. AND ISMAIL, I.,** 2017. Drilling fluid waste management in drilling for oil and gas wells. *Chemical Engineering Transactions*, 56, pp.1351-1356.
- JACQUES WHITFORD STANTEC LIMITED,** July 2009, Cuttings Treatment Technology Evaluation, Environmental Studies Research Funds Report No. 166. St. John's, NL. 100 p. Available at:
<https://www.esrfunds.org/sites/www.esrfunds.org/files/publications/ESRF166-Jacques-Whitford-Stantec-Limited.pdf>
- JAHROMI, A.E., JAHROMI, H.R.E., HEMMATI, F., SAEB, M.R., GOODARZI, V. AND FORMELA, K.,** 2016. Morphology and mechanical properties of polyamide/clay nanocomposites toughened with NBR/NBR-g-GMA: a comparative study. *Composites Part B: Engineering*, 90, pp. 478-484
- JORDAN, J., JACOB, K.I., TANNENBAUM, R., SHARAF, M.A. AND JASIUK, I.,** 2005. Experimental trends in polymer nanocomposites—a review. *Materials science and engineering: A*, 393(1-2), pp. 1-11
- JORDAN, J.L., CASEM, D.T., BRADLEY, J.M., DWIVEDI, A.K., BROWN, E.N. AND JORDAN, C.W.,** 2016. Mechanical properties of low density polyethylene. *Journal of dynamic behavior of materials*, 2(4), pp.411-420.
- KALEDOVA, A., MERINSKA, D., GERARD, J.F. AND SLOUF, M.,** 2013. Polymer/clay nanocomposites and their gas barrier properties. *Polymer composites*, 34(9), pp. 1418-1424
- KANDOLA, B.K., HORROCKS, A.R., PRICE, D. AND COLEMAN, G.V.,** 1996. Flame-retardant treatments of cellulose and their influence on the mechanism of cellulose pyrolysis. *Journal of Macromolecular Science, Part C: Polymer Reviews*, 36(4), pp. 721-794
- KARAJ-ABAD, S.G., ABBASIAN, M. and JAYMAND, M.,** 2016. Grafting of poly [(methyl methacrylate)-block-styrene] onto cellulose via nitroxide-mediated polymerization, and its polymer/clay nanocomposite. *Carbohydrate Polymers*, 152, pp. 297-305
- KASHIWAGI, T., DU, F., DOUGLAS, J.F., WINEY, K.I., HARRIS, R.H. AND SHIELDS, J.R.,** 2005. Nanoparticle networks reduce the flammability of polymer nanocomposites. *Nature materials*, 4(12), pp. 928-933
- KASHIWAGI, H., SCHWARTZ, M.A., EIGENTHALER, M., DAVIS, K.A., GINSBERG, M.H. AND SHATTIL, S.J.,** 1997. Affinity modulation of platelet integrin α IIb β 3 by β 3-endonexin, a selective binding partner of the β 3 integrin cytoplasmic tail. *The Journal of cell biology*, 137(6), pp. 1433-1443
- KELLY, J.R., DUKE, T.W., HARWELL, M.A. AND HARWELL, C.C.,** 1987. An ecosystem perspective on potential impacts of drilling fluid discharges on seagrasses. *Environmental management*, 11(4), pp. 537-562

KHAN, M.J., AL-JUHANI, A.A., SHAWABKEH, R., UL-HAMID, A. AND HUSSEIN, I.A., 2011. Chemical modification of waste oil fly ash for improved mechanical and thermal properties of low density polyethylene composites. *Journal of Polymer Research*, 18(6), pp. 2275-2284

KHODJA, M., CANSÉLIER, J.P., BERGAYA, F., FOURAR, K., KHODJA, M., COHAUT, N. AND BENMOUNAH, A., 2010. Shale problems and water-based drilling fluid optimisation in the Hassi Messaoud Algerian oil field. *Applied Clay Science*, 49(4), pp. 383-393

KHODJA, M., KHODJA-SABER, M., CANSÉLIER, J.P., COHAUT, N. AND BERGAYA, F., 2010. Drilling fluid technology: performances and environmental considerations. *Products and services; from R&D to final solutions*, , pp. 227-256

KILIARIS, P. and PAPANASTASIOU, C., 2010. Polymer/layered silicate (clay) nanocomposites: an overview of flame retardancy. *Progress in Polymer Science*, 35(7), pp. 902-958

KIM, S.W., JO, W.H., LEE, M.S., KO, M.B. AND JHO, J.Y., 2002. Effects of shear on melt exfoliation of clay in preparation of nylon 6/organoclay nanocomposites. *Polymer Journal*, 34(3), pp. 103-111

KŁOSEK-WAWRZYN, E., MAŁOLEPSZY, J. and MURZYN, P., 2013. Sintering behavior of kaolin with calcite. *Procedia Engineering*, 57, pp. 572-582

KNIGHT, R.L., KADLEC, R.H. and OHLENDORF, H.M., 1999. The use of treatment wetlands for petroleum industry effluents. *Environmental science & technology*, 33(7), pp. 973-980

KODJIE, S.L., LI, L., LI, B., CAI, W., LI, C.Y. AND KEATING, M., 2006. Morphology and crystallization behavior of HDPE/CNT nanocomposite. *Journal of Macromolecular Science, Part B: Physics*, 45(2), pp. 231-245

KOGBARA, R.B., AYOTAMUNO, J.M., ONUOMAH, I., EHIO, V. AND DAMKA, T.D., 2016. Stabilisation/solidification and bioaugmentation treatment of petroleum drill cuttings. *Applied Geochemistry*, 71, pp. 1-8

KOH, H.L. and TEH, S.Y., 2011. Simulation of drill cuttings dispersion and deposition in South China Sea. *Lecture Notes in Engineering and Computer Science*, 2189(1), pp. 1501-1506

KRISHNAMOORTI, R. and GIANNELIS, E.P., 1997. Rheology of end-tethered polymer layered silicate nanocomposites. *Macromolecules*, 30(14), pp. 4097-4102

KRUPSKAYA, V.V., ZAKUSIN, S.V., TYUPINA, E.A., DORZHIEVA, O.V., ZHUKHLISTOV, A.P., Belousov, P.E. and Timofeeva, M.N., 2017. Experimental study of montmorillonite structure and transformation of its properties under treatment with inorganic acid solutions. *Minerals*, 7(4), pp. 49

- LAGREGA, M.D., BUCKINGHAM, P.L. and EVANS, J.C.,** 2010. Hazardous waste management. Waveland Press.
- LAKSHMI, M.S., NARMADHA, B. and REDDY, B.,** 2008. Enhanced thermal stability and structural characteristics of different MMT-Clay/epoxy-nanocomposite materials. *Polymer Degradation and Stability*, 93(1), pp. 201-213
- LAN, T. and PINNAVAIA, T.J.,** 1994. Clay-reinforced epoxy nanocomposites. *Chemistry of materials*, 6(12), pp. 2216-2219
- LAOUTID, F., BONNAUD, L., ALEXANDRE, M., LOPEZ-CUESTA, J.M. AND DUBOIS, P.,** 2009. New prospects in flame retardant polymer materials: from fundamentals to nanocomposites. *Materials science and engineering: R: Reports*, 63(3), pp. 100-125
- LÁZARO, B.B.,** 2007. Illitization processes: Series of dioctahedral clays and mechanisms of formation. *Diagenesis and Low-Temperature Metamorphism. Theory, Methods and Regional Aspects. Seminarios SEM*, 3, pp. 31-39
- LÁZARO, B.B.,** 2015. Halloysite and kaolinite: two clay minerals with geological and technological importance. *Revista de la Academia de Ciencias Exactas, Físicas, Químicas y Naturales de Zaragoza*, (70), pp. 7-38
- LEBARON, P.C., WANG, Z. and PINNAVAIA, T.J.,** 1999. Polymer-layered silicate nanocomposites: an overview. *Applied Clay Science*, 15(1-2), pp. 11-29
- LEE, Y.H., KUBOKI, T., PARK, C.B., SAIN, M. AND KONTOPOULOU, M.,** 2010. The effects of clay dispersion on the mechanical, physical, and flame-retarding properties of wood fiber/polyethylene/clay nanocomposites. *Journal of Applied Polymer Science*, 118(1), pp. 452-461
- LESZCZYŃSKA, A., NJUGUNA, J., PIELICHOWSKI, K. AND BANERJEE, J.R.,** 2007. Polymer/montmorillonite nanocomposites with improved thermal properties: Part I. Factors influencing thermal stability and mechanisms of thermal stability improvement. *Thermochimica Acta*, 453(2), pp. 75-96
- LESZCZYŃSKA, A., NJUGUNA, J., PIELICHOWSKI, K. AND BANERJEE, J.R.,** 2007. Polymer/montmorillonite nanocomposites with improved thermal properties: Part II. Thermal stability of montmorillonite nanocomposites based on different polymeric matrixes. *Thermochimica Acta*, 454(1), pp. 1-22
- LEVY, R. and FRANCIS, C.,** 1975. Interlayer adsorption of polyvinylpyrrolidone on montmorillonite. *Journal of colloid and interface science*, 50(3), pp. 442-450
- LI, S., YUAN, H., YU, T., YUAN, W. AND REN, J.,** 2009. Flame-retardancy and anti-dripping effects of intumescent flame retardant incorporating montmorillonite on poly (lactic acid). *Polymers for Advanced Technologies*, 20(12), pp. 1114-1120

LI, X., LIU, Q., CHENG, H., ZHANG, S. AND FROST, R.L., 2015. Mechanism of kaolinite sheets curling via the intercalation and delamination process. *Journal of colloid and interface science*, 444, pp. 74-80

LICHTENBERG, J.J., WINTER, J.A., WEBER, C.I. and FRADKIN, L., 1988. Chemical and biological characterization of municipal sludges, sediments, dredge spoils, and drilling muds. American Society for Testing and Materials.

LIM, L., AURAS, R. and RUBINO, M., 2008. Processing technologies for poly (lactic acid). *Progress in polymer science*, 33(8), pp. 820-852

LIU, P., 2007. Polymer modified clay minerals: A review. *Applied Clay Science*, 38(1-2), pp. 64-76

LIU, S., MO, X., ZHANG, C., SUN, D. AND MU, C., 2004. Swelling inhibition by polyglycols in montmorillonite dispersions. *Journal of Dispersion Science and Technology*, 25(1), pp. 63-66

LIU, S.P., HWANG, S.S., YEH, J.M. AND HUNG, C.C., 2011. Mechanical properties of polyamide-6/montmorillonite nanocomposites—Prepared by the twin-screw extruder mixed technique. *International Communications in Heat and Mass Transfer*, 38(1), pp. 37-43

LIU, T.X., LIU, Z.H., MA, K.X., SHEN, L., ZENG, K.Y. AND HE, C.B., 2003. Morphology, thermal and mechanical behavior of polyamide 6/layered-silicate nanocomposites. *Composites Science and Technology*, 63(3-4), pp. 331-337

LU, H., HU, Y., LI, M., CHEN, Z. AND FAN, W., 2006. Structure characteristics and thermal properties of silane-grafted-polyethylene/clay nanocomposite prepared by reactive extrusion. *Composites Science and Technology*, 66(15), pp. 3035-3039

LU, S. and HAMERTON, I., 2002. Recent developments in the chemistry of halogen-free flame retardant polymers. *Progress in polymer science*, 27(8), pp. 1661-1712

LUO, J. and DANIEL, I.M., 2003. Characterization and modeling of mechanical behavior of polymer/clay nanocomposites. *Composites Science and Technology*, 63(11), pp. 1607-1616

MA, J., XU, J., REN, J.H., YU, Z.Z. AND MAI, Y.W., 2003. A new approach to polymer/montmorillonite nanocomposites. *Polymer*, 44(16), pp. 4619-4624

MADEJOVÁ, J., 2003. FTIR techniques in clay mineral studies. *Vibrational spectroscopy*, 31(1), pp. 1-10

MALONEY, K.O. and YOXTHEIMER, D.A., 2012. Production and disposal of waste materials from gas and oil extraction from the Marcellus Shale play in Pennsylvania. *Environmental Practice*, 14(4), pp. 278-287

MARSH, R., 2003. A database of archived drilling records of the drill cuttings piles at the North West Hutton oil platform. *Marine pollution bulletin*, 46(5), pp. 587-593

MASENELLI-VARLOT, K., VIGIER, G., VERMOGEN, A., GAUTHIER, C. AND CAVAILLE, J.Y., 2007. Quantitative structural characterization of polymer–clay nanocomposites and

discussion of an “ideal” microstructure, leading to the highest mechanical reinforcement. *Journal of Polymer Science Part B: Polymer Physics*, 45(11), pp. 1243-1251

MCCOSH, K.L., KAPILA, M., DIXIT, R., WAY, P.W. AND PHIPPS, J., 2009. Continuous improvement in slop-mud treatment technology. *SPE Drilling & Completion*, 24(03), pp. 418-423

MELTON HR, SMITH JP, MAIRS HL, BERNIER RF, GARLAND E, GLICKMAN AH, JONES FV, RAY JP, THOMAS D, CAMPBELL JA. Environmental aspects of the use and disposal of non aqueous drilling fluids associated with offshore oil & gas operations. In *SPE International Conference on Health, Safety, and Environment in Oil and Gas Exploration and Production 2004* Jan 1. Society of Petroleum Engineers.

MELTON, H., SMITH, J., MARTIN, C., NEDWED, T., MAIRS, H. and RAUGHT, D., 2000. Offshore discharge of drilling fluids and cuttings—a scientific perspective on public policy. *Rio Oil and Gas Conference*. Rio de Janeiro, Brazil.

MENEGHETTI, P. and QUTUBUDDIN, S., 2006. Synthesis, thermal properties and applications of polymer-clay nanocomposites. *Thermochimica Acta*, 442(1-2), pp. 74-77

MESSERSMITH, P.B. and GIANNELIS, E.P., 1995. Synthesis and barrier properties of poly (ϵ -caprolactone)-layered silicate nanocomposites. *Journal of Polymer Science Part A: Polymer Chemistry*, 33(7), pp. 1047-1057

MOKHALALATI, T., AL-SUWAIDI, A. and HENDI, A.E., 2000. Managing Onshore Drilling Wastes-Abu Dhabi Experience. *Abu Dhabi International Petroleum Exhibition and Conference*. Society of Petroleum Engineers.

MONIRUZZAMAN, M. and WINEY, K.I., 2006. Polymer nanocomposites containing carbon nanotubes. *Macromolecules*, 39(16), pp. 5194-5205

MORAWIEC, J., PAWLAK, A., SLOUF, M., GALESKI, A., PIORKOWSKA, E. AND KRASNIKOWA, N., 2005. Preparation and properties of compatibilized LDPE/organo-modified montmorillonite nanocomposites. *European Polymer Journal*, 41(5), pp. 1115-1122

MORGAN, A.B. and GILMAN, J.W., 2003. Characterization of polymer-layered silicate (clay) nanocomposites by transmission electron microscopy and X-ray diffraction: A comparative study. *Journal of Applied Polymer Science*, 87(8), pp. 1329-1338

MORGAN, A.B. and WILKIE, C.A., 2007. *Flame retardant polymer nanocomposites*. John Wiley & Sons.

MORLAT-THERIAS, S., FANTON, E., GARDETTE, J.L., DINTCHEVA, N.T., LA MANTIA, F.P. AND MALATESTA, V., 2008. Photochemical stabilization of linear low-density polyethylene/clay nanocomposites: towards durable nanocomposites. *Polymer Degradation and Stability*, 93(10), pp. 1776-1780

- MOSELEY JR, H.R.**, 1983, January. Summary of API onshore drilling mud and produced water environmental studies. In *IADC/SPE Drilling Conference*. Society of Petroleum Engineers.
- MURRAY, H.H.**, 1991. Overview—clay mineral applications. *Applied Clay Science*, 5(5-6), pp. 379-395
- MUSCHENHEIM, D. and MILLIGAN, T.**, 1996. Flocculation and accumulation of fine drilling waste particulates on the Scotian Shelf (Canada). *Marine pollution bulletin*, (10),
- NADEAU, P.**, 1985. The physical dimensions of fundamental clay particles. *Clay Minerals*, 20(4), pp. 499-514
- NAM, B., MIN, K. and SON, Y.**, 2015. Investigation of the nanostructure, thermal stability, and mechanical properties of polylactic acid/cellulose acetate butyrate/clay nanocomposites. *Materials Letters*, 150, pp. 118-121
- NATKAŃSKI, P., KUŚTROWSKI, P., BIAŁAS, A., PIWOWARSKA, Z. AND MICHALIK, M.**, 2012. Controlled swelling and adsorption properties of polyacrylate/montmorillonite composites. *Materials Chemistry and Physics*, 136(2-3), pp. 1109-1115
- NAYAK, P.S. and SINGH, B.**, 2007. Instrumental characterization of clay by XRF, XRD and FTIR. *Bulletin of Materials Science*, 30(3), pp. 235-238
- NEFF, J.M.**, 2005. Composition, environmental fates, and biological effect of water based drilling muds and cuttings discharged to the marine environment: A synthesis and annotated bibliography. Report prepared for the Petroleum Environmental Research Forum (PERF). Washington DC: American Petroleum Institute.
- NEFF, J., MCKELVIE, S. and AYERS, R.**, 2000. Environmental Impacts of Synthetic Based Drilling Fluids. US Department of Interior Minerals Management Services, Gulf of Mexico OCS Region,
- NGUYEN, Q.T. and BAIRD, D.G.**, 2006. Preparation of polymer–clay nanocomposites and their properties. *Advances in Polymer Technology: Journal of the Polymer Processing Institute*, 25(4), pp. 270-285
- NIU, J.**, 2016. Formation mechanisms of tubular structure of halloysite. *Developments in Clay Science*. Elsevier. pp. 387-408
- NJUGUNA, J., PIELICHOWSKI, K. and DESAI, S.**, 2008. Nanofiller-reinforced polymer nanocomposites. *Polymers for Advanced Technologies*, 19(8), pp. 947-959
- OGATA, N., JIMENEZ, G., KAWAI, H. AND OGIHARA, T.**, 1997. Structure and thermal/mechanical properties of poly (l-lactide)-clay blend. *Journal of Polymer Science Part B: Polymer Physics*, 35(2), pp. 389-396
- OIL & GAS UK**, 2015. Cuttings circulating in drilling fluid. Available at: <http://www.rigzone.com/images/howitworks/drillcuttings.gif>

- OKADA, A. and USUKI, A.**, 2006. Twenty years of polymer-clay nanocomposites. *Macromolecular materials and Engineering*, 291(12), pp. 1449-1476
- ONWUKWE, S. and NWAKAUDU, M.**, 2012. Drilling wastes generation and management approach. *International Journal of Environmental Science and Development*, 3(3), pp. 252
- ORMELOH, J.**, 2014. Thermomechanical cuttings cleaner–qualification for offshore treatment of oil contaminated cuttings on the Norwegian continental shelf and Martin Linge case study,
- OSPAR Commission**, 2015. OSPAR convention. In Available at: □ <https://www.ospar.org/convention> [accessed 23 February 2018].
- OUHADI, V. and YONG, R.**, 2003. Impact of clay microstructure and mass absorption coefficient on the quantitative mineral identification by XRD analysis. *Applied Clay Science*, 23(1-4), pp. 141-148
- PAGE, P.W., GREAVES, C., LAWSON, R., HAYES, S. and BOYLE, F.**, 2003. Options for the recycling of drill cuttings. SPE/EPA/DOE Exploration and Production Environmental Conference. Society of Petroleum Engineers.
- PAMUKCU, S., HIJAZI, M. and FANG, H.**, 1990. Study of possible reuse of stabilized petroleum contaminated soils as construction material. *Petroleum Contaminated Soils*, , pp. 203-214
- PAPPALARDO, S., RUSSO, P., ACIERNO, D., RABE, S. AND SCHARTEL, B.**, 2016. The synergistic effect of organically modified sepiolite in intumescent flame retardant polypropylene. *European Polymer Journal*, 76, pp. 196-207
- PARIJA, S., NAYAK, S.K. and JENA, S.**, 2007. Linear low density polyethylene/clay nanocomposites: Influence of MAH-g-PE as compatibilizer loading on the physico-mechanical properties and crystallization characteristics. *Polymer-Plastics Technology and Engineering*, 46(2), pp. 183-189
- PARLIAMENT E. DIRECTIVE** 2008/98/EC of the European Parliament and of the Council on waste and repealing certain Directives. *Official Journal of the European Union*, L. 2008; 312:3-30.
- PASHAEI, S. AND HOSSEINZADEH, S.**, 2016. Preparation of organo nanoclay incorporated polyamide/melamine cyanurate/nanoclay composites and study on thermal and mechanical behaviours. *Iranian Chemical Communication*, 4, pp. 102-114
- PATEL, A.D., MI LLC**, 2007. *Method for using reversible phase oil-based drilling fluid*. U.S. Patent 7,178,594.
- PAVLIDOU, S. and PAPASPYRIDES, C.**, 2008. A review on polymer–layered silicate nanocomposites. *Progress in polymer science*, 33(12), pp. 1119-1198
- PEETERBROECK, S., ALEXANDRE, M., NAGY, J.B., PIRLOT, C., FONSECA, A., MOREAU, N., PHILIPPIN, G., DELHALLE, J., MEKHALIF, Z., SPORKEN, R. AND BEYER,**

G., 2004. Polymer-layered silicate–carbon nanotube nanocomposites: unique nanofiller synergistic effect. *Composites Science and Technology*, 64(15), pp. 2317-2323

PENDLETON, S.J., 2014. The migration of radioactive caesium and strontium through a bentonite-like clay,

PEREIRA, C. and MARTINS, M., 2014. Flame retardancy of fiber-reinforced polymer composites based on nanoclays and carbon nanotubes. *Polymer Green Flame Retardants*. Elsevier. pp. 551-595

PHILLIPS, C., EVANS, J., HOM, W. AND CLAYTON, J., 1998. Long-term changes in sediment barium inventories associated with drilling-related discharges in the Santa Maria Basin, California, USA. *Environmental Toxicology and Chemistry: An International Journal*, 17(9), pp. 1653-1661

PISZCZ, K., LUCZAK, J. and HUPKA, J., 2014. Mobility of shale drill cuttings constituents. *Physicochemical Problems of Mineral Processing*, 50

POPPE, L.J., PASKEVICH, V.F., HATHAWAY, J.C. AND BLACKWOOD, D.S., 2001. A laboratory manual for X-ray powder diffraction. US Geological Survey open-file report, 1(041), pp. 1-88

POTTS, J.R., DREYER, D.R., BIELAWSKI, C.W. AND RUOFF, R.S., 2011. Graphene-based polymer nanocomposites. *Polymer*, 52(1), pp. 5-25

POZEBON, D., LIMA, E.C., MAIA, S.M. AND FACHEL, J.M., 2005. Heavy metals contribution of non-aqueous fluids used in offshore oil drilling. *Fuel*, 84(1), pp. 53-61

PRAMODA, K.P., LIU, T., LIU, Z., HE, C. AND SUE, H.J., 2003. Thermal degradation behavior of polyamide 6/clay nanocomposites. *Polymer Degradation and Stability*, 81(1), pp. 47-56

PRIOLO, M.A., GAMBOA, D. and GRUNLAN, J.C., 2010. Transparent clay– polymer nano brick wall assemblies with tailorable oxygen barrier. *ACS Applied Materials & Interfaces*, 2(1), pp. 312-320

PRIOLO, M.A., HOLDER, K.M., GAMBOA, D. AND GRUNLAN, J.C., 2011. Influence of clay concentration on the gas barrier of clay–polymer nanobrick wall thin film assemblies. *Langmuir*, 27(19), pp. 12106-12114

QIN, H., SU, Q., ZHANG, S., ZHAO, B. AND YANG, M., 2003. Thermal stability and flammability of polyamide 66/montmorillonite nanocomposites. *Polymer*, 44(24), pp. 7533-7538

QIN, H., ZHANG, S., ZHAO, C., FENG, M., YANG, M., SHU, Z. AND YANG, S., 2004. Thermal stability and flammability of polypropylene/montmorillonite composites. *Polymer Degradation and Stability*, 85(2), pp.807-813.

RABIA, H., 2002. *Well Engineering & Construction*. Entrac Consulting Limited London.

RANA, S., 2008. Facts and data on environmental risks-oil and gas drilling operations. SPE Asia Pacific Oil and Gas Conference and Exhibition. Society of Petroleum Engineers.

RANE, A.V., KANNY, K., ABITHA, V.K. AND THOMAS, S., 2018. Methods for synthesis of nanoparticles and fabrication of nanocomposites. Synthesis of inorganic nanomaterials. Elsevier. pp. 121-139

RAO, Y. and POCHAN, J.M., 2007. Mechanics of polymer- clay nanocomposites. *Macromolecules*, 40(2), pp. 290-296

RAY, S.S. and OKAMOTO, M., 2003. Polymer/layered silicate nanocomposites: a review from preparation to processing. *Progress in polymer science*, 28(11), pp. 1539-1641

REDDOCH, J., 2001. Method and apparatus for collecting, defluidizing and disposing of oil and gas well drill cuttings,

RIGHTMIRE, C., 1984. Description and hydrogeologic implications of cored sedimentary material from the 1975 drilling program at the Radioactive Waste Management Complex, Idaho. *Water-Resources Investigations Report*, 84, pp. 4071

ROBINSON, J.P., KINGMAN, S.W., SNAPE, C.E., BARRANCO, R., SHANG, H., BRADLEY, M.S.A. AND BRADSHAW, S.M., 2009. Remediation of oil-contaminated drill cuttings using continuous microwave heating. *Chemical Engineering Journal*, 152(2-3), pp. 458-463

SAASEN, A., OMLAND, T.H., EKRENE, S., BREVIERE, J., VILLARD, E., KAAGESON-LOE, N., TEHRANI, A., CAMERON, J., FREEMAN, M.A. and GROWCOCK, F., 2008. Automatic measurement of drilling fluid and drill cuttings properties. IADC/SPE drilling conference. Society of Petroleum Engineers.

SACHSE, S., SILVA, F., ZHU, H., IRFAN, A., LESZCZYŃSKA, A., PIELICHOWSKI, K., ERMINI, V., BLAZQUEZ, M., KUZMENKO, O. AND NJUGUNA, J., 2012. The effect of nanoclay on dust generation during drilling of PA6 nanocomposites. *Journal of Nanomaterials*, 2012

SADIQ, R. and HUSAIN, T., 2005. A fuzzy-based methodology for an aggregative environmental risk assessment: a case study of drilling waste. *Environmental Modelling & Software*, 20(1), pp. 33-46

SADIQ, R., HUSAIN, T., VEITCH, B. AND BOSE, N., 2003. Marine water quality assessment of synthetic-based drilling waste discharges. *International journal of environmental studies*, 60(4), pp.313-323.

SAHOO, N.G., RANA, S., CHO, J.W., LI, L. AND CHAN, S.H., 2010. Polymer nanocomposites based on functionalized carbon nanotubes. *Progress in polymer science*, 35(7), pp. 837-867

SAIN, M., PARK, S.H., SUHARA, F. AND LAW, S., 2004. Flame retardant and mechanical properties of natural fibre–PP composites containing magnesium hydroxide. *Polymer Degradation and Stability*, 83(2), pp. 363-367

SAMPER-MADRIGAL, M.D., FENOLLAR, O., DOMINICI, F., BALART, R. AND KENNY, J.M., 2015. The effect of sepiolite on the compatibilization of polyethylene–thermoplastic starch blends for environmentally friendly films. *Journal of Materials Science*, 50(2), pp. 863-872

SAMYN, F., BOURBIGOT, S., JAMA, C. AND BELLAYER, S., 2008. Fire retardancy of polymer clay nanocomposites: Is there an influence of the nanomorphology? *Polymer Degradation and Stability*, 93(11), pp. 2019-2024

SÁNCHEZ-VALDES, S., IBARRA-ALONSO, M.C., RAMÍREZ-VARGAS, E., RAMOS-DEVALLE, L.F., ESPINOZA-MARTÍNEZ, A.B., VALERA-ZARAGOZA, M., NARRO-CÉSPEDES, R.I. and CABRERA-ÁLVAREZ, E.N., 2017. Effect of Compatibilizer on Polyethylene/Clay/Silver Nanocomposite Properties. *Macromolecular Symposia*. Wiley Online Library. pp. 1600115

SÁNCHEZ-VALDES, S., LÓPEZ-QUINTANILLA, M.L., RAMÍREZ-VARGAS, E., MEDELLÍN-RODRÍGUEZ, F.J. AND GUTIERREZ-RODRIGUEZ, J.M., 2006. Effect of ionomeric compatibilizer on clay dispersion in polyethylene/clay nanocomposites. *Macromolecular Materials and Engineering*, 291(2), pp. 128-136

SCARFATO, P., INCARNATO, L., DI MAIO, L., DITTRICH, B. AND SCHARTEL, B., 2016. Influence of a novel organo-silylated clay on the morphology, thermal and burning behavior of low density polyethylene composites. *Composites Part B: Engineering*, 98, pp. 444-452

SCHICK, C., WURM, A. and MOHAMED, A., 2001. Vitrification and devitrification of the rigid amorphous fraction of semicrystalline polymers revealed from frequency-dependent heat capacity. *Colloid and Polymer Science*, 279(8), pp. 800-806

SCHICK, C., 2009. Study Rigid Amorphous Fraction in Polymer Nano-Composites by StepScan and HyperDSC,

SEYMOUR, R.B. and KIRSHENBAUM, G.S., 1986. High performance polymers, their origin and development. Springer.

SHAH, K.J., SHUKLA, A.D., SHAH, D.O. AND IMAE, T., 2016. Effect of organic modifiers on dispersion of organoclay in polymer nanocomposites to improve mechanical properties. *Polymer*, 97, pp. 525-532

SHAH, R.K. and PAUL, D.R., 2006. Organoclay degradation in melt processed polyethylene nanocomposites. *Polymer*, 47(11), pp. 4075-4084

SHEN, M., MARTINSON, L., WAGNER, M.S., CASTNER, D.G., RATNER, B.D. AND HORBETT, T.A., 2002. PEO-like plasma polymerized tetraglyme surface interactions with

leukocytes and proteins: in vitro and in vivo studies. *Journal of Biomaterials Science, Polymer Edition*, 13(4), pp. 367-390

SHENG, N., BOYCE, M.C., PARKS, D.M., RUTLEDGE, G.C., ABES, J.I. AND COHEN, R.E., 2004. Multiscale micromechanical modeling of polymer/clay nanocomposites and the effective clay particle. *Polymer*, 45(2), pp. 487-506

SHIH, Y.F., CHOU, M.Y., CHANG, W.C., LIAN, H.Y. AND CHEN, C.M., 2017. Completely biodegradable composites reinforced by the cellulose nanofibers of pineapple leaves modified by eco-friendly methods. *Journal of Polymer Research*, 24(11), pp. 209

SHISHAN, W., DINGJUN, J., XIAODONG, O., FEN, W. AND JIAN, S., 2004. The structure and properties of PA6/MMT nanocomposites prepared by melt compounding. *Polymer Engineering & Science*, 44(11), pp. 2070-2074

SICHINA, W., 2000. Measurement of Tg by DSC. *Thermal Analysis: Application Note*. Perkin Elmer ZDA: Norwalk, CT,

SIDDIQUE, S., KWOFFIE, L., ADDAE-AFOAKWA, K., YATES, K. and NJUGUNA, J., 2017. Oil based drilling fluid waste: an overview on environmentally persistent pollutants. *IOP conference series: materials science and engineering*. IOP Publishing. pp. 012008

SIDDIQUE, S., KWOFFIE, L., ADDAE-AFOAKWA, K., YATES, K. AND NJUGUNA, J., 2019a. The crystallinity and thermal degradation behaviour of polyamide 6/Oil Based Mud Fillers (PA6/OBMFs) nanocomposites. *Polymer degradation and stability*, 159, pp.139-152

SIDDIQUE, S., SMITH, G.D., YATES, K., MISHRA, A.K., MATTHEWS, K., CSETENYI, L.J. AND NJUGUNA, J., 2019b. Structural and thermal degradation behaviour of reclaimed clay nano-reinforced low-density polyethylene nanocomposites. *Journal of Polymer Research*, 26(6), pp. 154

SIDDIQUE, S., YATES, K. AND NJUGUNA, J., 2018; Characterisation of oil based mud waste to explore the possibility in transforming waste into a value added product. Presented at the 6th International conference on sustainable solid waste management (NAXOS 2018), 13-16 June 2018, Naxos, Greece. Athens: National Technical University of Athens [online], paper number 45. Available from: http://uest.ntua.gr/nax...S2018_Siddique_etal.pdf.

SILVA, F., NJUGUNA, J., SACHSE, S., PIELICHOWSKI, K., LESZCZYNSKA, A. AND GIACOMELLI, M., 2013. The influence of multiscale fillers reinforcement into impact resistance and energy absorption properties of polyamide 6 and polypropylene nanocomposite structures. *Materials & Design*, 50, pp. 244-252

SINGH, V.P., KAPUR, G. and CHOUDHARY, V., 2016. High-density polyethylene/needle-like sepiolite clay nanocomposites: effect of functionalized polymers on the dispersion of nanofiller, melt extensional and mechanical properties. *RSC advances*, 6(64), pp. 59762-59774

SMITH, K.P., ARNISH, J.J., WILLIAMS, G.P. AND BLUNT, D.L., 2003. Assessment of the disposal of radioactive petroleum industry waste in nonhazardous landfills using risk-based modeling,

SOCRATES, G., 2004. Infrared and Raman characteristic group frequencies: tables and charts. John Wiley & Sons.

SPE INTERNATIONAL. DRILLING FLUID TYPES. 2015; Available at: http://petrowiki.org/Drilling_fluid_types. Accessed 04/14/2016.

STEINSVÅG, K., BRÅTVEIT, M., MOEN, B., LI, V., AUSTGULEN, T., HOLLUND, B.E., HAALAND, I.M., NÆRHEIM, J., SVENDSEN, K. AND KROMHOUT, H., 2008. Expert assessment of exposure to carcinogens in Norway's offshore petroleum industry. *Journal of exposure science & environmental epidemiology*, 18(2), pp.175-182.

STRAWHECKER, K. and MANIAS, E., 2000. Structure and properties of poly (vinyl alcohol)/Na montmorillonite nanocomposites. *Chemistry of materials*, 12(10), pp. 2943-2949

SUN, L., GIBSON, R.F., GORDANINEJAD, F. AND SUHR, J., 2009. Energy absorption capability of nanocomposites: a review. *Composites Science and Technology*, 69(14), pp. 2392-2409

SUN, T. and GARCES, J.M., 2002. High-Performance Polypropylene–Clay Nanocomposites by In-situ Polymerization with Metallocene/Clay Catalysts. *Advanced Materials*, 14(2), pp. 128-130

SUSICH, M.L. and SCHWENNE, M.W., 2004. Onshore drilling waste management: Beneficial reuse of cuttings. SPE International Conference on Health, Safety, and Environment in Oil and Gas Exploration and Production. Society of Petroleum Engineers.

TAIWO, E. and OTOLORIN, J., 2009. Oil recovery from petroleum sludge by solvent extraction. *Petroleum Science and Technology*, 27(8), pp. 836-844

THERMTECH, A., 2012. Thermomechanical Cuttings Cleaner (TCC): Setting the global Standard for the treatment of oily drill cuttings. 2006. Available at: <http://www.thermtech.no>. Accessed in: oct, 31

TJONG, S., MENG, Y. and XU, Y., 2002. Structure and properties of polyamide-6/vermiculite nanocomposites prepared by direct melt compounding. *Journal of Polymer Science Part B: Polymer Physics*, 40(24), pp. 2860-2870

TRAN, N.H., DENNIS, G.R., MILEV, A.S., KANNANGARA, G.K., WILSON, M.A. AND LAMB, R.N., 2005. Interactions of sodium montmorillonite with poly (acrylic acid). *Journal of colloid and interface science*, 290(2), pp. 392-396

TULLOW OIL, 2009. Annex B drilling report formatted FH 23Jul09.doc - jubilee-field-eia-annex-b27.pdf. Available at: <https://www.tulloil.com/Media/docs/default-source/operations/ghana-eia/environmental-impact-statement/jubilee-field-eia-annex-b27.pdf?sfvrsn=2>

- TUNCAN, A., TUNCAN, M. and KOYUNCU, H.**, 2000. Use of petroleum-contaminated drilling wastes as sub-base material for road construction. *Waste Management & Research*, 18(5), pp. 489-505
- UDDIN, F.**, 2008. Clays, nanoclays, and montmorillonite minerals. *Metallurgical and Materials Transactions A*, 39(12), pp. 2804-2814
- USUKI, A., HASEGAWA, N., KATO, M. AND KOBAYASHI, S.**, 2005. Polymer-clay nanocomposites. *Inorganic polymeric nanocomposites and membranes*. Springer. pp. 135-195
- USUKI, A., KOJIMA, Y., KAWASUMI, M., OKADA, A., FUKUSHIMA, Y., KURAUCHI, T. AND KAMIGAITO, O.**, 1993. Synthesis of nylon 6-clay hybrid. *Journal of Materials Research*, 8(5), pp. 1179-1184
- UNITED STATES ENVIRONMENTAL PROTECTION AGENCY**, 2000. Development Document for Final Effluent Limitations Guidelines and Standards for Synthetic-Based Drilling Fluids and other Non-Aqueous Drilling Fluids in the Oil and Gas Extraction point source. EPA 821 B 00-013(December 2000)
- VAIA, R.A. and GIANNELIS, E.P.**, 1997. Polymer melt intercalation in organically-modified layered silicates: model predictions and experiment. *Macromolecules*, 30(25), pp. 8000-8009
- VAIA, R.A., PRICE, G., RUTH, P.N., NGUYEN, H.T. AND LICHTENHAN, J.**, 1999. Polymer/layered silicate nanocomposites as high performance ablative materials. *Applied Clay Science*, 15(1-2), pp. 67-92
- VASANTHAN, N. and SALEM, D.**, 2001. FTIR spectroscopic characterization of structural changes in polyamide-6 fibers during annealing and drawing. *Journal of Polymer Science Part B: Polymer Physics*, 39(5), pp. 536-547
- VEIL, J.A.**, 2002. Drilling waste management: past, present, and future. SPE annual technical conference and exhibition. Society of Petroleum Engineers.
- VLAEV, L., TURMANOVA, S. and DIMITROVA, A.**, 2009. Kinetics and thermodynamics of water adsorption onto rice husks ash filled polypropene composites during soaking. *Journal of polymer research*, 16(2), pp. 151-164
- WANG, K.H., CHOI, M.H., KOO, C.M., CHOI, Y.S. AND CHUNG, I.J.**, 2001. Synthesis and characterization of maleated polyethylene/clay nanocomposites. *Polymer*, 42(24), pp. 9819-9826
- WANG, N., CHENG, K., WU, H., WANG, C., WANG, Q. AND WANG, F.**, 2012. Effect of nano-sized mesoporous silica MCM-41 and MMT on corrosion properties of epoxy coating. *Progress in Organic Coatings*, 75(4), pp. 386-391
- WANG, R., LIU, J., GAO, F., ZHOU, J. AND CEN, K.**, 2012. The slurring properties of slurry fuels made of petroleum coke and petrochemical sludge. *Fuel Processing Technology*, 104, pp. 57-66

WANG, Y., CHEN, F.B., LI, Y.C. AND WU, K.C., 2004. Melt processing of polypropylene/clay nanocomposites modified with maleated polypropylene compatibilizers. *Composites Part B: Engineering*, 35(2), pp. 111-124

WANG, Y., HUANG, G. and ZHENG, J., 2016. Mechanochemistry modified waste rubber powder and its application in hydrogel. *Journal of Polymer Research*, 23(12), pp. 259

WEIL, E.D. and LEVCHIK, S.V., 2008. Flame retardants in commercial use or development for textiles. *Journal of Fire Sciences*, 26(3), pp. 243-281

WEN, X., WANG, Y., GONG, J., LIU, J., TIAN, N., WANG, Y., JIANG, Z., QIU, J. AND TANG, T., 2012. Thermal and flammability properties of polypropylene/carbon black nanocomposites. *Polymer Degradation and Stability*, 97(5), pp. 793-801

WILLIAMSON IV, W.P., WARD, T.J. AND WHITLATCH, S.P., BIOPATH AUTOMATION LLC, 2007. *Cassette for handling and holding tissue samples during processing, embedding and microtome procedures, and methods therefor*. U.S. Patent 7,179,424.

WU, T. and WU, J., 2002. Structural analysis of polyamide/clay nanocomposites. *Journal of Macromolecular Science, Part B*, 41(1), pp. 17-31

WURM, A., ISMAIL, M., KRETZSCHMAR, B., POSPIECH, D. AND SCHICK, C., 2010. Retarded crystallization in polyamide/layered silicates nanocomposites caused by an immobilized interphase. *Macromolecules*, 43(3), pp. 1480-1487

XIE, L., LV, X.Y., HAN, Z.J., CI, J.H., FANG, C.Q. AND REN, P.G., 2012. Preparation and performance of high-barrier low density polyethylene/organic montmorillonite nanocomposite. *Polymer-Plastics Technology and Engineering*, 51(12), pp. 1251-1257

XIE, W., GAO, Z., LIU, K., PAN, W.P., VAIA, R., HUNTER, D. AND SINGH, A., 2001. Thermal characterization of organically modified montmorillonite. *Thermochimica Acta*, 367, pp. 339-350

XU, B., ZHENG, Q., SONG, Y. AND SHANGGUAN, Y., 2006. Calculating barrier properties of polymer/clay nanocomposites: Effects of clay layers. *Polymer*, 47(8), pp. 2904-2910

XU, T., WANG, X., LI, T. AND ZHAN, X., 2018. Heavy metal pollution of oil-based drill cuttings at a shale gas drilling field in Chongqing, China: A human health risk assessment for the workers. *Ecotoxicology and environmental safety*, 165, pp. 160-163

YU, Z.Z., YAN, C., YANG, M. AND MAI, Y.W., 2004. Mechanical and dynamic mechanical properties of nylon 66/montmorillonite nanocomposites fabricated by melt compounding. *Polymer International*, 53(8), pp. 1093-1098

ZANETTI, M., BRACCO, P. and COSTA, L., 2004. Thermal degradation behaviour of PE/clay nanocomposites. *Polymer Degradation and Stability*, 85(1), pp. 657-665

ZAPATA, P., QUIJADA, R., RETUER, J. AND MONCADA, E., 2008. Preparation of nanocomposites by in situ polymerization. *Journal of the Chilean Chemical Society*, 53(1), pp. 1359-1360

- ZARE, Y.**, 2016. Effects of imperfect interfacial adhesion between polymer and nanoparticles on the tensile modulus of clay/polymer nanocomposites. *Applied Clay Science*, 129, pp. 65-70
- ZARE, Y., RHEE, K.Y. and PARK, S.**, 2019. A modeling methodology to investigate the effect of interfacial adhesion on the yield strength of MMT reinforced nanocomposites. *Journal of industrial and engineering chemistry*, 69, pp. 331-337
- ZHANG, J. and WILKIE, C.A.**, 2003. Preparation and flammability properties of polyethylene–clay nanocomposites. *Polymer Degradation and Stability*, 80(1), pp. 163-169
- ZHANG, M. and SUNDARARAJ, U.**, 2006. Thermal, rheological, and mechanical behaviors of LLDPE/PEMA/clay nanocomposites: effect of interaction between polymer, compatibilizer, and nanofiller. *Macromolecular Materials and Engineering*, 291(6), pp. 697-706
- ZHAO, C., QIN, H., GONG, F., FENG, M., ZHANG, S. AND YANG, M.**, 2005. Mechanical, thermal and flammability properties of polyethylene/clay nanocomposites. *Polymer Degradation and Stability*, 87(1), pp. 183-189
- ZHAO, H., ZHAO, G., TURNG, L.S. AND PENG, X.**, 2015. Enhancing nanofiller dispersion through prefoaming and its effect on the microstructure of microcellular injection molded polylactic acid/clay nanocomposites. *Industrial & Engineering Chemistry Research*, 54(28), pp. 7122-7130
- ZHAO, Y., ZOU, X., LIU, Q., WANG, C., GE, C. AND XU, M.**, 2018. Clay mineralogy indicates the muddy sediment provenance in the estuarine-inner shelf of the East China Sea. *Journal of Asian Earth Sciences*, 152, pp. 69-79
- ZHENG, H., ZHANG, Y., PENG, Z. AND ZHANG, Y.**, 2004. Influence of clay modification on the structure and mechanical properties of EPDM/montmorillonite nanocomposites. *Polymer Testing*, 23(2), pp. 217-223
- ZHONG, H., QIU, Z., HUANG, W. AND CAO, J.**, 2011. Shale inhibitive properties of polyether diamine in water-based drilling fluid. *Journal of Petroleum Science and Engineering*, 78(2), pp. 510-515
- ZHOU, D., ZHANG, Z., TANG, J., WANG, F. AND LIAO, L.**, 2016. Applied properties of oil-based drilling fluids with montmorillonites modified by cationic and anionic surfactants. *Applied Clay Science*, 121, pp. 1-8
- ZOPE, I.S., DASARI, A., GUAN, F. AND YU, Z.Z.**, 2016. Influence of metal ions on thermo-oxidative stability and combustion response of polyamide 6/clay nanocomposites. *Polymer*, 92, pp. 102-113

Appendix A

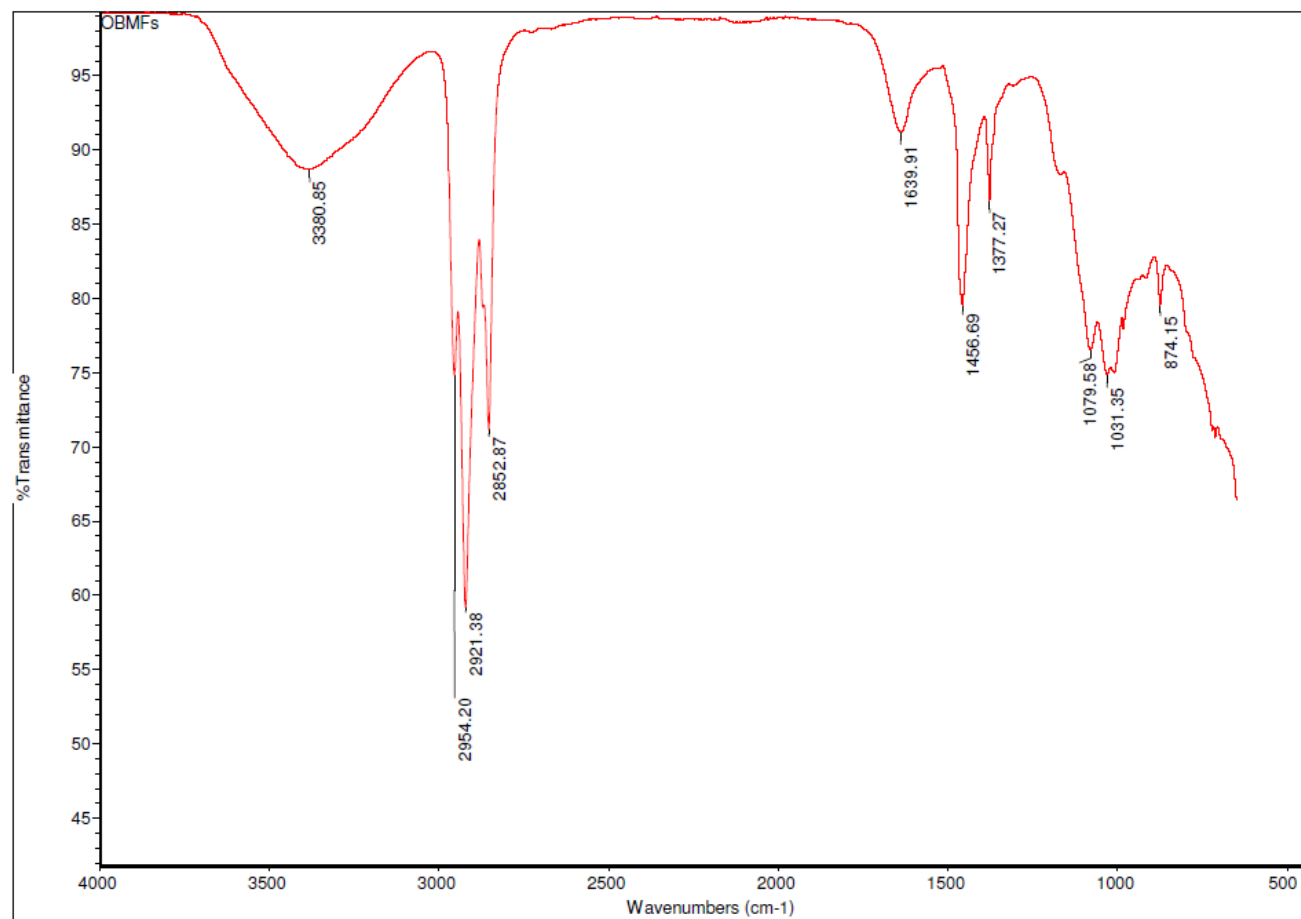


Figure A. 1 OBM waste

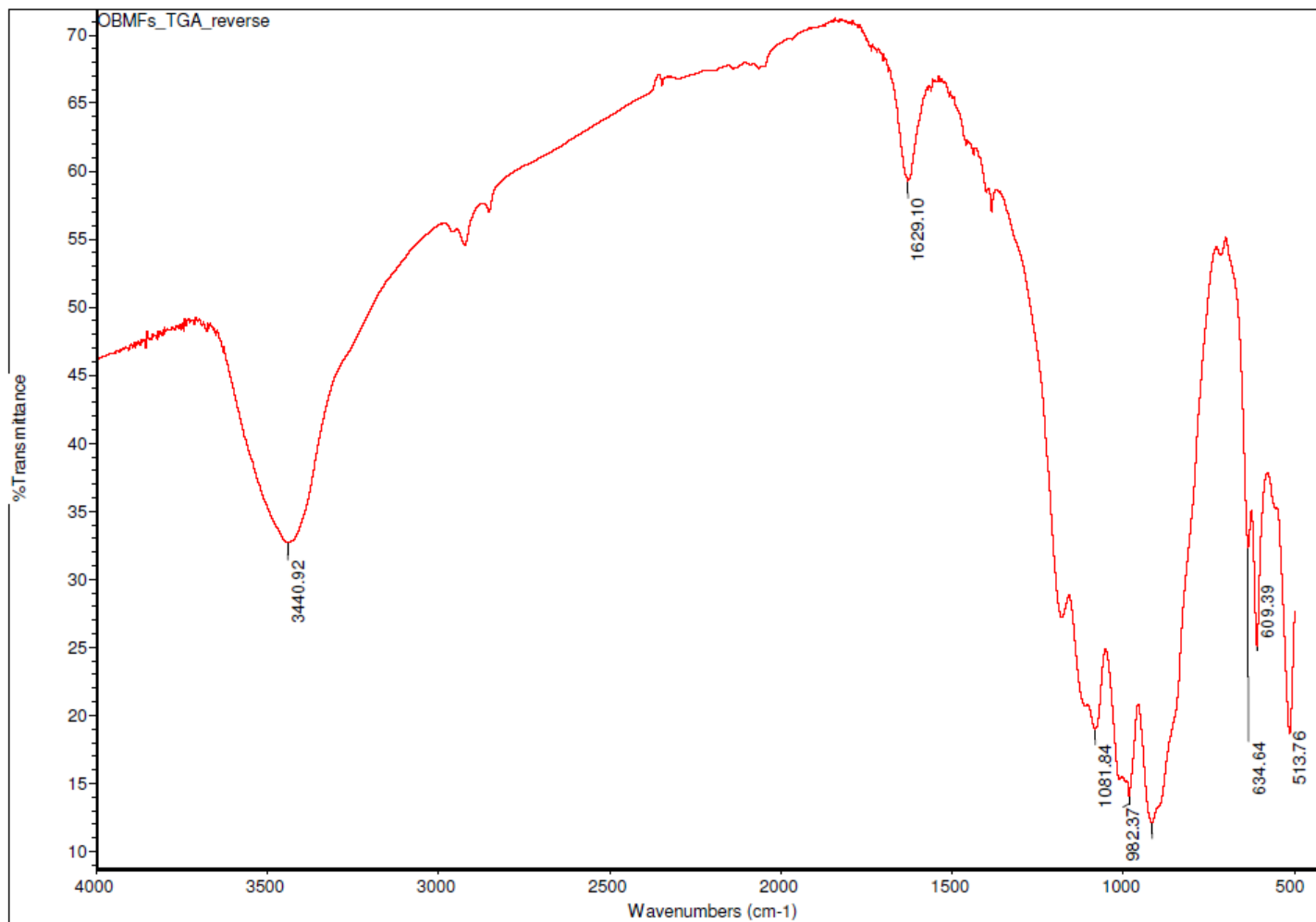


Figure A. 2 OBM waste residue after TGA

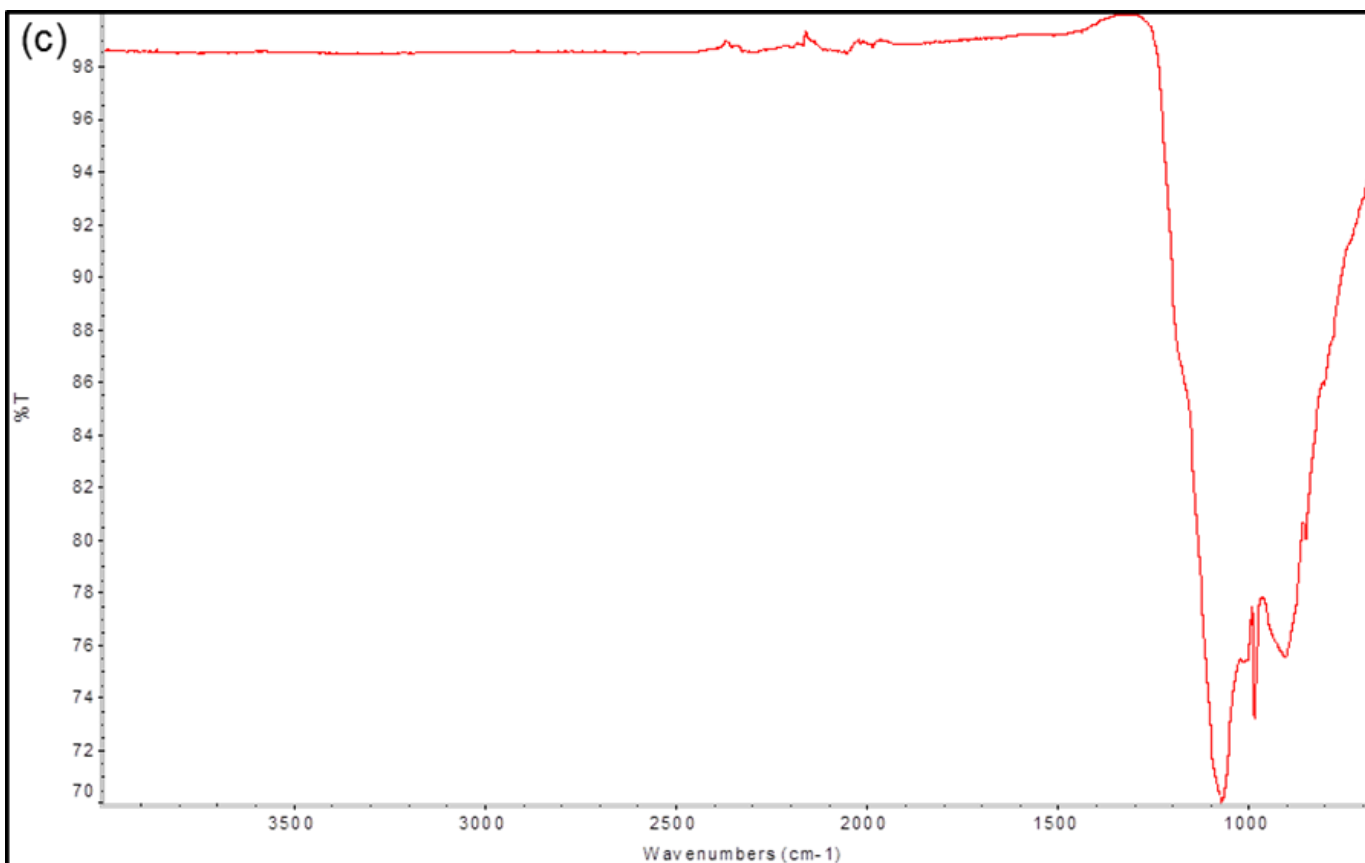


Figure A.3 OBM waste dry powder

Appendix B

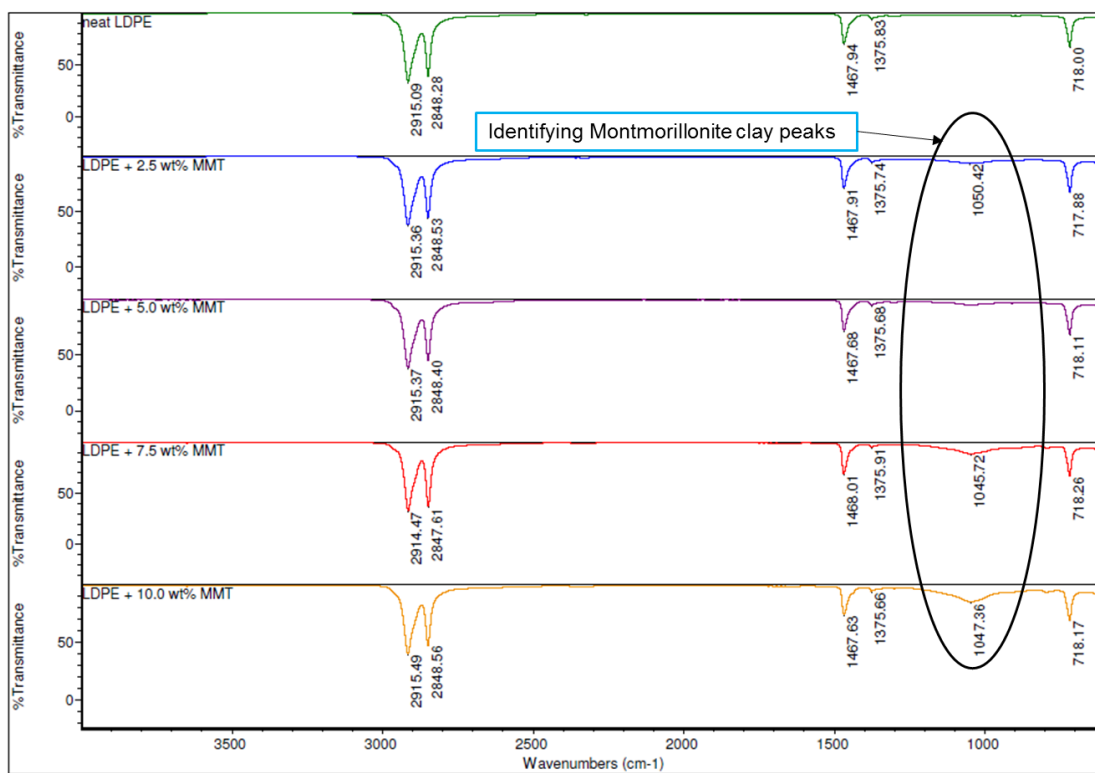


Figure B.1 Comparison of ATR-FTIR spectra of LDPE and LDPE/MMT nanocomposites

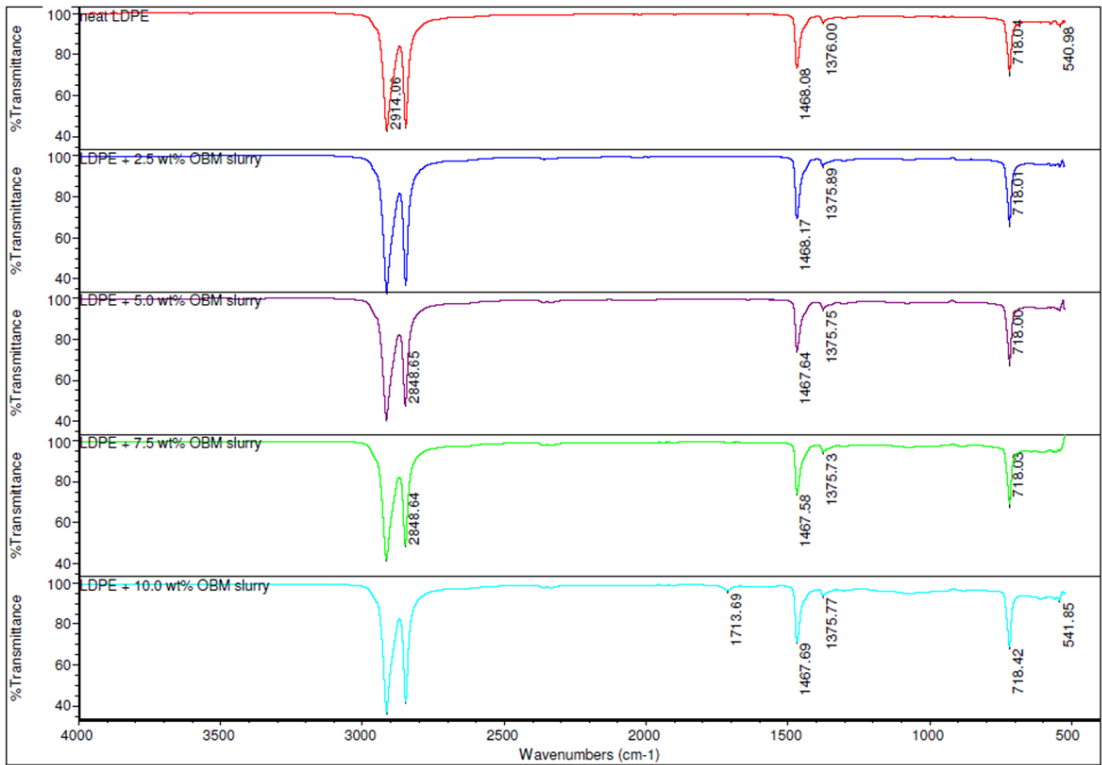


Figure B.2 Comparison of ATR-FTIR spectra of LDPE and LDPE/OBM slurry nanocomposites

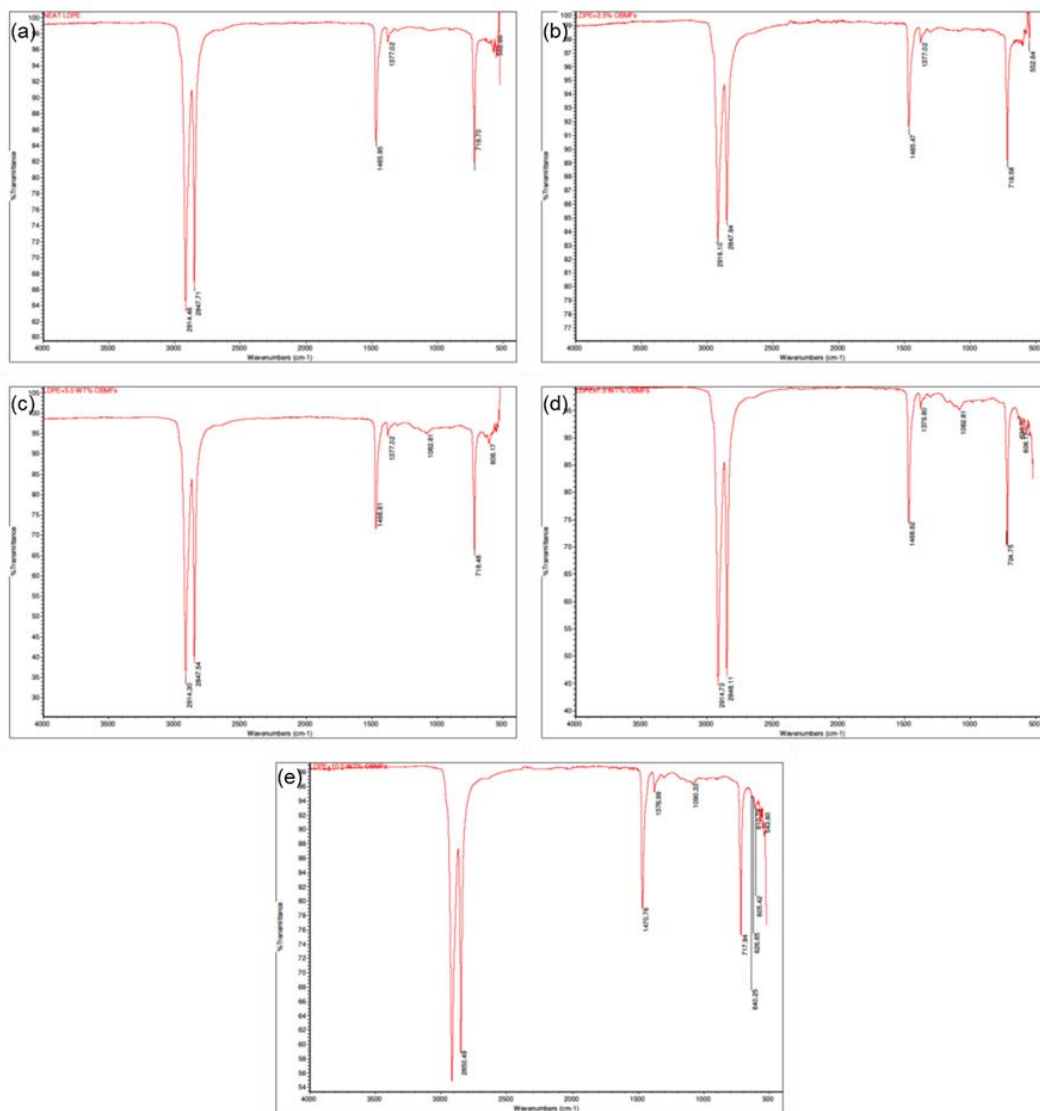


Figure B. 3 FTIR spectra of (a) LDPE; (b) LDPE with 2.5 wt% OBMFs; (c) LDPE with 5.0 wt% OBMFs; (d) LDPE with 7.5 wt% OBMFs; and (e) LDPE with 10.0 wt% OBMFs nanocomposites

Appendix C

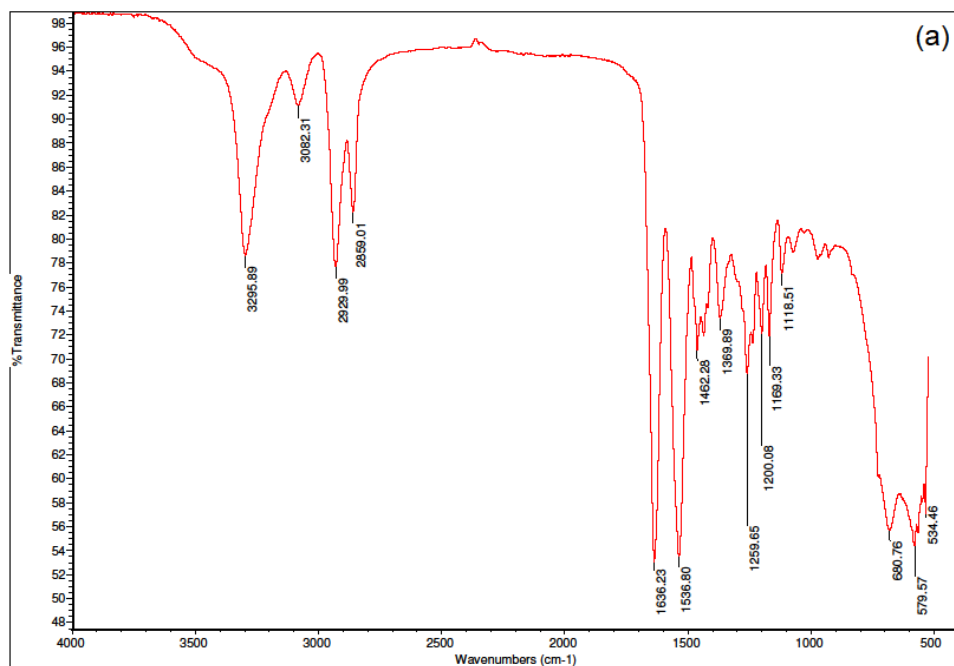


Figure C.1 ATR-FTIR spectra of PA6

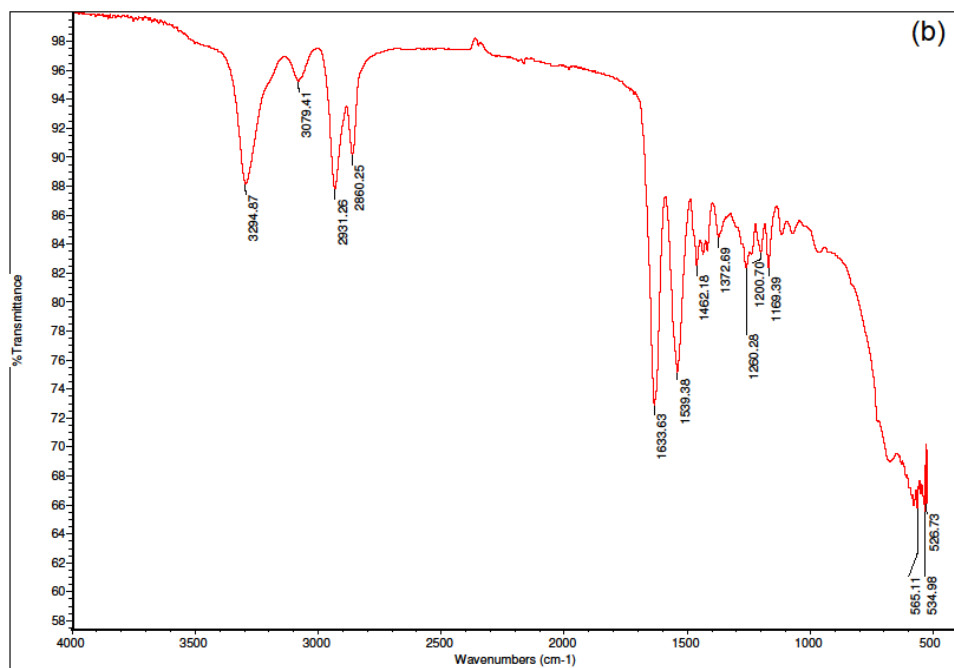


Figure C.2 ATR-FTIR spectra of PA6 with 2.5 wt% OBMFs

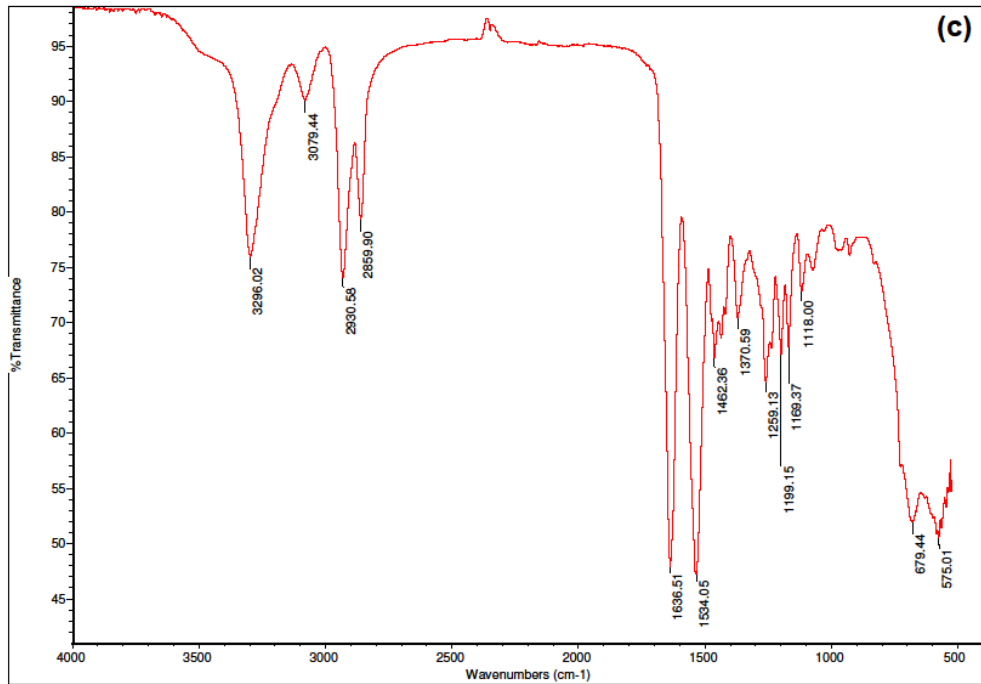


Figure C.3 ATR-FTIR spectra of PA6 with 5 wt% OBMFs

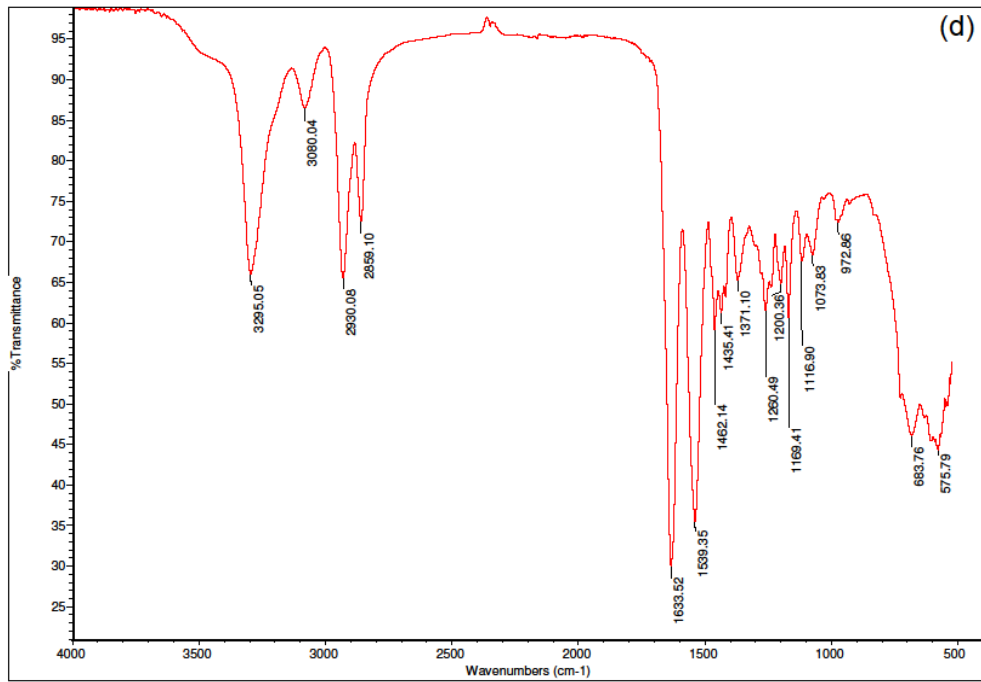


Figure C. 4 ATR-FTIR spectra of PA6 with 7.5 wt% OBMFs

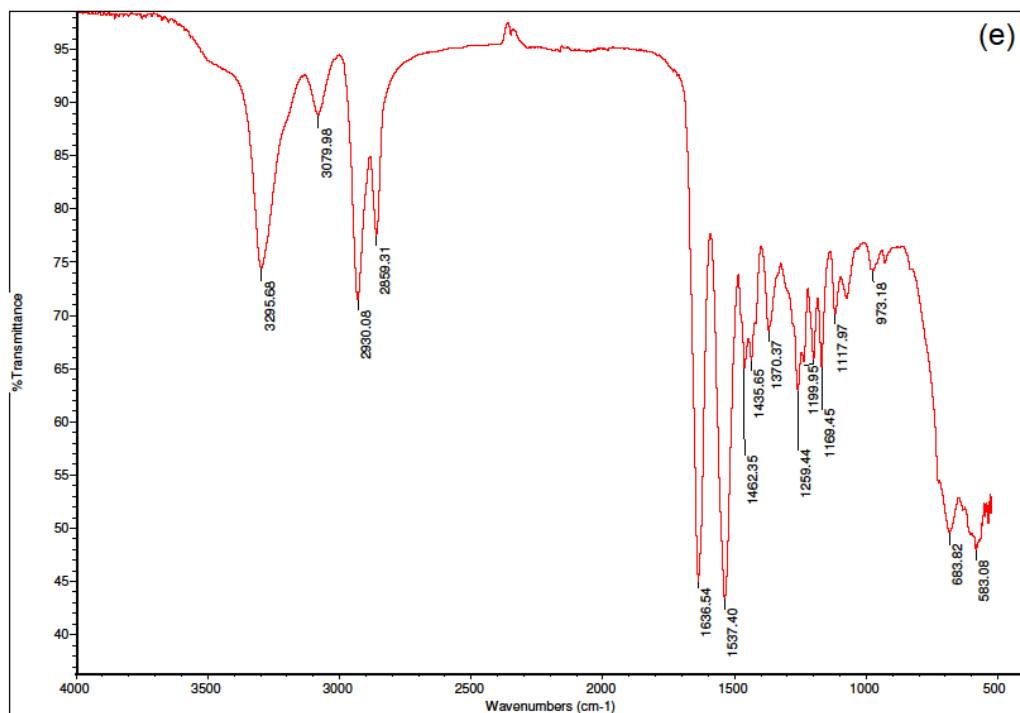


Figure C.5 ATR-FTIR spectra of PA6 with 10 wt% OBMFs

Appendix D

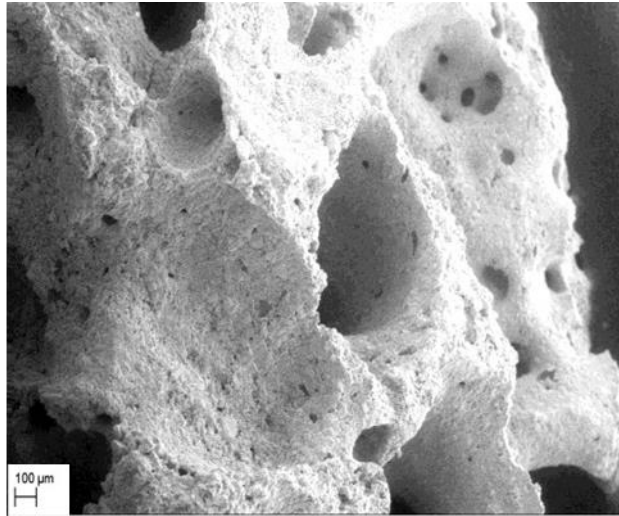


Figure D.1 Inspection of recovered drilling fluid waste (a) visual inspection and (b) SEM analysis

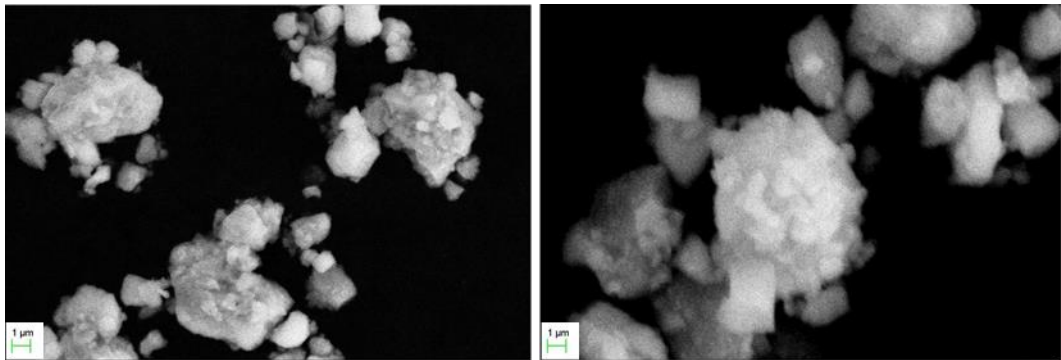


Figure D.2 SEM images of untreated OBMFs in different magnifications settings (a) 10.00 KX and (b) 25.00 KX